

**UNIVERSITY OF CRETE
DEPARTMENT OF CHEMISTRY**

Crystal Engineering, Growth and Design Laboratory



Doctoral Dissertation

**Chemical approaches to the inhibition of metallic
corrosion in geothermal waters**

Stefania Liakaki-Stavropoulou

Thesis Supervisor: Konstantinos Demadis

HERAKLION 2023

**ΠΑΝΕΠΙΣΤΗΜΙΟ ΚΡΗΤΗΣ
ΤΜΗΜΑ ΧΗΜΕΙΑΣ**

Εργαστήριο Μηχανικής, Ανάπτυξης και Σχεδιασμού Κρυστάλλων



Διδακτορική Διατριβή

**Χημικές προσεγγίσεις στην παρεμπόδιση της
μεταλλικής διάβρωσης σε γεωθερμικά ύδατα**

Στεφανία Λιακάκη-Σταυροπούλου

Υπεύθυνος Καθηγητής: Κωνσταντίνος Δημάδης

ΗΡΑΚΛΕΙΟ 2023

Dedicated to my precious Ruby

Examination Committee

Dr. Konstantinos D. Demadis

Professor, Department of Chemistry, University of Crete, *Thesis Supervisor*

Dr. Constantinos Milios

Professor, Department of Chemistry, University of Crete

Dr. Pantelis Trikalitis

Professor, Department of Chemistry, University of Crete

Dr. Apostolos Spyros

Associate Professor, Department of Chemistry, University of Crete

Dr. Constantinos Stoumpos

Associate Professor, Department of Materials Science and Technology, University of Crete

Dr. Antonios Kouloumpis

Assistant Professor, Department of Chemistry, University of Crete

Dr. Nikolaos Katsarakis

Professor, Department of Electrical and Computer Engineering, Hellenic Mediterranean
University

Acknowledgments

First and foremost, I would like to express my deepest appreciation to my supervisor Prof. Konstantinos D. Demadis. From the moment I showed up at his door until today, his support and his guidance has been a vital source of inspiration and motivation.

I'm extremely grateful to the company Kurita Europe for the funding, as well as for the opportunity to meet and collaborate with such remarkable people. Of course, I wish to thank all the members of my thesis committee for taking the time to evaluate this work. Also, I would like to thank Prof. Aurelio Cabeza-Diaz and his research group for their help regarding the powder XRD patterns.

I am thankful for the members of the Crystal Growth, Engineering and Design laboratory. As an athlete, I acknowledge the importance of a team whose members support and help each other. Special thanks to Dr.Iro Spinthaki, Georgia Skordalou, Elpiniki Chachlaki and Apostolis Fanourgiakis for their boost and support.

Words cannot express my gratitude to my friends. I could not have undertaken this journey without their helping hand. I would like to extend my sincere thanks to Dr.Daphne Davelou and to Dr.Argyro Moschona for their advice and encouragement. Being able to share common passions and experiences with my best friends will always be a privilege as I pursue my dreams. My heart is overwhelmed with gratitude for Giorgos Kostopoulos who never fails to make me laugh and is always there for me.

This endeavor would not have been possible without the unconditional love and support of my parents, Penny and Giannis, who stand by my side every day, my whole life. Everything I am, I owe to them.

For helping me get through the most challenging of seasons and find the strength to follow my dreams, for being the man he is, I would like to thank my partner, Giorgos Kalpias.

Curriculum Vitae

Stefania Liakaki-Stavropoulou

Address: Department of Chemistry, University of Crete, Campus Voutes 71003,
Heraklion Crete, Greece

Lab phone: +30 2810 54 5012

Mobile phone: +30 6976232463

e-mail address: stef.liak@hotmail.com

Date of birth: November 15th, 1987

Place of birth: Marousi, Athens, Greece

Nationality: Greek

Education

2023 PhD Candidate at the Department of Chemistry, University of Crete, under the supervision of Professor Konstantinos D. Demadis, titled “Chemical approaches to the inhibition of metallic corrosion in geothermal waters”.

2019 M. Sc. in Chemistry at the University of Crete (Greece).

Postgraduate Research Thesis at the Department of Chemistry, University of Crete, under the supervision of Professor Konstantinos D. Demadis, titled “Synthesis and characterization of Polyhedral Oligomeric Silsesquioxanes (POSS) and their phosphonate derivatives: application as consolidants for the protection of Cultural Heritage”.

2016 B. Sc. in Material Science and Technology at the University of Crete (Greece).

Undergraduate Research Thesis at the Department of Material Science and Technology, University of Crete, under the supervision of Assistant Professor Kelly Velonia, titled

“Synthesis of Biocompatible Responsive *Giant Amphiphiles Molecules* using atom transfer radical polymerization”.

Teaching Experience

- Supervisor of undergraduate / master students in Crystal Growth and Design Lab
- Teaching assistant in the undergraduate Analytical Chemistry Laboratory
- Teaching assistant in the undergraduate Laboratory of “Use of Computers”

Qualifications

- Radical Polymerization (ATRP)
- High Vacuum Handling
- Organic Synthesis
- Chromatography (Electrophoresis, Gel Permeation Chromatography, TLC)
- Nuclear Magnetic Resonance Spectroscopy
- Ultraviolet-Visible Spectroscopy
- ATR-IR Spectroscopy
- Drilling Resistance Measurement System (DRMS)
- Analytical techniques concerning water and wastewater analysis with spectrophotometers such as HACH 1900 of Hach Lange
- Corrosion inhibition and its application in cooling and geothermal environments

Scientific collaborations

- Kurita Europe GmbH in Mannheim, Germany.
- -Intraderma in Heraklion Crete, Greece.

Conferences

- Oral presentation of “Corrosion control of carbon steel with phosphonate-based inhibitors with potential applications in geothermal systems” in EUROCORR 2022: The European Corrosion Congress, Berlin, Germany, 28/8-1/9/**2022**.
- Oral presentation of “Chemical approaches to the inhibition of metallic corrosion in geothermal waters” in Three minute thesis Competition, Heraklion, Crete, Greece, 7/06/**2022**.
- Poster presentation of “Corrosion inhibitors for the protection of carbon steel in geothermal brines” in European Geothermal PhD Days 2022, Aachen, Germany, 27-29/4/**2022**.
- Oral presentation of “Corrosion inhibitors for the protection of carbon steel in geothermal brines” in EUROCORR 2021: The European Corrosion Congress, virtual event, 20-24/9/**2021**.
- Oral presentation of “Corrosion protection of carbon steels under geothermal stresses” in EUROCORR 2020: The European Corrosion Congress, virtual event, 7-11/9/**2020**.
- Oral presentation of “Innovative consolidants for the protection of cultural heritage” in Maria Hatzimarinaki Meeting, Heraklion, Crete, Greece, 22/11/**2019**.
- Oral presentation of “Synthesis and Characterization of Polyhedral Oligomeric Silsesquioxane and Derivatives” in the 20th Chemistry Postgraduates Conference, Heraklion, Crete, 25-27/6/**2018**.
- Poster presentation of “In Situ Hierarchical Formation of Giant Amphiphile Bionanoreactors” in the Multi-Functional Nano-Carbon Composite Materials Conference, Heraklion, Crete, Greece, 19-20/10/**2016**.
- Poster presentation of “Responsive Giant Amphiphile Supramolecular Assemblies” in the 11th Hellenic Polymer Society International Conference, Heraklion, Crete, Greece, 3-5/11/**2016**.

- Poster presentation of “Responsive Giant Amphiphile Supramolecular Assemblies” in the 2nd Israel-Greece Joint Meeting on Nanotechnology & Bionanoscience, Heraklion, Crete, Greece, 25-28/10/**2016**.
- Oral presentation of “Synthesis of Biocompatible Responsive Giant Amphiphiles Molecules using atom transfer radical polymerization” in the 18th Chemistry Postgraduates Conference, Heraklion, Crete, Greece, 26-28/3/**2016**.
- Poster presentation of “In Situ Hierarchical Formation of Giant Amphiphile Bionanoreactors” in the 18th Chemistry Postgraduates Conference, Heraklion, Crete, Greece, 26-28/3/**2016**.

Conferences Presentations (by other researchers)

- The versatility of phosphonate linkers in coordination polymers. Joint CTMNM/NAGC Conference, Spetses Island, Greece, 8-12/5/**2023**.
- Comparative Performance of Tetrakisphosphate and Diphosphate as Reverse Osmosis Scale Inhibitors. 6th International Scientific Conference Integration, Partnership and Innovation in Construction Science and Education, Moscow, Russia 14-16/11/**2018**.
- Comparative Antiscalant Performance of Systematically Variable Tetrakisphosphate and Diphosphate Scale Inhibitors. The 10th Eastern European Young Water Professionals Conference, Zagreb, Croatia, 7-12/5/**2018**.
- Synthesis and comparative performance research of tetrakisphosphate and diphosphate antiscalants with different chemical structure. XXI International Scientific Conference on Advances in Civil Engineering: Construction the Formation of Living Environment (FORM2018), Moscow, Russia, 25-27/4/**2018**.
- In Situ Hierarchical Formation of Giant Amphiphile Bionanoreactors. 2nd Israel-Greece Joint Meeting on Nanotechnology & Bionanoscience, Heraklion, Crete, 25-28/10/**2016**.

Conference Participations

- 19th Postgraduates Conference on Chemistry. Heraklion Crete, Greece, 2-4/5/**2017**.
- Intensive Course on Corrosion and Scale Inhibition: Theory, Testing, Application. Iserlohn, Germany, 18-20/2/**2020**.

Certified Seminars

- 2016** Attestation of Achievement “Nuclear Magnetic Resolution a Compass to Nanoworld” Platform FUN, Université de Lille 1
- 2015** Journal Analysis: Maximizing the chances of getting your work published – Building a research paper (using model like swales and feak’s cars to model and write articles) Associate Professor Tulpesh Patel, Department of Chemistry, University of Crete

Publications

- Andrianov, A.; Danilycheva, M.; Liakaki-Stavropoulou, S.; Demadis, K.D.; Efremov, R. Comparative Performance of Tetrphosphonate and Diphosphonate as Reverse Osmosis Scale Inhibitors, conf. paper MATEC Web of Conferences 251, 03049, 2018.
- Liakaki-Stavropoulou S.; Grammatikakis I.E.; Demadis K.D. Novel, multifunctional consolidants for the mitigation of gypsum stone deterioration at the Knossos Palace, Crete, Greece, **2023**, submitted.

Book Chapters

- M. Kamaratou, S. Liakaki-Stavropoulou, K.D. Demadis. Multifunctional additives for synergistic scale and corrosion inhibition in high stress systems. In Industrial scale inhibition: Principles, design and applications. C. Verma, I.Y. Yaagoob. Editors, 2023, . John Wiley and Sons, Inc., Chapter 20, in press.

Skills

- Data analysis for “The ecological services, social benefits and economic value of the ecosystem services in Natura 2000s sites in Crete [Life13 INF/GR/000188]”
Research supervisor: Christina Archontaki, Museum of Natural History – University of Crete
- Computer operating system: Windows, Linux
Languages: Fortran
Software: Office, Origin, Mestrenova, Bruker TopSpin, ChemDraw, ACDLabs

Abstract

Geothermal brines contain a variety of corrosive dissolved species, such as chloride and sulfate anions that can damage various system metallurgies *via* a number of corrosion processes. Several forms of corrosion can occur, the most common being uniform and pitting corrosion. The combination of low water quality with high-temperature and high-pressure conditions usually accelerate these corrosion processes, with undesirable results to the system's integrity. On the other hand, in addition to the above-mentioned conditions, the different corrosion products (eg. Fe oxides) can form films on the metal surface that influence the corrosion rate.

Among the several metallurgies that can be used in system components, carbon (mild) steel is one that is widely used in industry, due to its compatibility with other metals present, and, primarily, its comparatively low cost. The electrochemical reactions taking place during carbon steel corrosion promote formation of insoluble compounds of oxidized forms of Fe on the metal surface, such as iron oxides (magnetite, hematite) and hydroxides (lepidocrocite).

In this thesis, we furnish comparative results from corrosion inhibition experiments based on two quantifying methods: (a) gravimetric measurements based on the mass loss of each metallic specimen and (b) total iron quantification based on an established photometric methodology (iron-phenanthroline complex). In an effort to understand the corrosion behavior of carbon steel and the factors that influence it, a large number of experiments were carried out under several conditions, by studying the effect of certain variables (temperature, water quality, stirring speed, etc.). Finally, the anti-corrosion efficiency of several chemical additives was evaluated. The inhibitors were categorized as phosphonates and non-phosphonate additives. Emphasis was given to phosphonate-based corrosion inhibitors and their potential synergy with metal cations present in the brines.

The first step was the identification of the corrosion products under the experimental conditions. Lepidocrocite appear to form most often at ambient temperature and at 60 °C, while hematite and magnetite appear to form at higher temperatures. In addition, if bicarbonate is present, the formation of iron carbonate was observed. This study showed that the formation of different corrosion products can affect the corrosion rate.

Overall, the phosphonate inhibitors showed better performance in high salinity water. Furthermore, phosphonates exhibit great inhibition in medium salinity water under high pressure-high temperature conditions. Regarding the non-phosphonate inhibitors, each chemical additive was affected in a different way by the change in the experimental conditions. Two of the non-phosphonate inhibitors exhibited their highest anti-corrosion efficiency in deionized water, while the performance of the other two was best in medium salinity water. This research concluded that the optimum concentration depends on several conditions, such as the temperature and the water quality, regardless of the nature of the inhibitor. Finally, the results of the total iron determination method showed some variance from those of the mass loss measurements, especially in the presence of phosphonates.

Keywords: corrosion, geothermal, corrosion products, inhibitors, phosphonic acids, additives

Περίληψη

Τα γεωθερμικά ύδατα περιέχουν μια ποικιλία από διαλυμένα ιόντα, όπως χλωριούχα και θειικά, που μπορούν να προκαλέσουν προβλήματα σε διάφορα μεταλλικά τμήματα του συστήματος μέσω μιας σειράς διαδικασιών διάβρωσης. Η διάβρωση μπορεί να είναι ομοιόμορφη σε όλη την μεταλλική επιφάνεια ή να έχει εμφανιστεί τοπικά σε αυτή. Ο συνδυασμός χαμηλής ποιότητας νερού με συνθήκες υψηλής θερμοκρασίας και υψηλής πίεσης, συνήθως επιταχύνει τις διαδικασίες διάβρωσης, επηρεάζοντας την ομαλή λειτουργία του γεωθερμικού συστήματος. Εκτός από τις προαναφερθείσες συνθήκες, τα διάφορα προϊόντα διάβρωσης, όπως π.χ. οξειδία του σιδήρου, μπορούν να σχηματίσουν υμένια στη μεταλλική επιφάνεια επηρεάζοντας με την σειρά τους το ρυθμό διάβρωσης.

Στη βιομηχανία χρησιμοποιείται ευρέως ένα κράμα σιδήρου-άνθρακα, που ονομάζεται χάλυβας, λόγω της συμβατότητάς του με άλλα μεταλλικά τμήματα και του χαμηλού κόστους του. Οι ηλεκτροχημικές αντιδράσεις που λαμβάνουν χώρα κατά τη διάβρωση του χάλυβα, προάγουν το σχηματισμό δυσδιάλυτων ενώσεων στην επιφάνεια του μετάλλου, που αποτελούνται από οξειδωμένες μορφές του σιδήρου, όπως οξειδία (μαγνητίτης, αιματίτης) και υδροξειδία (λεπιδοκροκίτης).

Σε αυτή τη διδακτορική διατριβή, παρουσιάζονται συγκριτικά αποτελέσματα πειραμάτων παρεμπόδισης της διάβρωσης που βασίζονται σε δύο μεθόδους αξιολόγησης: (α) βαρυμετρικές μετρήσεις (με βάση την απώλεια μάζας κάθε μεταλλικού δείγματος) και (β) φωτομετρική ποσοτικοποίηση του οξειδωμένου σιδήρου (με βάση έγχρωμα σύμπλοκα του δισθενούς σιδήρου με το χηλικό αντιδραστήριο 1,10-φαινανθρολίνη). Σε μια προσπάθεια κατανόησης της συμπεριφοράς της διάβρωσης του χάλυβα και των παραγόντων που την επηρεάζουν, διεξήχθησαν πειράματα υπό διάφορες συνθήκες, μελετώντας την επίδραση ορισμένων μεταβλητών (θερμοκρασία, ποιότητα νερού, ταχύτητα ανάδευσης κ.λπ.). Τέλος, αξιολογήθηκε η αποτελεσματικότητα πληθώρας χημικών προσθέτων ως παρεμποδιστές της διάβρωσης. Οι παρεμποδιστές κατηγοριοποιήθηκαν σε φωσφονικούς και μη φωσφονικούς. Έμφαση δόθηκε στους πρώτους και την πιθανή συνέργειά τους με μεταλλικά ιόντα που υπάρχουν σε διαλύματα που προσομοιάζουν τα γεωθερμικά ύδατα.

Το πρώτο βήμα ήταν η ταυτοποίηση των προϊόντων διάβρωσης του χάλυβα που σχηματίζονται στις διαφορετικές πειραματικές συνθήκες. Ο λεπιδοκροκίτης φαίνεται να σχηματίζεται συχνότερα σε θερμοκρασία περιβάλλοντος και στους 60 °C, ενώ ο αιματίτης και ο μαγνητίτης σχηματίζονται σε υψηλότερες θερμοκρασίες. Επίσης, παρουσία ανθρακικών ιόντων στο διάλυμα, παρατηρήθηκε ο σχηματισμός ανθρακικού σιδήρου στη μεταλλική επιφάνεια. Η παρούσα μελέτη έδειξε ότι ο σχηματισμός διαφορετικών προϊόντων διάβρωσης μπορεί να επηρεάσει το ρυθμό της διάβρωσης.

Συνολικά, οι φωσφορικοί παρεμποδιστές παρουσίασαν υψηλότερη απόδοση σε νερό υψηλής αλατότητας. Επιπλέον, τα φωσφορικά παρουσιάζουν καλή παρεμποδιστική συμπεριφορά σε νερό μέτριας αλατότητας υπό συνθήκες υψηλής πίεσης-υψηλής θερμοκρασίας. Όσον αφορά τους μη φωσφορικούς παρεμποδιστές, το κάθε χημικό πρόσθετο επηρεάστηκε με διαφορετικό τρόπο από την αλλαγή των πειραματικών συνθηκών. Πιο συγκεκριμένα, δύο από τους μη φωσφορικούς παρεμποδιστές παρουσίασαν την υψηλότερη αντιδιαβρωτική τους απόδοση σε απιονισμένο νερό, ενώ η απόδοση των άλλων δύο ήταν καλύτερη σε νερό μέτριας αλατότητας. Αυτή η έρευνα κατέληξε στο συμπέρασμα ότι η βέλτιστη συγκέντρωση εξαρτάται από διάφορες συνθήκες, όπως η θερμοκρασία και η ποιότητα του νερού, ανεξάρτητα από τη φύση του παρεμποδιστή. Τέλος, τα αποτελέσματα της μεθόδου προσδιορισμού του ολικού σιδήρου έδειξαν αποκλίσεις από αυτά της μεθόδου απώλειας μάζας, ειδικά σε πειράματα παρουσία φωσφορικών.

Λέξεις-κλειδιά: διάβρωση, γεωθερμική ενέργεια, προϊόντα διάβρωσης, παρεμποδιστές, φωσφορικά οξέα, πρόσθετα

Table of Contents

1.1 Geothermal energy	1
1.2 The chemistry of corrosion	2
1.3 Most common types of corrosion.....	4
1.4 Materials selection.....	8
1.5 Factors influencing corrosion rate.....	9
1.6 Corrosion products	13
1.7 Corrosion inhibition	14
1.8 Phosphonates as corrosion inhibitors	15
1.9 Scope of the research.....	18
1.10 References	19
Chapter 2: Experimental Section	28
2.1 Instrumentation.....	28
2.2 Materials and Characterization.....	28
2.2.1 Reagents.....	28
2.2.2 Synthesis and characterization of the tetraphosphonate additives.....	30
2.3 Corrosion quantification and other determination methods.....	35
2.3.1 Gravimetric measurements	35
2.3.2 Total iron determination method	37
2.3.3 Sulfide determination	39
2.3.4 EDTA titration.....	40
2.4 Preparation of Stock and Working Solutions.....	41
2.5 Carbon steel sample preparation	43
2.6 Experimental set-up.....	43
2.7 References	45
Chapter 3: Corrosion experiments in artificial brine of medium salinity	47
3.1 Characterization of the corrosion products	47
3.2 Results	53
3.2.1. Phosphonate inhibitors	53
3.2.2 Non-phosphonate inhibitors	78

3.3 Concluding remarks	89
3.3.1 Phosphonate inhibitors	89
3.3.2 Non-phosphonate inhibitors	90
3.4 References	92
Chapter 4: Corrosion experiments in artificial brine of high salinity	93
4.1 Characterization of the corrosion products	93
4.2 Results	98
4.2.1 Phosphonate inhibitors	98
4.2.2 Non-phosphonate inhibitors	122
4.3 Concluding remarks	135
4.3.1 Phosphonate inhibitors	135
4.3.2 Non-phosphonate inhibitors	136
4.4 References	137
Chapter 5: Corrosion experiments under mild “stress”	138
5.1 Characterization of the corrosion products	138
5.2 Results	142
5.2.1 Phosphonate inhibitors	142
5.2.2 Non-phosphonate inhibitors	172
5.3 Concluding remarks	186
5.3.1 Phosphonate inhibitors	186
5.3.2 Non-phosphonate inhibitors	187
5.4 References	189
Chapter 6: A combined corrosion and scale inhibition study	192
6.1 Introduction	192
6.2 Calcium tolerance	192
6.3 Results and Discussion	193
6.4 Concluding remarks	198
6.5 References	199
Chapter 7: Concluding remarks and perspectives	201
7.1 Corrosion products	201
7.2 Corrosion inhibition studies	203

<i>Phosphonate inhibitors</i>	203
<i>Non-phosphonate inhibitors</i>	206
7.3 Perspectives.....	208
7.4 References	210
Chapter 8: Annex	212
8.1 Abbreviations	212
8.2 Characterization of tetraphosphonates	213
8.3 Calcium tolerance test	215
8.4 Crystal data for the minerals from American Mineralogist Crystal Structure Database. .	216
8.5 EDS analysis	219
8.6 Corrosion experiments data tables	222
8.7 Specimens from the corrosion experiments under HP-HT conditions.....	227
8.8 Characterization of the precipitates collected from the corrosion experiments	228
8.9 SEM/EDS study of the precipitates collected from the corrosion experiments	234

Chapter 1: Introduction to corrosion under geothermal stresses

1.1 Geothermal energy

Geothermal energy is a renewable form of thermal energy, originating from the heat that is constantly produced in the earth's interior ^[1]. Geothermal wells are, essentially, holes drilled deep into the underground reservoirs in order to access the steam and hot water that are present there. Specifically, production wells are used to extract heat or steam, while injection wells are used to inject water or other fluids into the reservoir to enhance or maintain its productivity ^[2]. A geothermal facility also contains heat exchangers that transfer the heat from the geothermal fluid to a secondary fluid, eventually guiding the geothermal energy to a geothermal power station in order to generate electricity ^[3]. Figure 1.1 presents schematically a typical geothermal system and its main components.

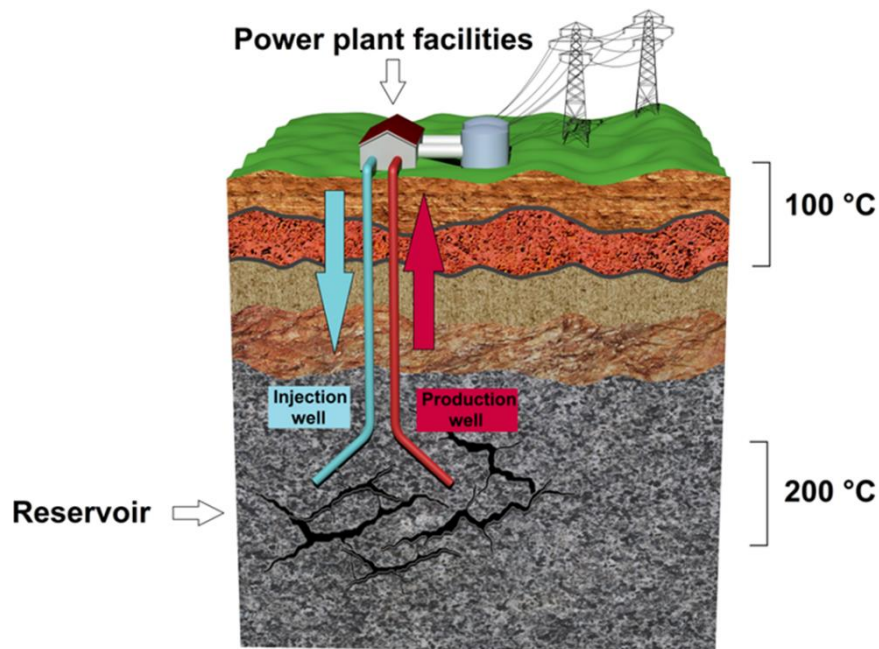


Figure 1.1. Schematic representation of a typical geothermal system. Taken from Reference 4.

The geothermal industry shares many common characteristics with the oil industry. Crude oil, or petroleum, is a fossil fuel that is extracted from the ground using drilling techniques. The first

step is called exploration. When the oil is discovered, it is extracted by pumping it to the surface. An oilfield is the specific location where this operation occurs. The next step concerns the refinement of oil into a variety of products, such as gasoline and diesel. In addition, oil is used as an energy source in a wide range of industries, eg. electricity generation. Despite the fact that geothermal and oilfield operations are based on two different energy sources, both methodologies extract and exploit natural resources to generate energy. Furthermore, both systems use specialized equipment, including wells and pipelines. Importantly, in both cases this equipment must operate under “high stress” conditions. In particular, the presence of a highly corrosive fluid (mainly due to high chloride and sulfate concentration) in combination with the high pressure and temperature conditions can lead to corrosion of the materials and equipment used in such systems. Specifically, geothermal facilities, wells, heat exchangers, pumps, pipes and pipelines generally consist of metals of various metallurgies. Likewise, in the oilfield, offshore platforms, pipelines and storage tanks can be subjected to corrosion processes ^[5]. Evidently, corrosion can significantly compromise the efficiency of these systems. For example, it can result in reduced heat transfer efficiency at the heat exchangers, or in reduced flow capacity through the pipelines. Eventually, this can cause costly failures and shut-downs of the entire production system.

1.2 The chemistry of corrosion

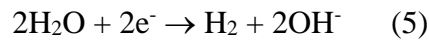
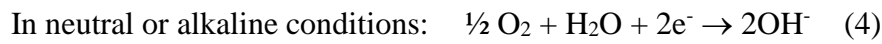
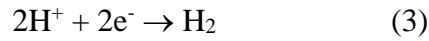
Corrosion is the natural process that occurs as a result of the interaction between a metal and a corrosive environment ^[6]. The environment can be in the form of a liquid, a gas or both. Corrosion can have a significant negative impact on several industrial sectors, including reducing the efficiency and lifespan of equipment, worsening the risk of equipment failure, and increasing maintenance and repair costs. All these affect the operational costs and economics ^[7]. In some cases, corrosion can also pose a safety hazard, for example in the case of pipelines or structures that may fail due to corrosion. The problematic effects of corrosion are enhanced in systems that operate under “high stress”. Geothermal and oilfield operations are particularly affected and compromised by corrosion.

According to the theory of Wagner and Traud, three steps are required for metallic corrosion to occur. The first is the loss of electrons from the site of the metal that can act as the anode of the

reaction because of the lower potential. During this step, iron (as the example) is oxidized to the Fe^{2+} ion (Eq. 1). The second is the movement of the released electrons from the anode to the cathode by the corrosive fluid which acts as an electrolyte. The final step involves the cathode that will absorb these electrons in order to balance the charges, with various electrochemical processes occurring [8].



At the cathode, different reactions of oxygen reduction or hydrogen evolution may take place, depending on the conditions (Eqs. 2-5) [8-10].



A generalized scheme depicting these processes is shown in Figure 1.2.

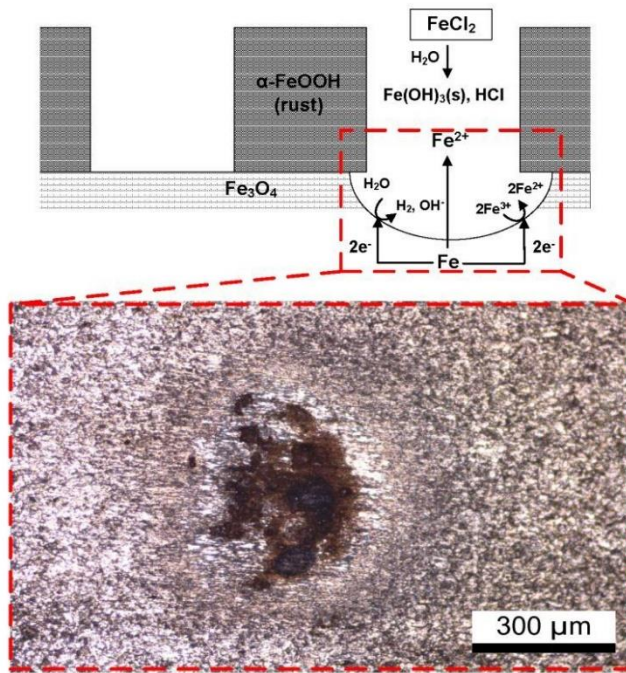
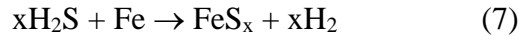
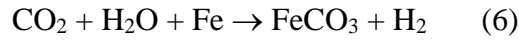


Figure 1.2. Electrochemical events occurring on a corroding metal surface. Taken from Reference 10.

In the presence of carbon dioxide or hydrogen sulfide in the aqueous medium, the following reactions take place on the metal surface (Eqs. 6,7) [11,12].



1.3 Most common types of corrosion

Materials and equipment used in high stress systems can be subjected to several forms of corrosion (see Figure 1.3). Some of the most common types are uniform, pitting, galvanic, crevice, erosion, stress cracking, sour and sweet corrosion.

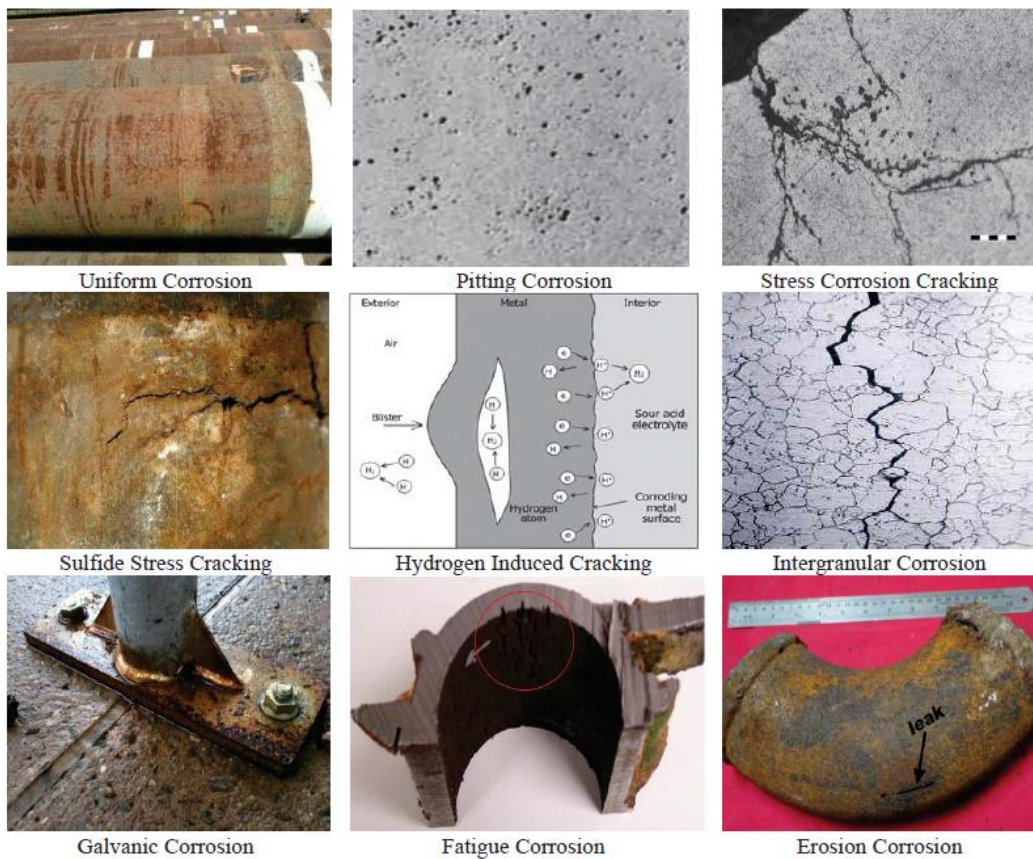


Figure 1.3. The different types of corrosion. Taken from Reference 13.

1.3.1. Uniform corrosion

Uniform corrosion, as the name suggests, occurs uniformly over the entire metal surface. In most geothermal systems, uniform corrosion can occur at carbon steel pipes, valves, and other equipment that are in contact with water or steam, and it is promoted by ammonium, chloride, sulfide or hydrogen ions ^[14,15]. Uniform corrosion can also occur in oilfields, where it can affect various types of equipment and infrastructure, such as pipelines, tanks, and other storage facilities. Unlike other types of corrosion that will be mentioned later, this type of corrosion is “preferred” because the lifetime of the affected equipment can be assessed through simple tests and predicted by appropriate calculations ^[16].

1.3.2. Pitting corrosion

There are cases where the passive oxide layer on the metal surface may be damaged at specific locations, thus resulting in a rapid increase of localized metal dissolution at specific points (spots) in the system. Pitting corrosion is a type of localized form of corrosion and most often occurs on corrosion resistant alloys (CRAs) due to the possibility of a breakdown of the surface passivation film or in the case of concentrated scales in small areas on a carbon steel surface. In geothermal systems, pitting corrosion is found at pipework, heat exchanges and pumps. Pit formation is very difficult to detect and predict ^[17].

1.3.3. Galvanic corrosion

Galvanic corrosion is a type of corrosion that occurs when two different (and incompatible) metals are in contact with each other. The presence of a liquid, such as water or oil, connects the two metals and acts as an electrolyte allowing an electrical current to flow between the two metals. This causes one of the metals to corrode faster than it would, if it were on its own. In geothermal systems, this type of corrosion is a major problem due to the high conductivity of the geothermal fluids. It is important to carefully consider the types of metallic materials that are used and ensure that they are compatible with each other, in order to minimize the risk of galvanic corrosion ^[18]. Specifically, the surface that consists of the metal with the lower potential acts as the anode. The

reaction is rapidly accelerated when the two different metals that are present have a large surface-to-surface ratio ^[19].

1.3.4. Crevice corrosion

Crevice corrosion occurs in small crevices, cracks or gaps on the metal surface where there is enough space for the fluid to penetrate but cannot flow through. It resembles pitting corrosion because it occurs locally on specific areas of the metal surface, where deposits (such as scales or corrosion products that are found concentrated in the crevice) cause corrosion ^[20]. Furthermore, oxygen concentration or aggressive brine solution trapped in the crevice promote this form of corrosion ^[21]. In addition, high chloride and hydrogen ion concentration enhance corrosion aggressiveness ^[22]. In geothermal systems crevice corrosion occurs at flange joints, threaded joints or small cavities filled with brine fluid. The initiation and acceleration of crevice corrosion is very difficult to predict ^[23]. In heat exchangers, crevices exist in the spots where tube and tube-sheet join and, in the spots where plate ridges and plate heat exchangers overlap ^[24].

1.3.5. Erosion corrosion

Erosion corrosion is a type of corrosion that occurs when a flowing fluid, such as water or oil, erodes the surface of a metal. High-velocity fluid, such as the oilfield check valve, results in unprotected metal surfaces, unable to form a passive film of corrosion products ^[25]. It is important to carefully design and maintain these systems to prevent erosion corrosion. In addition, it is important to maintain proper fluid flow and velocity, as well as to regularly inspect and maintain the system to identify and address any signs of corrosion.

1.3.6. Stress cracking corrosion

Stress cracking corrosion (SCC) is a dangerous type of corrosion which occurs when structural parts are in direct contact with a corrosive fluid in combination with a mechanical stress applied on the metal. The presence of oxygen as well as the increase in temperature accelerate corrosion ^[26]. The subjection of a metallic material to both chemical and mechanical stresses might cause rapid

cracking. SCC is a threat for medium and high-strength steels. SCC is a major problem in pipelines of systems that perform under high stresses ^[27]. In the case of a sulfide-containing solution as the corrosive environment, the type of corrosion is called sulfide stress corrosion (SSC) ^[28]. Oxygen concentration does not significantly affect corrosion aggressiveness. Higher temperatures result in less aggressive corrosion.

1.3.7. Sour corrosion

Hydrogen sulfide (H₂S) is the main compound that leads to sour corrosion in its different forms, which are sulfide stress cracking (SSC), stress cracking corrosion (SCC), hydrogen-induced cracking (HIC), stress-oriented hydrogen-induced cracking (SOHIC), and stepwise cracking corrosion (SWC) ^[29]. Sour corrosion typically refers to corrosion that occurs in the presence of sour crude oil, which is oil that has high sulfur content, resulting in the most damaging form of corrosion to drilling pipes.

1.3.8. Sweet corrosion

Sweet corrosion, or CO₂ corrosion, typically refers to corrosion that occurs in the presence of oil that has low sulfur content, although it is not uncommon for sweet corrosion to occur in geothermal systems. Flow rate and solution pH are two main factors that influence sweet corrosion, and both depend on the dissolved carbon dioxide concentration in water ^[30].

1.3.9. Oxygen corrosion

In the petroleum industry, oxygen corrosion can be a significant concern, as it can lead to the degradation of equipment and pipelines, leading to costly repairs and downtime. Some common materials that are susceptible to oxygen corrosion in the oilfield include steel, iron, and copper. Oxygen is not common to be present in geothermal fluids, especially at high concentrations. Still, even at low concentration it can accelerate the corrosion processes. Oxygen is an electron acceptor in the cathodic reaction; thus, it accelerates the corrosion process in the anode ^[31].

1.3.10. Microbiologically induced (influenced) corrosion

Microbiologically induced (influenced) corrosion (MIC) is a type of corrosion that is caused by the presence of microorganisms, such as bacteria. As a result of their activity, they produce waste products like CO₂ and H₂S. MIC can be difficult to detect and prevent, as the microorganisms that cause it are often not visible to the naked eye ^[32].

1.4 Materials selection

Materials used in industrial equipment must be able to abide harsh environments. It is important to carefully consider some specific requirements of the particular application when selecting materials for use in the geothermal industry. Commercially available materials should be selected, for which there is sufficient information on their reliability and knowledge of possible occurrence of failure. They should have a long-life cycle and have available replacements. Also, the amount of materials used should be reduced to a minimum, thus keeping costs low. In addition, the capability of applying corrosion protection techniques should be considered. Other factors to consider include the temperature and pressure of the fluids or gases the material will be exposed to, the presence of corrosive substances, and the mechanical stresses the material will be subjected to. Finally, materials should be friendly to humans and the environment, and should be compatible with other structural components of the system ^[33].

Among the several metallurgies that can be used in system components, carbon (mild) steel is one that is widely used in industry, due to its compatibility with other metals present, and its low cost. Uniform and localized forms of corrosion can occur in such steels. Therefore, it is selected for thick-walled pipe systems, as opposed to thin-walled ones, where the slightest material loss could be disastrous. Uniform corrosion occurs when chloride ion concentration is lower than 2 % and solution pH is higher than 6. The risk of pitting corrosion is higher when the chloride concentration is higher than 2 % ^[34,35].

In the case of stainless steel, uniform corrosion does not commonly occur. In contrast, the risk of pitting, stress cracking and erosion corrosion increases substantially. It is worth noting that the higher the temperature is, the more likely pitting corrosion will occur. The content of stainless steel in Cr and Mo affects the resistibility of the material. Adding nickel alloy to stainless steel

renders the material more corrosion resistant. Still, it should not be selected for systems where H₂S is present.

In conditions where the chloride ion concentration is lower than 10 %, titanium alloys can effectively resist pitting and cracking corrosion. However, apart from the higher cost, the temperature plays a decisive role, as at high temperatures such alloys are not resistant to pitting corrosion. Also, their highly cathodic nature requires special attention, because when used in combination with other metals, galvanic corrosion could be an issue ^[36].

1.5 Factors influencing corrosion rate

In geothermal systems, corrosion can be caused by a variety of factors, including the brine composition of the system, as well as the temperature and pressure conditions. Corrosion rate is directly related to solution pH. In most metals, like iron, corrosion is more aggressive at acidic pH values than at neutral and alkaline regimes. In addition, the solubility of the protective films that some of the metals form can be affected by the change in pH, resulting in their breakdown, hence considerably influencing the corrosion processes. High temperatures can accelerate the corrosion of metals and can also cause deterioration of non-metallic materials. In addition, temperature influences the formation of corrosion products ^[37]. Higher flow rates can increase the risk of corrosion due to the increased movement of the fluids, which can lead to a greater exposure of the materials to the corrosive environment.

Geothermal fluid travels through several sections of the entire system, starting from the reservoir and finally reaching the turbine. The chemical and physical characteristics of the geothermal fluid vary widely from one geothermal site to another, or even in different parts of a single system. Table 1.1 contains the analyses of several geothermal fluids obtained from different geothermal sites ^[38]. High chloride concentrations could lead to the breakage of the formed passive layers on the metal surfaces. Dissolved carbon dioxide at high concentrations causes a decrease in solution pH and consequently an increase in corrosion rate, albeit the presence of carbonates and bicarbonates results in a slight decrease in corrosion rate ^[39].

Table 1.1. The chemical composition of several geothermal fluids. Taken from Reference 38.

mg/kg	1	2	3	4	5	6	7	8	9	10	11	12
Li	194	219	327	45	2	27	27	6	44	0.3	11.7	13.2
Na	53,000	47,600	65,500	2850	407	2190	8300	2300	4800	212	1050	1250
K	16,700	12,600	12,450	927	64	400	2210	300	800	27	210	210
Rb	170	67					11	1		0.04	2.2	2.9
Cs	20	19					39	0.7	17	< 0.02	1.7	2.5
Mg	33	114	400	< 0.35	0.007	0.3	0.5	0.7	0.7		0.1	0.04
Ca	27,400	21,500	23,700	75	8	10	521	60	250	1.5	2.2	12
Sr	411	1043		2.8	0.4	1.4	16					
Ba	203	992	2260				11					
Fe	1560	3733	4160		< 0.01		1.5			0.1	< 0.01	< 0.01
B	257	221	282	119	9.9	27	9.4	60	206	0.6	48	29
Al	2	0.5	4.2		1.5		0.05					
SiO ₂	> 461	> 430	> 510	> 711	> 599	> 650	> 864	> 600	> 740	> 480	> 805	> 670
NH ₃	333	725		4	1.8			1.7		0.1	2.1	0.2
F	15	0.5		2	15.5	5	2.4	1.6	3	1.9	7.3	8.4
Cl	151,000	134,000	131,000	5730	438	3650	16.03	3950	9000	197	1740	2210
Br	99	87			0.32	2	17.7			0.45	5.7	5.5
I	20	6					0.6				0.8	0.3
CO ₂	1600	14,600		7800	4300		44		5500	55	128	17
H ₂ S	15	45		160						7.3	< 1	1
SO ₄	64	25		5	196	69	2	60	30	61	8	28

- (1) Salton Sea USA; McKibben and Hardie, 1997.
- (2) Brawley USA; Gallup, unpublished results.
- (3) Imperial USA; McKibben and Hardie, 1997.
- (4) Coso USA; Moore et al., 1989.
- (5) Dixie USA; Bruton et al., 1997.
- (6) Roosevelt USA; Unocal well file, 1980.
- (7) Cerro Prieto, Mexico; Mercado and Hurtado, 1992.
- (8) Miravalles, Costa Rica; Vaca et al., 1989.
- (9) El Tatio, Chile; Ellis and Mahon, 1977.
- (10) Hvergerdi, Iceland; Ellis and Mahon, 1977.
- (11) Broadlands, New Zealand; Ellis and Mahon, 1977.
- (12) Wairakei, New Zealand; Ellis and Mahon, 1977.
- (13) Rotokawa, New Zealand; Ellis and Mahon, 1977.

Miller et al. proposed a classification system for geothermal fluids, based on the most important chemical species, in terms of their corrosive effect ^[40]. Specifically, this study includes data from geothermal fluids of 45 geothermal sites and 7 countries and reported that the key species are oxygen (mostly from contamination), hydrogen ions, chloride ions, carbonates and bicarbonate ions, ammonia and ammonium ions, sulfate ions, hydrogen sulfide and carbon dioxide. In addition, the term TKS (it stands for **t**otal **k**ey **s**pecies) was used for this classification. TKS is the sum of the concentrations in ppm (mg/L) of chloride ions, carbonates, bicarbonate ions, sulfate ions, total sulfide and total ammonia species, and carbon dioxide. In liquid-dominated geothermal fluids, ammonia and sulfide concentrations are negligible. Table 1.2 contains the different types of this categorization along with their important characteristics.

Table 1.2. The classification of the geothermal fluids.

Type of corrosivity	Information
Class I	Hyper saline fluid with TKS above 100000 ppm (99 % chloride ions) and pH below 5 ^[41]
Class II	Acidic liquid-dominated reservoir with TKS between 1000 to 10000 ppm and pH below 4.5
Class III	High salinity fluid with TKS between 10000 and 20000 ppm and neutral pH
Class IV	Liquid-dominated reservoir with TKS between 500 and 10000 ppm and pH above 5
Class V	Low temperature and low salinity fluid with TKS below 5000 ppm i) pH between 6.7 and 7.6 and ii) pH between 7.8 and 9.5
Class VI	Vapor-dominated reservoir

Another classification for geothermal fluids was proposed by Sanada et al. This study developed guidelines for the selection of materials appropriate for deep geothermal wells ^[42]. Specifically, five types of geothermal fluids were introduced as it follows:

1. *Near neutral to alkaline pH fluid*

Most commonly found in geothermal systems. The chloride concentration could reach up to 10000 ppm. ^[29]

2. *Acid sulfate water*

The mixture of a large amount of volcanic gases with even a small amount of ground water results in the formation of a liquid consisting of high hydrochloric acid concentration ^[43].

3. *Acid chlorine water*

Volcanic exhalations cause sulfur species to exist ^[44].

4. *High salinity brine*

As the fluid moves from the geothermal well to the surface, the dissolved solids that exist deep flow and then the flashing causes an increase in the fluid salinity ^[45].

5. Super-heated steam with high hydrochloric acid concentration

At temperatures above 300°C, sodium chloride which is present in near-neutral brines will transform to hydrochloric acid steam [46].

The aforementioned classification systems were merged by Nogara and Zarouk [16] using information from published data on geothermal fluids [30,47-54]. Table 1.3 contains the merged types.

Table 1.3. Merging of the two classification systems.

Type of corrosivity	Resource type	Reference	TKS (ppm)	pH
Class I	Liquid-dominated	1 site in USA	> 100000	< 5 / 5 – 6
Class II-A	Liquid-dominated / Acid sulfate	4 sites in Philippines, 5 sites in Japan, 1 site in Costa Rica, 1 site in France and 1 site in Taiwan	1000 - 60000	> 3 / < 5
Class II-B	Liquid-dominated / Acid chlorine	2 site in Philippines, 3 sites in Japan, 1 site in Costa Rica), 1 site in Indonesia and 1 site in Mexico	500 - 40000	< 3
Class III	Liquid-dominated	1 site in Mexico and 1 site in USA	10000 - 20000	5 – 6 / > 6
Class IV	Liquid-dominated	1 site in El Salvador, 1 site in Iceland, 2 sites in Japan, 2 sites in New Zealand and 4 sites in USA	500 - 10000	>=5 / > 6
Class V-A	Liquid-dominated	3 sites in USA	< 5000	6.7 – 7.6 / Not applicable
Class V-B	Liquid-dominated	15 sites in Iceland and 1 site in USA	< 5000	7.8 – 9.85 / Not applicable
Class VI-A	Vapor-dominated / without HCl gas traces	10 sites in Italy, 1 site in USA and 1 site in Indonesia	< 1	Not applicable
Class VI-B	Vapor-dominated / with HCl gas	1 site in Turkey, 1 site in Iceland and 1 site in USA		

1.6 Corrosion products

As corrosion occurs, the formation of a corrosion product will form on the metal surface. Corrosion aggressiveness is strongly dependent on the structure of the rust film. Corrosion products consist of iron oxides and iron oxy/hydroxides. The film that forms from corrosion products can be composed of a single mineral or a mixture of several. Its thickness and the extent of its coverage of the metal surface are important factors that affect its protection ability. Hence, formation of such film can lead either to corrosion protection (passivation films) or to corrosion acceleration (rust layers). Passive films can form in a strongly oxidative environment (high anodic potential). Their thickness can reach a few nanometers, due to the high electrical field-assisted ionic migration mechanism, which is followed by the ionic transport through the film. Rust layers are not necessarily different in composition, although they can form by mild oxidation-reduction cycles. The oxidizing film is enhanced as the reduction-oxidation cycles are repeated, reaching several hundred μm thickness. Sakashita et al. showed that a Fe-oxyhydroxide rust layer is essentially a membrane with positive fixed charges and has a property of anionic (Cl^-) permselectivity, thus, in the presence of a Cl^- -enriched aqueous solution, Cl^- can penetrate into the rust layer and attack the surface ^[55].

The formation of corrosion products is the result of a precipitation reaction from a solution which contains the respective precursors. In this solution, several iron complexes exist in equilibrium and, as a result, the solidification of the corrosion product depends on these precursor complexes and their supersaturation and not on a stoichiometric reaction. Table 1.4 contains the mineral names of the most common corrosion products and their respective formulas. Among the several minerals, lepidocrocite, goethite, magnetite and hematite are found to form more frequently. Their ability to either retard the corrosion rate or accelerate it depends on the quality of the respective film. In general, magnetite appears to form more stable and dense protective layers, compared to the other oxides. Hematite can also form a protective film, although in some conditions it is not as efficient to decelerate corrosion as magnetite. On the contrary, the formation of lepidocrocite does not result in a protective layer ^[56].

Table 1.4. The most commonly observed corrosion products on iron surfaces.

Mineral name	Formula
Goethite	α -FeOOH
Akageneite	β -FeOOH
Lepidocrocite	γ -FeOOH
Feroxyhyte	δ -FeOOH
Hematite	α -Fe ₂ O ₃
Maghemite	γ -Fe ₂ O ₃
Magnetite	Fe ₃ O ₄

1.7 Corrosion inhibition

To mitigate corrosion, several methods can be used, including coatings, cathodic protection and chemical additives that can act as corrosion inhibitors. Corrosion inhibitors are able to protect the metal surface through either physisorption, which involves electrostatic forces, or chemisorption, which involves chemical bond formation^[57]. It is worth noting that the effectiveness of a corrosion inhibitor depends on several factors, including the type of metal being protected, the corrosive environment it is exposed to, and the specific mechanism by which the inhibitor works. An ideal corrosion inhibitor should be able to cover the entire surface of the metal and it should be stable over long periods of time. In addition, its use should be safe and environmentally friendly^[58].

In the past, inorganic inhibitors, such as chromates^[59], nitrites^[60] and molybdates^[61] were commonly used. Even though they exhibit high anticorrosion efficiency, they can cause severe damage to the environment and, chromate particularly, pose health hazards^[62]. Thus, the corrosion community's interest was shifted to organic inhibitors^[63]. These can be simple organic molecules, such as imidazolines, amines, amides or amidoamides^[64-67], or organic polymers, such as poly(vinylpyrrolidone)^[68]. These compounds can interact with the metal surface forming a protective film. They can act as anodic or cathodic inhibitors, preventing the anodic or the cathodic reaction of corrosion, respectively, or they can act as a combination of both types (mixed type inhibitors). In general, they can be effective, even at low concentrations. In addition, they exhibit

reduced toxicity and increased biodegradability, compared to the inorganic corrosion inhibitors [69,70].

Organic molecules that contain heteroatoms such as N, O, S or P in their structure are used as effective corrosion inhibitors [71]. This is due to the availability of their non-bonding electrons, which can be transferred to the metal surface and form coordinative covalent bonds with surface iron. Their anticorrosion efficiency depends on the electronegativity of the heteroatom, with phosphorus-based molecules being a popular family of corrosion inhibitors. Phosphates are the first phosphorus-based inorganic corrosion inhibitors, including the orthophosphates, the polyphosphates and the hexametaphosphates [72].

1.8 Phosphonates as corrosion inhibitors

Phosphonic acids are organic structural analogs of phosphates and have also been used as corrosion inhibitors [73]. The tetrahedral phosphorus (P) atom is bonded to one oxygen (O) with a double bond (P=O, phosphoryl group), two hydroxyl groups (P-OH) and a carbon atom (C) containing an organic substituent R. The C-P bond is stable and resistant to high thermal and hydrolytic stresses. In addition, the polar and hydrophilic group (-PO₃H₂) has the ability, depending on solution pH, to remain fully protonated (pH < 1), to undergo single deprotonation (pH = 1-7), or be fully deprotonated (pH > 7). Upon single or double deprotonation, the phosphonic groups become anionic and are able to strongly complex metal ions present in the brine system. In addition, phosphonates demonstrate high affinity for the metal oxide layer on the metal surfaces in contact with the brine fluid. A phosphonate can contain one or more phosphonate groups in its structure. Furthermore, the phosphonate groups can coexist with other functional groups such as the carboxyl (-COOH), the hydroxyl (-OH), the sulfonic (-SO₃H), the amino group (-NH₂), and a variety of heterocyclic rings.

The aminophosphonates constitute an important class of phosphonic acids, which can be regarded as structural analogs of natural amino acids. The presence of the amine group in their structure could enhance the inhibition efficiency because of the increased adsorption of the inhibitor to the metal surface. The amine groups are deprotonated at pH > 10, thus the coexistence of the protonated amino group with the deprotonated phosphonates at circumneutral pH, makes

the molecule a zwitterion (protonated cationic amine and deprotonated anionic phosphonic acid). A typical example is the tetraphosphonate EDTMP [ethylenediamine-*tetrakis*(methylenephosphonic acid)], which is a structural analogue of the well-known tetracarboxylate EDTA (ethylenediamine-tetraacetic acid).

Phosphonic acids have also been proven to be effective inhibitors against the formation and deposition of various scales, such as metal carbonates, sulfates and silicates ^[74]. Moreover, they are efficient corrosion inhibitors for carbon steel, especially in brines with high ion concentrations, since they can function synergistically with the metal ions present in the fluid. Phosphonate-based inhibitors are environmentally acceptable, but are resistant to breakdown by microorganisms, hence they are considered to exhibit low biodegradability.

Several researchers have focused their attention to the anticorrosion activity of several phosphonic acids, such as ethylenediamine-*tetrakis*(methylenephosphonic acid) (EDTMP) ^[75], 1-hydroxyethane-1,1-diphosphonic acid (HEDP) ^[76], hexamethylenediamine-*tetrakis*(methylenephosphonic acid) (HDTMP) ^[77], amino-*tris*(methylenephosphonic acid) (ATMP) ^[78], 2-Phosphonobutane-1,2,4-Tricarboxylic Acid (PBTC) ^[79], hydroxyphosphonoacetic acid (HPAA) ^[80], variable chain length diphosphonates ^[81] and tetraphosphonates ^[82], (see Figure 1.4). Relevant studies showed that their efficiency depends on several factors such as the concentration of the inhibitor, the number of phosphonic groups, the existence of additional substituents and the size of the alkyl chain. For example, HEDP exhibits a critical concentration above which it stops behaving as a corrosion inhibitor and becomes a rust cleaner ^[83]. Similar observations have been reported for PBTC ^[84].

An additional factor that influences the inhibitory activity of phosphonates is the presence of metal ions in the solution, due to their interaction with the available phosphonate groups on the inhibitor backbone and subsequent deposition of a metal phosphonate protective layer on the metal surface. Hence, corrosion experiments that included the presence of phosphonate inhibitors with several metals such as calcium ^[85], magnesium ^[86], strontium, barium ^[87] and zinc ^[88] have been reported in the literature. Figure 1.5 presents the metal binding modes of the phosphonate and the carboxylate group. In general, the existence of the metal ion in the solution enhances the anticorrosion efficiency of the phosphonate, although the behavior of the metal phosphonate

“complex” is variable and depends on several factors, such as the nature of the phosphonate and the metal ion, solution pH, metal:phosphonate molar ratio, etc [89].

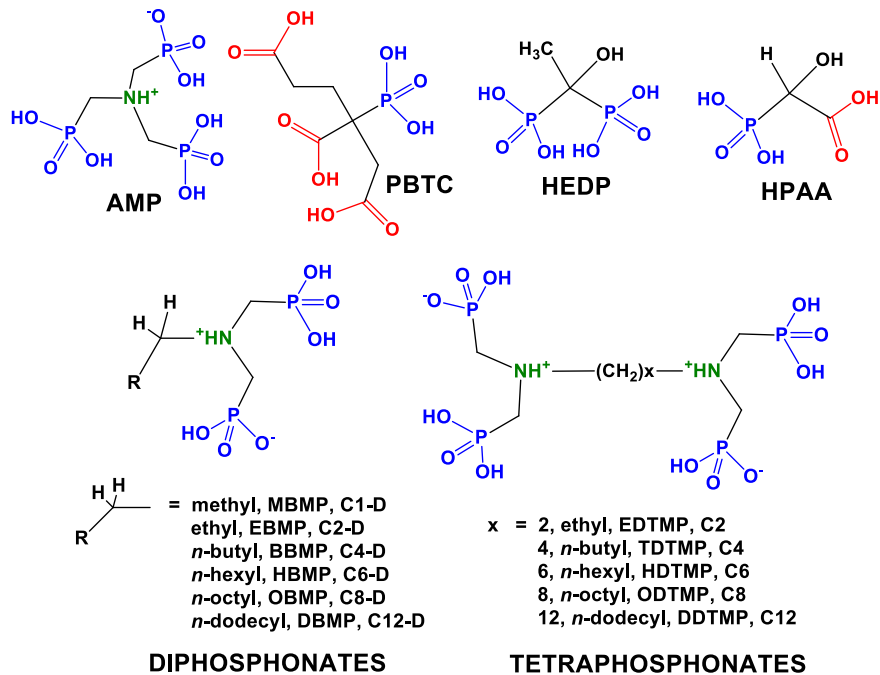


Figure 1.4. Schematic structures of several phosphonate inhibitors.

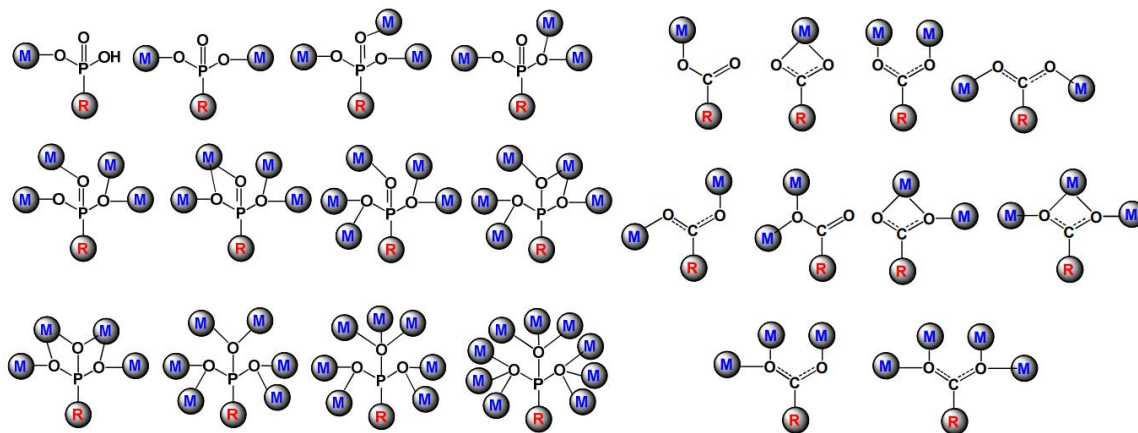


Figure 1.5. Binding modes of a phosphonate (left) and a carboxylate (right) group. Taken from Reference 90.

Phosphonate-based additives can act in a multifunctional manner, as corrosion inhibitors under variable conditions, including different water qualities and temperatures, and as antiscalants (scale inhibitors) for a variety of mineral scales. On the downside, the anticorrosion efficiency of the phosphonates can be affected by the presence of hydrogen sulfide in the corrosive environment even at low concentrations. Also, there is a risk of the breakage of the protective film resulting in localized corrosion, as for several other film-forming agents^[91], or decomposition of phosphonate inhibitors by oxidizing biocides^[92,93].

1.9 Scope of the research

In this Thesis, comparative results from corrosion inhibition experiments are presented based on two methodologies that quantify performance: (a) gravimetric measurements based on the mass loss of each metallic specimen^[9], and (b) total iron quantification based on a photometric methodology that takes advantage of a soluble colored iron-phenanthroline complex^[94,95].

In an effort to understand the corrosion behavior of carbon steel and the factors that influence it, a large number of experiments were performed under several conditions (relevant to geothermal systems), by studying the effect of certain variables, such as temperature, brine water quality and stirring speed. In addition, the full characterization of precipitates collected from the control corrosion experiments lead to the identification of the corrosion products under different conditions. Furthermore, the anti-corrosion efficiency of several, structurally diverse chemical additives was evaluated for several inhibitor concentrations. Three brine water qualities and four temperatures were selected to collect sufficient data to reliably compare the performance of the studied corrosion inhibitors under “mild” and “harsh” geothermal conditions. Finally, comparative results from combined scale and corrosion experiments in the presence of phosphonates, are presented.

1.10 References

1. DiPippo, R. Geothermal Power Plants; Butterworth-Heinemann, **2015**.
2. Zarrouk, S.J.; McLean, K. Geothermal Well Test Analysis; Academic Press, **2019**, Chapter 3, pp. 39-61.
3. Davidsdottir, B. Sustainable Energy Development: The Role of Geothermal Power, in Encyclopedia of the Anthropocene; Goldstein, M.I.; DellaSala, D. (Eds), Elsevier, Amsterdam, **2017**, pp. 357-379.
4. Vallejo Vitaller, A.; Angst, U.M.; Elsener, B. A Setup for Electrochemical Corrosion Testing at Elevated Temperature and Pressure. *Measurement* **2020**, 155, 107537.
5. Fink, J.K. Petroleum Engineer's Guide to Oil Field Chemicals and Fluids, Gulf Professional Publishing (an imprint of Elsevier), Amsterdam, **2012**, Chapter 6, pp. 218-252.
6. Groysman, A. Corrosion for Everybody.; Springer, **2014**.
7. Shannon, D.W. Economic impact of corrosion and scaling problems in geothermal energy systems. Other Information: PBD: 1 Jan **1975**.
<https://digital.library.unt.edu/ark:/67531/metadc1061477>.
8. Popoola, L.; Grema, A.; Latinwo, G.; Gutti, B.; Balogun, A. Corrosion Problems during Oil and Gas Production and Its Mitigation. *International Journal of Industrial Chemistry* **2013**, 4 (1), 35.
9. NACE Standard TM0169-95 (Item No. 21200), National Association of Corrosion Engineers, Houston TX, U.S.A. (www.nace.org).
10. Kim, Y.-S.; Kim, J.-G. Corrosion Behavior of Pipeline Carbon Steel under Different Iron Oxide Deposits in the District Heating System. *Metals* **2017**, 7 (5), 182.
11. Waard, C.D.; Lotz, U. Prediction of CO₂ Corrosion of Carbon Steel. N. p., United Kingdom, **1994**.
12. Goyal, K.L.; Chilingarian, G.V.; Robertson, J.O.; Kumar, S. Review Of: "Surface Operations in Petroleum Production", I (Amsterdam: Elsevier Scientific Publishing Company, 1987) 821pp. *Energy Sources* **1988**, 10 (1), 78–79.
13. Khasani; Kusmono; Utami, P.; Budiarto, R. Corrosion in Geothermal Facilities: Their Causes, Effects, Mitigation, and Worldwide Cases. Proceedings of the 13th AUN/SEED-

- NET Regional Conference on Materials (RCM 2020) and the 1st International Conference on Materials Engineering and Manufacturing (ICMEM 2020) **2021**.
14. Tayactac, R.; Basilia, B. Corrosion in the Geothermal Systems: A Review of Corrosion Resistance Alloy (CRA) Weld Overlay Cladding Applications. *IOP Conference Series: Earth and Environmental Science* **2022**, *1008* (1), 012018.
 15. Kaya, T.; Hoşhan, P.; Corrosion, P. *Corrosion and Material Selection for Geothermal Systems*. www.semanticscholar.org.
 16. Nogara, J.; Zarrouk, S.J. Corrosion in Geothermal Environment: Part 1: Fluids and Their Impact. *Renewable and Sustainable Energy Reviews* **2018**, *82*, 1333–1346.
 17. Akpanyung, K.V.; Loto, R.T. Pitting Corrosion Evaluation: A Review. *Journal of Physics: Conference Series* **2019**, *1378* (2), 022088.
 18. Palit, S. Recent Advances in Corrosion Science: A Critical Overview and a Deep Comprehension. *Direct Synthesis of Metal Complexes* **2018**, 379–411.
 19. Brondel, D.; Edwards, R.; Hayman, A.; Hill, D.; Mehta, S.; Semerad, T. Corrosion in the oil industry, **1994**.
 20. Betts, A.J.; Boulton, L.H. Crevice Corrosion: Review of Mechanisms, Modelling, and Mitigation. *British Corrosion Journal* **1993**, *28* (4), 279–296.
 21. Ning, F.; Tan, J.; Zhang, Z.; Wang, X.; Wu, X.; Han, E.-H.; Ke, W. Crevice Corrosion Behavior of Alloy 690 in High-Temperature Aerated Chloride Solution. *Materials* **2022**, *15* (15), 5434.
 22. Ning, F.; Tan, J.; Zhang, Z.; Wang, X.; Wu, X.; Han, E.-H.; Ke, W. Crevice Corrosion Behaviors of Alloy 690 and 405 Stainless Steel in Chloride Solutions with Different Concentrations of Thiosulfate. *Journal of Nuclear Materials* **2023**, *575*, 154226.
 23. Melchers, R.E. Predicting Long-Term Corrosion of Metal Alloys in Physical Infrastructure. *npj Materials Degradation* **2019**, *3* (1), 1–7.
 24. Davíðsdóttir, S.; Gunnarsson, B.G.; Kristjánsson, K.B.; Ledérsert, B.A.; Ólafsson, D.I. Study of Corrosion Resistance Properties of Heat Exchanger Metals in Two Different Geothermal Environments. *Geosciences* **2021**, *11* (12), 498.
 25. Wang, Z.B.; Zheng, Y.G. Critical Flow Velocity Phenomenon in Erosion-Corrosion of Pipelines: Determination Methods, Mechanisms and Applications. *Journal of Pipeline Science and Engineering* **2021**, *1* (1), 63–73.

26. Tong, C. Advanced Materials Enable Renewable Geothermal Energy Capture and Generation. *Introduction to Materials for Advanced Energy Systems* **2018**, 321–377.
27. Sridhar, N.; Thodla, R.; Gui, F.; Cao, L.; Anderko, A. Corrosion-Resistant Alloy Testing and Selection for Oil and Gas Production. *Corrosion Engineering, Science and Technology* **2017**, 53 (sup1), 75–89.
28. Kimura, M.; Totsuka, N.; Kurisu, T.; Amano, K.; Matsuyama, J.; Nakai, Y. Sulfide Stress Corrosion Cracking of Line Pipe. *CORROSION* **1989**, 45 (4), 340–346.
29. Wang, Q.; Al-Ajwad, H.; Shen, S.; Al-Salim, Y.; Chen, T.; Leal, J. *Sour Corrosion Products Formed in High H₂S Gas Wells*. onepetro.org.
30. Mundhenk, N.; Huttenloch, P.; Kohl, T.; Steger, H.; Zorn, R. Metal Corrosion in Geothermal Brine Environments of the Upper Rhine Graben – Laboratory and On-Site Studies. *Geothermics* **2013**, 46, 14–21.
31. Nalli, K. Corrosion and its mitigation in the oil and gas industries. In *Process Plant Equipment: Operation, Control, and Reliability*; Holloway, M.D.; Nwaoha, C.; Onyewuenyi, O.A., Eds.; John Wiley & Sons, Inc.: **2012**; pp 673-679.
32. Javaherdashti, R. Microbiologically Influenced Corrosion (MIC). In *Microbiologically Influenced Corrosion*; Springer: Cham, **2016**; Chapter 4, pp 29-79.
33. Lahiri, A.K. Material Selection and Performance in Oil and Gas Industry. In *Applied Metallurgy and Corrosion Control*; Springer: Singapore, **2017**; Chapter 9, pp 269-347.
34. Xue, F.; Wei, X.; Dong, J.; Wang, C.; Ke, W. Effect of Chloride Ion on Corrosion Behavior of Low Carbon Steel in 0.1 M NaHCO₃ Solution with Different Dissolved Oxygen Concentrations. *Journal of Materials Science & Technology* **2019**, 35 (4), 596–603.
35. Liu, Q.Y.; Mao, L.J.; Zhou, S.W. Effects of Chloride Content on CO₂ Corrosion of Carbon Steel in Simulated Oil and Gas Well Environments. *Corrosion Science* **2014**, 84, 165–171.
36. Bloyce, A.; Qi, P.-Y.; Dong, H.; Bell, T. Surface Modification of Titanium Alloys for Combined Improvements in Corrosion and Wear Resistance. *Surface and Coatings Technology* **1998**, 107 (2-3), 125–132.
37. Gao, W. *Developments in High Temperature Corrosion and Protection of Materials*; Elsevier, **2008**; Part 2, pp 495-520.
38. Gallup, D.L. Geochemistry of Geothermal Fluids and Well Scales, and Potential for Mineral Recovery. *Ore Geology Reviews* **1998**, 12 (4), 225–236.

39. Elgaddafi, R.; Naidu, A.; Ahmed, R.; Shah, S.; Hassani, S.; Osisanya, S.O.; Saasen, A. Modeling and Experimental Study of CO₂ Corrosion on Carbon Steel at Elevated Pressure and Temperature. *Journal of Natural Gas Science and Engineering* **2015**, *27*, 1620–1629.
40. Ellis, P.F.I.; Conover, M.F. Materials Selection Guidelines for Geothermal Energy Utilization Systems. **1981**.
41. Ellis, P.F.I., Smith, C.C.; Keeney, R.C.; Kirk, D.K.; Conover, M.F. Corrosion Reference for Geothermal Downhole Materials Selection. **1983**.
42. Sanada, N.; Kurata, Y.; Nanjo, H.; Kim, H.; Ikeuchi, J.; Lichti, K.A. IEA Deep Geothermal Resources Subtask C: Materials, Progress with a Database for Materials Performance in Deep and Acidic Geothermal Wells, **2000**.
43. Noguchi, K.; Goto, T.; Ueno, S.; Imahashi, M. A Geochemical Investigation of the Strong Acid Water from the Bored Wells in Hakone, Japan. *Geothermics* **1970**, *2*, 561–563.
44. Kiyosu, Y.; Kurahashi, M. Origin of Sulfur Species in Acid Sulfate-Chloride Thermal Waters, Northeastern Japan. *Geochimica et Cosmochimica Acta* **1983**, *47* (7), 1237–1245.
45. Goldberg, A.; Owen, L. B. Pitting Corrosion and Scaling of Carbon Steels in Geothermal Brine. *Corrosion* **1979**, *35* (3), 114–124.
46. D'Amore, F.; Bolognesi, L. Isotopic Evidence for a Magmatic Contribution to Fluids of the Geothermal Systems of Larderello, Italy, and the Geysers, California. *Geothermics* **1994**, *23* (1), 21–32.
47. Sanada, N.; Kurata, Y.; Lichti, K.A. Valuation and development of deep geothermal resources - materials subtask update of IEA research collaboration program, **1997**.
48. Einarsson, K.; Ingason, K.; Hauksson, T.; Ármannsson, H. Acid Wells in the Krafla Geothermal Field, **2010**.
49. Truesdell, A.H.; Haizlip, J.R.; Armannsson, H.; D'Amore, F. Origin and Transport of Chloride in Superheated Geothermal Steam. *Geothermics* **1989**, *18* (1-2), 295–304.
50. Abe, M. Long term use of acidic reservoir at Onikobe geothermal power plant. In Proceedings of the 15th New Zealand Geothermal Workshop; New Zealand, **1993**.
51. Marini, L.; Yock Fung, A.; Sanchez, E. Use of Reaction Path Modeling to Identify the Processes Governing the Generation of Neutral Na–Cl and Acidic Na–Cl–SO₄ Deep Geothermal Liquids at Miravalles Geothermal System, Costa Rica. *Journal of Volcanology and Geothermal Research* **2003**, *128* (4), 363–387.

52. Gherardi, F., C.P.; Yock-Fung, A.; Gerardo-Abaya, J. Preliminary notes on the acid fluids of the Miravalles geothermal field (Guanacaste, Costa Rica). Use of isotope techniques to trace the origin of acidic fluids in geothermal systems. In IAEA-TECDOC-1448, Proceedings of an International Workshop on Isotope Techniques in the Study of Past and Current Environmental Changes in the Hydrosphere and the Atmosphere, Vienna, Austria, 18–22 October **2004**; IAEA: Vienna, Austria, 2005; pp 61-82.
53. Koestono, H.; Siahaan, E.E.; Silaban, M.; Franzson, H. Geothermal Model of the Lahendong Geothermal Field, Indonesia, **2009**.
54. Ármannsson, H.; Fridriksson, T.; Gudfinnsson, G.H.; Ólafsson, M.; Óskarsson, F.; Thorbjörnsson, D. IDDP—The chemistry of the IDDP-01 well fluids in relation to the geochemistry of the Krafla geothermal system. *Geothermics* **2014**, 49, 66-75.
55. Nakashita, M.; Sato, N. *Corrosion Sci.* **1977**, 17, 473.
56. Ohtsuka, T. Characterization of Corrosion Products on Steel Surfaces; Waseda, Y., Suzuki, S., Eds.; Springer Berlin Heidelberg, **2006**; Chapter 2, pp 19-32.
57. Schott, T.; Liautaud, F. Monitoring and Mitigating Corrosion in Geothermal Systems. *Materials and Corrosion* **2022**.
58. Sastri, V.S. *Green Corrosion Inhibitors*; John Wiley & Sons, Inc.: Hoboken, NJ, USA, **2011**.
59. Kendig, M.W.; Davenport, A.J.; Isaacs, H.S. The Mechanism of Corrosion Inhibition by Chromate Conversion Coatings from X-Ray Absorption near Edge Spectroscopy (Xanes). *Corrosion Science* **1993**, 34 (1), 41–49.
60. Khani, H.; Arefinia, R. Inhibition Mechanism of Nitrite on the Corrosion of Carbon Steel in Simulated Cooling Water Systems. *Materials and Corrosion* **2017**, 69 (3), 337–347.
61. Allertshammer, W. The Role of Molybdate-Containing Inhibitors in Cases of Stress Corrosion Cracking in Closed Water Circuits. *Materials and Corrosion* **2020**, 72 (3), 528–533.
62. den Braver-Sewradj, S.P.; van Benthem, J.; Staal, Y.C.M.; Ezendam, J.; Piersma, A.H.; Hessel, E.V.S. Occupational Exposure to Hexavalent Chromium. Part II. Hazard Assessment of Carcinogenic Effects. *Regulatory Toxicology and Pharmacology* **2021**, 126, 105045.

63. Winkler, D.A.; Breedon, M.; Hughes, A.E.; Burden, F.R.; Barnard, A.S.; Harvey, T.G.; Cole, I. Towards Chromate-Free Corrosion Inhibitors: Structure–Property Models for Organic Alternatives. *Green Chem.* **2014**, *16* (6), 3349–3357.
64. Olajire, A.A. Corrosion Inhibition of Offshore Oil and Gas Production Facilities Using Organic Compound Inhibitors - a Review. *Journal of Molecular Liquids* **2017**, *248*, 775–808.
65. Kuznetsov, Y.I.; Kazansky, L.P. Physicochemical Aspects of Metal Protection by Azoles as Corrosion Inhibitors. *Russian Chemical Reviews* **2008**, *77* (3), 219–232.
66. Umoren, S.A.; Solomon, M.M. Recent Developments on the Use of Polymers as Corrosion Inhibitors - a Review. *The Open Materials Science Journal* **2014**, *8* (1), 39–54.
67. Olasunkanmi, L.O.; Obot, I.B.; Kabanda, M.M.; Ebenso, E.E. Some Quinoxalin-6-Yl Derivatives as Corrosion Inhibitors for Mild Steel in Hydrochloric Acid: Experimental and Theoretical Studies. *The Journal of Physical Chemistry C* **2015**, *119* (28), 16004–16019.
68. Al Juhaiman, L.A.; Abu Mustafa, A.; Mekhamer, W.K. Polyvinyl Pyrrolidone as a Green Corrosion Inhibitor for Carbon Steel in Alkaline Solutions Containing NaCl. *Anti-Corrosion Methods and Materials* **2013**, *60* (1), 28–36.
69. Goni, L.K.M.O.; Mazumder, M.A.J. Green Corrosion Inhibitors. *Corrosion Inhibitors* **2019**.
70. Verma, D.K.; Khan, F. Green Approach to Corrosion Inhibition of Mild Steel in Hydrochloric Acid Medium Using Extract of Spirogyra Algae. *Green Chemistry Letters and Reviews* **2016**, *9* (1), 52–60.
71. Quraishi, M.A.; Chauhan, D.S.; Saji, V.S. Heterocyclic Organic Corrosion Inhibitors: Principles and Applications, Elsevier: Amsterdam, **2020**.
72. Shen, Z.; Ren, H.; Xu, K.; Geng, J.; Ding, L. Inhibition Effect of Phosphorus-Based Chemicals on Corrosion of Carbon Steel in Secondary-Treated Municipal Wastewater. *Water Science and Technology* **2013**, *67* (11), 2412–2417.
73. Liu, L.; Cao, T.-T.; Zhang, Q.-W.; Cui, C.-W. Organic Phosphorus Compounds as Inhibitors of Corrosion of Carbon Steel in Circulating Cooling Water: Weight Loss Method and Thermodynamic and Quantum Chemical Studies. *Adv. Mater. Sci. Eng.* **2018**, Article ID 1653484.

74. Spinthaki, A.; Demadis, K.D. Chemical Methods for Scaling Control. *Corrosion and Fouling Control in Desalination Industry* **2020**, 307–342.
75. Demadis, K.D.; Barouda, E.; Stavgianoudaki, N.; Zhao, H. Inorganic–Organic Hybrid Molecular Ribbons Based on Chelating/Bridging, “Pincer” Tetraphosphonates, and Alkaline-Earth Metals. *Crystal Growth & Design* **2009**, 9 (3), 1250–1253.
76. Sekine, I.; Hirakawa, Y. Effect of 1-Hydroxyethylidene-1, 1-Diphosphonic Acid on the Corrosion of SS 41 Steel in 0.3% Sodium Chloride Solution. *CORROSION* **1986**, 42 (5), 272–277.
77. Laamari, R.; Benzakour, J.; Berrekhis, F.; Abouelfida, A.; Derja, A.; Villemin, D. Corrosion Inhibition of Carbon Steel in Hydrochloric Acid 0.5M by Hexa Methylene Diamine Tetramethyl-Phosphonic Acid. *Arabian Journal of Chemistry* **2011**, 4 (3), 271–277.
78. Labjar, N.; Lebrini, M.; Bentiss, F.; Chihib, N.-E.; Hajjaji, S. E.; Jama, C. Corrosion Inhibition of Carbon Steel and Antibacterial Properties of Aminotris-(Methylenephosphonic) Acid. *Materials Chemistry and Physics* **2010**, 119 (1-2), 330–336.
79. Prabakaran, M.; Ramesh, S.; Periasamy, V. Inhibitive Properties of a Phosphonate-Based Formulation for Corrosion Control of Carbon Steel. *Research on Chemical Intermediates* **2012**, 39 (8), 3507–3524.
80. Demadis, K.D.; Papadaki, M.; Raptis, R. G.; Zhao, H. 2D and 3D Alkaline Earth Metal Carboxyphosphonate Hybrids: Anti-Corrosion Coatings for Metal Surfaces. *Journal of Solid State Chemistry* **2008**, 181 (3), 679–683.
81. Moschona, A.; Plesu, N.; Colodrero, R. M. P.; Cabeza, A.; Thomas, A. G.; Demadis, K. D. Homologous Alkyl Side-Chain Diphosphonate Inhibitors for the Corrosion Protection of Carbon Steels. *Chemical Engineering Journal* **2021**, 405, 126864.
82. Moschona, A.; Plesu, N.; Mezei, G.; Thomas, A. G.; Demadis, K. D. Corrosion Protection of Carbon Steel by Tetraphosphonates of Systematically Different Molecular Size. *Corrosion Science* **2018**, 145, 135–150.
83. Veres, A.; Reinhard, G.; Kálmán, E. Chemical Passivation of Ferrous Materials in Presence of Salts of Phosphonic Acids. *British Corrosion Journal* **1992**, 27 (2), 147-150.
84. Demadis, K.D.; Lykoudis, P.; Raptis, R.G.; Mezei, G. Phosphonopolycarboxylates as Chemical Additives for Calcite Scale Dissolution and Metallic Corrosion Inhibition Based

- on a Calcium–Phosphonotricarboxylate Organic–Inorganic Hybrid. *Cryst. Growth Des.* **2006**, 6(5), 1064–1067.
85. Demadis, K. D.; Papadaki, M. Single-Crystalline Thin Films by a Rare Molecular Calcium Carboxyphosphonate Trimer Offer Prophylaxis from Metallic Corrosion. *ACS Applied Materials & Interfaces* **2010**, 2 (7), 1814–1816.
86. Maranescu, B.; Lupa, L.; Tara-Lunga Mihali, M.; Plesu, N.; Maranescu, V.; Visa, A. The Corrosion Inhibitor Behavior of Iron in Saline Solution by the Action of Magnesium Carboxyphosphonate. *Pure and Applied Chemistry* **2018**, 90 (11), 1713–1722.
87. Demadis, K.D.; Papadaki, M.; Raptis, R.G.; Zhao, H. Corrugated, Sheet-like Architectures in Layered Alkaline-Earth Metal *R,S*-Hydroxyphosphonoacetate Frameworks: Applications for Anticorrosion Protection of Metal Surfaces. *Chemistry of Materials* **2008**, 20 (15), 4835–4846.
88. Demadis, K.D.; Katarachia, S.D.; Koutmos, M. Crystal Growth and Characterization of Zinc–(Amino-Tris-(Methylenephosphonate)) Organic–Inorganic Hybrid Networks and Their Inhibiting Effect on Metallic Corrosion. *Inorganic Chemistry Communications* **2005**, 8 (3), 254–258.
89. Papadaki, M.; Demadis, K.D. Structural mapping of hybrid metal phosphonate corrosion inhibiting thin films. *Comments on Inorganic Chemistry* **2009**, 30 (3-4), 89–118.
90. Spinthaki, A.; Matheis, J.; Hater, W.; Demadis, K.D. Antiscalant-Driven Inhibition and Stabilization of “Magnesium Silicate” under Geothermal Stresses: The Role of Magnesium–Phosphonate Coordination Chemistry. *Energy & Fuels* **2018**, 32 (11), 11749–11760.
91. Chirkunov, A; Kouznetsov, Y. Corrosion Inhibitors in Cooling Water Systems. In *Mineral Scales and Deposits: Scientific and Technological Approaches*; Amjad, Z.; Demadis, K. D., Eds.; Elsevier: Amsterdam, **2015**; Chapter 4, pp 85–105.
92. Demadis, K.D.; Ketsetzi, A. Degradation of Phosphonate-Based Scale Inhibitor Additives in the Presence of Oxidizing Biocides: “Collateral Damages” in Industrial Water Systems. *Separation Science and Technology* **2007**, 42 (7), 1639–1649.
93. Demadis, K.D.; Lykoudis, P. Chemistry of Organophosphonate Scale Growth Inhibitors: 3. Physicochemical Aspects of 2-Phosphonobutane-1,2,4-Tricarboxylate (PBTC) and Its

Effect on CaCO₃ Crystal Growth. *Bioinorganic Chemistry and Applications* **2005**, 3 (3-4), 135–149.

94. Gendel, Y.; Lahav, O. Accurate Determination of Fe(II) Concentrations in the Presence of a Very High Soluble Fe(III) Background. *Applied Geochemistry* **2008**, 23 (8), 2123–2129.
95. Elmagirbi, A.; Sulistyarti, H.; Atikah, A. Study of Ascorbic Acid as Iron(III) Reducing Agent for Spectrophotometric Iron Speciation. *The Journal of Pure and Applied Chemistry Research* **2012**, 1 (1), 11–17.

Chapter 2: Experimental Section

2.1 Instrumentation

A KERN ABJ-NM/ABS-N analytical balance was used to weigh the solids. All pH adjustments/measurements were performed with a TwpH315i pH-meter, with a SeTix 41 pH electrode. Attenuated total reflectance–infrared (ATR–IR) spectra were collected on a Thermo Electron Nicolet 6700 Fourier transform infrared (FTIR) optical spectrometer. Scanning Electron Microscopy (SEM) and Energy Dispersive X-ray Spectroscopy (EDS) studies were carried out on two scanning electron microscopes: i. JEOL JSM-IT700HR and ii. LEO VP-35 FEM. A Hach 1900 spectrophotometer from the Hach Co. (Loveland, CO, U.S.A.) was used for the total iron determination and the methylene blue method. Nuclear Magnetic Resonance (NMR) spectra were collected on a Bruker DPX-300 instrument. A PANalytical X'Pert Pro x-ray diffractometer was used for x-ray powder diffraction (XPRD). A WITEG water bath (22 L capacity) was used for the corrosion experiments that were performed at $T = 60\text{ }^{\circ}\text{C}$ and $T = 90\text{ }^{\circ}\text{C}$, whereas the corrosion experiments at $T = 130\text{ }^{\circ}\text{C}$ were carried out in a SWON smart oven from WITEG.

2.2 Materials and Characterization

2.2.1 Reagents

All chemicals were purchased from commercial sources and were used as received. Calcium chloride dihydrate ($\text{CaCl}_2 \cdot 2\text{H}_2\text{O}$), and sulfuric acid (H_2SO_4) were purchased from Sigma-Aldrich. Sodium bicarbonate (NaHCO_3) was purchased from EM Science (Merck). Magnesium chloride hexahydrate ($\text{MgCl}_2 \cdot 6\text{H}_2\text{O}$), *N,N*-Dimethyl-*p*-phenylenediamine sulfate ($\text{C}_{10}\text{H}_{16}\text{N}_2 \cdot \text{H}_2\text{SO}_4$), 1,4-diaminobutane 99 % ($\text{H}_2\text{N}(\text{CH}_2)_4\text{NH}_2$), 1,8-diaminooctane 98 % ($\text{H}_2\text{N}(\text{CH}_2)_8\text{NH}_2$), iron(III) chloride anhydrous 98 % (FeCl_3), 1,10-phenanthroline monohydrochloride monohydrate 99 % ($\text{C}_{12}\text{H}_8\text{N}_2 \cdot \text{HCl} \cdot \text{H}_2\text{O}$), calconcarboxylic acid 94 % ($\text{C}_{21}\text{H}_{14}\text{N}_2\text{O}_7\text{S}$) and ethylenediaminetetraacetic acid tetrasodium salt 98 % ($\text{C}_{10}\text{H}_{12}\text{N}_2\text{Na}_4\text{O}_8 \cdot x\text{H}_2\text{O}$) were purchased from Alfa Aesar. Sodium chloride (NaCl), acetic acid glacial (CH_3COOH), formaldehyde (CH_2O , 36.5 % w/w aqueous solution) and ammonium acetate reagent grade ($\text{CH}_3\text{COONH}_4$) were purchased from Scharlau. Sodium sulfate (Na_2SO_4) was purchased from EM science. L-ascorbic acid reagent grade ($\text{C}_6\text{H}_8\text{O}_6$)

was purchased from SERVA. Phosphorus acid 98+ % (H_3PO_3) was purchased from Thermo Fisher Scientific. 1,12-diaminododecane 98 % ($\text{H}_2\text{N}(\text{CH}_2)_{12}\text{NH}_2$) was purchased from Fluorochem, sodium hydroxide (NaOH) was purchased from Merck and hydrochloric acid 37 % (HCl) was purchased from Riedel de Haen. Deuterium oxide (D_2O) was used as the solvent for the NMR studies. Deionized (DI) water from a laboratory ion-exchange column with an electrical conductivity of $< 0.05 \mu\text{S}/\text{cm}$ was used for all experiments.

The phosphonate additives EDTMP and HDTMP are members of the Dequest[®] series supplied by ThermPhos Inc. (acquired by Italmatch) with the following commercial names: EDTMP Dequest 2046 and HDTMP Dequest 2054. All the other organophosphonic acids were synthesized via the Mannich-type (Irani-Moedritzer) reaction (see below). Table 2.1 contains the notation and the chemical structures of the phosphonate additives.

Table 2.1. Phosphonate additives		
Name of inhibitor	Description	Molecular weights
EDTMP	ethylenediamine- <i>tetrakis</i> (methylenephosphonic acid	546.13 g/mol (as pentasodium salt)
TMTMP	tetramethylenediamine- <i>tetrakis</i> (methylenephosphonic acid	464 g/mol
HDTMP	hexamethylenediamine- <i>tetrakis</i> (methylenephosphonic acid	721 g/mol
ODTMP	octamethylenediamine- <i>tetrakis</i> (methylenephosphonic acid)	520 g/mol
DDTMP	dodecamethylenediamine- <i>tetrakis</i> (methylenephosphonic acid	586 g/mol

Due to confidentiality reasons, the chemical identity regarding the non-phosphonate additives cannot be disclosed. Table 2.2 contains the notation and some of the structural features of the non-phosphonate additives.

Table 2.2. Non-phosphonate additives

Name of inhibitor	Description
SLD	Amino acid derivative
ACAB	Blend of organic amines
DLD	Fatty amine derivative
HAD	Imidazole derivative
PELB	Phosphate ester blend
MORD	Amine derivative
ADB	Amine derivatives blend

2.2.2 Synthesis and characterization of the tetraphosphonate additives

TMTMP (C4), ODTMP (C8) and DDTMP (C12) were prepared via a Mannich type reaction, according to published procedures ^[1,2,3] and isolated as high-purity (> 98 %) solids in > 65 % yields. Figure 2.1 shows their structures and their abbreviated names. All tetraphosphonates were characterized by NMR (¹H, ¹³C, and ³¹P) and ATR-IR spectroscopy.

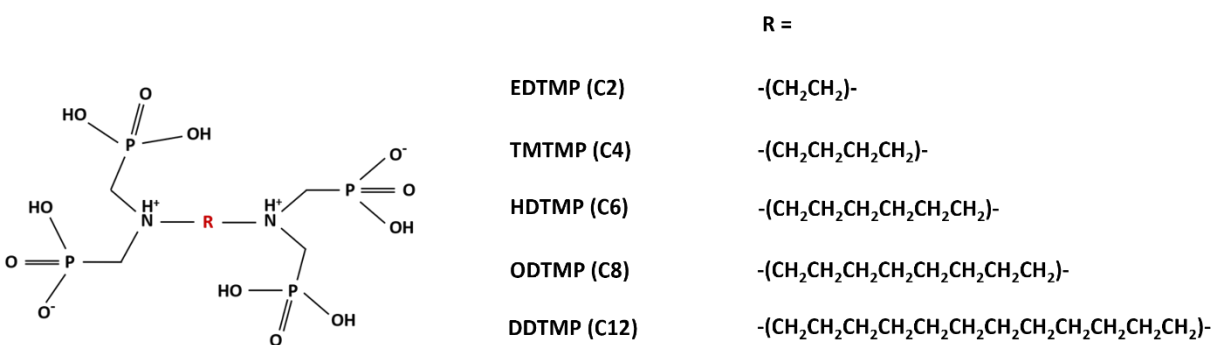


Figure 2.1. The generalized schematic structure (left) of the phosphonate-based additives and their abbreviated names (right).

Synthesis of TMTMP (C4)

5 mL of deionized water, 1.256 mL (0.0125 mol) of 1,4 diaminobutane, 4.1 g (0.05 mol) of phosphorus acid and 5 mL of hydrochloric acid (37 %) were introduced in a two-necked round bottom flask equipped with a magnetic stirring bar and a reflux condenser and heated to reflux at 120 °C. After 1 hour, 7.5 mL (0.1 mol) of formaldehyde solution was slowly added in a dropwise manner. The reaction mixture was kept at reflux for 3 hours. Then, the condenser was removed, and the mixture remained at 120°C in order to evaporate the solvent, resulting in the formation of a yellow viscous solution. In order to isolate the product in its solid form, 50 mL of methanol were added, the solution was stirred, and the oil was turned into a solid, which was isolated by filtration. The corresponding NMR spectra of C4 are shown in Figure 2.2. ^1H NMR (300 MHz, D_2O): δ 3.46 (m, 12H, CH_2), 1.79 (m, 4H, CH_2), ^{13}C NMR (300 MHz, D_2O) δ 55.53 (s), 51.26 (d, $^1\text{J}(\text{P},\text{C})=139.37\text{Hz}$, 4 CH_2), 20.20 (s), ^{31}P NMR (300 MHz, D_2O) δ 16.42 (s).

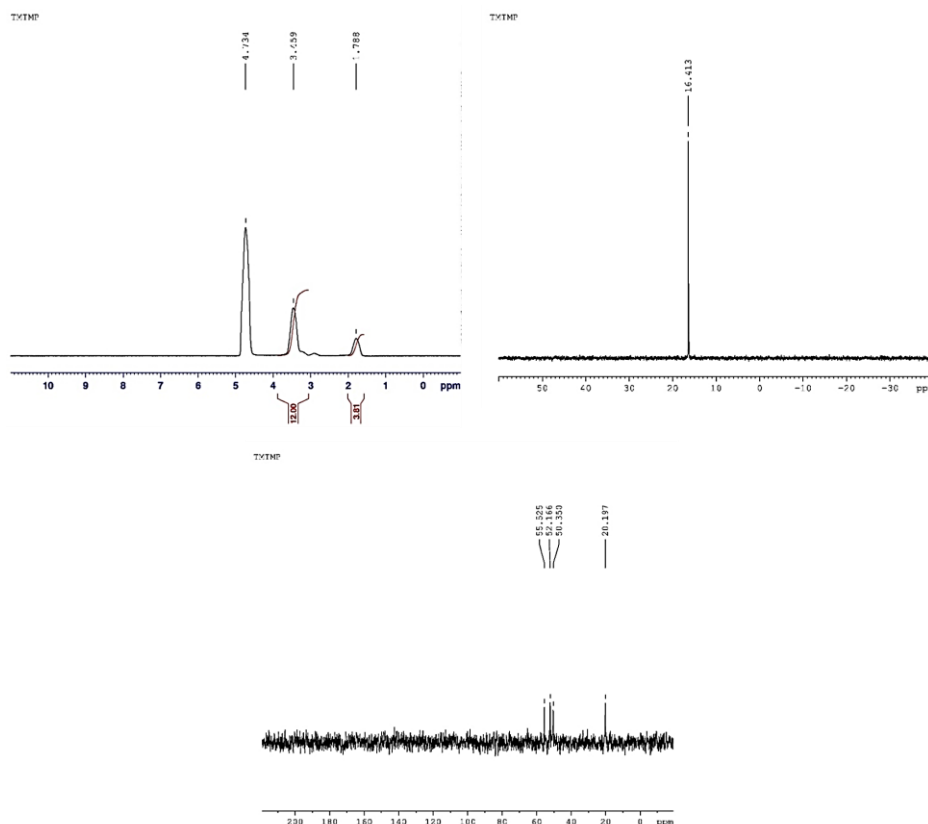


Figure 2.2. (upper left) ^1H NMR spectrum, (upper right) ^{31}P NMR spectrum and (bottom) ^{13}C NMR spectrum for C4.

Synthesis of ODTMP (C8)

5 mL of deionized water, 1.804 g (0.0125 mol) of 1,8 diaminooctane, 4.1 g (0.05 mol) of phosphorus acid and 5 mL of hydrochloric acid (37 %) were introduced in a two-necked round bottom flask equipped with a magnetic stirring bar and a reflux condenser and heated to reflux at 120°C. After 1 hour, 7.5 mL (0.1 mol) of formaldehyde solution was added dropwise. The reaction mixture was kept at reflux for 3 hours. Then, the condenser was removed, and the mixture remained at 120°C in order to evaporate the solvent, resulting in the formation of a yellow viscous solution. In order to isolate the product in its solid form, 50 mL of ethanol were added, the solution was stirred, and the oil was turned into a solid, which was isolated by filtration. The corresponding NMR spectra of C8 are shown in Figure 2.3. ^1H NMR (300 MHz, D_2O): δ 3.40 (m, 12H, CH_2), 1.65 (m, 4H, CH_2), 1.25 (m, 8H, CH_2), ^{13}C NMR (300 MHz, D_2O) δ 56.82 (s), 51.30 (d, $^1\text{J}(\text{P},\text{C})=136.63\text{Hz}$, 4 CH_2), 27.68 (s), 25.17 (s), 22.96 (s), ^{31}P NMR (300 MHz, D_2O) δ 16.50 (s).

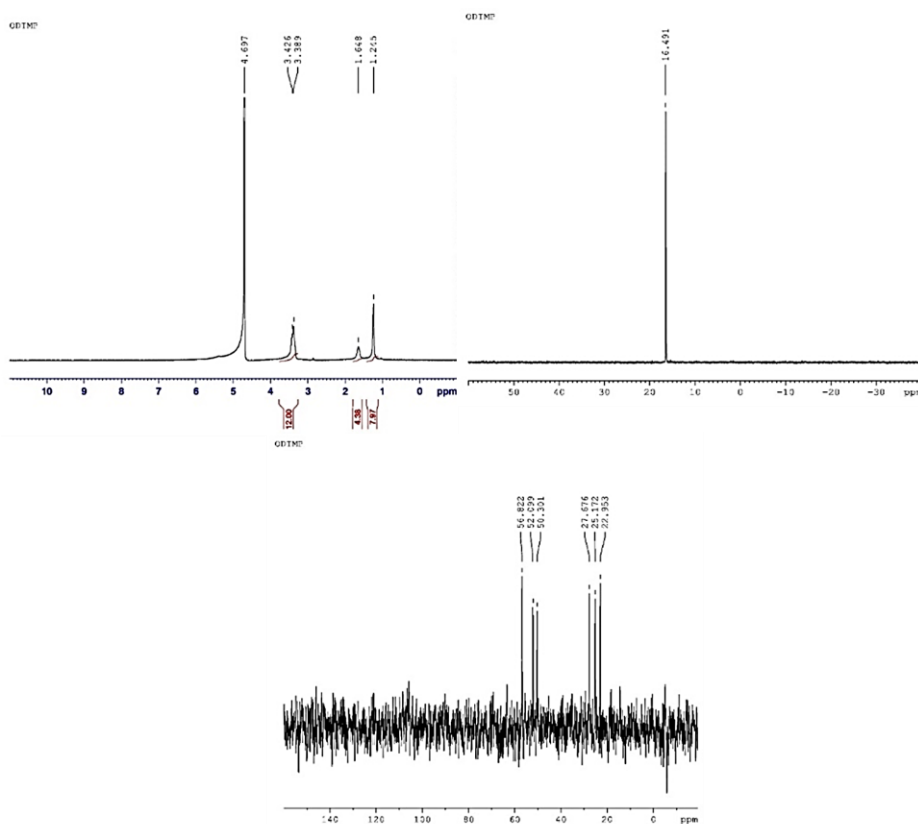


Figure 2.3. (upper left) ^1H NMR spectrum, (upper right) ^{31}P NMR spectrum and (bottom) ^{13}C NMR spectrum for C8.

Synthesis of DDTMP (C12)

5 mL of deionized water, 2.504 g (0.0125 mol) of 1,12 diaminododecane, 4.1 g (0.05 mol) of phosphorus acid and 5 mL of hydrochloric acid (37 %) were introduced in a two-necked round bottom flask equipped with a magnetic stirring bar and a reflux condenser and heated to reflux at 120°C. After 1 hour, 7.5 mL (0.1 mol) of formaldehyde solution was added dropwise. The reaction mixture was kept at reflux for 3 hours. Then, the condenser was removed, and the mixture remained at 120°C in order to evaporate the solvent, resulting in the formation of a yellow viscous solution. In order to isolate the product in its solid form, 50 mL of ethanol were added, the solution was stirred, and the oil was turned into a solid, which was isolated by filtration. The corresponding NMR spectra of C12 are shown in Figure 2.4. ^1H NMR (300 MHz, D_2O): δ 3.38 (m, 12H, CH_2), 1.65 (m, 4H, CH_2), 1.18 (m, 16H, CH_2), ^{13}C NMR (300 MHz, D_2O) δ 55.65 (d, $^1\text{J}(\text{P},\text{C})=162.06\text{Hz}$, 4 CH_2), 52.92 (s), 28.66 (d), 28.47 (s), 25.67 (s), 23.36 (s), ^{31}P NMR (300 MHz, D_2O) δ 16.47 (s).

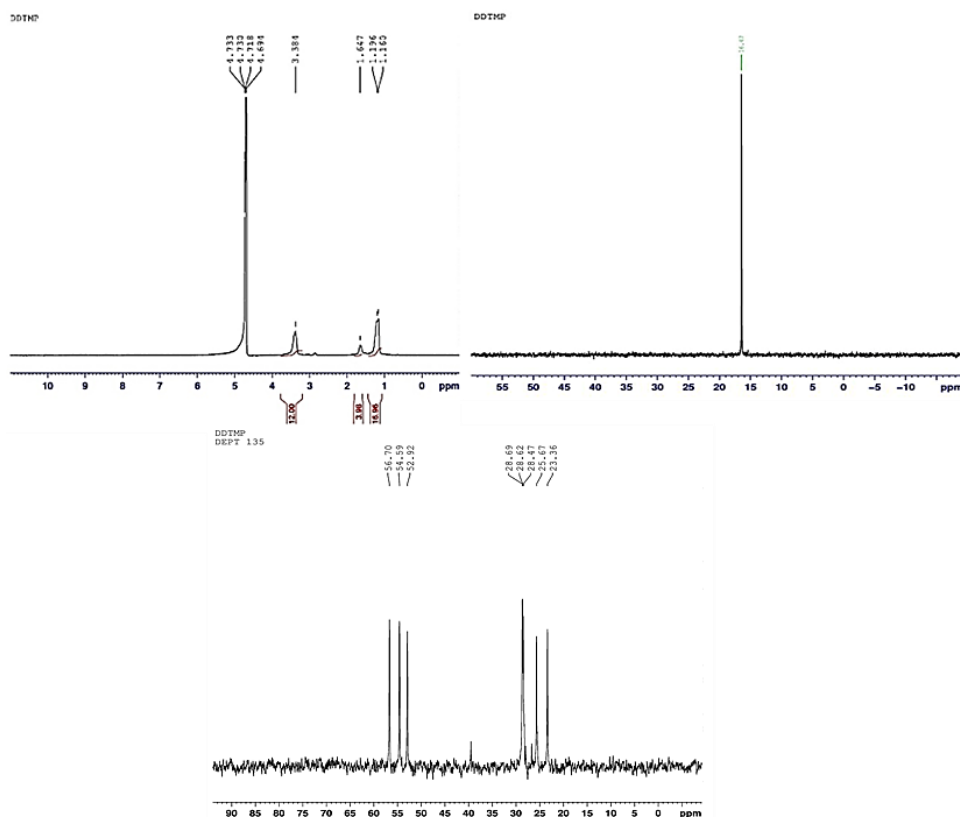


Figure 2.4. (upper left) ^1H NMR spectrum, (upper right) ^{31}P NMR spectrum and (bottom) ^{13}C NMR spectrum for C12.

Furthermore, all tetraphosphonates were characterized by ATR-IR spectroscopy. Table 2.3 contains the characteristic bands for the tetraphosphonates and their assignments, and Figure 2.5 shows the corresponding spectra. Note that C2 and C6 are commercially available products, and their NMR and ATR-IR spectra are shown in the Annex. Comparing the different spectra of the tetraphosphonates, the vibrational bands assigned to CH₂ appear gradually enhanced in intensity, as the length of the carbon chain increases. The observed bands are in agreement with those expected, according to literature [4-8].

Table 2.3. Vibrational bands and their assignments for the tetraphosphonates C4, C8, and C12.

Assignments	C4	C8	C12
ν_{as} and ν_{sym} of CH ₂	2991, 2941	2991, 2936, 2859	2996, 2918, 2855
$\nu(\text{OH}, \text{P}(\text{OH}))$	2768, 2632, 2368	2732, 2532, 2363	2736, 2658, 2363
$\delta(\text{CH}_2)$ and/or $\nu(\text{C-N})$	1444, 1419, 1390, 1338	1512, 1458, 1394, 1331	1508, 1454, 1398, 1335
$\nu(\text{P=O}, \text{P-O(H)})$	1271, 1228, 1171, 1128, 1069, 941	1276, 1235, 1135, 1007, 939	1285, 1225, 1154, 936
$\nu(\text{C-P})$	827, 775, 718	853, 816, 716	850, 813, 711
$\nu(\text{OH}, \text{P}(\text{OH}))$	623 - 400	622 - 400	615 - 400

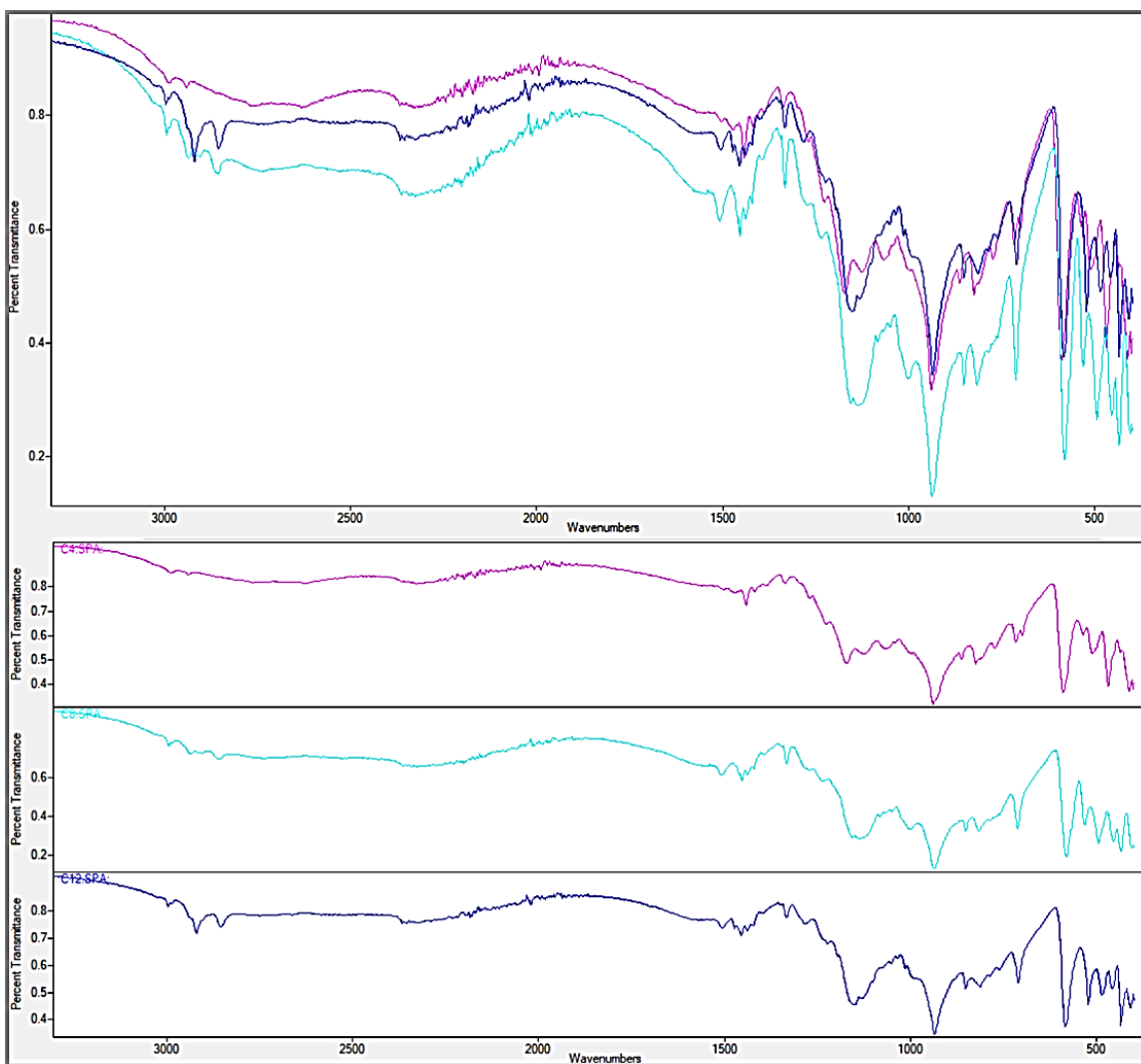


Figure 2.5. ATR-IR spectra for the tetraphosphonates C4, C8, and C12.
 Color codes: *purple C4, light blue C8 and blue C12.*

2.3 Corrosion quantification and other determination methods

2.3.1 Gravimetric measurements

During steel corrosion, iron surface layers are converted to Fe oxides and oxyhydroxides (depending on the specific conditions). At the end of each experiment, the corrosion products are removed. Hence, the specimen weight is reduced. Specifically, when corrosion is extensive, weight loss is high, and when corrosion is inhibited, the weight loss is zero (ideally) or very small. Hence,

this method can quantify the corrosion rate (CR, commonly expressed as mm/y, millimeters per year) by using the weight loss of each specimen, according to the Equation 1:

$$CR = \frac{\text{mass loss} \times 87.6}{\text{area} \times \text{time} \times \text{metal density}} \quad (\text{mm/y}) \quad (1)$$

where CR is expressed in mm/year, mass loss is in mg, specimen surface area is in cm² and refers only to the surface of the specimen in contact with the aqueous medium, time is in hours and metal density is in g/cm³^[9]. In this work, two different types of carbon steel specimens were used. In the case of the corrosion experiments at ambient temperature (RT), 60 °C and 90 °C, the surface of the sample that was immersed in the solution was 19.62 cm² and the time of the corrosion experiment was 168 hours, while at 130°C the surface of the sample was 15.52 cm² and the time was 24 hours. In both cases, the density of the metal was 7.87 g/cm³. The error associated with the gravimetric measurements is ± 10 %.

Procedure: Carbon steel specimens (coupons) were exposed to aqueous solutions of different water chemistry, with different inhibitor concentrations and pH values for a specific period. Each specimen was weighed before and at the end of the experiment, but after being air-dried and mildly cleaned using abrasive paper. Corrosion rates were calculated according to Equation 1, above. Figure 2.6 shows the appearance of some representative specimens, at the end of the experiments carried out in the presence of different inhibitors (before the surface cleaning procedure).



Figure 2.6. Visual representation of carbon steel specimens at the end of different experiments.

The inhibition efficiency (%) was calculated based on the equation 2:

$$\text{Inhibition efficiency (\%)} = \frac{\text{CR}_{\text{control}} - \text{CR}_{\text{inhibitor}}}{\text{CR}_{\text{control}}} \times 100 \% \quad (2)$$

where $\text{CR}_{\text{control}}$ represents the corrosion rate value of the control experiment (in the absence of corrosion inhibitors) and $\text{CR}_{\text{inhibitor}}$ represents the corrosion rate value of the experiment in the presence of a corrosion inhibitor.

2.3.2 Total iron determination method

The Phenanthroline method (Program: HACH DR1900: 255 Iron Ferrous) is based on the photometric quantification of a colored iron-phenanthroline complex. Three molecules of phenanthroline chelate one ferrous iron, leading to the formation of a stable complex of orange-red color, which is called Ferriin. The reaction is shown in Figure 2.7. Ammonium acetate buffer is used to maintain the pH at 3.5, resulting in a rapid color development in the presence of excess phenanthroline ^[10,11]. The ferric iron is reduced to the ferrous state by boiling a sampled solution with hydrochloric acid and ascorbic acid (the reductant). The absorbance is recorded at $\lambda = 510$ nm. The error of the total iron determination method is $\pm 13.3\%$.

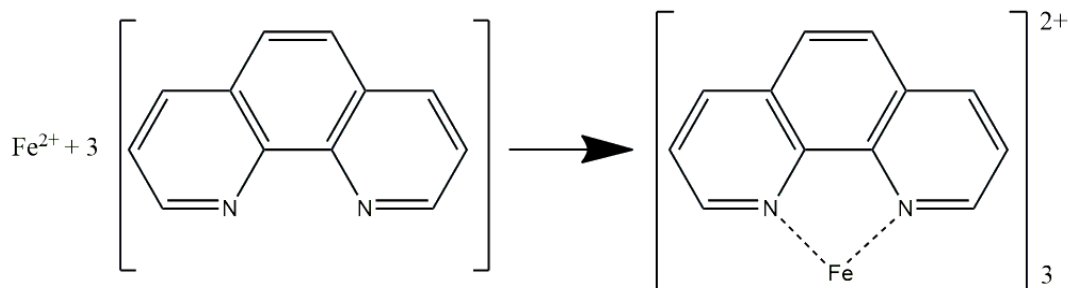


Figure 2.7 The reaction of the iron-phenanthroline complex.

Procedure: At the end of the corrosion experiment, a 0.2 mL sample of the aqueous solution (in which the coupons were immersed) is withdrawn and then placed into a glass sample cell (25 mm round, 10-20-25 mL marks) containing 0.56 mL “1+1” hydrochloric acid. 0.1 mL of ascorbic acid and 2 mL of deionized water are added and then the mixture is heated to a boil until the volume is reduced to half (approximately 10 min). After cooling to ambient temperature, 3 mL of ammonium acetate buffer and 1.2 mL of phenanthroline were added. The solution is carefully stirred and then left aside for 7 minutes. Finally, the color intensity of the solution was measured. DI water is used as a “blank” to zero the instrument before the measurement. See Section 2.4 for the preparation of stock and working solutions.

Figure 2.8 presents a visual representation of the intensity of the colored solutions, concerning samples taken from the experiments in the presence of different inhibitors, depending on the effectiveness of each inhibitor.

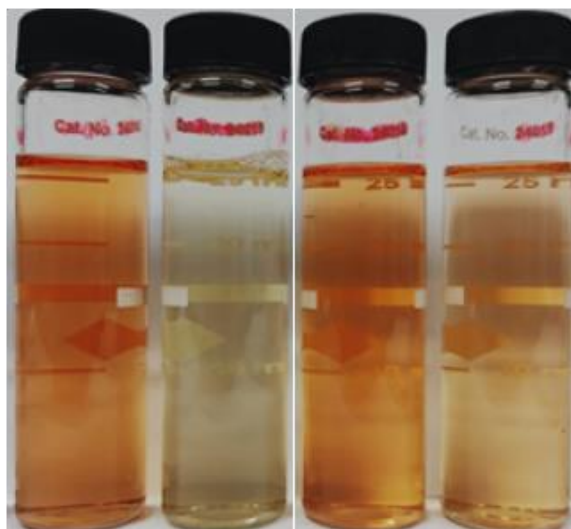


Figure 2.8. Visual representation of the orange-colored solutions that develop during the phenanthroline method. The intensity of the color can be used as a measure of the corrosion inhibitor efficiency: The color intensity is directly proportional to the inhibitor efficiency.

The inhibition efficiency (%) was calculated based on the equation 3:

$$\text{Inhibition efficiency (\%)} = \frac{Fe_{\text{control}} - Fe_{\text{inhibitor}}}{Fe_{\text{control}}} \times 100 \% \quad (3)$$

where Fe_{control} represents the iron concentration of the control experiment (in the absence of corrosion inhibitors) and $Fe_{\text{inhibitor}}$ represents the iron concentration of the experiment in the presence of a corrosion inhibitor.

2.3.3 Sulfide determination

The Methylene Blue method (Program: HACH DR1900: 691 Sulfide HR) is based on the reaction of sulfide, ferric chloride and dimethyl-*p*-phenylenediamine (DMPD) to produce methylene blue ^[12,13]. The reaction is shown in Figure 2.9. The absorbance is recorded at $\lambda = 664$ nm. The error of detection of the sulfide determination is ± 4 %.

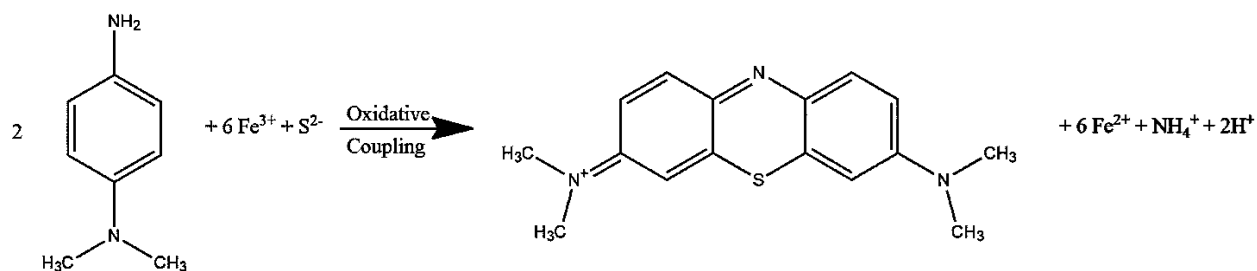


Figure 2.9 Sulfide conversion into methylene blue ^[13].

Procedure: A 0.1 mL aliquot from the working solution is diluted to 25 mL in a special cylindrical cell of 1 cm path length. Then, 1 mL amine-sulfuric acid reagent is added along with 3 drops of ferric chloride. The solution is carefully stirred and then left aside for 5 minutes. Finally, the color intensity of the solution was measured. The following step is optional: 1.6 mL bisammonium hydrogen phosphate solution is added. DI water is used to zero the instrument before the measurement. See Section 2.4 for the preparation of stock and working solutions.

Figure 2.10 presents a visual representation of the intensity of the colored solutions, concerning samples taken from the experiments with different sulfide concentrations.

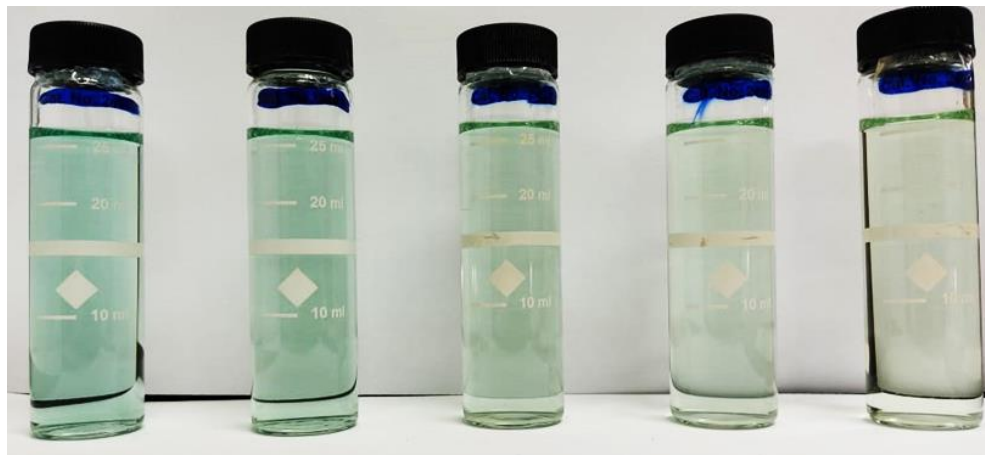


Figure 2.10. Visual representation of the color intensity that develops, depending on sulfide concentration (highest to the left, lowest to the right).

2.3.4 EDTA titration

The EDTA titration method was used for soluble Ca^{2+} ion quantification. This method is based on the reaction of EDTA with Ca^{2+} ions, forming a very stable Ca-EDTA complex. The addition of Calcon indicator in a solution containing Ca^{2+} ions results in the formation of a pink-colored Ca-EDTA complex. The color of the solution slowly changes, as the quantity of EDTA in the solution increases, until it becomes blue. The error of this method is $< 1\%$ [12,14].

Procedure: A burette is filled with EDTA stock solution (0.001M). 1 mL sample of the working solution is filtered and then added to an Erlenmeyer flask, followed by the addition of 9 mL of DI water. Next, the pH of the solution is adjusted to 12-13, so that the presence of soluble Mg^{2+} in the solution will be precipitated as $\text{Mg}(\text{OH})_2$. In this way, the Mg^{2+} ions will not react with EDTA and will not interfere with the Ca^{2+} measurement. Then, 5 drops of the Calcon indicator are added, resulting in a pink solution. Finally, the EDTA solution is added dropwise under stirring, until the color of the solution turns blue. See Section 2.4 for the preparation of stock and working solutions.

The inhibition efficiency (%) was calculated based on the equation 4:

$$\text{Inhibition efficiency (\%)} = \frac{Ca_{\text{inhibitor}} - Ca_{\text{control}}}{Ca_{\text{control}}} \times 100 \% \quad (4)$$

where Ca_{control} represents the calcium concentration of the control experiment (in the absence of corrosion inhibitors) and $Ca_{\text{inhibitor}}$ represents the calcium concentration of the experiment in the presence of a corrosion inhibitor.

2.4 Preparation of Stock and Working Solutions

Phenanthroline method: The ammonium acetate buffer solution (I) was prepared by dissolving 25 g of ammonium acetate ($\text{CH}_3\text{COONH}_4$) in a mixture of 15 mL of DI water and 70 mL of acetic acid glacial (CH_3COOH). The phenanthroline solution (II) was prepared by dissolving 0.130 g of 1,10-phenanthroline monohydrochloride monohydrate 99 % ($\text{C}_{12}\text{H}_8\text{N}_2 \cdot \text{HCl} \cdot \text{H}_2\text{O}$) in 100 mL of DI water, followed by the addition of 2-3 drops of concentrated hydrochloric acid. “1+1” Hydrochloric acid (III) was prepared by diluting 10 mL concentrated hydrochloric acid to 10 mL of DI water. The L-ascorbic acid solution (IV) was prepared by dissolving 2.5 g of L-ascorbic acid reagent grade ($\text{C}_6\text{H}_8\text{O}_6$) in 10 mL of DI water. “1+1” Sulfuric acid (V) was prepared by diluting 10 mL concentrated sulfuric acid to 10 mL of DI water in an ice bath.

Methylene blue method: The amine-sulfuric acid stock solution (VI) was prepared by dissolving 2.7 gr of *N,N*-Dimethyl-*p*-phenylenediamine sulfate in an iced mixture of “1+1” Sulfuric acid (V) (the total volume was 10 mL). The mixture was cooled and diluted to 100 mL with DI water. The amine-sulfuric acid reagent (VII) was prepared by diluting 2.5 mL of amine-sulfuric acid stock solution (VI) in 100 mL of a “1+1” Sulfuric acid (V). Ferric chloride solution (VIII) was prepared by dissolving 50 g of $\text{FeCl}_3 \cdot 6\text{H}_2\text{O}$ in 20 mL of DI water.

EDTA titration method: Ethylenediaminetetracetic acid (EDTA) stock solution (IX) was prepared by dissolving 0.19 g of tetrasodium EDTA in 500 mL of DI water. NaOH stock solution

(X) was prepared by dissolving 20 g of NaOH in 250 mL DI water. Calcon stock solution (XI) was prepared by dissolving 0.1 g of calconcarboxylic acid (C₂₁H₁₄N₂O₇S) in 20 mL of methanol.

Brine solutions: The calcium chloride stock solution (A) was prepared by dissolving 36.661 g of calcium chloride dehydrate (CaCl₂·2H₂O) in 100 mL of DI water (10,0000 ppm). The sodium chloride stock solution (B) was prepared by dissolving 36.661 g of sodium chloride (NaCl) in 100 mL of DI water (10,0000 ppm). The sodium sulfate stock solution (C) was prepared by dissolving 1.479 g of sodium sulfate (Na₂SO₄) in 100 mL of DI water (10,000 ppm). The sodium bicarbonate stock solution (D) was prepared by dissolving 13.768 g of sodium bicarbonate (NaHCO₃) in 100 mL of hot DI water (10,0000 ppm). The magnesium chloride stock solution (E) was prepared by dissolving 8.365 g of magnesium chloride hexahydrate (MgCl₂·6H₂O) in 100 mL of DI water (10,000 ppm). Artificial brine solution was prepared by diluting the desired volumes of stock solutions A, B, C, D and E, to perform corrosion experiments in two different representative geothermal fluids. Specifically, Brine 1 contains 200 ppm Ca²⁺, 1000 ppm Cl⁻, 200 ppm SO₄²⁻ and 1220 ppm HCO₃⁻ and Brine 2 contains 7218 ppm Ca²⁺, 486 ppm Mg²⁺, 57000 ppm Cl⁻ and 170 ppm SO₄²⁻.

Synergy tests: The calcium chloride stock solution (F) was prepared by dissolving 0.3528 g of calcium chloride dehydrate (CaCl₂·2H₂O) in 200 mL of DI water (12 mM). The magnesium chloride stock solution (G) was prepared by dissolving 0.4879 g of magnesium chloride hexahydrate (MgCl₂·6H₂O) in 200 mL of DI water (12 mM).

The phosphonate inhibitor stock solutions (12 mM) were prepared by dissolving the appropriate amount of the respective tetraphosphonate in 200 mL of DI water. Table 2.4 contains specific quantities for all phosphonate inhibitors. Non-phosphonate inhibitor stock solutions (10,000 ppm) were prepared by dissolving 1 g of the inhibitor in 100 mL of DI water.

Table 2.4. Quantities for the preparation of 12 mM inhibitor stock solutions				
C2	C4	C6	C8	C12
5.160 g	1.114 g	7.524 g	1.248 g	1.407 g

2.5 Carbon steel sample preparation

Corrosion Carbon Steel Alloy C1010 specimens were prepared according to a modified protocol based on NACE Standard TM0169-05 (Item No. 21200), National Association of Corrosion Engineers, Houston TX, USA [9]. Specifically, the specimens used in the corrosion experiments at ambient temperature, at $T = 60\text{ }^{\circ}\text{C}$ and at $T = 90\text{ }^{\circ}\text{C}$ (dimensions: 7.6 cm x 1.2 cm x 0.1 cm) were cleaned and weighted before the experimental procedure. In addition, specimens used in the experiments at $T = 130\text{ }^{\circ}\text{C}$ (dimensions: 5 cm x 1.5 cm x 0.05 cm) were bent to fit inside the Teflon reaction vessels of the high-throughput system (see below).

Specimens were immersed in aqueous solutions containing of different inhibitor concentrations at pH 7. In addition, corrosion experiments in the absence of phosphonate inhibitors were performed and used as “control” experiments. After 168 hours (for experiments at RT, $60\text{ }^{\circ}\text{C}$ and $90\text{ }^{\circ}\text{C}$) and 24 hours (for experiments at $130\text{ }^{\circ}\text{C}$), specimens were removed from the test solutions, air-dried and cleaned to determine corrosion rates from mass loss according to the NACE standard method.

2.6 Experimental set-up

Corrosion experiments at RT, $60\text{ }^{\circ}\text{C}$ and $90\text{ }^{\circ}\text{C}$ were performed in glass bottles with screw caps, an inner diameter of 56 mm, a height of 100 mm and a total volume of 130 mL. Corrosion experiments at $130\text{ }^{\circ}\text{C}$ were performed using a high-throughput system. The autoclave block is made of aluminum and contains 6 reaction chambers in a 3×2 array. Teflon reactors have an inner diameter of 19 mm, a depth of 18 mm and a total volume of 5 mL. A thin sheet of Teflon covers the reaction vessels, which are then sealed inside a specially designed aluminum autoclave. At the end of this type of experiment (24 hours), the system was left to cool down to RT for 30 minutes. The experimental setups for these conditions are shown in Figure 2.11.

Furthermore, corrosion experiments under stirring at RT were performed in glass bottles with screw caps with an inner diameter of 11.5 cm, a height of 24 cm and a total volume of 1400 mL. In this case, specimens did not rest at the bottom of the glass bottle (to avoid any contact with the magnetic stirrer) but were hung inside the solution with a cotton thread. Finally, corrosion experiments at RT in the presence of 50 ppm S^{2-} were performed both in glass bottles with caps,

allowing oxygen to be present in the solution, and in Erlenmeyer flasks with an inner diameter of 6.5 cm, a height of 10.5 cm and a total volume of 130 mL. In this case, each flask is equipped with a rubber septum, so that argon can be injected and maintain an inert atmosphere. The experimental setups for these conditions are shown in Figure 2.12.



Figure 2.11. Experimental set-up depending on the desired conditions. *left* Glass bottles with screw caps for corrosion experiments at RT, 60 °C and 90 °C and *right* High-throughput system containing multiple reaction vessels for HP-HT corrosion experiments (upper: side-view, lower: top view).



Figure 2.12. Experimental set-up depending on the desired conditions. Left: Glass bottles with screw caps for corrosion experiments at RT under stirring. Right: Erlenmeyer flasks for corrosion experiments in the presence of 50 ppm S^{2-} .

2.7 References

1. Hellal, A.; Chafaa, S.; Chafai, N. Synthesis, Characterization and Computational Studies of Three α -Amino-Phosphonic Acids Derivatives from Meta, Ortho and Para Aminophenol. *Journal of Molecular Structure* **2016**, *1103*, 110–124.
2. Moedritzer, K.; Irani, R.R. The Direct Synthesis of α -Aminomethylphosphonic Acids. Mannich-Type Reactions with Orthophosphorous Acid. *The Journal of Organic Chemistry* **1966**, *31* (5), 1603–1607.
3. Mady, M.F.; Kelland, M.A. Overview of the Synthesis of Salts of Organophosphonic Acids and Their Application to the Management of Oilfield Scale. *Energy & Fuels* **2017**, *31* (5), 4603–4615.
4. Demadis, K.D.; Barouda, E.; Zhao, H.; Raptis, R.G. Structural Architectures of Charge-Assisted, Hydrogen-Bonded, 2D Layered Amine···Tetraphosphonate and Zinc···Tetraphosphonate Ionic Materials. *Polyhedron* **2009**, *28* (15), 3361–3367.
5. Zenobi, M.C.; Luengo, C.V.; Avena, M.J.; Rueda, E.H. An ATR-FTIR Study of Different Phosphonic Acids Adsorbed onto Boehmite. *Spectrochimica Acta Part A: Molecular and Biomolecular Spectroscopy* **2010**, *75* (4), 1283–1288.
6. Chaplais, G.; Le Bideau, J.; Leclercq, D.; Vioux, A. Polarized-Dependent IR ATR Study for the Structural Characterization of Solid-State Phosphonates: Case of Aluminum (4-Carboxyphenyl)methylphosphonate. *Chemistry of Materials* **2003**, *15* (10), 1950–1956.
7. Princz, E.; Szilágyi, I.; Mogyorósi, K.; Labádi, I. *Journal of Thermal Analysis and Calorimetry* **2002**, *69* (2), 427–439.
8. Moschona, A.; Plesu, N.; Mezei, G.; Thomas, A.G.; Demadis, K.D. Corrosion Protection of Carbon Steel by Tetraphosphonates of Systematically Different Molecular Size. *Corrosion Science* **2018**, *145*, 135–150.
9. Standard TM0169-95 (Item No. 21200), National Association of Corrosion Engineers, Houston TX, U.S.A. (www.nace.org).
10. Gendel, Y.; Lahav, O. Accurate Determination of Fe(II) Concentrations in the Presence of a Very High Soluble Fe(III) Background. *Applied Geochemistry* **2008**, *23* (8), 2123–2129.
11. Elmagirbi, A.; Sulistyarti, H.; Atikah, A. Study of Ascorbic Acid as Iron(III) Reducing Agent for Spectrophotometric Iron Speciation. *The Journal of Pure and Applied Chemistry Research* **2012**, *1* (1), 11–17.

12. Eaton, A.D.; Clesceri, L.S.; Rice, E.W.; Greenberg, A.E.; Franson, M.H. Standard Methods for Examination of Water & Wastewater, American Public Health Association, Washington DC, **2005**.
13. Hassan, S.S.M.; Marzouk, S.A.M.; Sayour, H.E.M. Methylene Blue Potentiometric Sensor for Selective Determination of Sulfide Ions. *Analytica Chimica Acta* **2002**, 466 (1), 47–55.
14. Patton, J.; Reeder, W. New Indicator for Titration of Calcium with (Ethylenedinitrilo) Tetraacetate. *Analytical Chemistry*, **1956**, 28 (6), 1026-1028.

Chapter 3: Corrosion experiments in artificial brine of medium salinity

3.1 Characterization of the corrosion products

The corrosion rate is a reliable tool by which corrosion aggressiveness is evaluated. It gives a quantitative evaluation of the general corrosion. As mentioned in Chapter 1, there are several parameters that influence the speed (rate) of the corrosion process. Factors and variables that play a decisive role in the corrosion “stress” include the nature of the metal (metallurgy), the chemical composition of the aqueous medium that is in contact with the metal surface (corrosive species), the temperature and the acidity (pH) of the fluid that is in direct contact with the metal surface, as well as the concentration of dissolved oxygen. It is important to mention that most of these parameters vary from one geothermal site to another or even in different parts of the same system, as the temperature and the pressure of the geothermal fluid changes as the fluid passes through the different depths of the geothermal well. In the framework of the present research, the protection of carbon steel from corrosion was studied in the presence of diverse corrosion inhibitors. The selected chemical additives were categorized as (a) phosphonate inhibitors and (b) non-phosphonate inhibitors, and their anticorrosion efficiency was evaluated in a range of different inhibitor concentrations, in order to uncover the optimum inhibitor dosage.

The aim of this research is the direct application of the most effective inhibitors in geothermal plants. Hence, appropriate experimental conditions were selected based on the realistic needs of the geothermal industry. More specifically, carbon steel alloy specimens were used, which were exposed to brine solutions of variable severity at pH 7, in closed containers in order to keep the dissolved oxygen concentration constant during the experiment. In this chapter, the corrosion experiments were performed in an artificial geothermal brine of “medium” salinity, named “Brine 1”. Table 3.1 contains the chemical composition of Brine 1. Note that the different dissolved species are expressed as follows: Ca^{2+} as “ppm Ca”, Cl^- as “ppm Cl”, SO_4^{2-} as “ppm SO_4 ”, and HCO_3^- as “ppm HCO_3 ”. The total key species (TKS) is 2660 ppm, 37.6 % of which are chloride ions. Three different temperatures were selected, in an effort to model the different pressure and temperature conditions of the geothermal systems. In addition, experiments were performed at ambient temperature (RT), for comparison reasons. Instrumentation, reagents, stock solution

preparation and experimental set up for the corrosion experiments under the different conditions are mentioned in detail in Chapter 2.

Table 3.1. Chemical composition of Brine 1.

Ca ²⁺	Cl ⁻	SO ₄ ²⁻	HCO ₃ ⁻
260 ppm	1000 ppm	200 ppm	1200 ppm

Herein, the anticorrosion efficiency of the chemical additives was exploited by varying three principal parameters: water quality, temperature and inhibitor concentration. In order to understand the factors that influence the formation of corrosion products, as well as the conditions under which corrosion is accelerated, experiments were carried out in the absence of any chemical additive, under several experimental conditions. The results of which were then used as a “baseline” comparison tool (control) to evaluate the anticorrosion efficiency of the inhibitors. Corrosion rates and iron concentrations of the control experiments are presented in Table 3.2 and Figure 3.1.

Table 3.2. Corrosion rates and iron concentrations of the control corrosion experiments.

T (°C)	RT		60		90		130	
	CR (mm/y)	Fe (ppm)	CR (mm/y)	Fe (ppm)	CR (mm/y)	Fe (ppm)	CR (mm/y)	Fe (ppm)
Brine 1	0.062	95	0.110	168	0.087	133	0.148	448

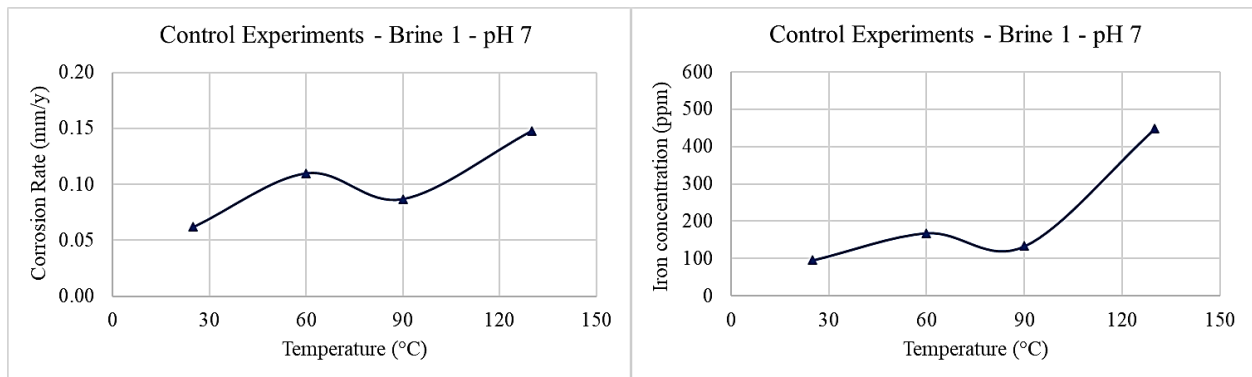


Figure 3.1. Results obtained in the absence of chemical additives in Brine 1 at pH 7. *left* Corrosion Rates and *right* Iron concentrations.

In general, an increase in temperature causes the speed of a chemical reaction to increase (except exothermic reactions), so it is expected to accelerate corrosion processes as well. However, there are multiple factors that must be taken into account, because the solubility of the components of the aqueous medium is influenced by the increase in temperature and pressure. A typical example is the case of dissolved oxygen. Increasing the temperature initially causes the corrosion rate to increase, but then this rate will drop due to the reduced solubility of the dissolved oxygen in the solution. Nevertheless, no linear relationship between the increase in temperature and corrosion rate was observed. Interestingly, as will be discussed in Chapter 4 and Chapter 5, the same “S-shaped” trend was observed for all water qualities, with the corrosion rates being at their lowest value for the experiments performed at room temperature and their highest value for the experiments performed at 130 °C. The results obtained at the two “intermediate” temperatures are intriguing, as the corrosion rate values at 90 °C are lower than the corresponding values at 60 °C.

The formation of an oxide layer on the metallic surface can act either slow down or accelerate corrosion processes, depending on the chemical composition of the iron oxide deposit and the quality of the layer which is formed on the surface ^[1]. Therefore, in addition to the other parameters, the corrosion product itself should be taken into account as well. Temperature plays a significant role in the most thermodynamically stable iron phase, resulting in the formation of different corrosion products.

Comparing the surfaces of the samples exposed to experiments (see Figure 3.2), the color difference between the different corrosion products is obvious. In the case of 90 °C and 130 °C, the grey-black color is a strong indication of the formation of a magnetite film ^[2,3,4]. The precipitates were selected from the corresponding experiments and then characterized by ATR-IR spectroscopy and X-Ray Powder Diffraction, so that the corrosion products can be reliably identified. The amount of the precipitate which was collected from the control experiment at 130 °C was very small and could not be removed from the filter membrane. Thus, samples from the pristine membrane were taken and used as a background for the ATR-IR studies, so the bands associated with its material can be easily identified (see the grey inset at the bottom spectrum). The respective spectrum of the membrane filter is shown in the Annex (Chapter 8).



Figure 3.2. Corroded carbon steel surfaces of the specimens exposed to “control” solutions in Brine 1, at pH 7.

Figure 3.3 presents the ATR-IR spectra of the control experiments. All samples present vibration bands of adsorbed water around 3400 cm^{-1} and 1625 cm^{-1} . The corrosion products formed at RT and $60\text{ }^{\circ}\text{C}$ showed identical ATR-IR spectra. Comparison with the reported bands in literature indicates that formation of chukanovite has taken place, as vibration bands in a reference spectrum at 871 cm^{-1} , 934 cm^{-1} , 1408 cm^{-1} , and 1476 cm^{-1} are observed in the corresponding spectra of the corrosion products. The identified iron hydroxide-carbonate corrosion product has a pale green color; however, it turns to brown after being transformed at the surface. In general, chukanovite tends to convert to the more stable magnetite ^[5]. The latter appears to be true for the $90\text{ }^{\circ}\text{C}$ experiment, as the dark layer of the deposit on the specimen surface indicates. Unfortunately, its reliable identification was not successful.

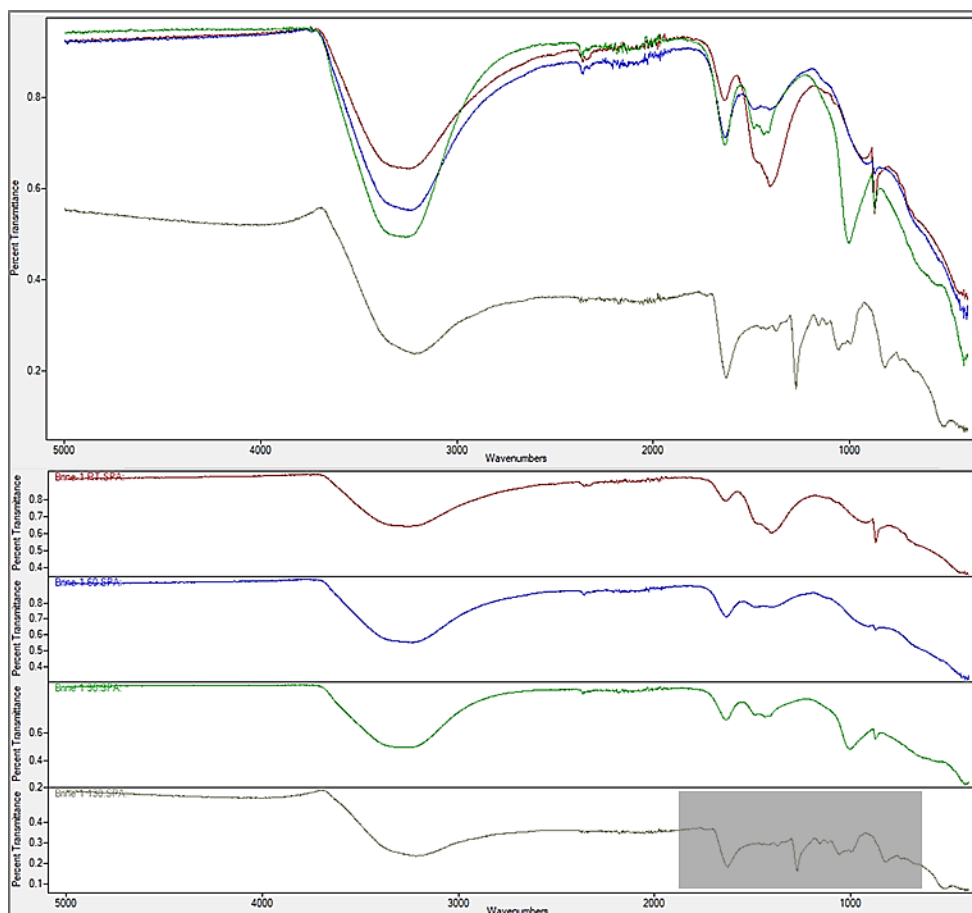


Figure 3.3. ATR-IR spectra of the precipitates collected from control corrosion experiments in Brine 1. Color codes: *red* RT, *blue* 60°C, *green* 90°C and *grey* 130°C.

Figure 3.4 presents the powder XRD patterns of the control experiments. The patterns of the corrosion products collected from the experiments at RT, 60 °C and 90 °C showed the characteristic peaks of calcite at 2θ values 29.42°, 36°, 39.44°, 43.19°, 47.54° and 48.54° [6]. The respective pattern of the precipitate which was collected from the experiment at 130 °C indicates the formation of magnetite, as the characteristic diffraction peak at 35.5° is observed [7]. The crystal data of the aforementioned structures are shown for comparison in the Annex. The broad peak at 26° which is observed in the respective XRD pattern of the control experiment at 130 °C is attributed to the filter membrane [8].

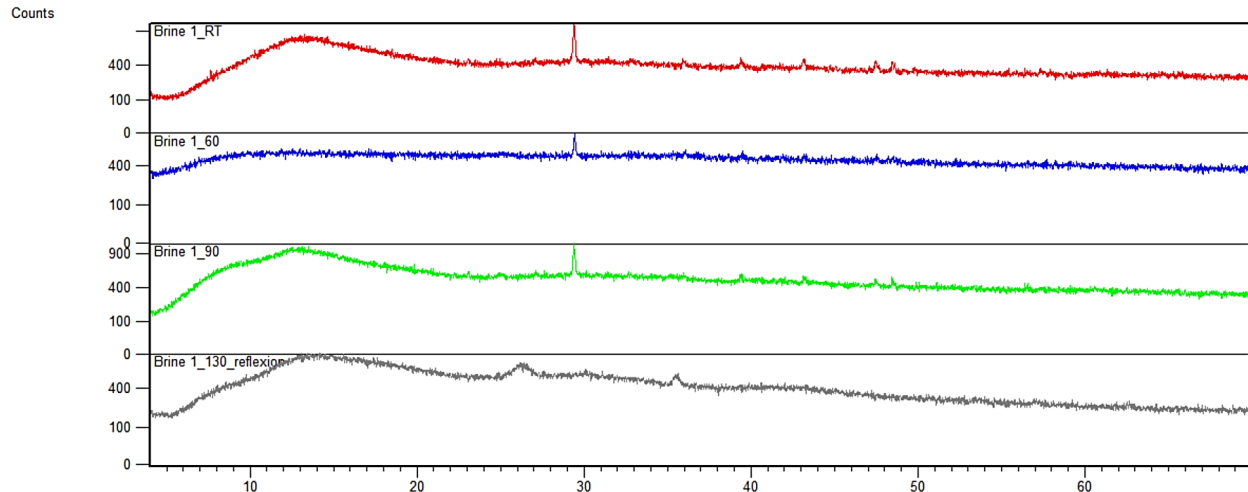


Figure 3.4. Powder XRD patterns of the precipitates collected from control corrosion experiments in Brine 1. Color codes: *red* RT, *blue* 60°C, *green* 90°C and *grey* 130°C.

Furthermore, the precipitates were studied by Scanning Electron Microscopy (SEM) in order to examine the morphology, the texture and the size of the particles. Figure 3.5 shows the SEM images. At first glance, the deposit morphology appears to be similar. Severe particle aggregation is observed, and no individual particles or crystals are evident. The primary particle size appears to be similar in the precipitates from all three temperatures and is around 0.5 μm .

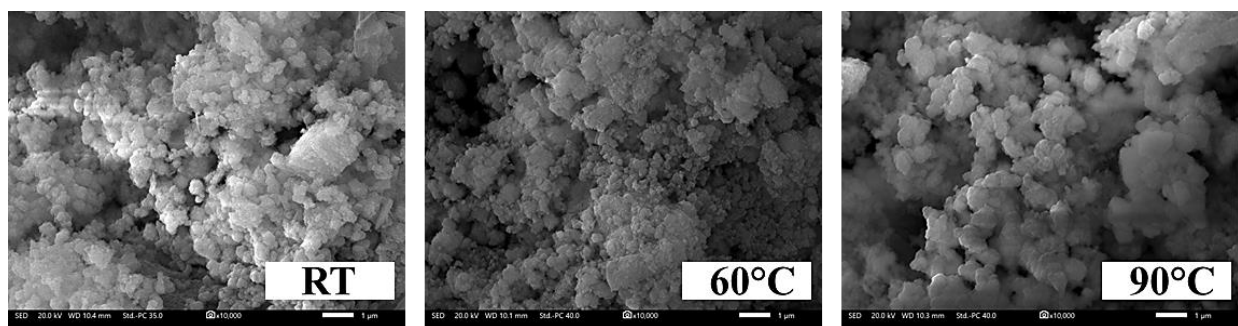


Figure 3.5. SEM images of the precipitates that collected from the experiments at *left* RT, *center* 60°C and *right* 90°C.

3.2 Results

3.2.1. Phosphonate inhibitors

This section focuses on the results of the experiments performed in the presence of phosphonate-based inhibitors in Brine 1 at four temperatures (RT, 60 °C, 90 °C and 130 °C) for four inhibitor concentrations (0.01 mM, 0.1 mM, 1 mM and 2 mM). In addition, at 130 °C (High Pressure – High Temperature conditions, HP-HT), experiments in the presence of inhibitors at higher concentrations (3 mM, 4 mM and 5 mM) were additionally performed. The different working solutions were prepared by diluting the desired volumes of the corresponding inhibitor stock solutions in Brine 1, followed by the pH adjustment to 7, if needed. The total volume of each experiment was 120 mL for the corrosion studies at RT, 60 °C and 90 °C, and 4 mL for 130 °C experimental set-up.

Each specimen was weighed before and after the experiment, after being first dried and cleaned using abrasive paper. Corrosion rates were calculated according to Equation 1, given in Chapter 2.3. Furthermore, aliquots were taken from the working solution at the end of the experimental period, to determine the iron concentration for each corrosion experiment. One of the goals here was to evaluate whether the iron determination method could be used for corrosion evaluation and quantification. Inhibition efficiencies (in %) based on both methods were calculated according to Equation 2 and Equation 3, as given in Chapter 2.3.

EDTMP-C2

Corrosion rate and iron concentration values obtained from the experiments performed under these conditions in the presence of C2, as well as the calculated inhibition efficiency (in %), are presented in Table 3.3.

Table 3.3. Corrosion rates, iron concentrations and inhibition efficiencies (%), based on both methods in the presence of C2 in Brine 1.								
T (°C)	RT		60		90		130	
c (mM)	CR (mm/y)	Fe (ppm)	CR (mm/y)	Fe (ppm)	CR (mm/y)	Fe (ppm)	CR (mm/y)	Fe (ppm)

<i>Control</i>	<i>0.062</i>	<i>95</i>	<i>0.110</i>	<i>168</i>	<i>0.087</i>	<i>133</i>	<i>0.148</i>	<i>448</i>
0.01	0.056 <i>10 %</i>	92 <i>3 %</i>	0.124 <i>- 13 %</i>	186 <i>- 11 %</i>	0.011 <i>88 %</i>	109 <i>18 %</i>	0.099 <i>33 %</i>	209 <i>53 %</i>
0.10	0.042 <i>32 %</i>	64 <i>33 %</i>	0.091 <i>18 %</i>	160 <i>5 %</i>	0.086 <i>1 %</i>	165 <i>- 24 %</i>	0.093 <i>37 %</i>	287 <i>36 %</i>
1.00	0.050 <i>19 %</i>	91 <i>4 %</i>	0.076 <i>31 %</i>	129 <i>23 %</i>	0.041 <i>53 %</i>	45 <i>66 %</i>	0.066 <i>56 %</i>	166 <i>63 %</i>
2.00	0.068 <i>- 10 %</i>	117 <i>- 23 %</i>	0.107 <i>3 %</i>	198 <i>- 18 %</i>	0.116 <i>- 34 %</i>	167 <i>- 26 %</i>	0.099 <i>33 %</i>	270 <i>40 %</i>
3.00	-	-	-	-	-	-	0.131 <i>11 %</i>	244 <i>46 %</i>
4.00	-	-	-	-	-	-	0.134 <i>9 %</i>	389 <i>13 %</i>
5.00	-	-	-	-	-	-	0.152 <i>- 3 %</i>	429 <i>4 %</i>

Figure 3.6 presents data from corrosion experiments in the presence of C2. At RT, the lowest corrosion rate is observed for 0.1 mM inhibitor concentration, therefore, in this case C2 demonstrates the highest inhibition efficiency, 32 %. The highest corrosion rate for C2 is obtained at 2 mM concentration, enhancing the corrosion. Comparing the gravimetric measurement with the iron determination, similar results are observed. Regarding the experiments performed at 60 °C, 1 mM of C2 shows the lowest corrosion rate (31 % inhibition). The iron concentration results follow similar trend as corrosion rate values. At 90 °C, it is observed that 0.01 mM of C2 is the most beneficial concentration under these conditions, presenting high anticorrosion efficiency, 88 %. It is worth noting that 0.01 mM of C2 shows a high iron amount, despite the low corrosion rate. Finally, under HP-HT conditions (130 °C), C2 appears to be most effective at the dosage of 1 mM, showing 56 % inhibition, verified also by the iron determination method.

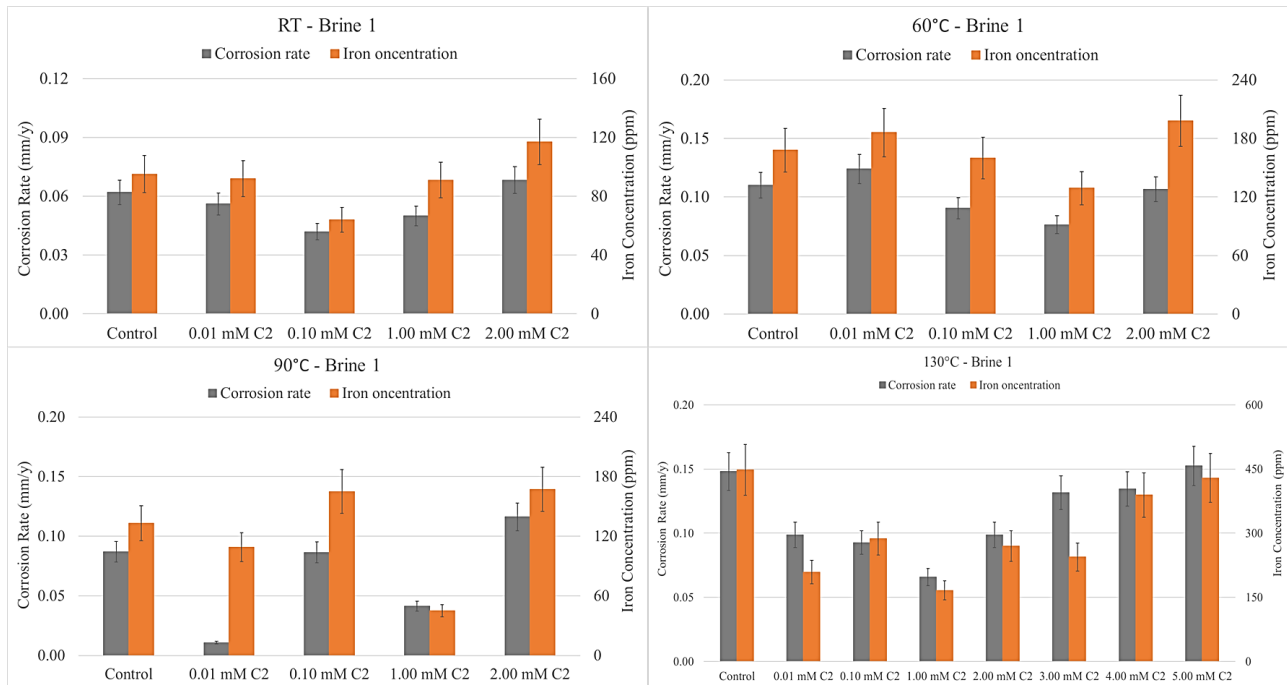

















Figure 3.6. Corrosion experiments in the presence of C2 in Brine 1 at a. RT (upper left), b. 60 °C (upper right), c. 90 °C (bottom left), and d. 130 °C (bottom right). Color codes: *grey* Corrosion rate and *orange* Iron concentration.

Table 3.4 shows visuals of the specimens from the corrosion experiments in the presence of C2 at RT, 60 °C and 90 °C. Even though at RT C2 performs better as corrosion inhibitor for the 0.1 mM concentration, it is noticeable that a concentration increase of C2 results in metal surfaces that appear less corroded. This means that C2 at high concentrations leads to iron dissolution under these conditions of high dosage. The same is true for the experiments at 60 °C, regarding the specimen from the experiments in the presence of 2 mM C2. At 90 °C, C2 presents the highest efficiency for 0.01 mM, however the specimen from the corresponding experiment shows much higher iron concentrations than the specimens from the corrosion experiments at the other temperatures. The specimens from the experiments under HP-HT conditions are shown in the Annex.

Table 3.4. Visual representation of the specimens from the experiments of C2 in Brine 1.

	RT	60 °C	90 °C
Control			
0.01 mM			
0.10 mM			
1.00 mM			
2.00 mM			

TMTMP-C4

Corrosion rate and iron concentration values obtained from the experiments performed under these conditions in the presence of C4, as well as the calculated inhibition efficiency (in %), are presented in Table 3.5.

Table 3.5. Corrosion rates, iron concentrations and inhibition efficiencies (%), based on both methods in the presence of C4 in Brine 1.

T (°C)	RT		60		90		130	
c (mM)	CR (mm/y)	Fe (ppm)	CR (mm/y)	Fe (ppm)	Fe (mm/y)	Fe (ppm)	CR (mm/y)	Fe (ppm)
<i>Control</i>	<i>0.062</i>	<i>95</i>	<i>0.110</i>	<i>168</i>	<i>0.087</i>	<i>133</i>	<i>0.148</i>	<i>448</i>
0.01	0.070 - 13 %	86 9 %	0.114 - 4 %	114 32 %	0.026 71 %	153 - 15 %	0.066 56 %	232 48 %
0.10	0.043 31 %	74 22 %	0.071 36 %	71 58 %	0.071 18 %	101 24 %	0.054 64 %	412 8 %
1.00	0.043	79	0.069	113	0.047	64	0.105	374

	<i>31 %</i>	<i>17 %</i>	<i>37 %</i>	<i>33 %</i>	<i>46 %</i>	<i>52 %</i>	<i>29 %</i>	<i>17 %</i>
2.00	0.044	90	0.121	125	0.038	72	0.173	384
	<i>29 %</i>	<i>5 %</i>	<i>- 10 %</i>	<i>26 %</i>	<i>56 %</i>	<i>46 %</i>	<i>- 17 %</i>	<i>14 %</i>
3.00	-	-	-	-	-	-	0.167	442
							<i>- 13 %</i>	<i>1 %</i>
4.00	-	-	-	-	-	-	0.173	584
							<i>- 17 %</i>	<i>- 30 %</i>
5.00	-	-	-	-	-	-	0.182	629
							<i>- 23 %</i>	<i>- 40 %</i>

Figure 3.7 presents the results of the corrosion experiments in the presence of C4. At room temperature, C4 presents similar good performance for the concentrations 0.1 mM, 1 mM and 2 mM (29-31 % inhibition), verified also by the lowest iron concentration. At 60 °C, the most effective concentrations are 0.1 mM and 1 mM of C4, presenting 36 % and 37 % inhibition, respectively. Iron determination results follow a similar pattern as the corrosion rates, except in the case of 1 mM in which C2 presents high iron levels. In the case of 90 °C, the highest inhibition is noticed at the concentration of 0.01 mM, 71 %, even though the iron determination method showed the highest iron concentration for this inhibitor dosage compared to the rest. Finally, concerning the experiments at 130 °C, the most beneficial inhibitor concentration is 0.1 mM, followed by 0.01 mM, presenting 64 % and 56 % inhibition, respectively.

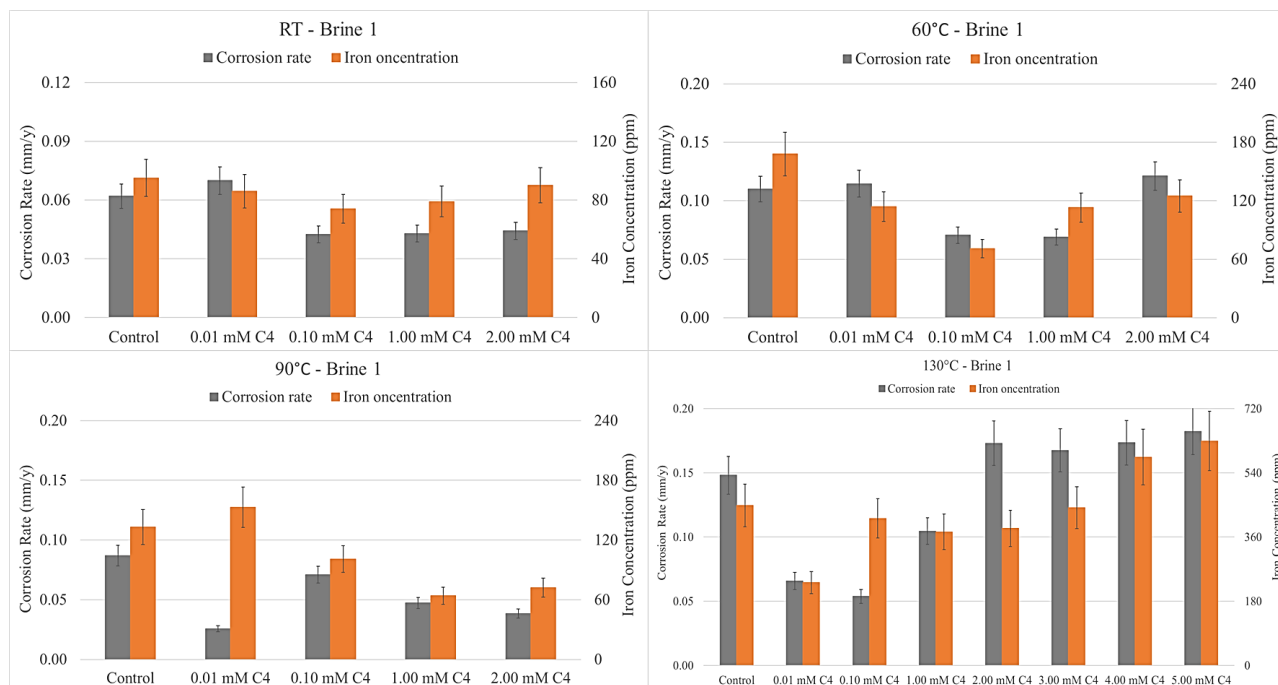
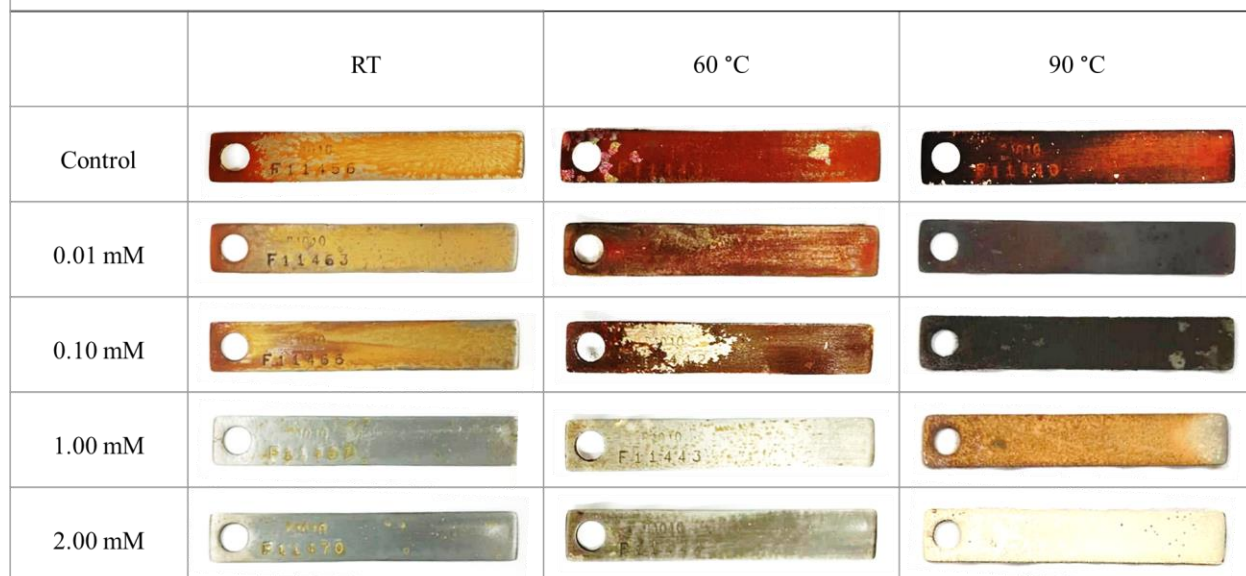


Figure 3.7. Corrosion experiments in the presence of C4 in Brine 1 at a. Room temperature (upper left), b. 60 °C (upper right), c. 90 °C (bottom left), and d. 130 °C (bottom right). Color codes: *grey* Corrosion rate and *orange* Iron concentration.

Table 3.6 shows the specimens from the corrosion experiments in the presence of C4 at RT, 60 °C and 90 °C. At RT, increased inhibitor concentrations favor the anticorrosion efficiency of C4, thus (visually) less corroded surfaces of the corresponding specimens are observed, as expected. Importantly, in the case of 60 °C, and comparing the concentrations 0.1 mM and 1 mM, a substantial difference in the appearance of the specimens is noted, despite the fact that these inhibitor dosages show similar results (CRs and Fe). Finally, focusing on the two highest inhibitor concentrations at 90 °C, white precipitates are observed on the metallic surfaces.

Table 3.6. Visual representation of the specimens from the experiments of C4 in Brine 1.**HDTMP-C6**

Corrosion rate and iron concentration values obtained from the experiments performed under these conditions in the presence of C6, as well as the calculated inhibition efficiency (in %), are presented in Table 3.7.

Table 3.7. Corrosion rates, iron concentrations and inhibition efficiencies (%), based on both methods in the presence of C6 in Brine 1.

T (°C)	RT		60		90		130	
	CR (mm/y)	Fe (ppm)	CR (mm/y)	Fe (ppm)	CR (mm/y)	Fe (ppm)	CR (mm/y)	Fe (ppm)
<i>Control</i>	<i>0.062</i>	<i>95</i>	<i>0.110</i>	<i>168</i>	<i>0.087</i>	<i>133</i>	<i>0.148</i>	<i>448</i>
0.01	0.049 20 %	78 18 %	0.112 - 2 %	94 44 %	0.054 38 %	35 74 %	0.072 52 %	260 42 %
0.10	0.044 29 %	63 34 %	0.140 - 28 %	138 18 %	0.073 16 %	32 76 %	0.108 27 %	339 24 %

1.00	0.037 40 %	68 28 %	0.064 42 %	118 30 %	0.053 39 %	92 31 %	0.066 56 %	293 35 %
2.00	0.039 37 %	88 7 %	0.083 24 %	154 8 %	0.069 21 %	165 - 24 %	0.060 60 %	459 - 2 %
3.00	-	-	-	-	-	-	0.111 25 %	552 - 23 %
4.00	-	-	-	-	-	-	0.114 23 %	481 - 7 %
5.00	-	-	-	-	-	-	0.102 31 %	409 9 %

Figure 3.8 presents results from corrosion experiments carried out in the presence of C6. At RT, C6 shows lower corrosion rate values for 1 mM and 2 mM concentration (efficiencies of 40 % and 37 % respectively), while iron concentration values follow the same pattern as corrosion rates, except in the case of 2 mM, in which higher iron amount than expected is noted. For the temperatures 60 °C and 90 °C, the most beneficial concentration of C6 is 1 mM at both temperatures (42 % and 39 % inhibition, respectively). At 130 °C, the lowest corrosion rate is observed for 2 mM C6, followed by 1 mM and 0.01 mM (efficiencies of 60 %, 56 % and 52 % respectively).

Table 3.8 shows the specimens from the corrosion experiments in the presence of C6 at RT, 60°C and 90°C. At RT and at 60°C, increased inhibitor concentrations favor the anticorrosion efficiency of C4, thus less corroded surfaces of the corresponding specimens are observed as expected. In the case of 90°C, a big difference between the appearance of the specimens from the experiments in the presence of 0.01 mM, 1 mM and 2 mM is noticed, despite the fact that these inhibitor dosages show similar results in terms of anticorrosion efficiency.

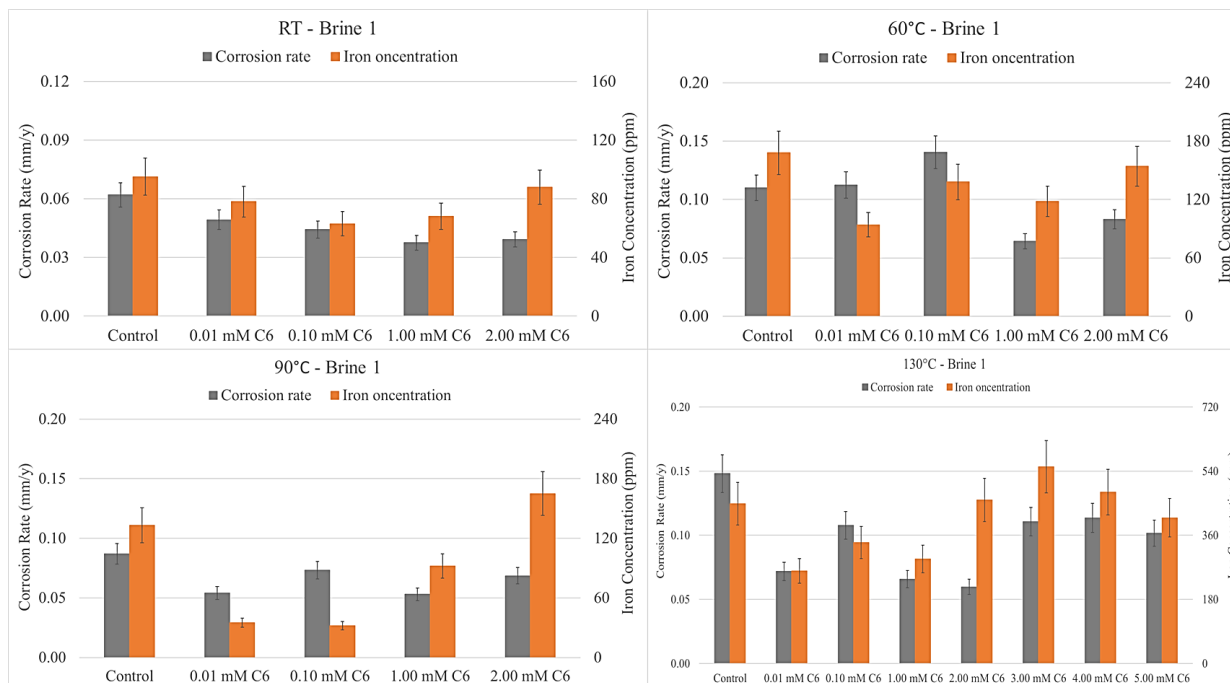


Figure 3.8. Corrosion experiments in the presence of C6 in Brine 1 at a. Room temperature (upper left), b. 60 °C (upper right), c. 90 °C (bottom left), and d. 130 °C (bottom right). Color codes: *grey* Corrosion rate and *orange* Iron concentration.

Table 3.8. Visual representation of the specimens from the experiments of C6 in Brine 1.

	RT	60 °C	90 °C
Control			
0.01 mM			
0.10 mM			
1.00 mM			
2.00 mM			

ODTMP-C8

Corrosion rate and iron concentration values obtained from the experiments performed under these conditions in the presence of C8, as well as the calculated inhibition efficiency (in %), are presented in Table 3.9.

Table 3.9. Corrosion rates, iron concentrations and inhibition efficiencies (%), based on both methods in the presence of C8 in Brine 1.								
T (°C)	RT		60		90		130	
c (mM)	CR (mm/y)	Fe (ppm)	CR (mm/y)	Fe (ppm)	CR (mm/y)	Fe (ppm)	CR (mm/y)	Fe (ppm)
<i>Control</i>	<i>0.062</i>	<i>95</i>	<i>0.110</i>	<i>168</i>	<i>0.087</i>	<i>133</i>	<i>0.148</i>	<i>448</i>
0.01	0.058 7 %	93 2 %	0.145 - 32 %	75 55 %	0.076 12 %	103 23 %	0.057 62 %	172 62 %
0.10	0.045 28 %	55 42 %	0.085 23 %	59 65 %	0.054 38 %	51 62 %	0.099 33 %	175 61 %
1.00	0.040 36 %	65 32 %	0.043 61 %	28 83 %	0.040 55 %	17 87 %	0.087 41 %	447 0 %
2.00	0.047 25 %	80 16 %	0.055 50 %	63 63 %	0.041 53 %	15 89 %	0.111 25 %	320 29 %
3.00	-	-	-	-	-	-	0.075 50 %	361 19 %
4.00	-	-	-	-	-	-	0.081 45 %	435 3 %
5.00	-	-	-	-	-	-	0.093 37 %	472 - 5 %

Figure 3.9 presents results from corrosion experiments carried out in the presence of C8. At room temperature, the lowest corrosion rate is observed for 1 mM C8 concentration, thus C8 presents the highest inhibition efficiency percentage, 36 %, although at this concentration the iron

determination method shows a higher iron level compared to that expected, given the low corrosion rate. At 60 °C, the 1 mM concentration gives the lowest corrosion rate (61 % inhibition), verified also by the low iron concentration. At 90 °C, it is observed that 1 mM of C8 is the most beneficial concentration (55 % inhibition), followed by 2 mM of C8 (53 % inhibition). Iron concentrations follow the same trend as corrosion rates. Finally, at 130 °C, 0.01 mM C8 appears to be the most effective concentration, with 62 % inhibition.

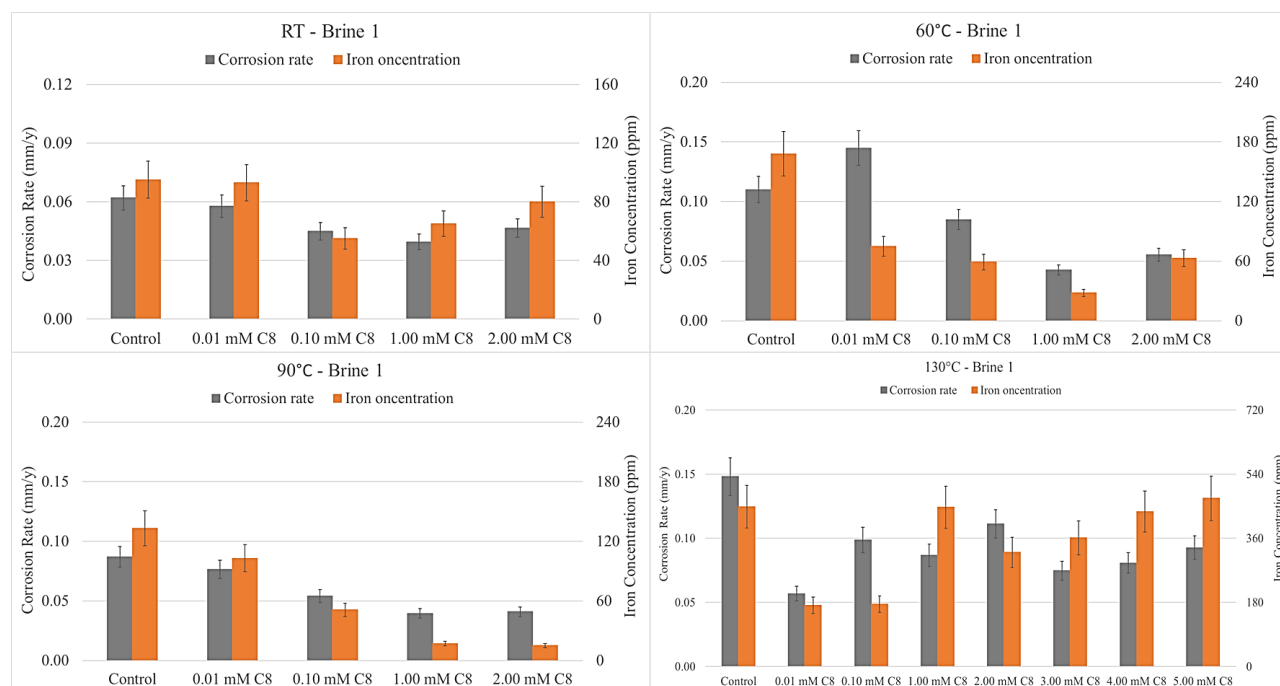

















Figure 3.9. Corrosion experiments in the presence of C8 in Brine 1 at a. Room temperature (upper left), b. 60°C (upper right), c. 90°C (bottom left) and d. 130°C (bottom right). Color codes: *grey* Corrosion rate and *orange* Iron concentration.

Table 3.10 shows visuals of the specimens from the corrosion experiments in the presence of C8 at RT, 60 °C and 90 °C. In all cases, increased inhibitor concentrations favor the anticorrosion efficiency of C8, thus less corroded surfaces of the corresponding specimens are observed as expected. In addition, at 60 °C and at 90 °C, white precipitates are observed on the metallic surfaces at the two highest inhibitor concentrations.

Table 3.10. Visual representation of the specimens from the experiments of C8 in Brine 1.

	RT	60 °C	90 °C
Control			
0.01 mM			
0.10 mM			
1.00 mM			
2.00 mM			

DDTMP-C12

Corrosion rate and iron concentration values obtained from the experiments performed under these conditions in the presence of C12, as well as the calculated inhibition efficiency (in %), are presented in Table 3.11.

Table 3.11. Corrosion rates, iron concentrations and inhibition efficiencies (%), based on both methods in the presence of C12 in Brine 1.

T (°C)	RT		60		90		130	
	CR (mm/y)	Fe (ppm)	CR (mm/y)	Fe (ppm)	CR (mm/y)	Fe (ppm)	CR (mm/y)	Fe (ppm)
<i>Control</i>	<i>0.062</i>	<i>95</i>	<i>0.110</i>	<i>168</i>	<i>0.087</i>	<i>133</i>	<i>0.148</i>	<i>448</i>
0.01	0.051 18 %	81 15 %	0.120 - 9 %	189 - 13 %	0.070 19 %	49 63 %	0.126 15 %	201 55 %
0.10	0.041 34 %	55 42 %	0.111 - 1 %	122 27 %	0.084 3 %	104 22 %	0.087 41 %	149 67 %

1.00	0.040 36 %	63 34 %	0.045 59 %	15 91 %	0.044 49 %	28 79 %	0.069 54 %	210 53 %
2.00	0.038 38 %	73 23 %	0.043 61 %	12 93 %	0.046 47 %	22 83 %	0.048 68 %	111 75 %
3.00	-	-	-	-	-	-	0.045 70 %	82 82 %
4.00	-	-	-	-	-	-	0.042 72 %	62 86 %
5.00	-	-	-	-	-	-	0.042 72 %	42 91 %

Figure 3.10 presents results from corrosion experiments carried out in the presence of C12. In general, an increase in inhibitor dosage enhances the anticorrosion efficiency. In addition, the two different methods show results with very close agreement. At RT, the lowest corrosion rate values are noted for 1 mM and 2 mM concentration (36 % and 38 % inhibition, respectively). The concentrations of 1 mM and 2 mM of C12 at 60 °C exhibit the highest inhibition, 59 % and 61 %, respectively. At 90 °C, once again the two higher inhibitor dosages enhance the anticorrosion efficiency of C12 reaching 49 % and 47 %, respectively. Impressively, at 130 °C corrosion rates decrease gradually as C12 dosage increases, reaching 72 % inhibition for the 5 mM concentration. In most cases, both corrosion quantification methods are in good agreement, with the sole exception of 0.01 mM C12 at 90 °C, where lower iron concentration is observed, compared to the respective results of the corrosion rates.

Table 3.12 shows visuals of the specimens from the corrosion experiments in the presence of C12 at RT, 60 °C and 90 °C. In all cases, increased inhibitor concentrations enhance the anticorrosion efficiency of C12, thus less corroded surfaces of the corresponding specimens are observed, as expected. In addition, at 60 °C and at 90 °C, white precipitates are observed on the metallic surfaces at the two highest inhibitor concentrations.

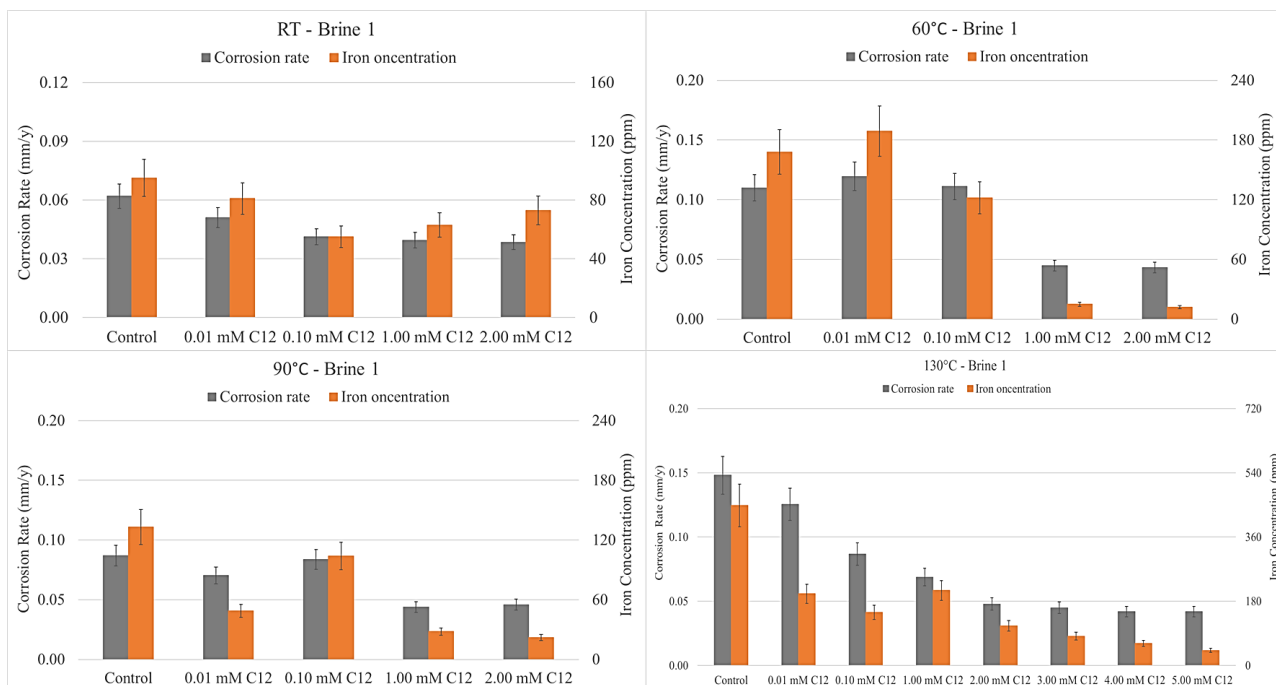


Figure 3.10. Corrosion experiments in the presence of C12 in Brine 1 at a. Room temperature (upper left), b. 60 °C (upper right), c. 90 °C (bottom left), and d. 130 °C (bottom right). Color codes: *grey* Corrosion rate and *orange* Iron concentration.

Table 3.12. Visual representation of the specimens from the experiments of C12 in Brine 1.

	RT	60 °C	90 °C
Control			
0.01 mM			
0.10 mM			
1.00 mM			
2.00 mM			

Comparing the inhibition efficiencies (%) at RT based on the different methods, the members of the tetraphosphonate family show the expected iron concentration compared to the respective

values of corrosion rates. Some exceptions concerning 2 mM of C4 and 2 mM of C6 are observed. Both inhibitors showed higher iron amounts than expected, under these conditions. At 60 °C, in most cases, lower iron concentrations are observed when the concentration of each inhibitor is low, except C12 in the case of which the difference between the two methods is noticed at high dosages. Concerning the experiments at 90 °C, no trend was observed regarding the difference between the two methods. Higher iron concentrations are observed at 0.01 mM of C2, 0.01 mM of C4 and 2 mM C6, while lower iron concentrations are noted at 0.01 mM and 0.1 mM of C6, 1 mM and 2 mM of C8 and 0.01 mM, 1 mM and 2 mM of C12. On the contrary, in most corrosion experiments performed at 130 °C, at high inhibitor concentrations a trend of higher iron concentrations is observed, except for the experiments in the presence of C12, where lower iron concentrations are observed.

Effect of concentration

As mentioned in the Introduction, the behavior of the inhibitors was studied at four different concentrations for the experiments performed at room temperature, at 60 °C and at 90 °C, and for seven different concentrations for the experiments under HP-HT conditions (130 °C). This section focuses on the effect of inhibitor concentration, step-by-step from lowest to highest. Figure 3.11 shows the fluctuation of corrosion rates, as the concentration of each inhibitor gradually increases.

At RT, and 60 °C, increasing the concentration of C2 from 0.01 mM to 0.1 mM lowers the corrosion rate values, while at 90 °C a higher corrosion rate is observed. At 130 °C, corrosion rates remain almost constant, despite the increase in inhibitor dosage. Further dosage increase at RT results in higher corrosion rates. At 60 °C and at 90 °C, dosage increase to 1 mM enhances efficiency, but further increase to 2 mM causes a drop in C2 efficiency. At 130 °C, dosage increase from 0.1 mM to 1 mM results in lower corrosion rates and, finally, further increase in C2 concentration shows gradually higher corrosion rates.

Regarding C4 at RT, increasing the concentration from 0.01 mM to 0.1 mM results in a lower corrosion rate and then the values remain almost constant, regardless of the concentration. At 60 °C, 0.1 mM C4 shows a lower corrosion rate than 0.01 mM. At 1 mM, C4 shows the same corrosion rate values as 0.1 mM inhibitor concentration and further increase results in higher corrosion rate.

At 90 °C, increasing inhibitor concentration, at first results in higher corrosion rate (0.1 mM), which then gradually decreases. At 130 °C, increasing inhibitor concentration, at first results in lower corrosion rates, which then gradually increase.

In the RT experiments with C6, increasing the concentration from 0.01 mM to 1 mM, results in lower corrosion rates, but further increase to 2 mM does not affect its efficiency. At 60 °C increasing the concentration from 0.01 mM 0.1 mM results in a higher corrosion rate. In the case of 1 mM, the corrosion rate reaches its lowest value and then, at 2 mM, increases again, but still lower than the corrosion rates of the two lower concentrations. At 90 °C, C6 follows an “S-shaped” trend, as corrosion rate is lower at 0.01 mM than at 0.1 mM, then decreases for 1 mM inhibitor concentration and then increases again. Finally, at 130 °C, 0.1 mM C6 shows the highest corrosion rate, while the respective values for the rest of the inhibitor dosages are approximately equal.

In the case of C8, increasing the concentration from 0.01 mM to 1 mM results in lowering the corrosion rate and then the values remain almost constant, regardless of the concentration for the experiments performed at RT, 60 °C and 90 °C. Finally, at 130 °C C8 shows an “S-shaped” trend, as the corrosion rate is lower at 0.01 mM than at 0.1 mM, then decreases for 1 mM inhibitor concentration and then increases again.

Regarding C12 at RT and at 60 °C, the increase in concentration from 0.01 mM to 1 mM causes the corrosion rate values to decrease and then remain almost constant. At 90 °C, at first, the corrosion rate increases when the concentration increases from 0.01 mM to 0.1 mM, and then a further increase in inhibitor dosage results in lower corrosion rates. At 130 °C, corrosion rates decrease gradually as C12 concentration increases, reaching 72 % inhibition.

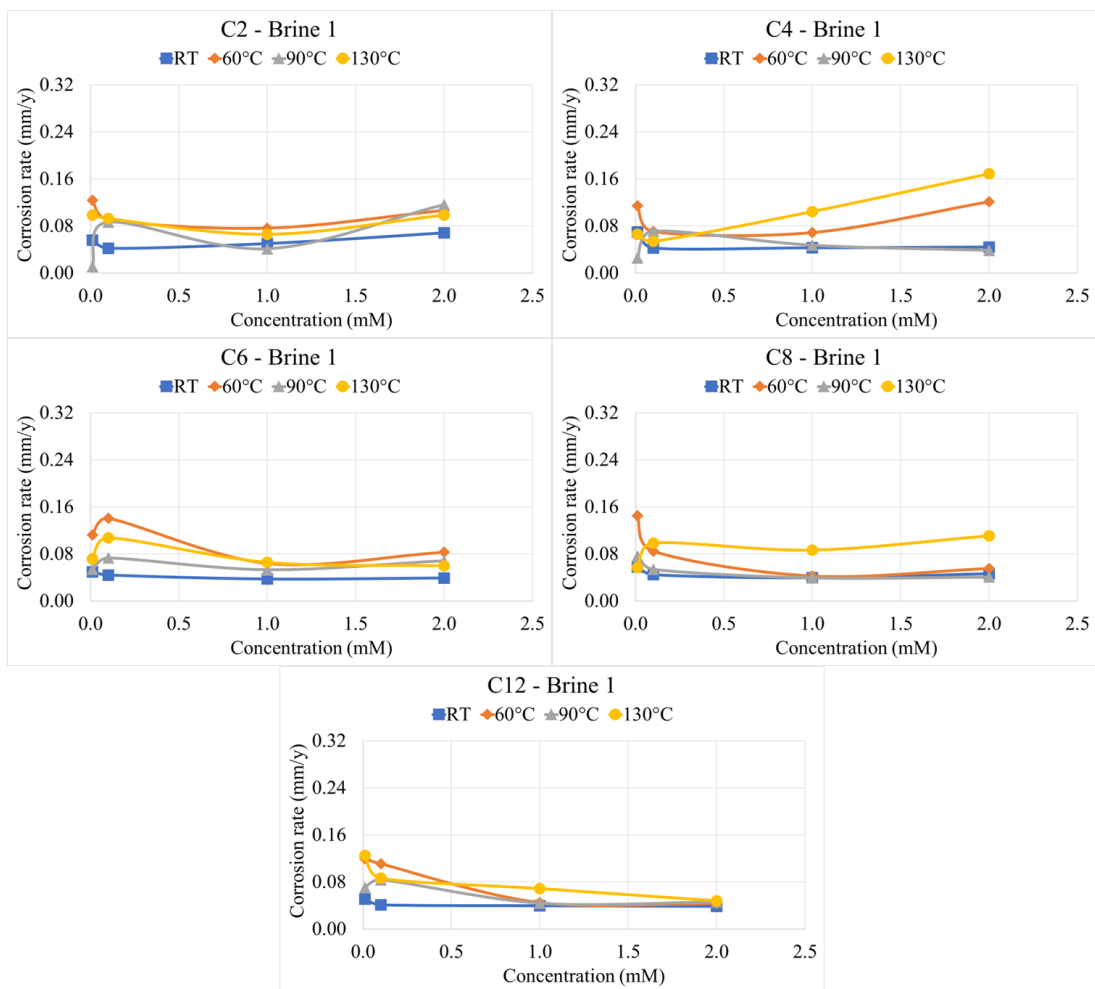


Figure 3.11. Correlation between corrosion rates and inhibitor concentration for the tetraphosphonate inhibitors in Brine 1. Color codes: *blue* RT, *orange* 60 °C, *grey* 90 °C and *yellow* 130 °C.

Further experiments were performed at 130 °C (High Pressure–High Temperature conditions, HP-HT), with higher inhibitor concentrations (3 mM, 4 mM and 5 mM). Figure 3.12 shows the results of these experiments as well as the lower concentrations for comparison.

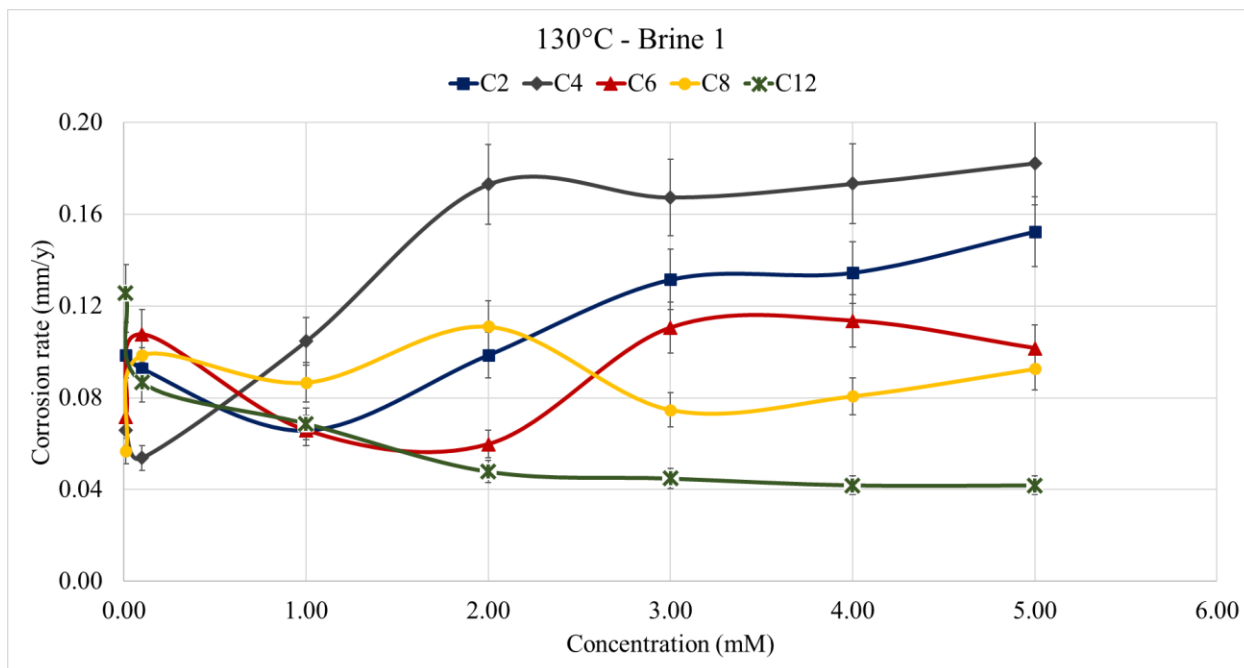


Figure 3.12. Correlation between corrosion rates and inhibitor concentration in Brine 1 at 130 °C. Color codes: *blue C2, grey C4, red C6, yellow C8 and green C12.*

The aforementioned results from the corrosion experiments for all inhibitors under these conditions were grouped by concentration at each temperature in an attempt to examine a possible pattern of their behavior.

Experiments performed at RT

- Concentration increase from 0.01 mM to 0.1 mM: an increase in the efficiency of all the corrosion inhibitors is observed.
- Concentration increase from 0.1 mM to 1 mM: for C4 and C12 no significant change in the efficiency is observed, while C6 and C8 show slightly better performance. On the contrary, C2 shows lower performance.
- Concentration increase from 1 mM to 2 mM: Small drop in the efficiency of C2 and C8. For C4, C6 and C12 the efficiency is kept almost constant.

Experiments performed at 60 °C

- Concentration increase from 0.01 mM to 0.1 mM: the increased concentration is beneficial for C2, C4 and C8. C6 presents lower inhibition, while the efficiency of C12 does not change.
- Concentration increase from 0.1 mM to 1 mM: efficiency is enhanced for all tetraphosphonates, except C4, where no significant change is observed.
- Concentration increase from 1 mM to 2 mM: efficiency is reduced for all inhibitors, except C12, the efficiency of which is almost constant.

Experiments performed at 90 °C

- Concentration increase from 0.01 mM to 0.1 mM: Drop in efficiency for all the inhibitors, except C12 the efficiency of which is enhanced.
- Concentration increase from 0.1 mM to 1 mM: higher inhibition for all the inhibitors is noted.
- Concentration increase from 1 mM to 2 mM: for C4, C8 and C12 corrosion rates remain almost constant, while in the case of C2 and C6 the efficiency drops.

Experiments performed at 130 °C

- Concentration increase from 0.01 mM to 0.1 mM: an increase in the anticorrosion performance of C12 is observed, while a decrease is observed in the case of C6 and C8. The performances of C2 and C4 are almost constant.
- Concentration increase from 0.1 mM to 1 mM: higher inhibition for all the inhibitors, except C4, where a drop in anticorrosion efficiency is noted.
- Concentration increase from 1 mM to 2 mM: The efficiency of C2, C4 and C8 drops, while the efficiency of C6 is almost constant. C12 demonstrates lower corrosion rates.
- Concentration increase to 3 mM – 4 mM – 5 mM: overall, no enhanced efficiencies are observed.

A very important observation is that inhibitors exhibit lower corrosion rates for 1 mM inhibitor concentration in about half of the cases. In addition, it is observed that “high” concentrations (1 mM, 2 mM and 5 mM) are beneficial for the anticorrosion efficiency of C6, C8 and C12.

Effect of temperature

In the following section, the effect of temperature on the efficiency of each tetraphosphonate is examined in detail. Due to different corrosion rate values of the control experiments at different temperatures, the comparisons are made based on % inhibition, thus Figure 3.13 presents correlations between % inhibition efficiencies and temperature, at each inhibitor concentration.

Regarding the experiments in the presence of 0.01 mM of each inhibitor, the members of the tetraphosphonate family appear to be most effective at the two highest temperatures, with the sole exception of the “largest” inhibitor C12, in the presence of which the highest inhibition is observed at 90 °C, followed by RT. In addition, the highest inhibition is observed at 90 °C for C2 and C4, followed by the experiments at 130 °C. Conversely, for C6 and C8, the highest inhibition percentages are observed at 130 °C, followed by 90 °C. When the temperature of the corrosion experiments is 60°C, all inhibitors showed corrosive behaviors, presenting corrosion rates higher than the respective control experiments. In addition, C4 is corrosive at RT as well, under these conditions.

At 0.1 mM inhibitor concentration, tetraphosphonates are most effective at high temperatures. Specifically, C2, C4 and C12 showed the highest inhibition at 130 °C, while C6 and C8 at 90 °C. C2, C6 and C12 at RT present the second highest efficiency. On the contrary, 130 °C is the second most beneficial temperature in the case of C8. The lowest inhibition percentages are observed at 90 °C for the “smaller” size inhibitors C2 and C4, and at 60 °C for the “larger” size inhibitors C6, C8 and C12.

At 1 mM inhibitor concentration, the highest inhibition percentages are observed at 130 °C for C2 and C6, followed by 90 °C and 60 °C, respectively. C4 presents its higher inhibition efficiency at 90 °C, followed by 60 °C. C8 and C12 are two examples which show the best inhibitory activity at 60 °C. The lowest inhibition is observed at RT for C2, C8 and C12, at 130 °C for C4 and at 90 °C for C6.

At 2 mM inhibitor concentration, the highest inhibition is observed at 130 °C for C2, C6 and C12, and at 90 °C for C4 and C8. In the case of C2 and C4, corrosive behavior is noted for the rest of the experiments, except C4 at RT. In addition, the worst behavior of C8 and of C12 is observed at RT.

Overall, it was not possible to establish a universal trend regarding the effect of temperature on anticorrosion efficiency. In an attempt to draw conclusions by evaluating the results statistically, it is observed that the tetraphosphonate inhibitors perform better at 90 °C and at 130 °C, while the worst behavior is noted for the experiments performed at RT and at 60 °C, for most of the cases. However, the performance of each inhibitor is affected in a different fashion by temperature and, importantly, the inhibitory activity of the phosphonates highly depends on their concentration.

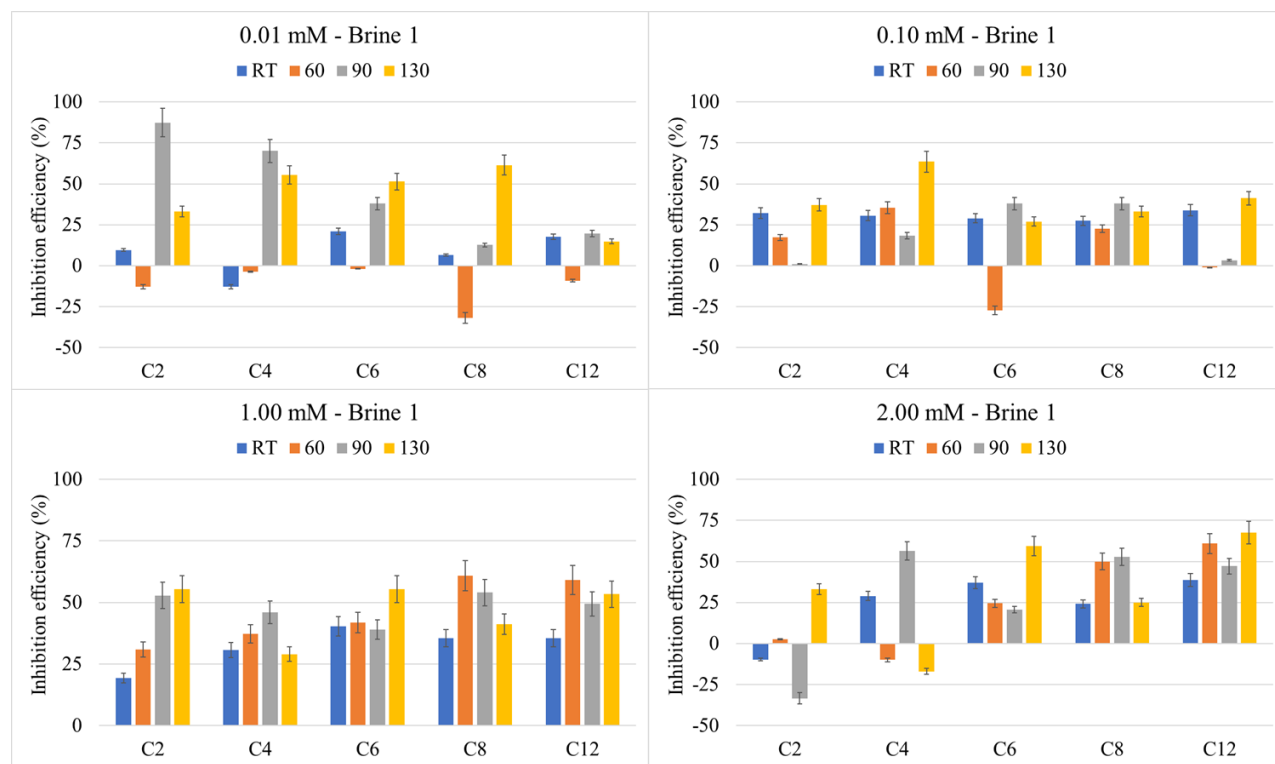


Figure 3.13. Correlation between inhibition efficiency (%) and temperature for tetraphosphonates in Brine 1 for concentrations a. 0.01 mM (upper left), b. 0.10 mM (upper right), c. 1 mM (bottom left), and d. 2 mM (bottom right). Color codes: *blue* RT, *orange* 60°C, *grey* 90°C and *yellow* 130°C.

Effect of inhibitor molecular size

A structural feature of this family of tetraphosphonate inhibitors is the systematically elongated carbon (polymethylene) chain connecting the two N atoms on each side of the molecule. In other words, as we visualize the structures of these inhibitors, moving from C2 up to C12, the length (or the size) of the molecule increases. In the following section, we attempt to correlate the length of the carbon chain between the amine groups with the efficiency of the corresponding inhibitor. Hence, the values of corrosion rates are presented in comparison with the number of carbon atoms contained in the structure of each phosphonate inhibitor. In addition, iron concentrations of the respective experiments are presented as well. Zero carbon atoms represent the respective control corrosion experiments.

Figure 3.14 refers to the experiments performed at RT. Regarding the lowest concentration of 0.01 mM, C6 seems to be the most effective inhibitor, followed by C12 and C2. Higher corrosion rates are noted in the case of C8 and C4. Iron concentration values follow the same pattern as corrosion rates, except C4 in the presence of which lower iron levels than expected are observed. For 0.1 mM inhibitor dosage, all tetraphosphonates show similar inhibitory activity. In addition, C4 presents higher iron concentration and C8 lower iron concentration compared to the respective corrosion rate values. For 1 mM inhibitor dosage, a gradual decrease in the corrosion rates is observed while the number of carbon atoms increases from 2 to 6. For C8 a slightly higher corrosion rate value is observed, which remains almost constant when the carbon atom number is 12. Iron concentrations decrease as the size of the carbon chain increases. For 2 mM inhibitor dosage, the “largest” size molecule C12 shows the best anticorrosion performance, verified by both gravimetric and iron determination data. A trend of lower corrosion rates and iron concentrations as the size of the inhibitor increases is noticed, except C8, the corrosion rate of which is the second highest, after C2.

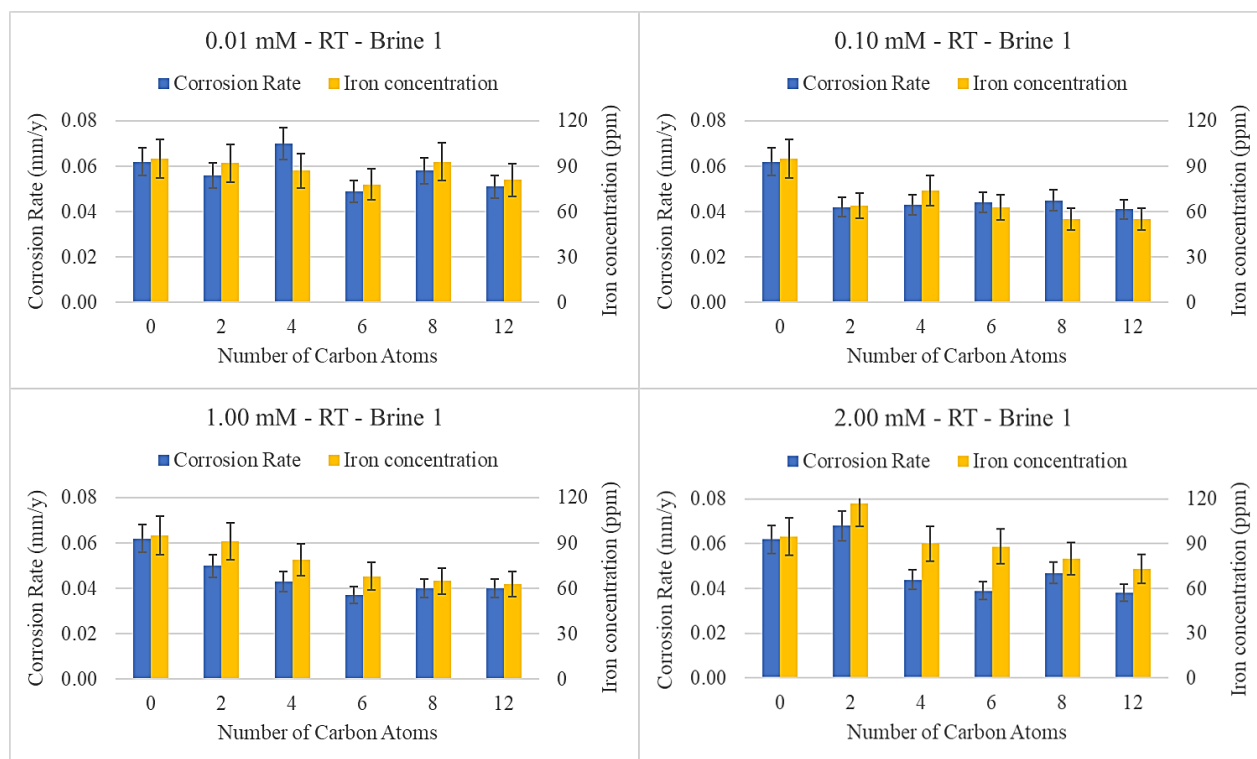


Figure 3.14. Correlation between the number of carbon atoms on the polymethylene linker of each phosphonate inhibitor and the results obtained from the corrosion experiments performed at RT in Brine 1.

Figure 3.15 refers to the experiments performed at 60 °C. Regarding the lowest concentration of 0.01 mM, C8 is the least effective inhibitor, while the rest of the tetraphosphonates exhibit similar behavior. Iron levels decrease as the number of carbon atoms increases from 2 to 8 and then increase, reaching the highest values under these conditions, in the case of the “larger” size inhibitor, C12. For the 0.1 mM inhibitor dosage, C4 is the most effective inhibitor, followed by C2. For C6 the highest corrosion rate is noted, followed by C12 and then C8. In addition, C2 presents higher and C8 lower iron levels compared with the respective corrosion rates. For the 1 mM inhibitor dosage, higher efficiency is observed by increasing the size of the inhibitor, verified by both methods, except the case of C6, for which the iron concentration is higher than that for C8. For 2 mM inhibitor dosage, the best performance is noted for the “larger” size inhibitor C12. Decreasing the length of the carbon chain causes a drop in efficiency, except for C4 for which the

corrosion rate is higher than that for C2. Furthermore, C2 and C6 showed higher iron concentrations than expected.

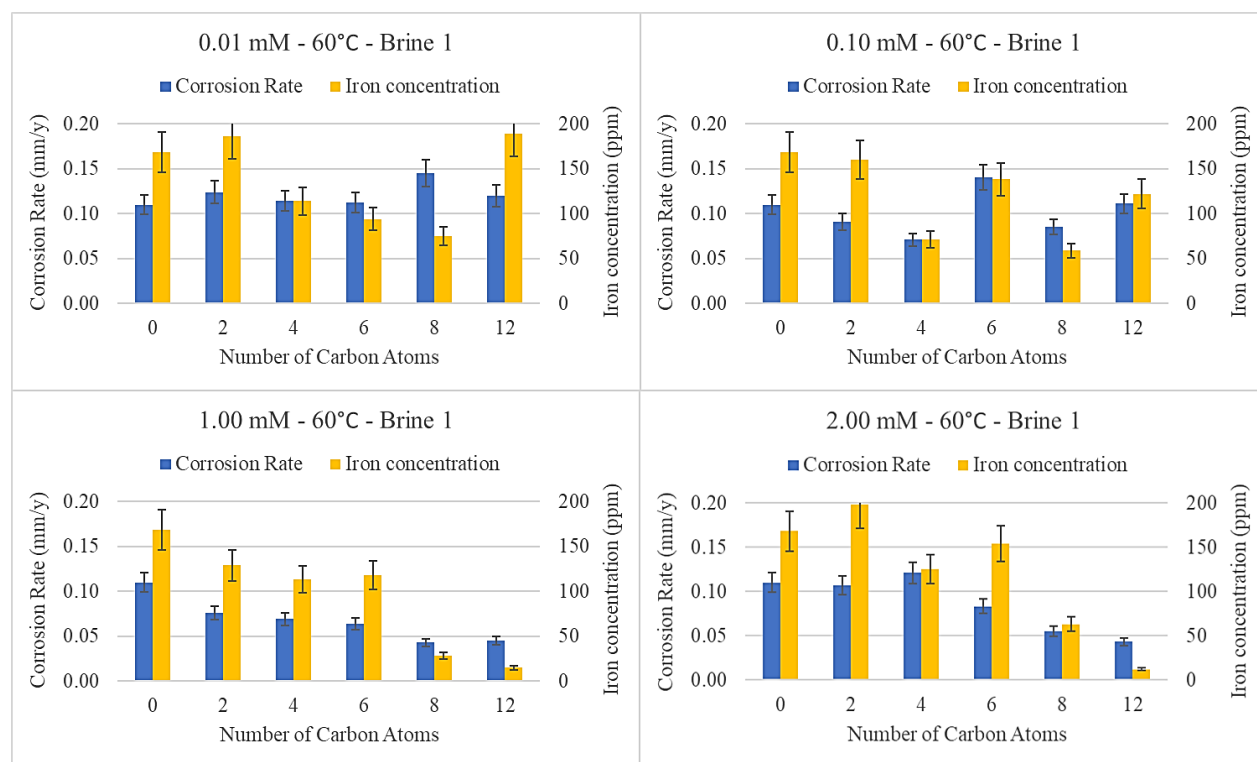


Figure 3.15. Correlation between the number of carbon atoms on the polymethylene linker of each phosphonate inhibitor and the results obtained from the corrosion experiments performed at 60 °C in Brine 1.

Figure 3.16 refers to the experiments performed at 90 °C. Regarding the lowest concentration of 0.01 mM, C8 is the least effective inhibitor, but concerning the rest of the tetraphosphonates, higher corrosion rates are observed as the number of carbon atoms increases. C2 and C4 present higher iron concentrations, while C12 presents lower iron concentrations than expected. For the 0.1 mM inhibitor dosage, a “U-shaped” pattern is observed regarding both methods. Specifically, corrosion rates decrease as the size of the inhibitor increases from 2 to 6, then the rates remain constant for 8 carbon atoms (C8) and they finally increase in the case of C12. For the 1 mM inhibitor dosage, a trend is observed that lower efficiencies occur as the size of the inhibitor increases from C2 to C6, verified by both methods. Then the efficiency increases for C8 and C12, in the case of which corrosion rates are approximately equal to the respective value of C2. The two

“larger” size inhibitors exhibit the lowest iron levels. For the 2 mM inhibitor dosage, C4, C8 and C12 present lower corrosion rates than C2 and C6. Specifically, C8 is the most effective inhibitor and C2 is the least effective inhibitor under these conditions. Based on the iron determination method, C6 shows high iron, while C8 and C12 show low iron in the working solutions of the corresponding experiments.

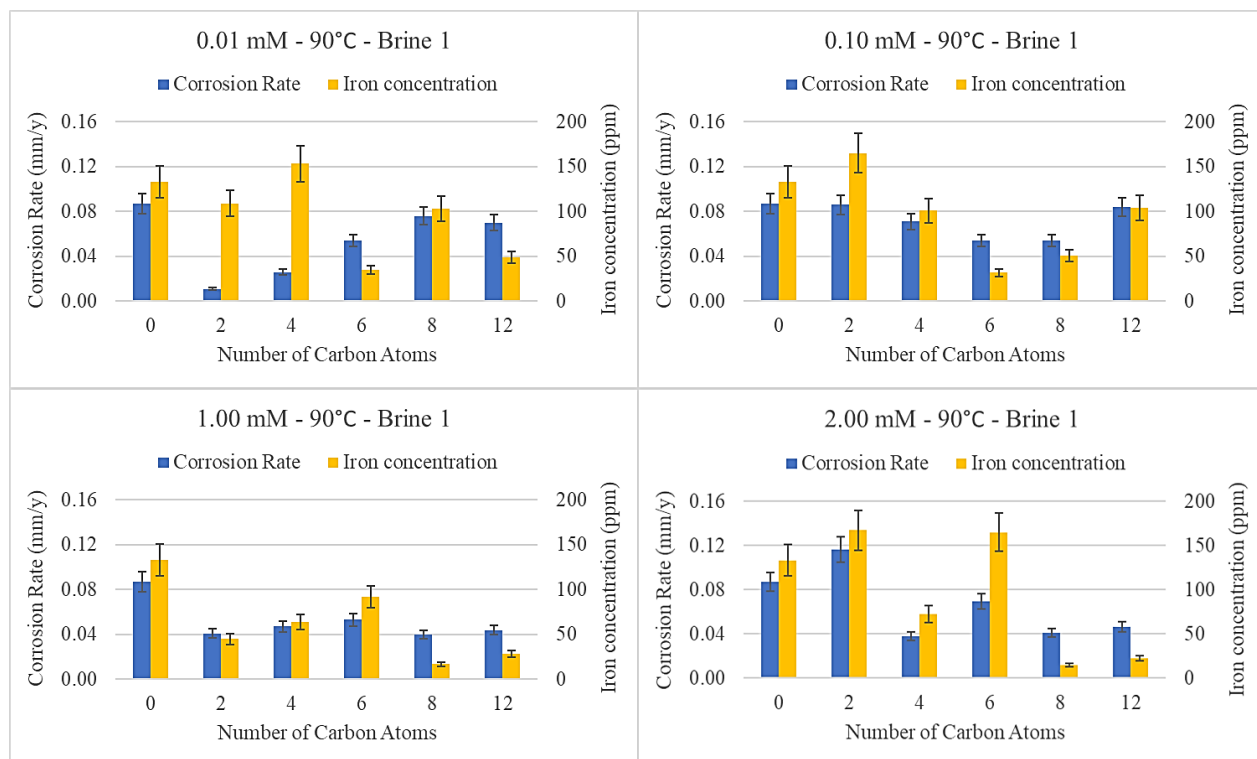


Figure 3.16. Correlation between the number of carbon atoms on the polymethylene linker of each phosphonate inhibitor and the results obtained from the corrosion experiments performed at 90 °C in Brine 1.

Figure 3.17 refers to the experiments performed at 130°C. Regarding the lowest concentration of 0.01 mM, C12 is the least effective inhibitor, followed by C2. On the contrary, C8 shows the lowest corrosion rate, followed by C4 and finally C6. For the 0.1 mM inhibitor dosage, C4 exhibits the lowest corrosion rate. Regarding the rest of the phosphonates, similar corrosion rates are noted, although there is a tendency of lower CR values as the number of carbon atoms increases from 6

to 12. For the 1 mM inhibitor dosage, C2, C6 and C12 show similar behavior, presenting lower corrosion rates compared to the rest two inhibitors. In addition, C4 shows the higher corrosion rate. For 2 mM inhibitor dosage, the “larger” size inhibitor C12 presents the lowest corrosion rate, followed by C6. In addition, C2 and C8 show essentially the same corrosion rates. Finally, in the presence of C4, the highest CR is observed. As far as iron levels are concerned, a high discrepancy between the results of the two methods is observed under these conditions.

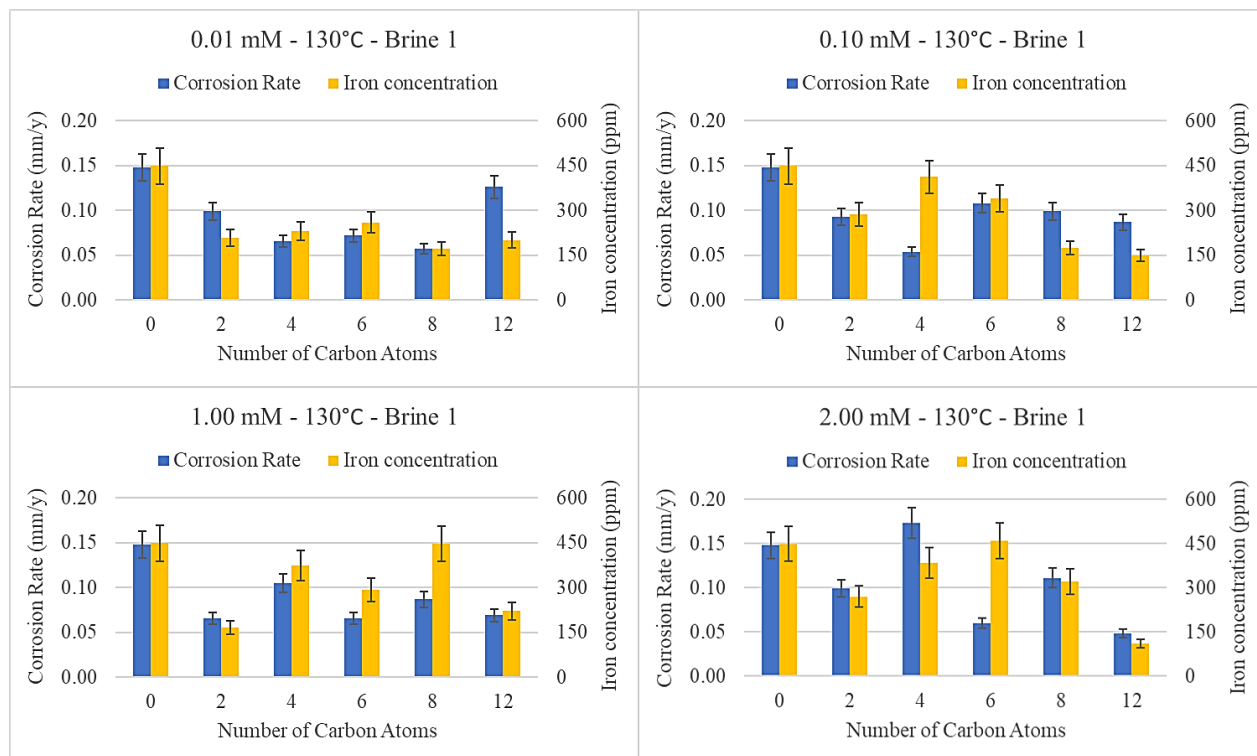


Figure 3.17. Correlation between the number of carbon atoms on the polymethylene linker of each phosphonate inhibitor and the results obtained from the corrosion experiments performed at 130°C in Brine 1.

3.2.2 Non-phosphonate inhibitors

This section presents the results of the experiments performed in the presence of non-phosphonate inhibitors in Brine 1 at three temperatures (RT, 60 °C and 90 °C) for two inhibitor concentrations (100 ppm and 250 ppm). The necessary inhibitor solutions were prepared by

diluting the desired volumes of the corresponding inhibitor stock solutions in DI water, followed by pH adjustment to 7, if needed. The total volume of each experiment was 120 mL. Corrosion rate values calculated from the mass loss and iron data under these conditions, as well as the calculated inhibition efficiency (%), categorized by inhibitor concentration, are presented in Table 3.13 and Table 3.14.

Table 3.13. Corrosion rates, iron concentrations and inhibition efficiency (%) based on both methods for 100 ppm of non-phosphonate inhibitors in Brine 1.						
T (°C)	RT		60		90	
	CR (mm/y)	Fe (ppm)	CR (mm/y)	Fe (ppm)	CR (mm/y)	Fe (ppm)
<i>Control</i>	0.062	95	0.110	168	0.087	133
SLD	0.042 32 %	41 57 %	0.104 5 %	199 - 18 %	0.067 23 %	31 77 %
ACAB	0.034 46 %	43 55 %	0.066 40 %	71 58 %	0.096 - 11 %	47 65 %
DLD	0.044 29 %	80 16 %	0.050 55 %	66 61 %	0.026 70 %	80 40 %
HAD	0.037 41 %	59 38 %	0.061 44 %	120 29 %	0.134 - 54 %	104 22 %

Table 3.14. Corrosion rates, iron concentrations and inhibition efficiency (%) based on both methods for 250 ppm of non-phosphonate inhibitors in Brine 1.						
T (°C)	RT		60		90	
	CR (mm/y)	Fe (ppm)	CR (mm/y)	Fe (ppm)	CR (mm/y)	Fe (ppm)
<i>Control</i>	0.062	95	0.110	168	0.087	133
SLD	0.033 47 %	46 52 %	0.023 79 %	48 71 %	0.043 51 %	20 85 %

ACAB	0.040 36 %	64 33 %	0.042 62 %	74 56 %	0.124 - 42 %	31 77 %
DLD	0.023 62 %	89 6 %	0.054 51 %	70 58 %	0.030 65 %	90 32 %
HAD	0.031 50 %	53 44 %	0.094 14 %	144 14 %	0.097 - 12 %	106 20 %

Figure 3.18 shows the results of the corrosion experiments in the presence of non-phosphonate inhibitors at RT. ACAB exhibits the lowest corrosion rate for 100 ppm dosage, followed by HAD, presenting 46 % and 41 % inhibition, respectively. In addition, SLD and DLD show similar corrosion rates, with 32 % and 29 % inhibition, respectively. The iron determination test verified these results, with the sole exception of SLD, in the case of which lower iron levels than expected were noted. For the 250 ppm inhibitor dosage, the best performance is observed for DLD, with 62 % inhibition. HAD and SLD present similar corrosion rates, with 50 % and 47 % inhibition, respectively. The lowest inhibition efficiency is presented by ACAB (36 % inhibition). The iron determination test verified these results, except in the case of DLD, where higher iron concentrations than expected were measured.

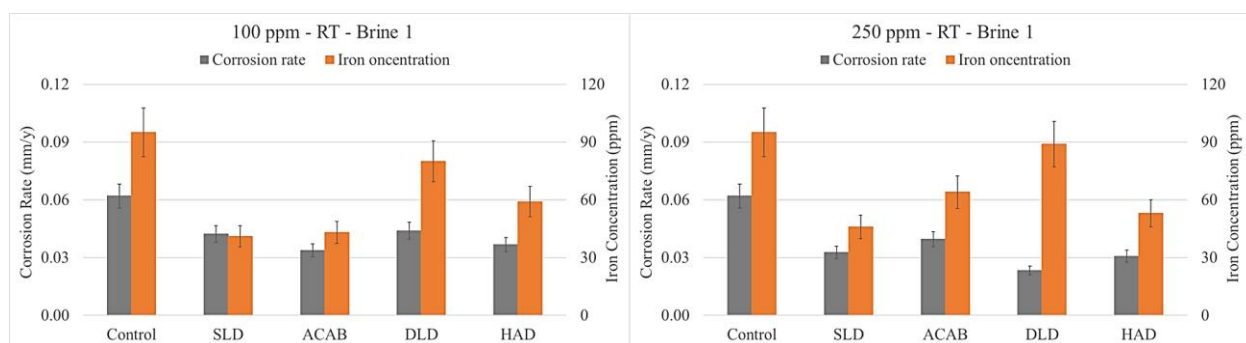


Figure 3.18. Corrosion experiments in the presence of non-phosphonate inhibitors in Brine 1 at RT. (left) 100 ppm and (right) 250 ppm. Color codes: *grey* Corrosion rate and *orange* Iron concentration.

Figure 3.19 presents the results of the corrosion experiments in the presence of non-phosphonate inhibitors at 60 °C. For the 100 ppm inhibitor dosage, DLD is the most effective inhibitor, with 55 % inhibition. HAD and ACAB present similar corrosion rates, with 44 % and 40 % inhibition, respectively. The lowest inhibition efficiency is demonstrated by SLD (5 % inhibition). The iron determination test verified these results, except in the case of SLD, in which lower iron levels than expected were measured. For the 250 ppm inhibitor concentration, the best performance was observed for SLD (79 % inhibition), followed by ACAB (62 % inhibition) and then DLD (51 % inhibition). The lowest inhibition efficiency was shown by HAD (14 % inhibition). The iron determination test verified these results, except in the case of DLD, where higher iron concentrations than expected, were observed.

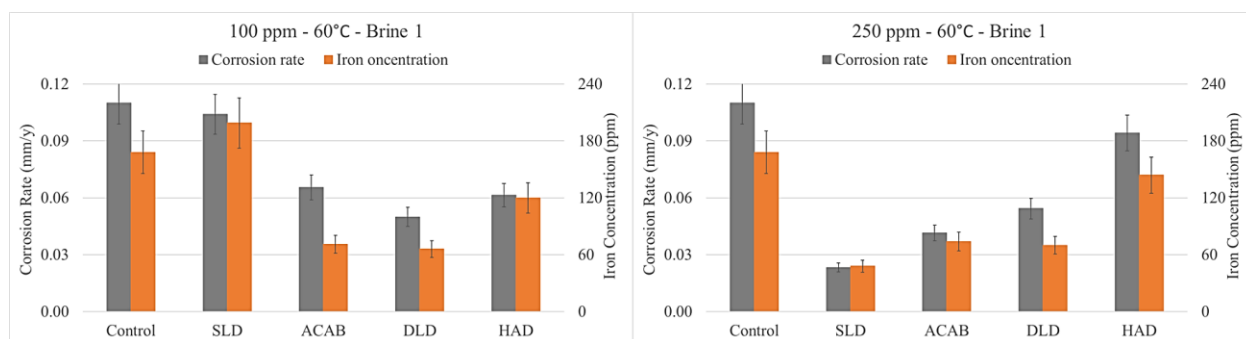


Figure 3.19. Corrosion experiments in the presence of non-phosphonate inhibitors in Brine 1 at 60 °C. (left) 100 ppm and (right) 250 ppm. Color codes: *grey* Corrosion rate and *orange* Iron concentration.

Figure 3.20 presents the results of the corrosion experiments in the presence of non-phosphonate inhibitors at 90 °C. Again, for the 100 ppm dosage, DLD is the most effective inhibitor, presenting 70 % inhibition. The next highest inhibition efficiency is much lower and observed in the presence of SLD (23 % inhibition). Both ACAB and HAD show corrosive behavior, yielding corrosion rates higher than the corresponding control. The same conclusion is true for the 250 ppm inhibitor dosage. DLD shows its highest inhibition (65 %), followed by SLD (51 %). Both ACAB and HAD show corrosive behavior at this concentration as well. Unfortunately, large differences are observed when comparing the results of the gravimetric measurements and the iron determination method results.

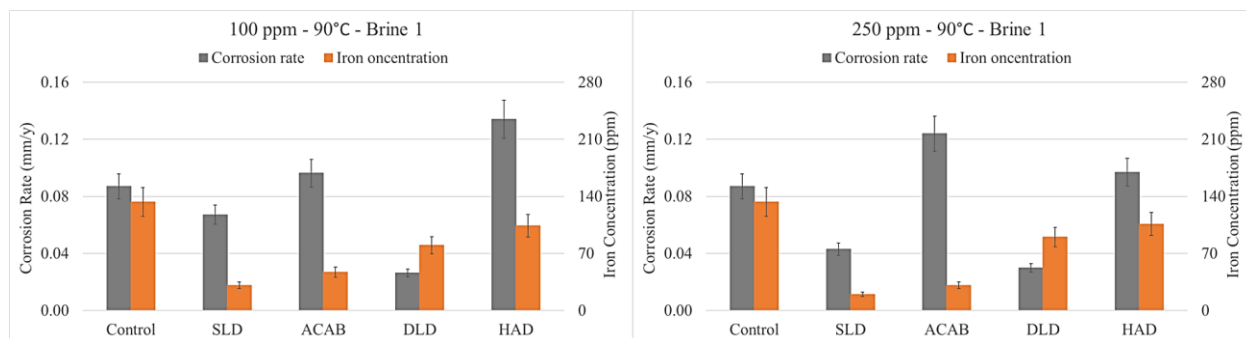


Figure 3.20. Corrosion experiments in the presence of non-phosphonate inhibitors in Brine 1 at 90 °C. (left) 100 ppm and (right) 250 ppm. Color codes: *grey* Corrosion rate and *orange* Iron concentration.

The glass bottles with the specimens of the corrosion experiments in the presence of non-phosphonate inhibitors at the end of the experimental period are presented in Figure 3.21. Overall, the visual observations are in agreement with the corresponding results of the gravimetric measurements and of the iron determination test, with very few exceptions. In experiments in the presence of HAD (250 ppm, RT), higher iron levels are observed in solution, despite the fact that HAD presents the second best inhibition performance under these conditions. It is worth noting that working solutions in the presence of 250 ppm of ACAB at RT look turbid/hazy. Finally, in the case of ACAB (250 ppm, 60 °C), high iron levels are observed in solution, although it is the second most efficient inhibitor under these conditions.

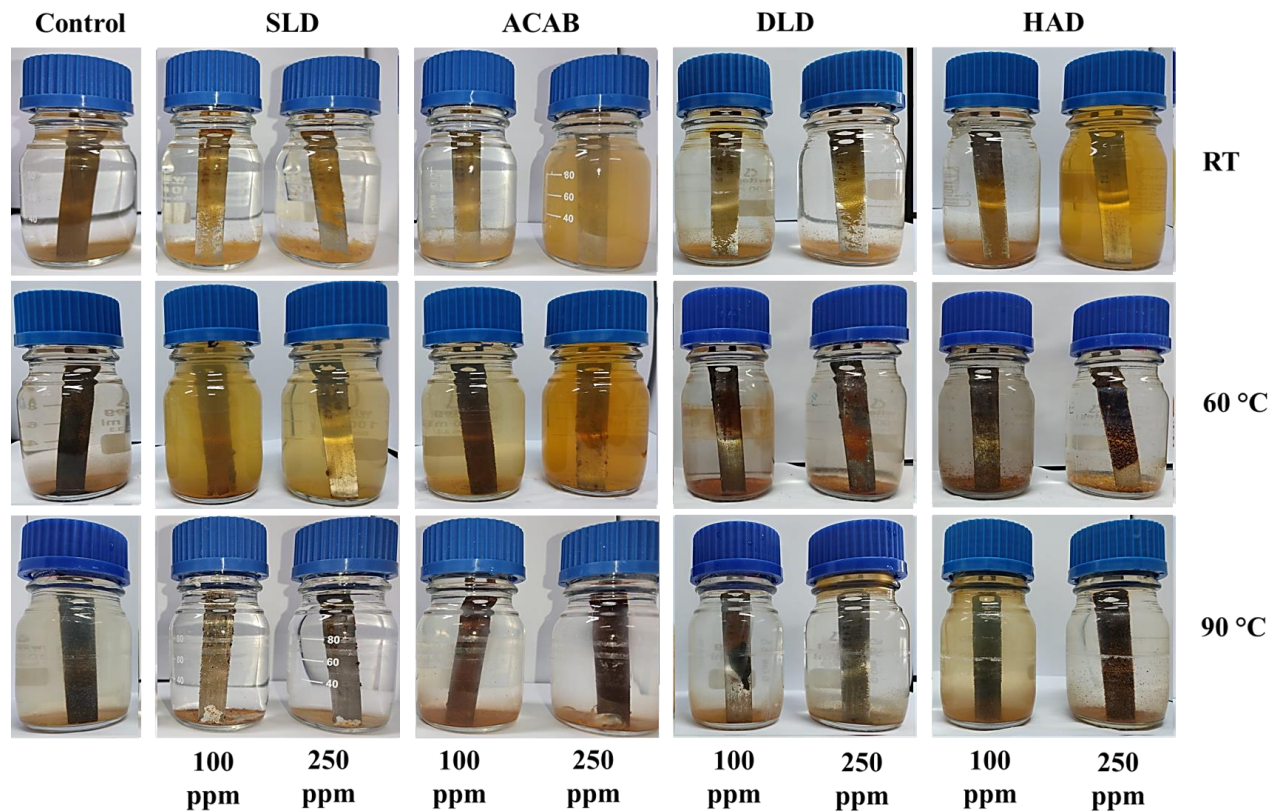


Figure 3.21. Visual representation of the experiments in the presence of non-phosphonate inhibitors in Brine 1 at RT, 60 °C and 90 °C.

Effect of concentration

Figure 3.22 presents the correlation between concentration and corrosion rate values obtained in the presence of each inhibitor at RT, 60 °C and 90 °C. SLD shows lower corrosion rates as its concentration increases at all temperatures. At RT and 90 °C, ACAB shows higher corrosion rates at higher concentrations, however, at 60 °C increased concentration results in slightly lower corrosion rates. In the case of DLD at RT, corrosion rates decrease as the concentration increases, while at 60 °C and 90 °C, increase in concentration does not appear to affect efficiency. In the presence of HAD at RT, a slightly lower corrosion rate is observed. On the contrary, raising the temperature to 60 °C, a higher corrosion rate is observed at higher inhibitor concentration, while at 90 °C a lower corrosion rate is observed.

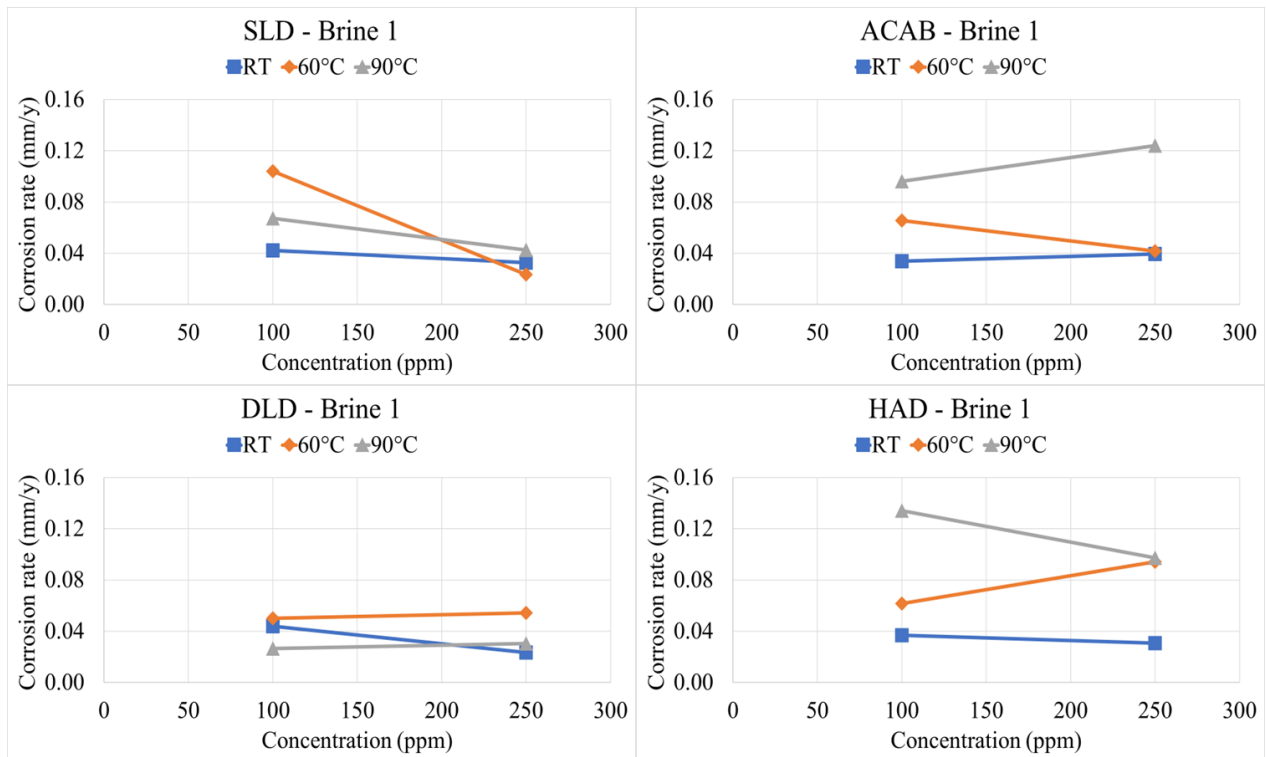


Figure 3.22. The correlation between corrosion rates and inhibitor concentration for non-phosphonates in DI water. Color codes: *blue* RT, *orange* 60 °C and *grey* 90 °C. Lines are added to aid the reader.

Effect of temperature

Figure 3.23 presents correlations between temperature and corrosion rate values obtained in the presence of each inhibitor at 100 ppm and 250 ppm inhibitor concentration. Regarding 100 ppm inhibitor concentration, 60 °C is the least favorable temperature for SLD, followed by 90 °C and then RT. ACAB presents lower % inhibition efficiency as the temperature increases. In the case of DLD, the increase in temperature leads to higher inhibition efficiency percentages. For HAD, slightly higher inhibition is observed at 60 °C than RT, while at 90 °C a significant drop in efficiency is noted. At 250 ppm inhibitor concentration, 60 °C is the most favorable temperature for SLD and ACAB. Regarding the remaining experiments, SLD presents a slightly lower efficiency at 90 °C than at RT. On the contrary, ACAB shows higher inhibition at RT, but at 90 °C a significant drop in efficiency is noted. HAD presents lower % inhibition efficiency as the temperature increases.

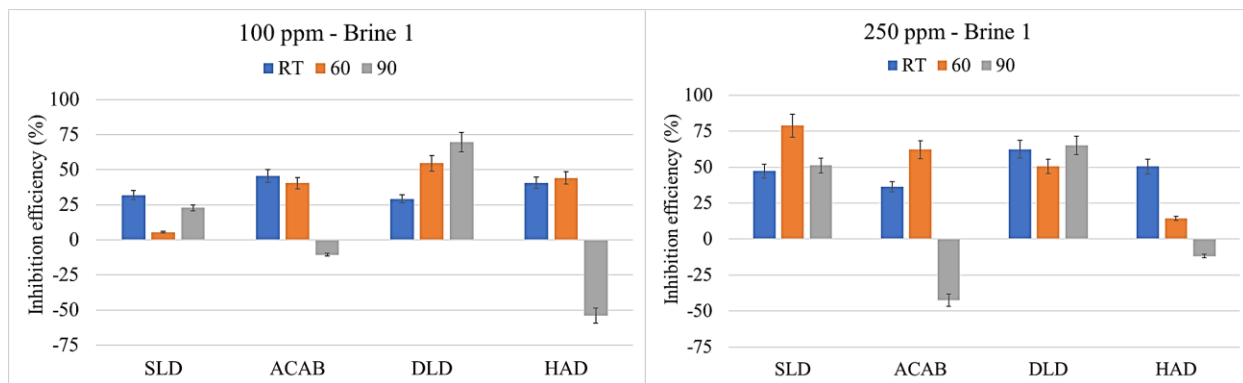


Figure 3.23. The correlation between corrosion rates and temperature for non-phosphonates in Brine 1 for inhibitor concentrations, a. 100 ppm (left), and b. 250 ppm (right). Color codes: *blue* RT, *orange* 60°C and *grey* 90°C.

Effect of mechanical stirring

Corrosion experiments under stirring were performed at RT in large glass bottles of total experiment volume 1200 mL. In this case, the specimens did not rest at the bottom of the bottle, in order to avoid any contact with the magnetic stirrer. Two different stirring rates were selected (200 rpm and 400 rpm). The same experiments were also performed under the same conditions and with the same experimental set-up under non-stirring conditions. The dosage of each inhibitor was 100 ppm.

Figure 3.24 shows the corrosion rates and the % inhibition of three different inhibitors. It is worth mentioning that increasing the stirring rate results in higher corrosion rates in the control experiments. Comparing the results between no stirring and the two different stirring rates, a trend is observed that enhanced anticorrosion efficiencies are noted as the stirring rate increases in the cases of HAD and ACAB. On the contrary, the performance of SLD drops as the stirring rate increases. Overall, no trend was established regarding the anti-corrosion efficiency. We found that the results were inhibitor specific.

The glass bottles with the carbon steel specimens in the presence of the various non-phosphonate inhibitors at the end of the experimental period are presented in Figure 3.25. Precipitates at the bottom of the containers are noted for most of the cases. In addition, at 400 rpm stirring rate, an orange color is observed in solutions containing the inhibitors, indicating higher

iron concentrations than the respective experiments at static conditions or at 200 rpm, despite the fact that HAD and ACAB present higher efficiency as the stirring rate increases.

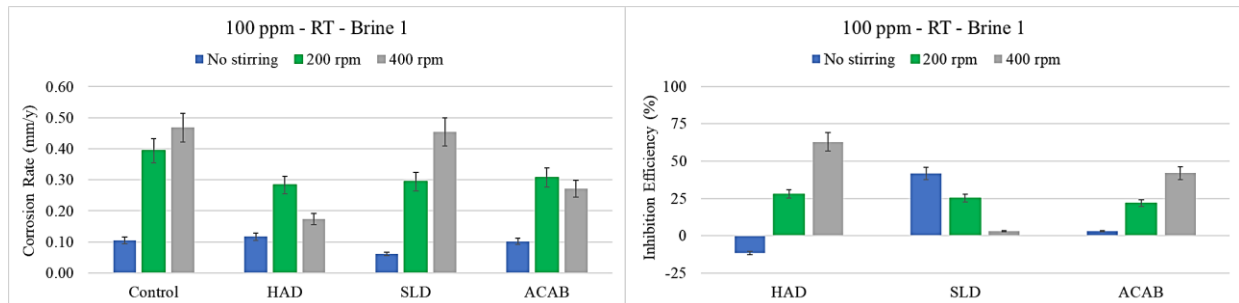


Figure 3.24. Correlation between : corrosion rates and stirring rates (left) and % inhibition efficiency and stirring rates (right) for non-phosphonate inhibitors in Brine 1 at RT. Color codes: *blue* no stirring, *green* 200 rpm and *grey* 400 rpm.

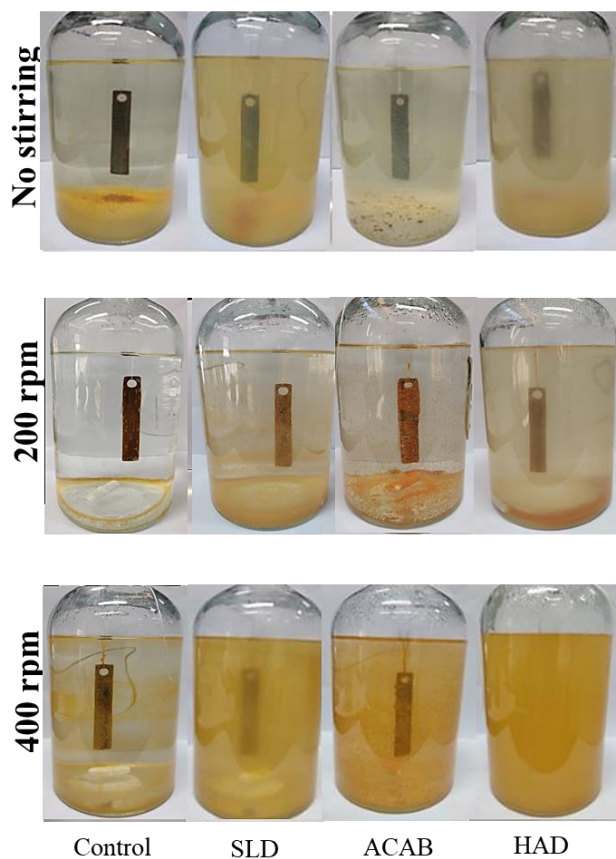


Figure 3.25. Visual representation of the experiments at different stirring rates, as shown.

Effect of sulfides

Corrosion experiments in the presence of sulfides were performed at RT. Two types of experiments were designed, in order to observe corrosion aggressiveness and inhibitor performance, both in the presence and in the absence of dissolved oxygen in the solution, along with the presence of sulfides. Thus, in addition to the experiments in glass bottles with caps, experiments were performed under inert atmosphere (argon), as well. In order to remove the dissolved oxygen from the solution, each working solution was thoroughly degassed for at least 30 minutes, by bubbling argon.

Soluble sulfide levels were determined before and after the experiments with the methylene blue method (see Chapter 2.3). Figure 3.26 shows the results of corrosion experiments in the presence of 50 ppm sulfides (expressed as “ppm S²⁻”), for three different inhibitors (HAD, SLD and ACAB) at 100 ppm and 250 ppm dosages.

In the presence of both oxygen and sulfides in solution, higher corrosion rates are observed than those under pure argon atmosphere. In the presence of oxygen, for 100 ppm inhibitor concentration, HAD appears to be the most effective inhibitor, while SLD and ACAB show higher corrosion rates than the corresponding control experiment. For 250 ppm, ACAB appears to be the most effective inhibitor, followed by HAD. SLD shows again a higher corrosion rate than the respective control experiment.

Under a pure argon atmosphere, HAD exhibits the best performance for the protection of carbon steel, regardless of its concentration. For the 100 ppm inhibitor dosage, the second most effective inhibitor is ACAB. SLD shows again a higher corrosion rate than the respective control. For the 250 ppm dosage, the second most effective inhibitor is SLD. This is the first time that SLD has not shown corrosive behavior, however, its efficiency is essentially zero. On the contrary, ACAB presents a higher corrosion rate than the control under these conditions.

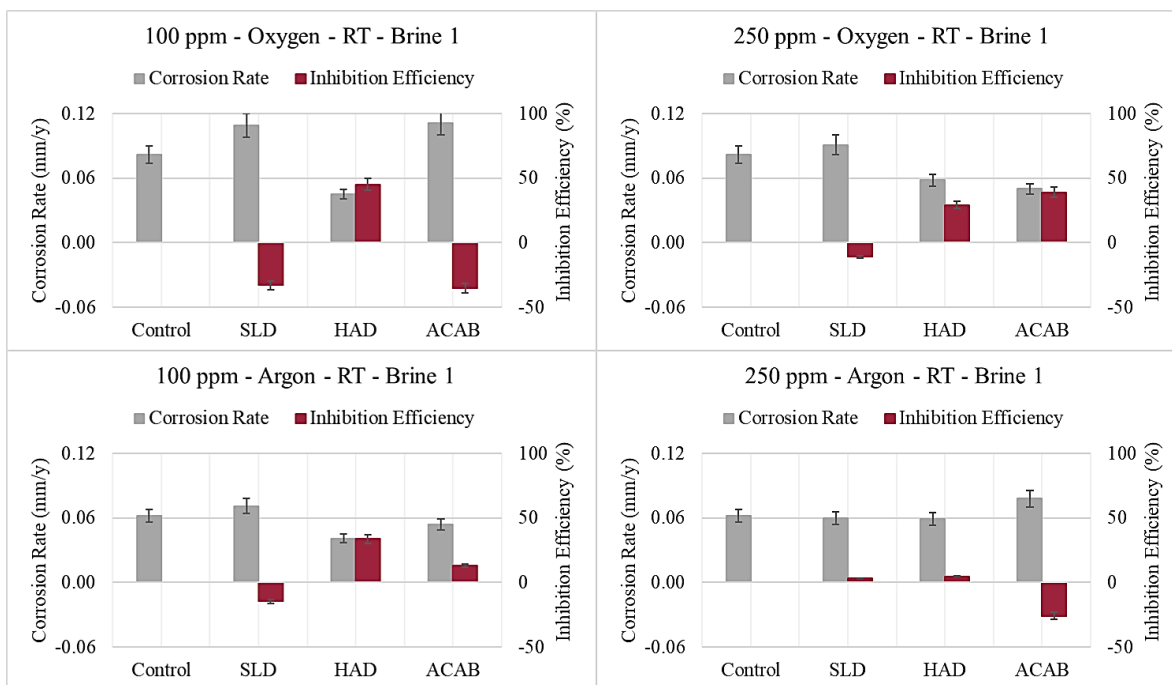


Figure 3.26. Results obtained in the absence (control) and presence of non-phosphonate inhibitors in DI water at RT in the presence of 50 ppm S^{2-} for: 100 ppm inhibitor concentration under oxygen (upper left), 250 ppm inhibitor concentration under oxygen (upper right), 100 ppm inhibitor concentration under argon (bottom left) and 100 ppm inhibitor concentration under argon (bottom right). Color codes: *grey* Corrosion rates and *burgundy* % inhibition efficiency.

The glass bottles with the specimens of the corrosion experiments in the presence of non-phosphonate inhibitors at the end of the experimental period are presented in Figure 3.27. In the presence of oxygen, HAD produced dark green solutions, despite the fact that it is the most effective inhibitor for the 100 ppm, and the second best for the 250 ppm dosage. In addition, light green solutions are observed in the presence of HAD under pure argon atmosphere. This color is a strong indication of the presence of Fe(II) formation. For the remaining corrosion experiments, the familiar black color of iron sulfide is observed. In the case of ACAB, for 250 ppm under both atmospheres, white precipitates are also noted.

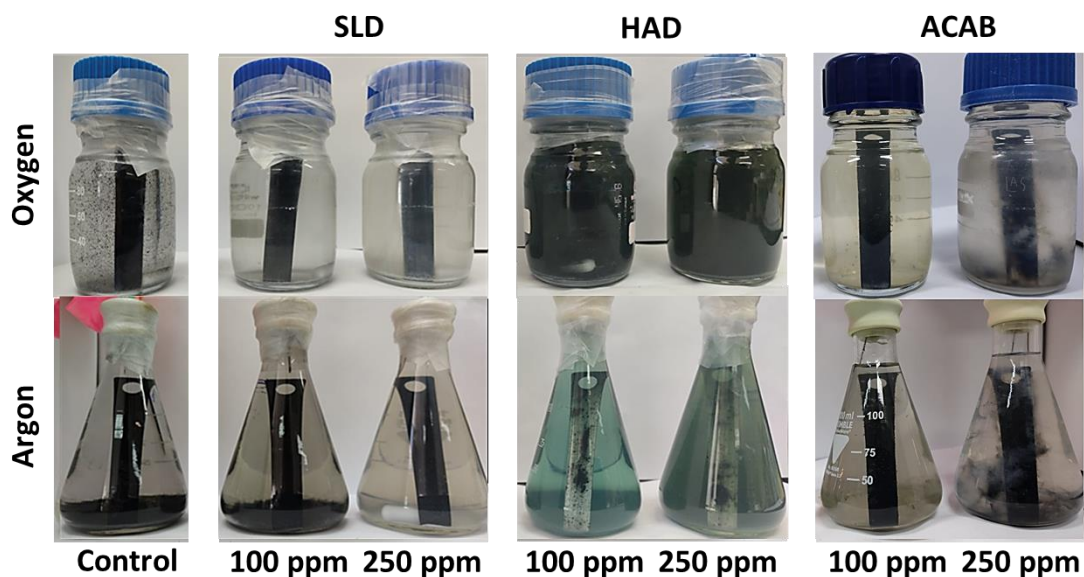


Figure 3.27. Visual representation of the experiments in the presence of sulfides.

3.3 Concluding remarks

In this chapter, corrosion experiments were performed in artificial Brine 1, at pH 7. The anticorrosion efficiency of the inhibitors was examined at different temperatures and several concentrations (dosages). Their performance was quantified by gravimetric measurements, according to the NACE standard method ^[9]. Comparing the % inhibition between the two methods tested, the results of the colorimetric method of total iron determination showed a deviation from the results based on mass loss in several cases.

3.3.1 Phosphonate inhibitors

Overall, C2 seems to perform better at low dosages at RT and 90 °C. Regarding the temperatures of 60 °C and 130 °C its most efficient dosage is 1 mM. In the case of C4, 0.1 mM inhibitor concentration exhibits its highest anticorrosion efficiency, except the experiments at 90 °C, at which the 0.01 mM dosage is the most efficient (70 % inhibition). In general, C6 presents higher inhibition at higher dosages. Regarding C8, 1 mM is the most beneficial dosage at RT, 60 °C and 90 °C, while at 130 °C it exhibited a higher efficiency at the lowest dosage, reaching 60 %

inhibition. Finally, C12 presents higher inhibition at higher concentrations as the temperature increases.

A global correlation between structure and anticorrosion efficiency cannot be discerned, however some conclusions could be drawn for specific conditions. At RT, most of inhibitors present similar anticorrosion efficiency. Some exceptions of lower inhibition performance than the rest of the phosphonates are observed in the presence of 0.01 mM C4 and 1-2 mM C2. At 60 °C, a trend of higher inhibition is observed as the length of carbon chain increases for the higher inhibitor concentrations. On the contrary, at 90 °C and 0.01 mM dosage, the efficiency increases as the size of the molecule decreases.

In several cases, white precipitates were observed on the metal surfaces. They were isolated and characterized by ATR-IR spectroscopy. Their spectra are shown in Chapter 8.6. The vibrational bands assigned to the phosphonate groups are shifted, compared to those of the corresponding pure phosphonates. This is an indication of a metal-phosphonate formation.

3.3.2 Non-phosphonate inhibitors

At RT, ACAB shows the highest inhibition for the 100 ppm dosage and DLD for the 250 ppm dosage. At 60 °C, DLD is the best-performing inhibitor at 100 ppm, however dosage increase to 250 ppm results in a significant inhibition enhancement for SLD, thus making it the best-performing inhibitor under these conditions. The increase in temperature to 90 °C favors the anticorrosion efficiency of DLD for both dosages.

Furthermore, experiments in the presence of non-phosphonate inhibitors were performed under stirring conditions. It is worth noting that the corrosion rate of the control experiment under *non stirring* conditions is 4-5 times lower than the respective values of the experiments *under stirring*. Overall, no trend was established regarding the anti-corrosion efficiency. Each inhibitor exhibits different behavior. For example, a trend of enhanced anticorrosion efficiencies as the stirring rate increases is observed in the case of HAD and ACAB. In contrast, SLD appears to perform better as the stirring rate decreases.

Finally, corrosion experiments in the presence of sulfides concluded that when both oxygen and sulfides are present in solution, corrosion rates are higher than those in experiments performed under argon atmosphere. HAD appears to be the most effective inhibitor in the presence of oxygen at 100 ppm dosage, while ACAB is the best at 250 ppm. Under argon atmosphere, HAD exhibits the highest inhibition efficiency at 100 ppm. In the case of the 250 ppm concentration, none of the non-phosphonate inhibitors present inhibitory activity.

3.4 References

1. Ohtsuka, T. Characterization of Corrosion Products on Steel Surfaces; Waseda, Y., Suzuki, S., Eds.; Springer Berlin Heidelberg, **2006**; Chapter 2, pp 19-32.
2. Faria, D.; Antunes, R. Characterization of Corrosion Products Formed on Steels in the First Months of Atmospheric Exposure. *Materials Research* **2003**.
3. Schwertmann, U.; Cornell, R.M. Iron Oxides in Laboratory. *Soil Science* **1993**, *156* (5), 369.
4. Bowles, J. F. W. *Oxides* in *Encyclopedia of Geology*. Elias, S. A.; Alderton, D.H.M.; Academic Press: London; San Diego, Ca, United States, **2021**.
5. Schmeide, K.; Rossberg, A.; Bok, F.; Shams Aldin Azzam, S.; Weiss, S.; Scheinost, A.C. Technetium Immobilization by Chukanovite and Its Oxidative Transformation Products: Neural Network Analysis of EXAFS Spectra. *Science of The Total Environment* **2021**, *770*, 145334.
6. Vu, H. H. T.; Khan, M.D.; Tran, V. T.; Quang, D.V.; Dao, V.D.; Lee, S.; Ahn, J.W.; Jung, S. Use of Calcite Mud from Paper Factories in Phosphorus Treatment. *Sustainability* **2020**, *12* (15), 5982.
7. Machmudah, S.; Zulhijah, R.; Wahyudiono; Setyawan, H.; Kanda, H.; Goto, M. Magnetite Thin Film on Mild Steel Formed by Hydrothermal Electrolysis for Corrosion Prevention. *Chemical Engineering Journal* **2015**, *268*, 76–85.
8. Lavagna, L.; Nisticò, R.; Musso, S.; Pavese, M. Hydrophobic Cellulose Ester as a Sustainable Material for Simple and Efficient Water Purification Processes from Fatty Oils Contamination. *Wood Science and Technology* **2018**, *53* (1), 249–261.
9. NACE Standard TM0169-95 (Item No. 21200), National Association of Corrosion Engineers, Houston TX, U.S.A. (www.nace.org).

Chapter 4: Corrosion experiments in artificial brine of high salinity

4.1 Characterization of the corrosion products

In this chapter, the results of the corrosion experiments performed in an artificial geothermal brine of high salinity, named “Brine 2”, are presented. The chemical composition of Brine 2 is shown in Table 4.1. Note that the different dissolved species are expressed as follows: Ca^{2+} as “ppm Ca”, Mg^{2+} as “ppm Mg”, Cl^- as “ppm Cl” and SO_4^{2-} as “ppm SO_4 ”. The total key species (TKS) content is 64860 ppm, 87.9 % of which are chloride ions. The total key species (TKS) content for Brine 1 is 2660 ppm (37.6 % Cl^-). Obviously, the significant increase in salinity makes these conditions more “stressful”. Specifically, calcium and chloride ion concentrations are much higher in Brine 2 than in Brine 1. In addition, Brine 2 contains magnesium ions but no bicarbonate ions. As mentioned in Chapter 3, three different temperatures were selected, mimicking the different pressure and temperature conditions of the geothermal systems. In addition, experiments were performed at room temperature for comparison reasons.

Ca^{2+}	Mg^{2+}	Cl^-	SO_4^{2-}
7200 ppm	490 ppm	57000 ppm	170 ppm

Corrosion experiments were performed in the absence of any chemical additive, under several different conditions, the results of which were then used as a comparison tool (control) to evaluate the anticorrosion efficiency of the inhibitors. Corrosion rates and iron concentrations of the control experiments are presented in Table 4.2 and Figure 4.1. As aforementioned in Chapter 3, no linear relationship between the increase in temperature and corrosion rate was observed.

T (°C)	RT		60		90		130	
	CR (mm/y)	Fe (ppm)	CR (mm/y)	Fe (ppm)	CR (mm/y)	Fe (ppm)	CR (mm/y)	Fe (ppm)
Brine 2	0.053	80	0.103	157	0.094	143	0.177	536

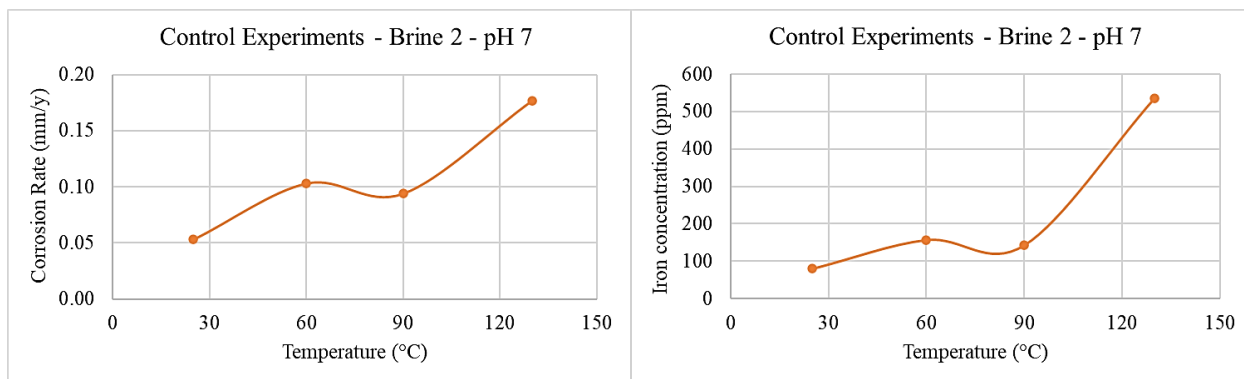


Figure 4.1. Results obtained in the absence of chemical additives in Brine 2 at pH 7. *left* Corrosion Rates and *right* Iron concentrations.

Comparing the surfaces of the control samples exposed to different temperatures (see Figure 4.2), a color difference between the different corrosion products is observed. It is noticeable that, as the temperature increases, the color of the corrosion products becomes darker. In order to identify these products, precipitates were collected and then characterized by ATR-IR spectroscopy and powder X-Ray Diffraction. The amount of the precipitate which was collected from the control experiment at 130 °C was very small and could not be removed from the filter membrane used for the filtration. Thus, samples from the pristine membrane were taken and used as a background for the ATR-IR studies, so the bands associated with its material can be easily identified (see the grey inset at the bottom spectrum). The respective spectrum of the membrane filter is shown in the Annex (Chapter 8).



Figure 4.2. Corroded carbon steel surfaces of the specimens exposed to “control” solutions in Brine 2 at pH 7.

Figure 4.3 presents the ATR-IR spectra of the control experiments. By examination of the ATR-IR spectra of the control experiments at RT and 60 °C, it is observed that they are identical to a reference spectrum of lepidocrocite taken from the literature, showing the characteristic vibration bands at 1152 cm^{-1} , 1017 cm^{-1} and 737 cm^{-1} [1]. The characteristic vibrational bands of magnetite and hematite appear at low frequencies, ie. 570 cm^{-1} and 390 cm^{-1} for magnetite, and 535 cm^{-1} , 464 cm^{-1} and 308 cm^{-1} for hematite [2,3]. Unfortunately, the lack of sufficient peak resolution did not allow reliable conclusions to be drawn about the iron species formed in the case of $T = 130\text{ }^{\circ}\text{C}$. Furthermore, the broad band in the spectrum of the control experiment at 90 °C located at frequencies $> 3000\text{ cm}^{-1}$ is attributed to the ubiquitous water of the sample. The ATR-IR spectrum at 90 °C is similar to the respective spectrum in Brine 1, excluding the vibration bands assigned to the carbonate ion. All samples present vibration bands of adsorbed water around 3400 cm^{-1} and 1625 cm^{-1} . In addition, the broad peak around 3400 cm^{-1} shows a split which can be attributed to the typical O–H stretching vibration band of oxyhydroxides around 3142 cm^{-1} . This split is observed for lepidocrocite. On the contrary, the split cannot be observed in magnetite.

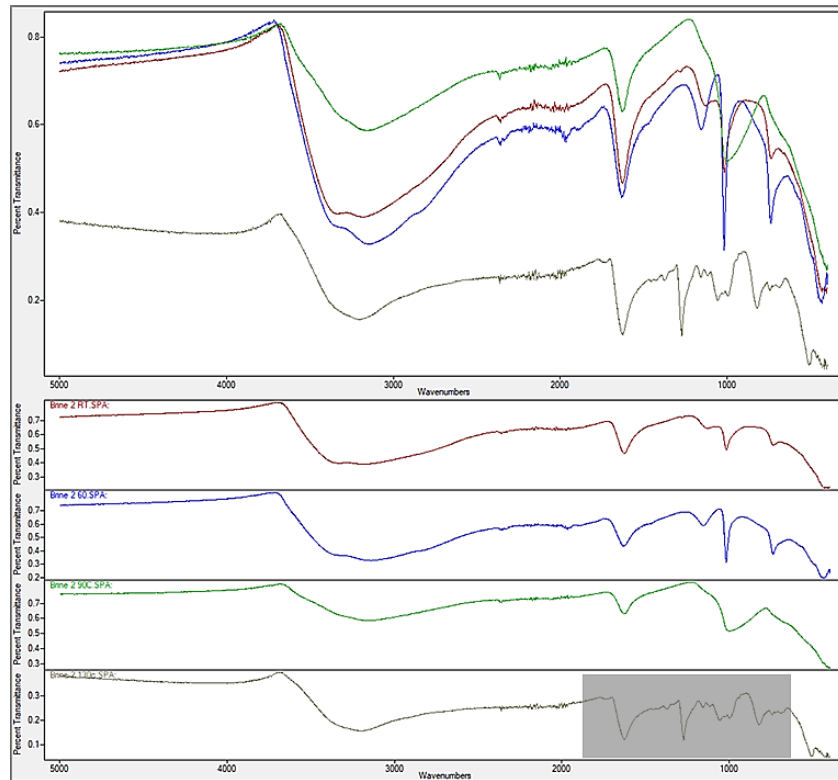


Figure 4.3. ATR-IR spectra of the precipitates collected from control corrosion runs in Brine 2. Color codes: *red* RT, *blue* 60°C, *green* 90°C and *grey* 130°C.

Figure 4.4 presents the powder XRD patterns of the control experiments. In the X-Ray diffraction patterns of the control corrosion products at RT, 60 °C and 90 °C, the characteristic peaks of lepidocrocite at 2θ values 14.29°, 27.16° and 36.54° are observed [4]. However, the XRD patterns of the control experiments at RT and 90 °C showed the presence of halite, based on its characteristic peaks at 2θ values 32.15° and 47.14° [5]. In addition, in the case of 90 °C, the existence of the peak at 35.5° is an indication that this corrosion product is a mixture of lepidocrocite and magnetite, resulting most probably in a denser and more adherent layer on the metallic surface [6]. Regarding the characterization of the control experiments at 130 °C, it is concluded that both magnetite and hematite are present in the corrosion product, as the characteristic peaks of both are observed at 35.46° and 33.15°, respectively [7]. The crystal data of the aforementioned structures are shown for comparison in the Annex. The broad peak at 26° which is observed in the respective XRD pattern of the control experiment at 130 °C is attributed to the filter membrane [8].

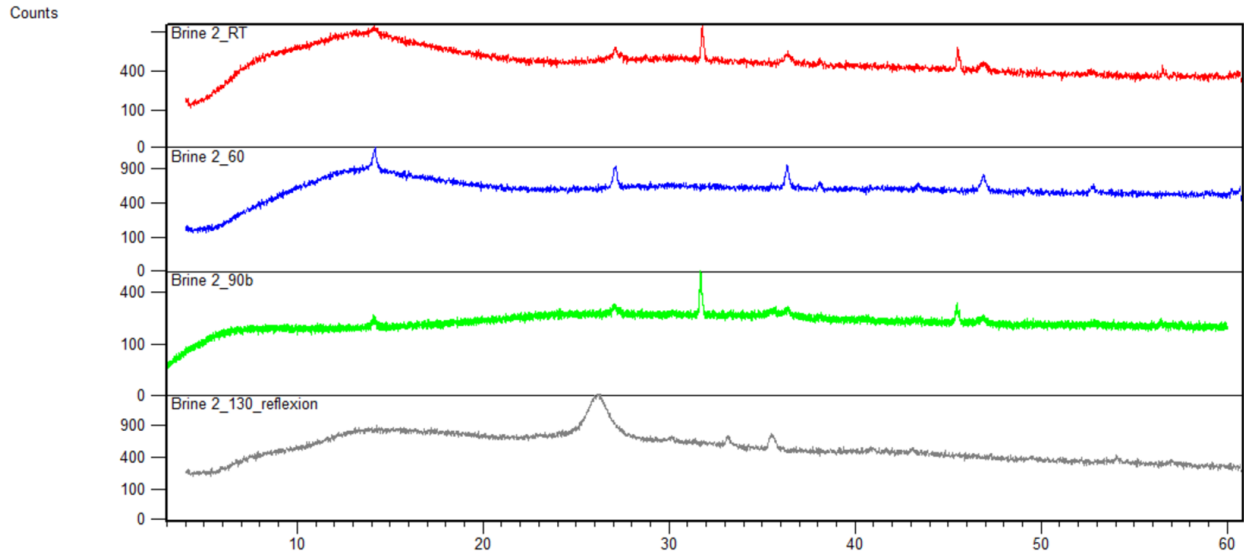


Figure 4.4. Powder XRD spectra of the precipitates collected from control corrosion experiments in Brine 2. Color codes: *red* RT, *blue* 60 °C, *green* 90 °C and *grey* 130 °C.

In addition, the precipitates were studied by Scanning Electron Microscopy (SEM) in order to examine the morphology, the texture and the size of the particles. Figure 4.5 shows the SEM images. The increase in temperature appears to affect the morphology of lepidocrocite. At RT, the agglomeration of spherical iron hydroxide particles is observed, while at 60 °C, the particles changed to needle shape nanorods. Finally, at 90 °C, the particles presented uniform and organized nanorods.

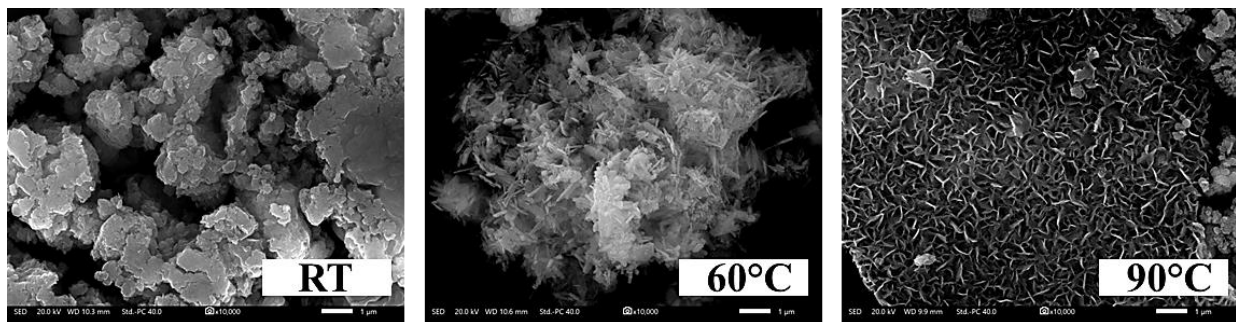


Figure 4.5. SEM images of the precipitates that collected from the experiments at *left* RT, *center* 60°C and *right* 90°C.

4.2 Results

4.2.1 Phosphonate inhibitors

This section discusses the results from experiments performed in the presence of phosphonate-based inhibitors in Brine 2 at four temperatures (RT, 60 °C, 90 °C and 130 °C) for four inhibitor concentrations (0.01 mM, 0.1 mM, 1 mM and 2 mM). In addition, at 130 °C (High Pressure – High Temperature conditions, HP-HT), additional experiments in the presence of inhibitors at even higher concentrations (3 mM, 4 mM and 5 mM) were performed. The inhibitor solutions were prepared by diluting the desired volumes of the corresponding inhibitor stock solutions in Brine 2, followed by pH adjustment to 7, if needed. The total volume of each experiment was 120 mL for corrosion studies at RT, 60 °C and 90 °C, and 4 mL for 130 °C experimental set-up.

Each specimen was weighed before and after the experiment, after first being dried and mildly cleaned using abrasive paper. Corrosion rates were calculated according to Equation 1, given in Chapter 2.3. Furthermore, aliquots were taken from the working solution at the end of the experimental period, in order to determine the iron concentration for each corrosion experiment. One of the goals here was to evaluate whether the iron determination method could be used for corrosion evaluation and quantification. Inhibition efficiencies (in %) based on both methods were calculated according to Equation 2 and Equation 3, as given in Chapter 2.3 .

EDTMP-C2

Corrosion rate and iron concentration values obtained from the experiments performed under these conditions in the presence of C2, as well as the calculated inhibition efficiency (in %), are presented in Table 4.3.

Table 4.3. Corrosion rates, iron concentrations and inhibition efficiency percentages based on both methods in the presence of C2 in Brine 2.								
T (°C)	RT		60		90		130	
c (mM)	CR (mm/y)	Fe (ppm)	CR (mm/y)	Fe (ppm)	CR (mm/y)	Fe (ppm)	CR (mm/y)	Fe (ppm)
<i>Control</i>	<i>0.053</i>	<i>80</i>	<i>0.103</i>	<i>157</i>	<i>0.094</i>	<i>143</i>	<i>0.177</i>	<i>536</i>

0.01	0.027 50 %	43 46 %	0.091 12 %	159 - 1 %	0.062 34 %	72 50 %	0.269 - 52 %	386 28 %
0.10	0.020 63 %	26 68 %	0.069 33 %	114 27 %	0.053 43 %	79 45 %	0.158 11 %	396 26 %
1.00	0.018 66 %	27 66 %	0.037 64 %	69 56 %	0.068 28 %	57 60 %	0.084 53 %	166 69 %
2.00	0.019 65 %	35 56 %	0.039 62 %	53 66 %	0.044 53 %	61 57 %	0.134 24 %	435 19 %
3.00	-	-	-	-	-	-	0.123 31 %	495 8 %
4.00	-	-	-	-	-	-	0.114 36 %	506 6 %
5.00	-	-	-	-	-	-	0.114 36 %	493 8 %

Figure 4.6 presents the results from corrosion experiments carried out in the presence of C2. At RT, C2 exhibits excellent anticorrosion efficiency that does vary substantially with concentration, 50-66 %. These results are also verified by the iron determination method. At 60 °C, lower corrosion rate values are obtained at the highest inhibitor dosages of 1 mM and 2 mM, 64 % and 62 % inhibition, respectively. Regarding iron concentrations, in the case of 1 mM, a lower amount of iron than expected is observed. Regarding the experiments performed at 90 °C, the lowest corrosion rate is observed for 2 mM of C2 (53 % inhibition), followed by 0.1 mM of C2 (43 % inhibition), despite the fact that the lower iron concentrations are noted for the two highest inhibitor concentrations, 57 ppm and 61 ppm. Finally, at 130 °C, 1 mM appears to be the most efficient concentration (53 % inhibition), followed by 3-5 mM of C2 (31-36 % inhibition). Unfortunately, the iron determination method shows higher iron concentrations than expected compared to the gravimetric measurement, especially for higher inhibitor dosages.

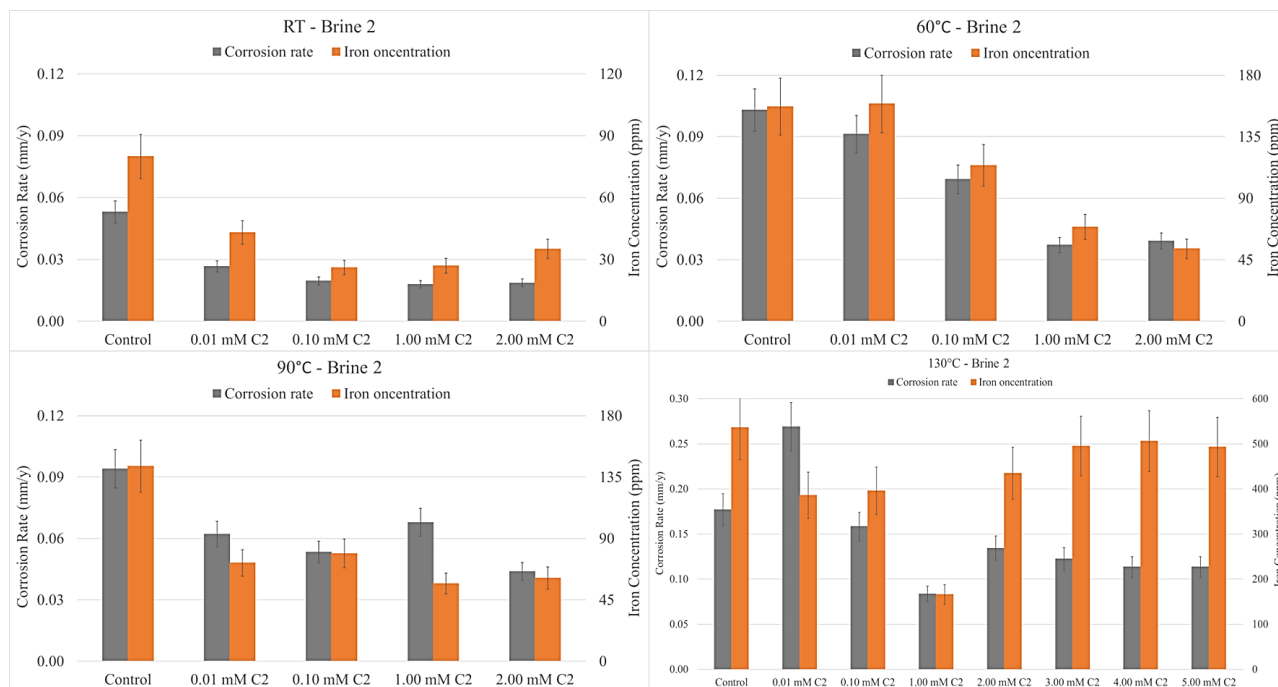

















Figure 4.6. Corrosion experiments in the presence of C2 in Brine 2 at: a. Room temperature (upper left), b. 60 °C (upper right), c. 90 °C (bottom left) and d. 130 °C (bottom right). Color codes: *grey* Corrosion rate and *orange* Iron concentration.

Table 4.4 shows a visual representation of the specimens from the corrosion experiments in the presence of C2 at RT, 60 °C and 90 °C. At RT and 60 °C, increased inhibitor concentrations in general favor the anticorrosion efficiency of C2, thus less corroded surfaces of the corresponding specimens are observed, as expected. Importantly, in the case of 60 °C, the iron oxide corrosion products are not spread out on the entire surface of the metallic specimens, in contrast to what was observed so far. At 90 °C, C2 presents the highest efficiency for 2 mM, followed by 0.1 mM of C2. In addition, the copious deposit on the metallic surface of the specimen from the experiment in the presence of 1 mM of C2 is in agreement with the corresponding high corrosion rate. The specimens from the experiments under HP-HT conditions are shown in the Annex.

Table 4.4. Visual representation of the specimens from the experiments of C2 in Brine 2.

	RT	60 °C	90 °C
Control			
0.01 mM			
0.10 mM			
1.00 mM			
2.00 mM			

TMTMP-C4

Corrosion rate and iron concentration values obtained from the experiments performed under these conditions in the presence of C4, as well as the calculated inhibition efficiency (in %), are presented in Table 4.5.

Table 4.5. Corrosion rates, iron concentrations and inhibition efficiency percentages based on both methods in the presence of C4 in Brine 2.

T (°C)	RT		60		90		130	
c (mM)	CR (mm/y)	Fe (ppm)	CR (mm/y)	Fe (ppm)	CR (mm/y)	Fe (ppm)	CR (mm/y)	Fe (ppm)
<i>Control</i>	<i>0.053</i>	<i>80</i>	<i>0.103</i>	<i>157</i>	<i>0.094</i>	<i>143</i>	<i>0.177</i>	<i>536</i>
0.01	0.033 38 %	49 39 %	0.085 17 %	57 64 %	0.087 7 %	142 1 %	0.170 4 %	405 24 %
0.10	0.018 66 %	24 70 %	0.070 32 %	63 60 %	0.072 24 %	85 41 %	0.211 -19 %	359 33 %
1.00	0.016	28	0.049	60	0.049	75	0.126	598

	70 %	65 %	53 %	62 %	48 %	48 %	29 %	- 12 %
2.00	0.011	22	0.047	57	0.024	39	0.090	466
	79 %	73 %	54 %	64 %	74 %	73 %	49 %	13 %
3.00	-	-	-	-	-	-	0.126	521
							29 %	3 %
4.00	-	-	-	-	-	-	0.146	658
							17 %	- 23 %
5.00	-	-	-	-	-	-	0.126	580
							29 %	- 8 %

Figure 4.7 presents the results from corrosion experiments in the presence of C4. At RT and 60 °C, C4 presents a similar behavior to C2, under these conditions. Specifically, at RT high anticorrosion efficiency is observed for the C4 concentrations 0.1 mM, 1 mM and 2 mM (66-79 % inhibition), while the iron measurements show a similar pattern as the corrosion rates. At 60 °C, lower corrosion rates are seen at the highest inhibitor dosages of 1 mM and 2 mM (53 % and 54 % inhibition, respectively). Similar iron concentrations are noted for all C4 dosages (57-63 ppm). In the case of 90 °C, the highest inhibition performance is noted at 2 mM, 74 %, also verified by the iron determination test. Finally, concerning the experiments at 130 °C, the most efficient inhibitor concentration is 2 mM, 49 % inhibition, similar to what was observed for the 90 °C temperature. Unfortunately, under these conditions, iron concentrations do not follow the same pattern as corrosion rates. Specifically, C4 at high dosages yields higher iron concentrations than expected, in difference to the corresponding corrosion rates.

Table 4.6 shows visuals of the specimens from the corrosion experiments in the presence of C2 at RT, 60 °C and 90 °C. Overall, increased inhibitor concentrations of C4 enhanced its anticorrosion efficiency, thus less corroded surfaces of the corresponding specimens are observed, as expected. The specimens from the experiments under HP-HT conditions are shown in the Annex.

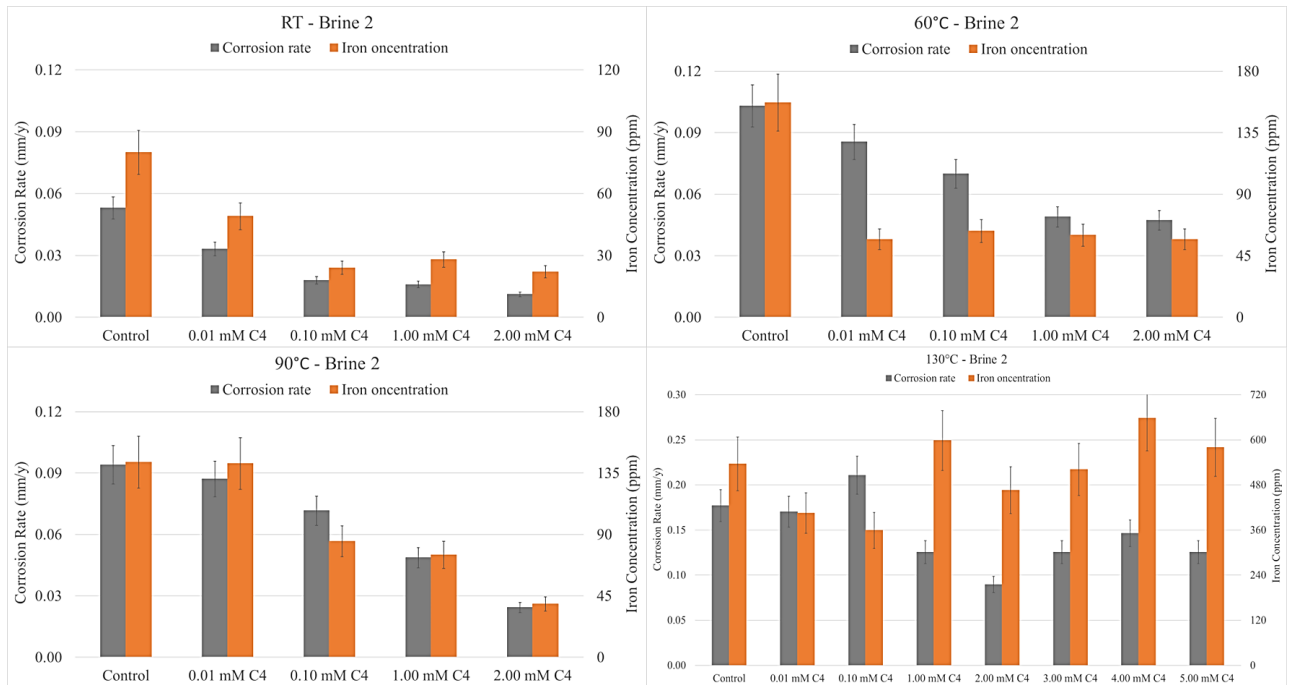


Figure 4.7. Corrosion experiments in the presence of C4 in Brine 2 at: a. Room temperature (upper left), b. 60 °C (upper right), c. 90 °C (bottom left) and d. 130 °C (bottom right). Color codes: *grey* Corrosion rate and *orange* Iron concentration.

Table 4.6. Visual representation of the specimens from the experiments of C4 in Brine 2.

	RT	60 °C	90 °C
Control			
0.01 mM			
0.10 mM			
1.00 mM			
2.00 mM			

HDTMP-C6

Corrosion rate and iron concentration values obtained from the experiments performed under these conditions in the presence of C6, as well as the calculated inhibition efficiency (in %), are presented in Table 4.7.

Table 4.7. Corrosion rates, iron concentrations and inhibition efficiency percentages based on both methods in the presence of C6 in Brine 2.

T (°C)	RT		60		90		130	
c (mM)	CR (mm/y)	Fe (ppm)	CR (mm/y)	Fe (ppm)	CR (mm/y)	Fe (ppm)	CR (mm/y)	Fe (ppm)
<i>Control</i>	<i>0.053</i>	<i>80</i>	<i>0.103</i>	<i>157</i>	<i>0.094</i>	<i>143</i>	<i>0.177</i>	<i>536</i>
0.01	0.024 54 %	41 49 %	0.065 37 %	57 64 %	0.049 48 %	62 57 %	0.179 - 1 %	260 51 %
0.10	0.014 75 %	22 73 %	0.067 36 %	48 69 %	0.047 50 %	55 62 %	0.149 16 %	339 37 %
1.00	0.010 81 %	25 69 %	0.026 75 %	49 69 %	0.030 68 %	48 66 %	0.087 51 %	234 56 %
2.00	0.010 82 %	21 74 %	0.032 69 %	50 68 %	0.031 67 %	39 73 %	0.087 51 %	316 41 %
3.00	-	-	-	-	-	-	0.126 29 %	558 - 4 %
4.00	-	-	-	-	-	-	0.117 34 %	664 - 24 %
5.00	-	-	-	-	-	-	0.167 5 %	700 - 31 %

Results from corrosion experiments in the presence of C6 are presented in Figure 4.8. At RT and 60 °C, C6 presents similar behavior to C2 and C4, under these conditions. Specifically, at RT high anticorrosion efficiency is observed for the three higher C6 dosages (75-82 % inhibition), while iron concentration results show a similar pattern as the corrosion rates. At 60 °C, lower

corrosion rates are achieved by the highest inhibitor dosages of 1 mM and 2 mM (75 % and 69 % inhibition, respectively). Regarding iron concentrations, similar values are measured for all C4 dosages (48-57 ppm). The same observation is valid for the experiments performed at 90 °C, where the highest inhibition efficiencies are noted at 1 mM and 2 mM, 68 % and 67 %, respectively. Iron concentrations decrease as inhibitor concentration decreases as well, with 39 ppm as its lowest value. Finally, at 130 °C, similarly to 90 °C, the two most beneficial inhibitor concentrations are 1 mM and 2 mM, both at 51 % inhibition. Regarding iron concentrations, C6 at high dosages presents higher iron concentrations than expected by comparison with the respective corrosion rates. These results are similar to those from experiments in the presence of C2 and C4, under these conditions.

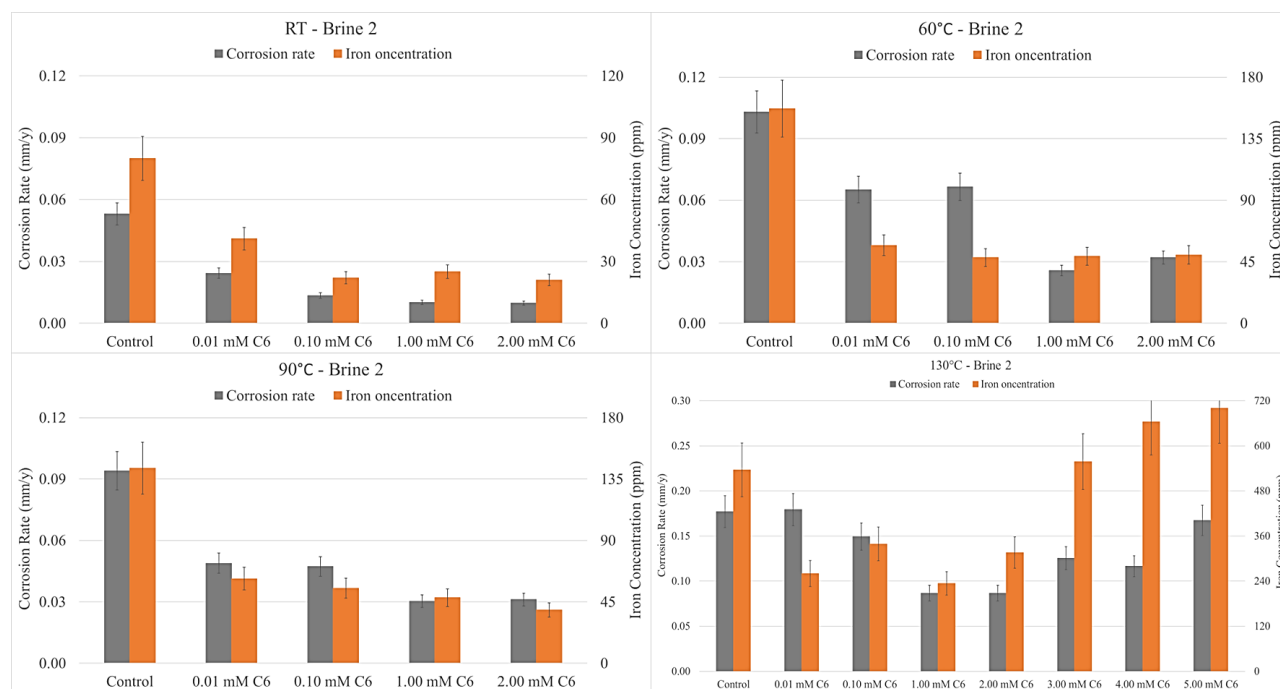

















Figure 4.8. Corrosion experiments in the presence of C6 in Brine 2 at: a. Room temperature (upper left), b. 60 °C (upper right), c. 90 °C (bottom left) and d. 130 °C (bottom right). Color codes: *grey* Corrosion rate and *orange* Iron concentration.

Table 4.8 shows the specimens from the corrosion experiments in the presence of C6 at RT, 60 °C and 90 °C. Visual observations agree with the results of the gravimetric measurements. The specimens from the experiments under HP-HT conditions are shown in the Annex.

Table 4.8. Visual representation of the specimens from the experiments of C6 in Brine 2.			
	RT	60 °C	90 °C
Control			
0.01 mM			
0.10 mM			
1.00 mM			
2.00 mM			

ODTMP-C8

Corrosion rate and iron concentration values obtained from the experiments performed under these conditions in the presence of C8, as well as the calculated inhibition efficiency (in %), are presented in Table 4.9.

Table 4.9. Corrosion rates, iron concentrations and inhibition efficiency percentages based on both methods in the presence of C8 in Brine 2.								
T (°C)	RT		60		90		130	
c (mM)	CR (mm/y)	Fe (ppm)	CR (mm/y)	Fe (ppm)	CR (mm/y)	Fe (ppm)	CR (mm/y)	Fe (ppm)
<i>Control</i>	<i>0.053</i>	<i>80</i>	<i>0.103</i>	<i>157</i>	<i>0.094</i>	<i>143</i>	<i>0.177</i>	<i>536</i>
0.01	0.021 60 %	28 65 %	0.087 16 %	100 36 %	0.067 29 %	103 28 %	0.212 - 20 %	172 68 %

0.10	0.025 52 %	27 66 %	0.058 43 %	67 57 %	0.043 54 %	56 61 %	0.128 27 %	218 59 %
1.00	0.013 75 %	22 73 %	0.045 57 %	60 62 %	0.057 40 %	69 52 %	0.123 31 %	447 17 %
2.00	0.014 73 %	29 64 %	0.038 63 %	60 62 %	0.060 36 %	58 59 %	0.125 29 %	320 40 %
3.00	-	-	-	-	-	-	0.155 12 %	728 - 36 %
4.00	-	-	-	-	-	-	0.173 2 %	523 2 %
5.00	-	-	-	-	-	-	0.134 24 %	483 10 %

Results from corrosion experiments in the presence of C8 are presented in Figure 4.9. At RT and 60 °C, C8 presents its highest anticorrosion efficiency for the 1 mM and 2 mM concentrations. Specifically, the highest inhibitory activities at RT reach 75 % and 73 %, respectively, while at 60 °C these performances are 57 % and 63 %, respectively. Iron concentration results show a similar pattern as the corrosion rates. At 90 °C, the lowest corrosion rate is observed for the C8 concentration 0.1 mM (54 % inhibition), also verified by the low iron concentration (56 ppm). Finally, at 130 °C, 0.1 mM, 1 mM and 2 mM of C8 produce similar corrosion rates, with the corresponding efficiencies to be the highest under these conditions, ranging between 27 and 31 %. C8 at high dosages (1 mM and higher) presents higher iron concentrations than expected in comparison with the respective corrosion rates.

Table 4.10 shows visuals of the specimens from the corrosion experiments in the presence of C8 at RT, 60 °C and 90 °C. At RT and 60 °C, increased inhibitor concentrations favor the anticorrosion efficiency of C8, thus less corroded surfaces of the corresponding specimens are observed, as expected. In contrast, in the case of 90 °C, no significant difference is observed in the appearance of the specimens. The specimens from the experiments under HP-HT conditions are shown in the Annex.

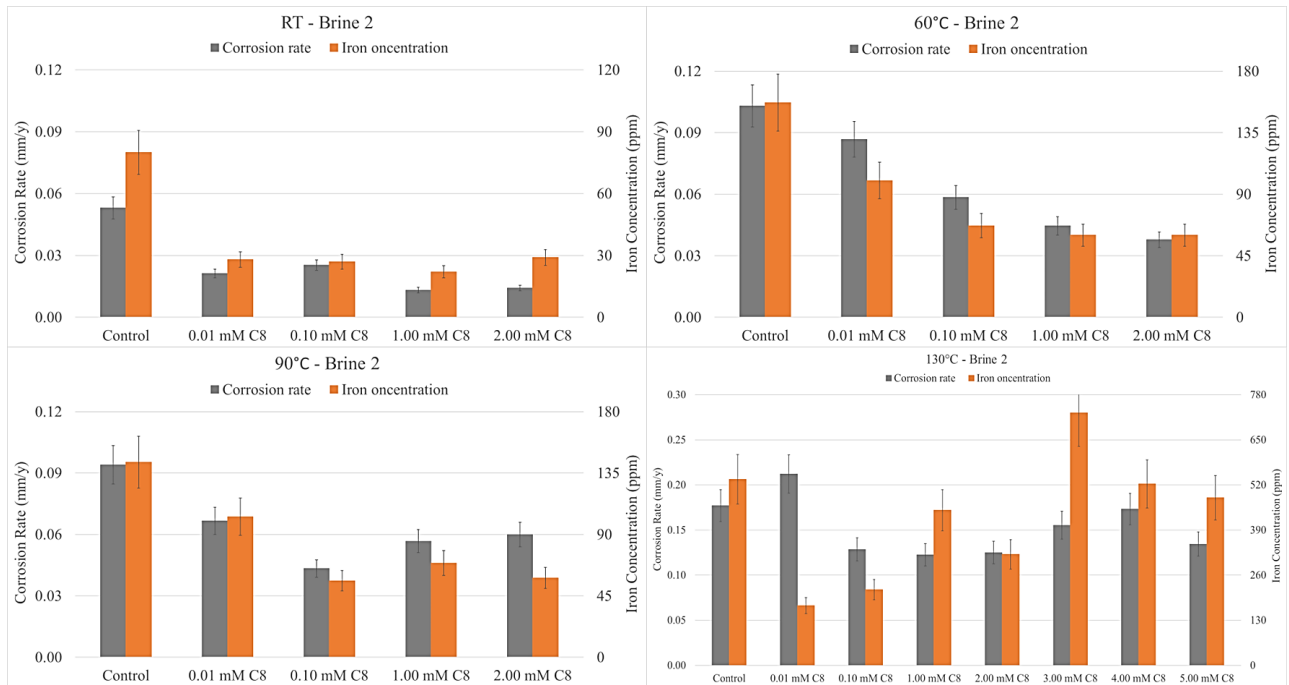


Figure 4.9. Corrosion experiments in the presence of C8 in Brine 2 at: a. Room temperature (upper left), b. 60 °C (upper right), c. 90 °C (bottom left), and d. 130 °C (bottom right). Color codes: *grey* Corrosion rate and *orange* Iron concentration.

Table 4.10. Visual representation of the specimens from the experiments of C8 in Brine 2.

	RT	60 °C	90 °C
Control			
0.01 mM			
0.10 mM			
1.00 mM			
2.00 mM			

DDTMP-C12

Corrosion rate and iron concentration values obtained from the experiments performed under these conditions in the presence of C12, as well as the calculated inhibition efficiency (in %), are presented in Table 4.11.

Table 4.11. Corrosion rates, iron concentrations and inhibition efficiency percentages based on both methods in the presence of C12 in Brine 2.								
T (°C)	RT		60		90		130	
c (mM)	CR (mm/y)	Fe (ppm)	CR (mm/y)	Fe (ppm)	CR (mm/y)	Fe (ppm)	CR (mm/y)	Fe (ppm)
<i>Control</i>	<i>0.053</i>	<i>80</i>	<i>0.103</i>	<i>157</i>	<i>0.094</i>	<i>143</i>	<i>0.177</i>	<i>536</i>
0.01	0.019 64 %	33 59 %	0.073 30 %	133 15 %	0.060 36 %	69 52 %	0.152 14 %	339 37 %
0.10	0.025 53 %	25 69 %	0.078 25 %	39 75 %	0.059 38 %	79 45 %	0.197 - 11 %	373 30 %
1.00	0.022 59 %	25 69 %	0.028 73 %	78 50 %	0.038 60 %	54 62 %	0.152 14 %	406 24 %
2.00	0.028 48 %	31 61 %	0.048 53 %	107 32 %	0.062 34 %	74 48 %	0.152 14 %	507 5 %
3.00	-	-	-	-	-	-	0.206 - 16 %	82 85 %
4.00	-	-	-	-	-	-	0.161 9 %	700 - 31 %
5.00	-	-	-	-	-	-	0.206 - 16 %	623 - 16 %

Results from corrosion experiments in the presence of C12 are presented in Figure 4.10. At RT, C12 presents its highest anticorrosion efficiency at its lowest concentration, 64 %. At 60 °C and at 90 °C, 1 mM of C12 yield the lowest corrosion rate values (73 % and 60 % inhibition, respectively). Overall, iron determination shows the same pattern to the gravimetric measurements, except the case of 0.1 mM of C12 at 60 °C, where the iron concentration is lower

than expected. Finally, at 130 °C, the efficiency of C12 drops significantly, showing the highest inhibition for the concentrations 0.01 mM, 1 mM and 2 mM, equal to only 14 %. Iron concentrations are lower than expected compared to corrosion rates, for 0.01 mM, 0.1 mM and 3 mM of C12.

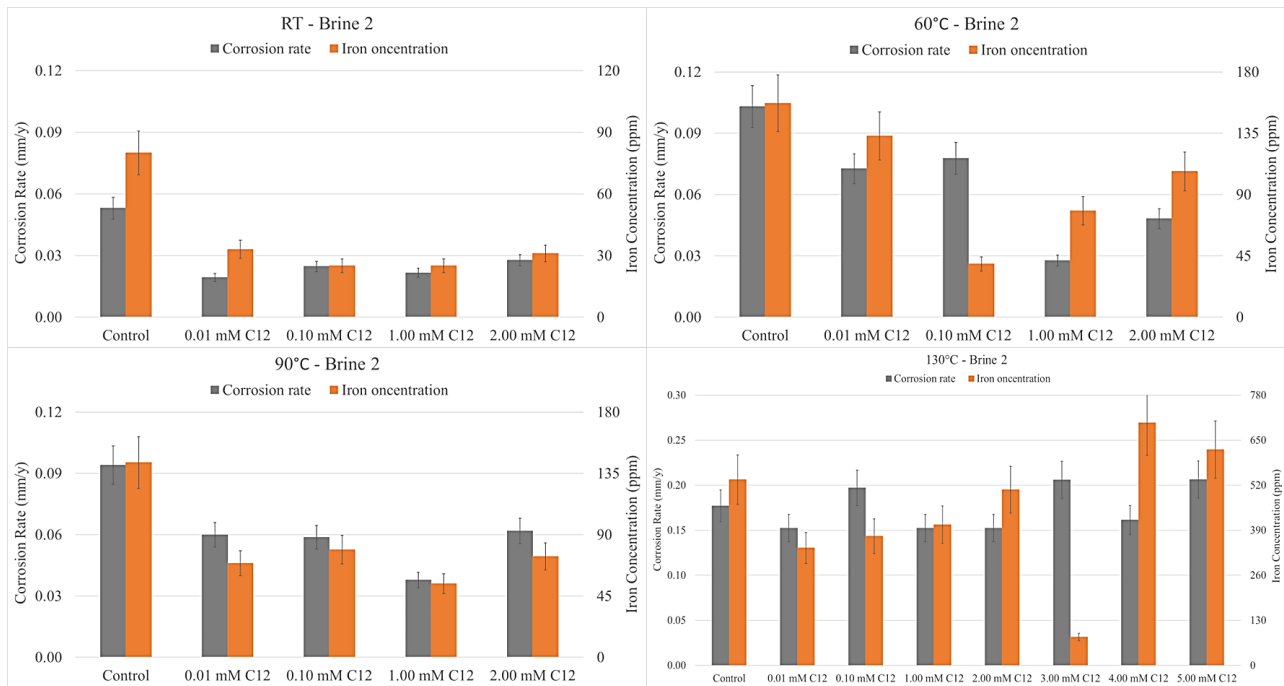

















Figure 4.10. Corrosion experiments in the presence of C12 in Brine 2 at: a. Room temperature (upper left), b. 60 °C (upper right), c. 90 °C (bottom left), and d. 130 °C (bottom right). Color codes: *grey* Corrosion rate and *orange* Iron concentration.

Table 4.12 shows visuals of the specimens from the corrosion experiments in the presence of C12 at RT, 60 °C and 90 °C. At RT, 0.01 mM of C12 present slightly higher anticorrosion efficiency than the rest of the dosages, but the surfaces of the specimens appear less corroded as the concentration increases. Hence, C12 seems to lead to iron dissolution at high concentrations. Regarding the specimens of the experiments at 60 °C and 90 °C, the most effective concentration is 1 mM of C12 and in both cases that is also verified by the appearance of the corresponding specimens. The specimens from the experiments under HP-HT conditions are shown in the Annex.

Table 4.12. Visual representation of the specimens from the experiments of C12 in Brine 2.

	RT	60 °C	90 °C
Control			
0.01 mM			
0.10 mM			
1.00 mM			
2.00 mM			

Upon comparison of the % inhibition efficiencies at RT, the two methods seem to be in agreement, considering their respective experimental errors. The same conclusion is true for the results obtained from experiments at 60 °C and 90 °C, but with a few exceptions. In the case 60 °C for the concentrations 0.01 mM and 0.1 mM for C4 and C6, as well as in the case of 0.1 mM for C12, lower than expected iron levels are observed. Similar is the iron concentration for 1 mM of C2 at 90 °C. In contrast, in most corrosion experiments performed at 130 °C, a substantial deviation between the two methods is observed. Specifically, for the 22 out of 35 experiments performed in total under these conditions, the results show inconsistencies. Unfortunately, no specific trend was established.

Effect of concentration

As mentioned in the Introduction, the behavior of the inhibitors was studied for four different concentrations for the experiments performed at room temperature, at 60 °C and at 90 °C, and for seven different concentrations for the experiments under HP-HT conditions (130 °C). This section discusses the effect of inhibitor concentration, step-by-step from the lowest to the highest. Figure

4.11 shows the fluctuation of corrosion rate values as the concentration of each inhibitor systematically increases.

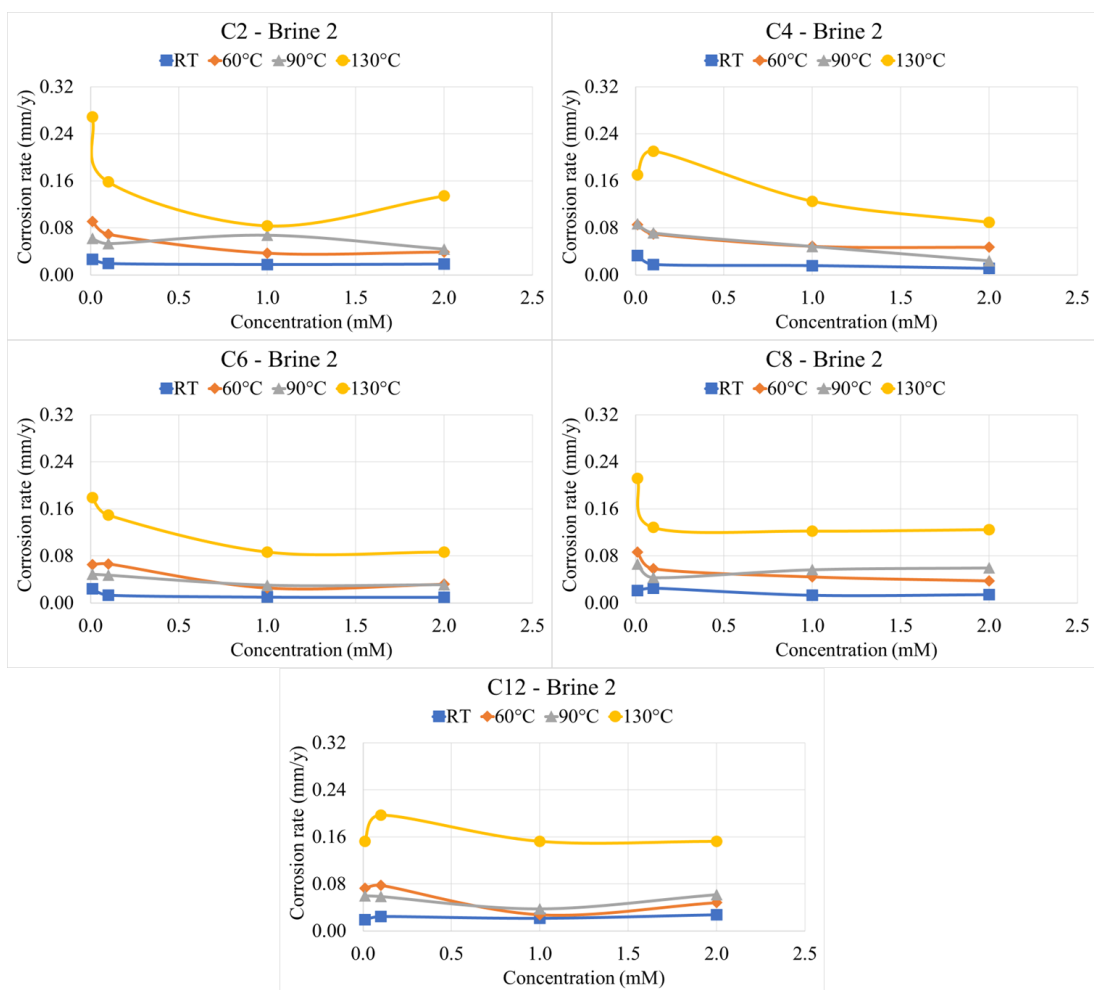


Figure 4.11. Correlation between corrosion rates and inhibitor concentrations in Brine 2. Color codes: *blue* RT, *orange* 60 °C, *grey* 60 °C and *yellow* 130 °C.

In general, when increasing C2 concentration from 0.01 mM to 0.1 mM, lower corrosion rate values are observed. Further dosage increase at RT does not affect corrosion rates, while at 60 °C efficiency is enhanced. At 90 °C, concentration increase from 0.1 mM to 1 mM results in a higher corrosion rate and then, further increase to 2 mM results in lower corrosion rate again. Hence, C2 shows an S-shaped trend in its dosage dependence. At 130 °C, a dosage increase from 0.1 mM to

1 mM results in lower corrosion rates and finally further increase does not significantly affect corrosion rates.

Regarding C4 at RT and 60 °C, an identical behavior to C2 is observed under these conditions. At 90 °C, upon increasing C4 concentration, corrosion rates gradually decrease. At 130 °C, increasing inhibitor concentration from 0.01 mM to 0.1 mM, at first results in higher corrosion rates, and then further increase up to 2 mM, results in a gradual decrease of corrosion rate values. Higher C4 dosages do not enhance its efficiency.

For C6 at RT and 60 °C, similar observations are noted as C2 under these conditions. At 60 °C, increasing the concentration from 0.01 mM 0.1 mM, has no effect on corrosion rate, while an increase up to 1 mM results in lower corrosion rate. Then, at 2 mM of C6, corrosion rate remains almost constant. At 90 °C, 0.01 mM and 0.1 mM of C6 present similar corrosion rate values. Increasing the concentration to 1 mM, results in lower corrosion rate, but a further increase has no additional effect. Finally, at 130 °C, dosage increase from 0.01 mM to 1 mM leads to lower corrosion rates. However, corrosion rate remains constant when the concentration is increased to 2 mM. Further increase does not enhance C6 efficiency.

In the case of C8 at RT, an initial concentration increase results in a higher corrosion rate and then the values decrease. Regarding the experiments at 60 °C, increasing the concentration leads to lower corrosion rate values. At 90 °C, concentration increase from 0.01 mM to 1 mM results in a lower corrosion rate, but then corrosion rate increases for 1 mM, and, finally, remains constant when the concentration is further increased to 2 mM. Lastly, at 130 °C, a concentration increase from 0.01 mM to 1 mM leads to lower corrosion rates. Then, the corrosion rate remains constant upon further concentration increase to 2 mM. Further concentration increase causes a drop in C6 anti-corrosion efficiency.

Regarding C12, at RT, increasing the concentration at first results in a higher corrosion rate but then the values remain essentially constant. At 60 °C and 90 °C, 0.01 mM and 0.1 mM of C12 yield similar corrosion rates. Then, for 1 mM C12 concentration the corrosion rates decrease. Finally, corrosion rates increase for 2 mM of C12. At 130 °C, in general, C12 does not exhibit good inhibitory performance, regardless of the concentration of C12. C12 shows an S-shaped behavior, with lowest values of corrosion rate for 0.01 mM, 1 mM and 2 mM concentrations,

followed by 4 mM. In addition, higher corrosion rates are observed for 0.1 mM, 3 mM and 5 mM inhibitor dosage.

Experiments in the presence of phosphonate inhibitors at higher concentrations (3 mM, 4 mM and 5 mM) at 130 °C (HP-HT conditions) were performed as well. Figure 4.12 shows the results from these experiments, and the lower concentrations as well, for comparison.

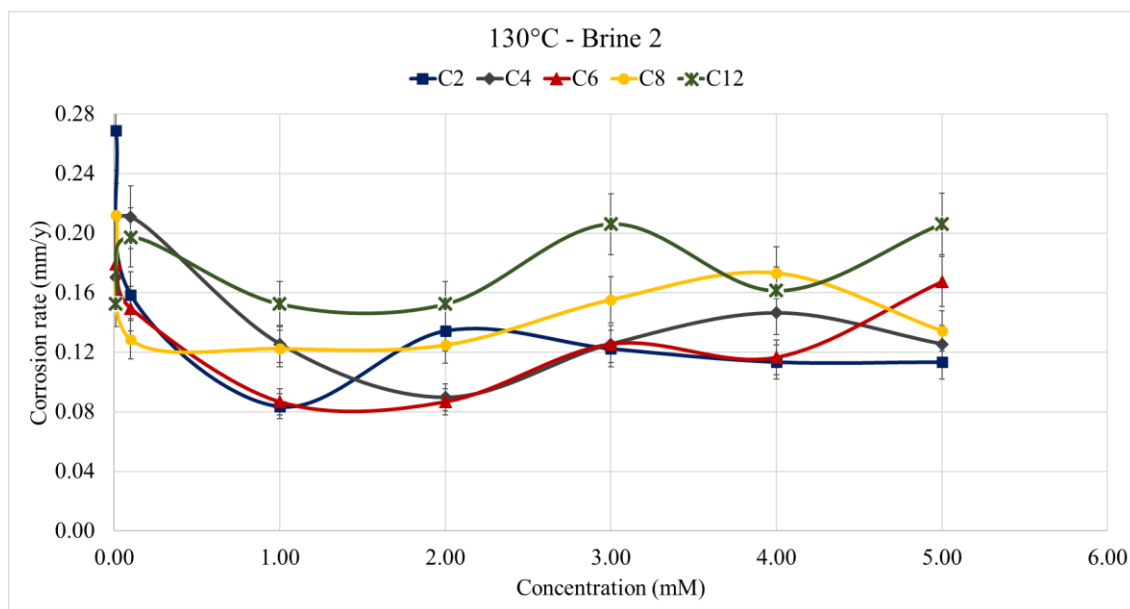


Figure 4.12. The correlation between corrosion rates and inhibitor concentration in Brine 2 at 130 °C. Color codes: *blue* C2, *grey* C4, *red* C6, *yellow* C8 and *green* C12.

The aforementioned results from all corrosion experiments for all inhibitors under these conditions were grouped according to inhibitor concentration at each temperature in an attempt to draw a potential pattern of their behavior.

Experiments performed at RT

- Concentration increase from 0.01 mM to 0.1 mM: an increase in the efficiency of C2, C4 and C6 is noted, while a drop is observed for C8 and C12.

- Concentration increase from 0.1 mM to 1 mM: for C2, C4 and C6 no significant change in the inhibitory efficiency is observed, while C8 showed enhanced performance. On the contrary C12 showed low performance.
- Concentration increase from 1 mM to 2 mM: Small drop in the efficiency of C12, while for the rest of the inhibitors, an almost constant efficiency is observed.

Experiments performed at 60 °C

- Concentration increase from 0.01 mM to 0.1 mM: increasing the concentration is beneficial for C2, C4 and C8, while the efficiency of C6 and C12 does not change.
- Concentration increase from 0.1 mM to 1 mM: the efficiency is enhanced for all of the tetraphosphonate inhibitors.
- Concentration increase from 1 mM to 2 mM: the efficiencies of the inhibitors are kept almost constant, except a drop in the efficiency of C12.

Experiments performed at 90 °C

- Concentration increase from 0.01 mM to 0.1 mM: the efficiency of C2, C4 and C8 is enhanced, while corrosion rate values of C6 and C12 remain constant.
- Concentration increase from 0.1 mM to 1 mM: higher inhibition activities are observed for C4, C6 and C12, while lower ones are noted for C2 and C8.
- Concentration increase from 1 mM to 2 mM: for C6 and C8 corrosion rates remain almost unchanged, while in the case of C2 and C6 the efficiency drops and for C2 and C4 higher inhibition is observed.

Experiments performed at 130 °C

- Concentration increase from 0.01 mM to 0.1 mM: an increase in the anticorrosion performance of C2, C6 and C8 is observed, while a decrease is observed in the case of C4 and C12.
- Concentration increase from 0.1 mM to 1 mM: higher inhibition percentages for all the inhibitors, except C8, where no change in efficiency is noted.

- Concentration increase from 1 mM to 2 mM: The efficiency of C2 drops, while those of C6, C8 and C12 are kept almost unchanged. C4 shows lower corrosion rates.
- Further concentration increase to 3 mM – 4 mM – 5 mM: overall, no enhanced efficiencies are observed.

A very important observation is that inhibitors exhibit lower corrosion rates for 1 mM inhibitor concentration in about half of the cases.

Effect of temperature

In this section, the effect of temperature on the efficiency of each tetraphosphonate will be discussed in detail. Due to different corrosion rate values of the control at different temperatures, the comparisons are based on % inhibition efficiency values. Thus, Figure 4.13 shows the correlation between inhibition efficiencies and temperature, at each inhibitor concentration.

In the case of C4 at 0.01 mM concentration, increasing the temperature, inhibition efficiency gradually decreases. Importantly, for the rest of the phosphonate inhibitors, a pattern similar to the corrosion rates of each temperature is observed. Specifically, as mentioned in Chapter 3, upon temperature increase, the corrosion rate values follow an S-shaped trend, exhibiting the lowest corrosion rate at RT, followed by the corresponding value at 90 °C and then by the value at 60 °C. The highest corrosion rate is reported for T = 130 °C. At 0.1 mM inhibitor concentration, the same conclusion can be reached. Inhibitors exhibit the exact same behavior as at 0.01 mM. At 1 mM inhibitor concentration, when increasing the temperature, the inhibition efficiency decreases for all inhibitors, with two exceptions. First, in the presence of C2 the lowest inhibition is noted at 90 °C, followed by 130 °C. Secondly, in the presence of C12 the highest inhibition is shown at 60 °C, followed by 90 °C and RT. However, the lowest inhibition is observed at 130 °C, as for most of the members of the tetraphosphonate family. At 2 mM inhibitor concentration, increasing the temperature in the case of C2, C6 and C8, inhibition efficiency decreases. The behavior of C4 follows the same pattern as that of the corrosion rates at the different temperatures. Finally, in the presence of C12, the highest inhibition is shown at 60 °C, followed by RT and 90 °C. The lowest inhibition is observed at 130 °C, as for the rest of the inhibitors under these conditions. Overall,

corrosion experiments carried out at 130 °C represent the “worst case” scenario for all inhibitors, with the sole exception of 1 mM of C2. The inhibitors exhibit the highest anticorrosion efficiency at RT, except for the two highest concentrations of C12. In general, for 1 mM and for 2 mM inhibitor concentration, the phosphonates presented lower inhibition as the temperature increased, while for the lower dosages, most of the inhibitors showed the familiar S-shaped trend.

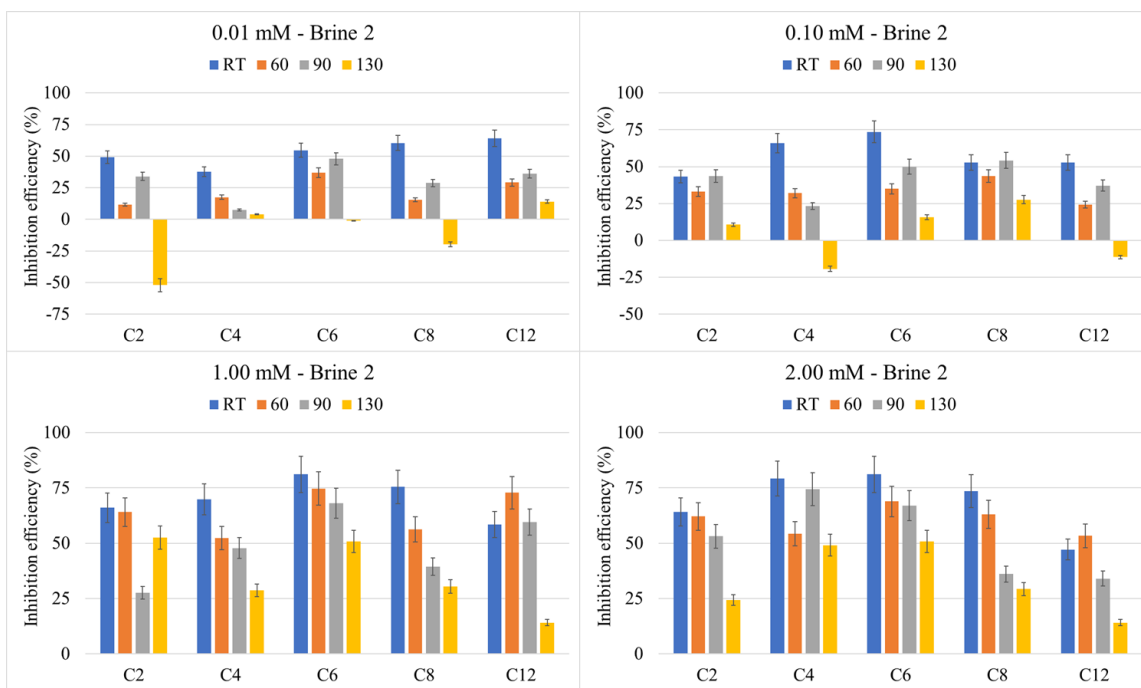


Figure 4.13. Correlation between % inhibition efficiency and temperature for all tetraphosphonate inhibitors in Brine 2 for concentrations: a. 0.01 mM (upper left), b. 0.10 mM (upper right), c. 1 mM (bottom left) and d. 2 mM (bottom right). Color codes: *blue* RT, *orange* 60 °C, *grey* 60 °C and *yellow* 130 °C.

Effect of inhibitor molecular size

A structural feature of this family of tetraphosphonate inhibitors is the systematically elongated carbon (polymethylene) chain connecting the two N atoms on each side of the molecule. In other words, as we visualize the structures of these inhibitors, moving from C2 up to C12, the length (or the size) of the molecule increases. In the following section, we attempt to correlate the length of the carbon chain between the amine groups with the efficiency of the corresponding inhibitor. Hence, the values of corrosion rates are presented in comparison with the number of carbon atoms

contained in the structure of each phosphonate inhibitor. In addition, iron concentrations of the respective experiments are presented as well. Zero carbon atoms represent the respective control corrosion experiments.

Figure 4.14 refers to the experiments performed at RT. Regarding the lowest concentration of 0.01 mM, lower corrosion rates are observed as the number of carbon atoms on the linker increases, except C4 in the presence of which the highest corrosion rate under these conditions is noted. For the 0.1 mM inhibitor dosage, lower corrosion rates are observed as the size of the inhibitor increases from C2 to C6. Then, upon size increase for C6 and C12, the values are still lower than C2. Increasing the concentration to 1 mM and to 2 mM, lower corrosion rates are observed, upon an increase of the inhibitor size, from C2 to C6. Then, corrosion rates increase for C8 and C12. C12 is the least effective inhibitor under these conditions. These results are also confirmed by the iron measurements.

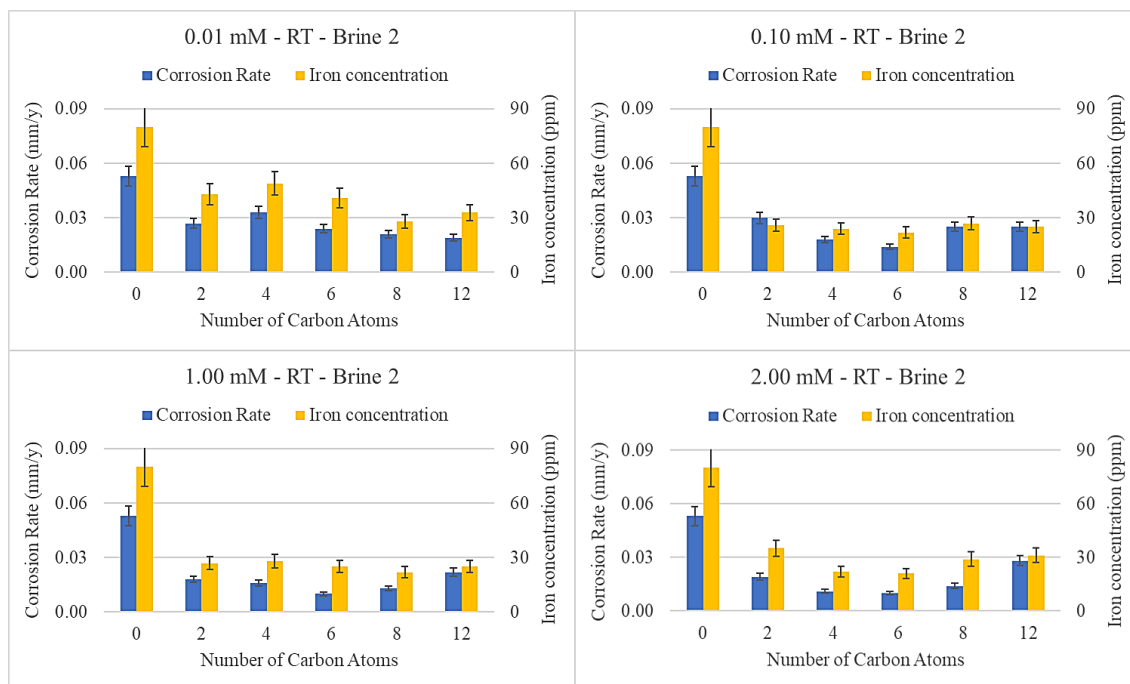


Figure 4.14. Correlation between the number of carbon atoms on the polymethylene linker of each phosphonate inhibitor and the results obtained from the corrosion experiments performed at RT in Brine 2.

Figure 4.15 refers to the experiments performed at 60 °C. Regarding the lowest concentration of 0.01 mM, increasing the number of carbon atoms from 2 to 6, lowers the corrosion rate values. For C8, the corrosion rate is higher, still lower than that for C2. Finally, in the case of C12 the corrosion rate drops, however, it is not lower than that for C6. For 0.1 mM inhibitor concentration, C2, C4 and C6 present similar corrosion rates. For C8, the corrosion rate decreases and then increases in the present of C12, the latter being the least effective inhibitor. For 1 mM inhibitor concentration, C4 and C8 show similar low corrosion rates, followed by C2, showing slightly increased values. Finally, C6 and C12 show the highest corrosion rates. The most efficient inhibitor is C6 and the least efficient is C4. For 2 mM inhibitor concentration, corrosion rate values increase as the number of carbon atoms increases from 2 to 4, but then decreases for 6 carbons and finally increases again in the range of 6 to 12 carbons. C12 is the least effective inhibitor under these conditions. Regarding the iron determination test, in general, iron concentrations follow the same pattern as the corrosion rate trend, with a few exceptions concerning the lowest concentration of all the inhibitors, 0.1 mM of C4, C6 and C12, and 1 mM and 2 mM of C12.

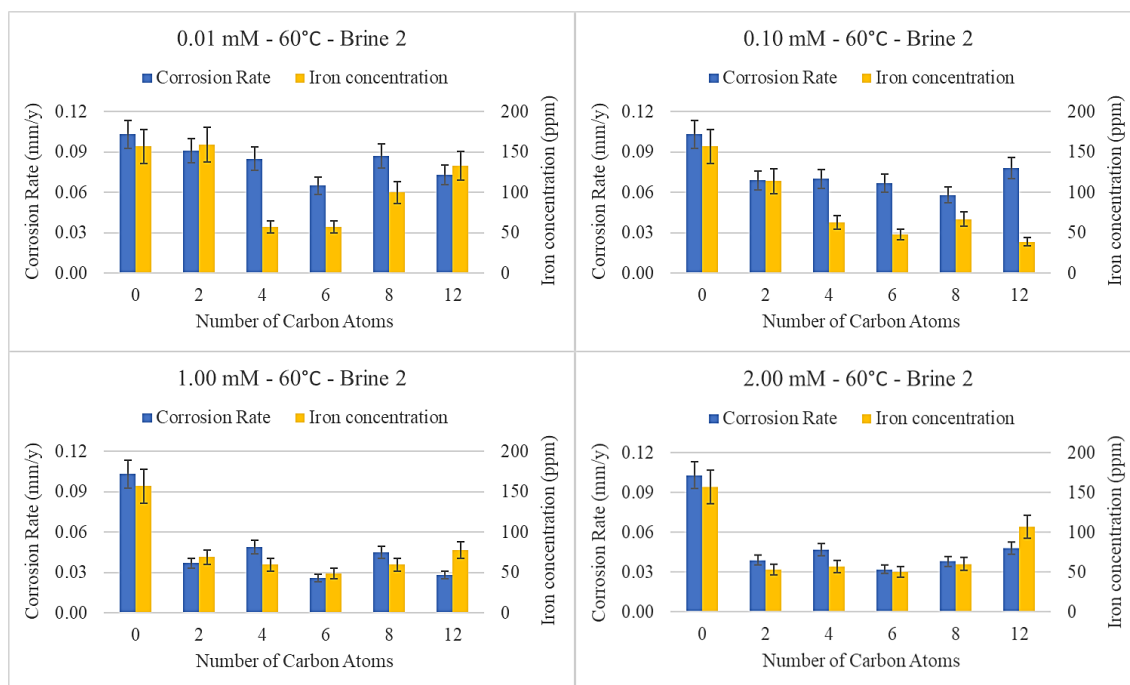


Figure 4.15. Correlation between the number of carbon atoms on the polymethylene linker of each phosphonate inhibitor and the results obtained from the corrosion experiments performed at 60 °C in Brine 2.

Figure 4.16 refers to the experiments performed at 90 °C. Regarding the lowest concentration of 0.01 mM, the corrosion rate increases as the number of carbon atoms increases from 2 to 4, decreases for 6 carbons, increases again for 8 carbons and finally decreases again for 12 carbons. The most effective inhibitor is C6, while the least effective inhibitor is C4. For 0.1 mM inhibitor dosage, corrosion rate increases as the number of carbon atoms increases from 2 to 4, decreases from 4 to 8 carbons and finally increases again for 12 carbons. The most effective inhibitor is C8, while the least effective inhibitor is C4. For the 1 mM inhibitor dosage, corrosion rate decreases as the number of carbon atoms increases from 2 to 6, decreases for 6 carbons, increases for 8 carbons and finally decreases again for 12 carbons. The most effective inhibitor is C6, while the least effective inhibitor is C2. For the 2 mM inhibitor dosage, corrosion rate increases as the number of carbon atoms increases from 2 to 4, decreases from 4 to 8 carbons and finally remains essentially unchanged for 12 carbons. Regarding the iron determination test, in general, iron concentrations follow the same pattern as that of the corrosion rate, with a few exceptions concerning 0.1 mM of C4, 1 mM of C2 and 2 mM of C8.

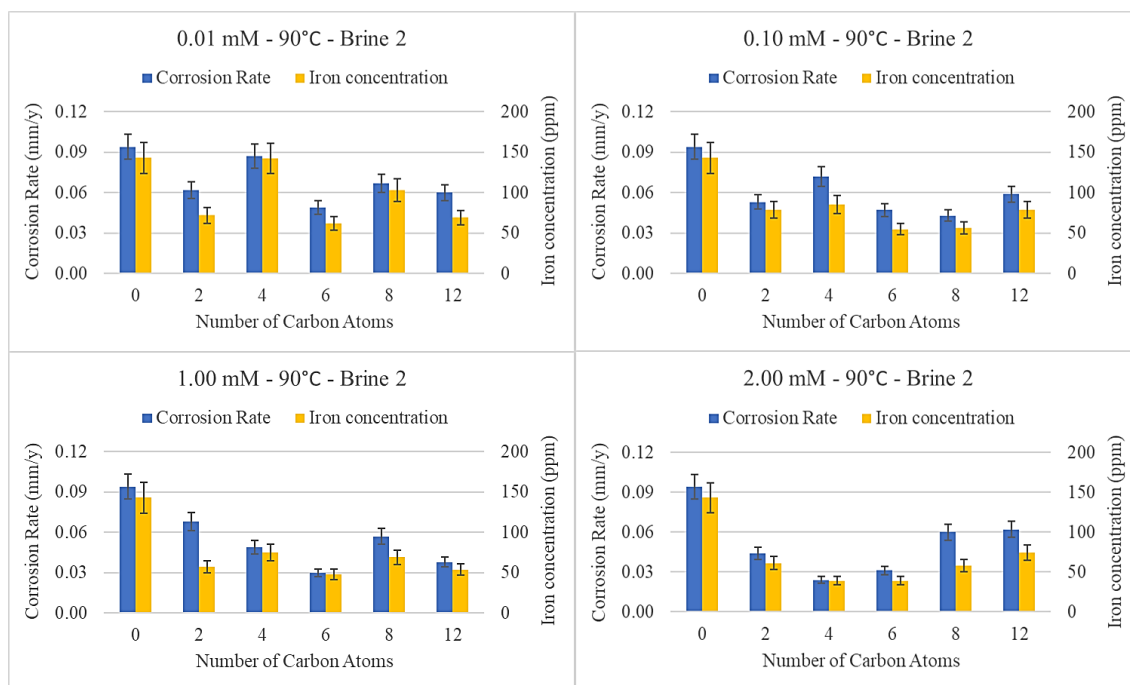


Figure 4.16. Correlation between the number of carbon atoms on the polymethylene linker of each phosphonate inhibitor and the results obtained from the corrosion experiments performed at 90 °C in Brine 2.

Figure 4.17 refers to the experiments performed at 60 °C. Regarding the lowest concentration of 0.01 mM, corrosion rate decreases as the number of carbon atoms increases from 2 to 4, then remains almost constant for 6 carbons, then increases again for 8 carbons and finally decreases again for 12 carbons. The most effective inhibitor is C12, while the least effective inhibitor is C2. For the 0.1 mM inhibitor dosage, corrosion rate increases as the number of carbon atoms increases from 2 to 4, decreases from 4 to 8 carbons and finally increases again for 12 carbons. The most effective inhibitor is C8, while the least effective inhibitor is C4. For the 1 mM inhibitor dosage, corrosion rate decreases as the number of carbon atoms increases from 2 to 4, decreases for 6 carbons, then decreases for 6 carbons, and finally increases as the number of carbon atoms increases from 6 to 12. The two most effective inhibitors are C2 and C6, while the least effective inhibitor is C12. For the 2 mM inhibitor dosage, corrosion rate decreases as the number of carbon atoms increases from 2 to 4, then remains almost constant for 6 carbons, and finally increases as the number of carbon atoms increases from 6 to 12. The two most effective inhibitors are C4 and C6, while the least effective inhibitor is C12. Unfortunately, a discrepancy between the results of the gravimetric measurements and the iron determination test results is observed. Specifically, at lower inhibitor concentrations, lower iron concentrations than expected are noted. On the contrary, higher iron concentrations comparing to the respective corrosion rate values are observed for higher inhibitor dosages.

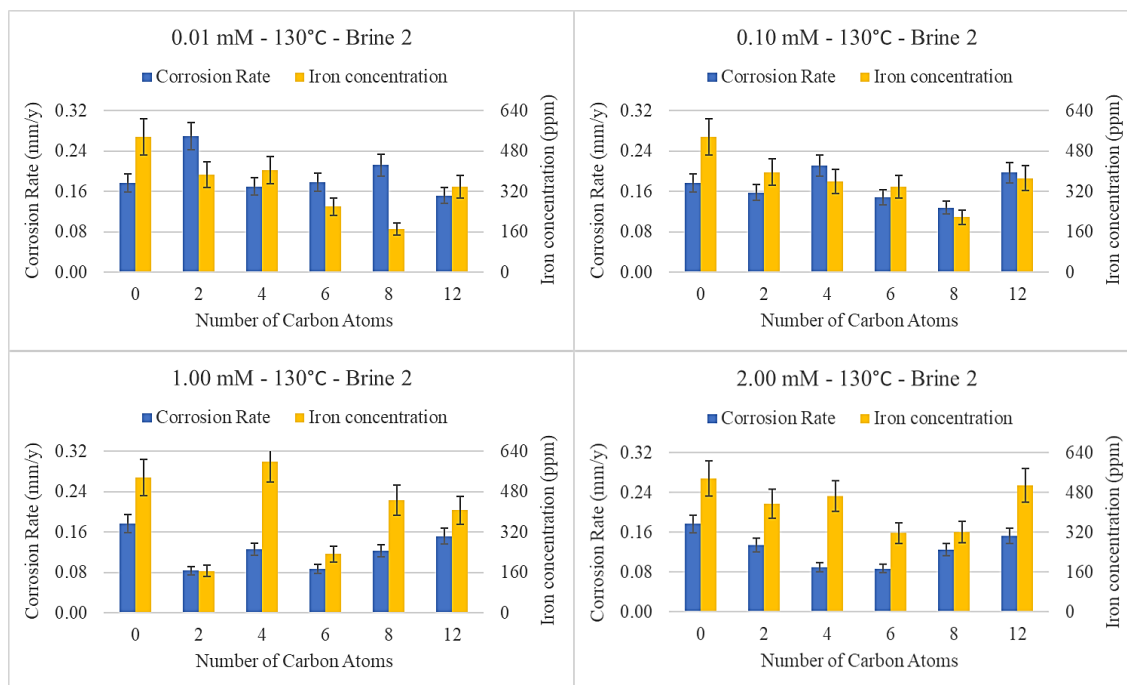


Figure 4.17. Correlation between the number of carbon atoms on the polymethylene linker of each phosphonate inhibitor and the results obtained from the corrosion experiments performed at 130 °C in Brine 2.

4.2.2 Non-phosphonate inhibitors

This section presents the results of the experiments performed in the presence of non-phosphonate inhibitors in Brine 2 at three temperatures (RT, 60 °C and 90 °C) for two inhibitor concentrations (100 ppm and 250 ppm). The necessary inhibitor solutions were prepared by diluting the desired volumes of the corresponding inhibitor stock solutions in DI water, followed by pH adjustment to 7, if needed. The total volume of each working solution was 120 mL. Corrosion rate values obtained from the experiments performed under these conditions, as well as the calculated % inhibition efficiencies, categorized by inhibitor concentration, are presented in Table 4.13 and Table 4.14.

Table 4.13. Corrosion rates, iron concentrations and inhibition efficiency percentages based on both methods for 100 ppm of non-phosphonate inhibitors in Brine 2.

T (°C)	RT		60		90	
	CR (mm/y)	Fe (ppm)	CR (mm/y)	Fe (ppm)	CR (mm/y)	Fe (ppm)
<i>Control</i>	0.053	80	0.103	157	0.094	143
SLD	0.037 30 %	69 14 %	0.046 56 %	81 48 %	0.087 7 %	180 - 26 %
ACAB	0.035 34 %	66 18 %	0.074 28 %	88 44 %	0.084 10 %	192 - 34 %
DLD	0.047 11 %	92 - 15 %	0.060 41 %	123 22 %	0.063 32 %	182 - 27 %
HAD	0.030 43 %	41 49 %	0.048 53 %	110 30 %	0.066 30 %	90 37 %

Table 4.14. Corrosion rates, iron concentrations and inhibition efficiency percentages based on both methods for 250 ppm of non-phosphonate inhibitors in Brine 2.

T (°C)	RT		60		90	
	CR (mm/y)	Fe (ppm)	CR (mm/y)	Fe (ppm)	CR (mm/y)	Fe (ppm)
<i>Control</i>	0.053	80	0.103	157	0.094	143
SLD	0.035 34 %	71 11 %	0.055 47 %	76 52 %	0.053 44 %	110 23 %
ACAB	0.034 36 %	68 15 %	0.112 - 9 %	140 11 %	0.121 - 28 %	241 - 69 %
DLD	0.049 8 %	121 - 51 %	0.088 14 %	142 10 %	0.081 13 %	148 - 3 %
HAD	0.029 46 %	60 25 %	0.054 47 %	106 32 %	0.076 20 %	75 48 %

Figure 4.18 presents bar graphs of the results from corrosion experiments in the presence of non-phosphonate inhibitors at RT. HAD exhibits the lowest corrosion rates at both concentrations, 43 % inhibition for 100 ppm and 46 % inhibition for 250 ppm, followed by ACAB with 34 % and 36 % inhibition, respectively, and SLD with 30 % and 34 % inhibition, respectively. It appears that, overall, DLD is the least effective inhibitor under these conditions, showing only 11 % and 8 % inhibition for the 100 ppm and 250 ppm dosage, respectively. Regarding iron determination method, all inhibitors except HAD, seem to present higher iron concentrations, compared to the corresponding corrosion rates for both inhibitor concentrations.

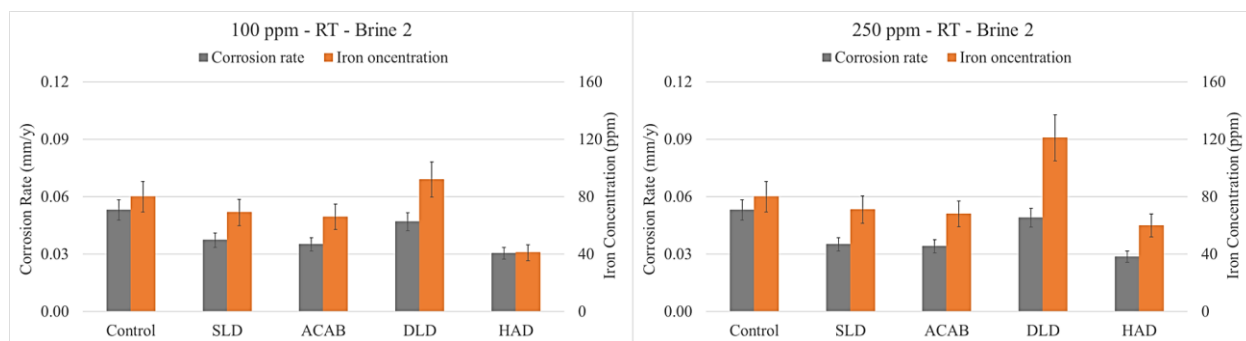


Figure 4.18. Corrosion experiments in the presence of non-phosphonate inhibitors in Brine 2 at RT. (left) 100 ppm and (right) 250 ppm. Color codes: *grey* Corrosion rate and *orange* Iron concentration.

Figure 4.19 presents the results of the corrosion experiments in the presence of non-phosphonate inhibitors at 60 °C. SLD exhibits the lowest corrosion rates at both concentrations, with 56 % (100 ppm) and 47 % (250 ppm) inhibition, followed by HAD with 53 % and 47 % inhibition, respectively, and DLD with 41 % and 14 % inhibition, respectively. ACAB is the least effective inhibitor under these conditions, with 28 % inhibition for 100 ppm dosage and, interestingly, for the 250 ppm dosage ACAB presents a higher corrosion rate than the respective control experiment. Based on the iron determination method, DLD and HAD show higher iron concentrations, compared to the corresponding corrosion rates for both inhibitor concentrations.

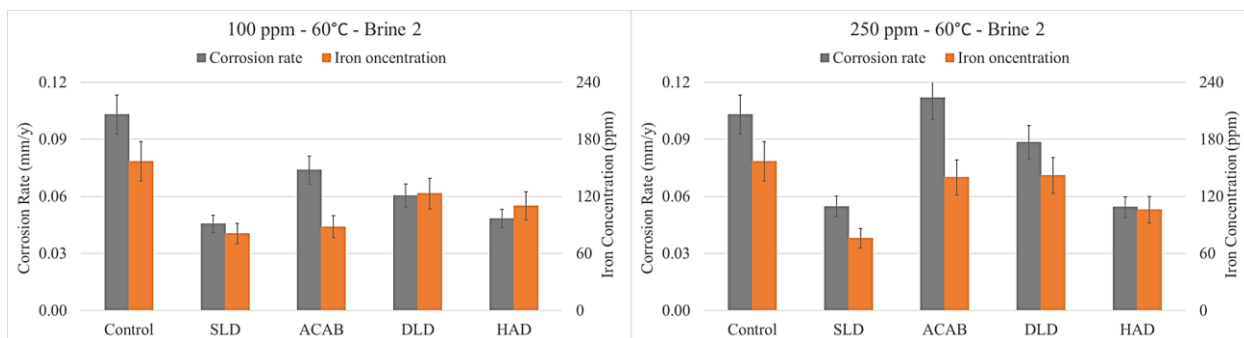


Figure 4.19. Corrosion experiments in the presence of non-phosphonate inhibitors in Brine 2 at 60 °C. (left) 100 ppm and (right) 250 ppm. Color codes: *grey* Corrosion rate and *orange* Iron concentration.

Figure 4.20 presents the results of corrosion experiments in the presence of non-phosphonate inhibitors at 90 °C. For 100 ppm inhibitor dosage, DLD shows the lowest corrosion rates (32 % inhibition), followed by HAD (30 % inhibition). ACAB and SLD show similar corrosion rates, with 10 % and 7 % inhibition, respectively. For the 250 ppm dosage, SLD is the most effective inhibitor, 44 % inhibition, followed by HAD, 20 % inhibition. DLD induces 13 % inhibition, while ACAB (similarly to 60 °C) shows higher corrosion rates than the control. Based on the iron determination method, HAD (at 250 ppm) shows lower iron concentrations than expected, while the rest of the inhibitors give lower iron concentrations at both concentrations.

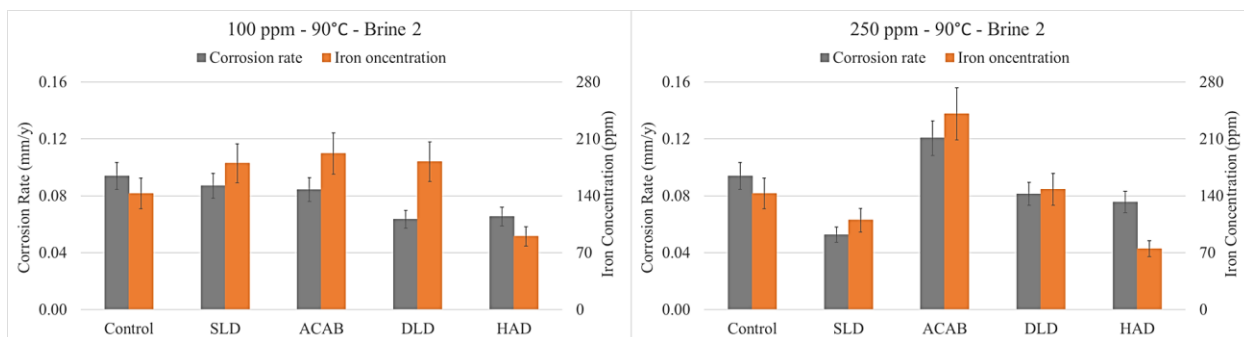


Figure 4.20. Corrosion experiments in the presence of non-phosphonate inhibitors in Brine 2 at 90 °C. (left) 100 ppm and (right) 250 ppm. Color codes: *grey* Corrosion rate and *orange* Iron concentration.

Visuals of the glass bottles with the steel specimens of the corrosion experiments in the presence of non-phosphonate inhibitors at the end of the experimental period are presented in Figure 4.21. Overall, visual observations are in agreement with the corresponding results of the gravimetric and iron measurements.

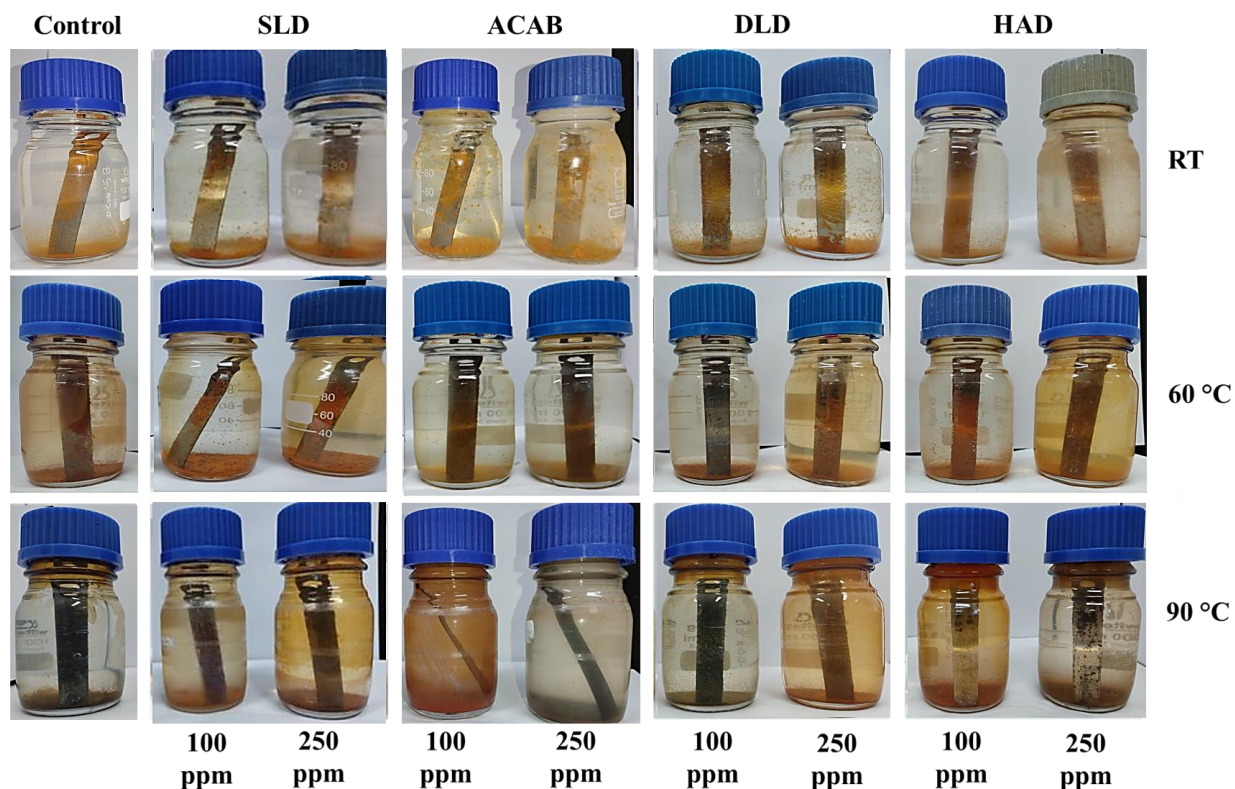


Figure 4.21. Visual representation of the experiments in the presence of non-phosphonate inhibitors in Brine 2 at RT, 60 °C and 90 °C.

Effect of concentration

Figure 4.22 presents a correlation between concentration and corrosion rate values obtained in the presence of each inhibitor at RT, 60 °C and 90 °C. For all inhibitors at RT, an increase in inhibitor concentration does not affect their efficiency. The same conclusion is valid for the experiments in the presence of SLD and ACAB at 60 °C. In the case of DLD and ACAB, increasing the dosage results in higher corrosion rates. At 90 °C, DLD, HAD and ACAB present higher

corrosion rates when the concentration is increased, while in the case of SLD the efficiency is enhanced.

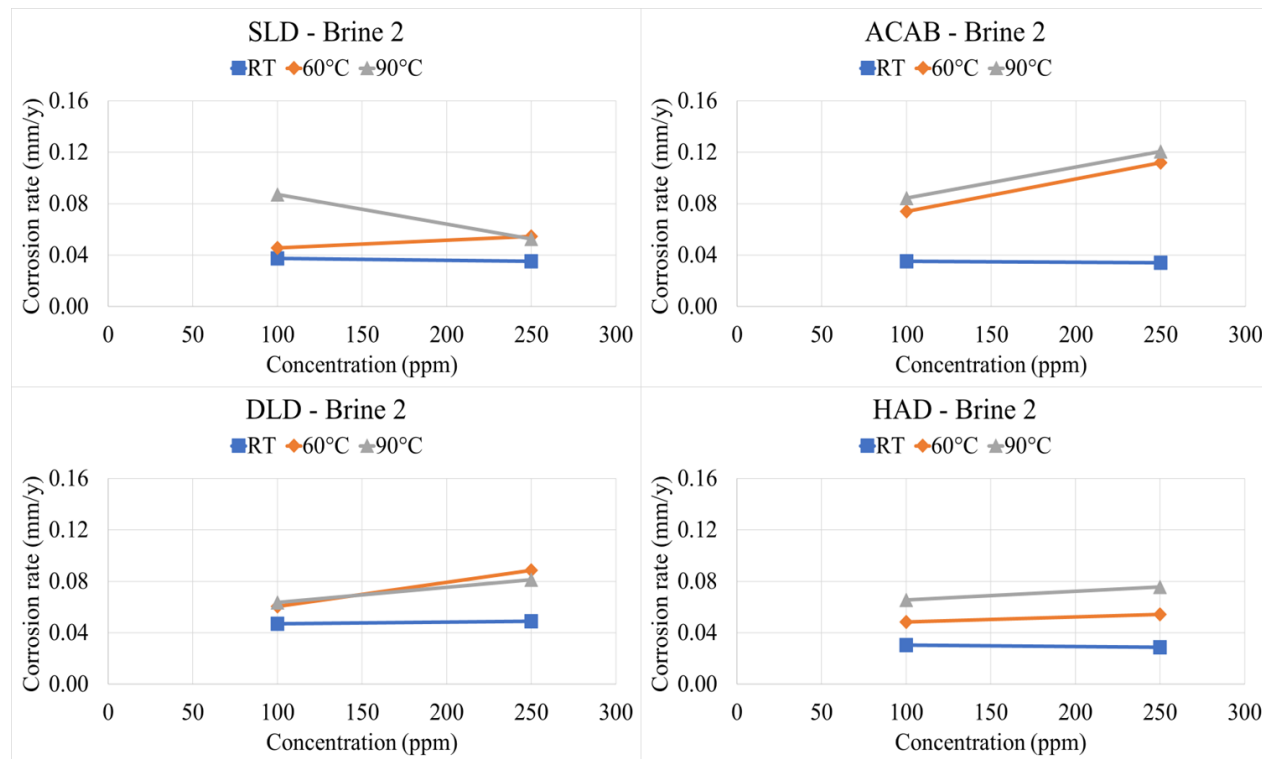


Figure 4.22. The correlation between corrosion rates and inhibitor concentration for non-phosphonates in Brine 2. Color codes: *blue* RT, *orange* 60 °C and *grey* 90 °C.

In addition, corrosion experiments at RT were performed, in the presence of several non-phosphonate inhibitors of different concentrations. Figure 4.23 focuses on the correlation between corrosion rates and inhibitor concentration under these conditions. It should be noted that, in some cases, corrosion rates of different inhibitors are exactly the same or very close and they are not clearly visible in the graph. Therefore, Table 4.15 can be used to show the corrosion rates more clearly.

Upon increasing SLD concentration from 25 ppm to 250 ppm, gradually lower corrosion rate values are observed. The inhibition efficiency, from -27 % at the lowest concentration, reaches 34 % for 250 ppm and then drops to 9 % for 500 ppm. In the case of ACAB, in general, the same

pattern is observed, ie. inhibition starts from -15 % at 25 ppm concentration and increases to 36 % at 250 ppm, although for 500 ppm it again drops to -25 %. The increase in concentration does not significantly affect the performance of the remaining non-phosphonate inhibitors, and higher corrosion rates than the respective control values observed in all cases.

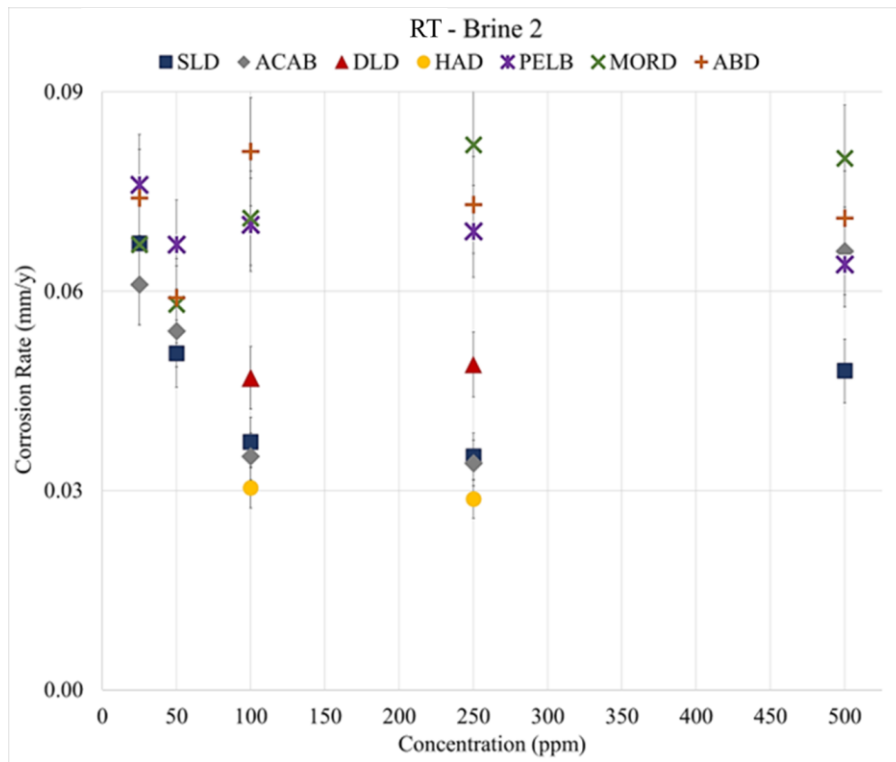


Figure 4.23. The correlation between corrosion rates and inhibitor concentration for non-phosphonate inhibitors in Brine 2, at RT. Color codes: *blue* SLD, *grey* ACAB, *red* DLD, *yellow* HAD, *purple* PELB, *green* MORD and *brown* ABD.

Table 4.15. Corrosion rates obtained in the presence of non-phosphonate inhibitors.

Inhibitor	Concentration (ppm)				
	25	50	100	250	500
	Corrosion Rates (mm/y)				
SLD	0.067	0.051	0.037	0.035	0.048
ACAB	0.061	0.054	0.035	0.034	0.066
DLD	-	-	0.047	0.049	-
HAD	-	-	0.030	0.029	-
PELB	0.076	0.067	0.070	0.069	0.064
MORD	0.067	0.058	0.071	0.082	0.080
ABD	0.074	0.059	0.081	0.073	0.071

Effect of temperature

Figure 4.24 presents the correlation between temperature and corrosion rate values obtained in the presence of each inhibitor, at the dosages of 100 ppm and 250 ppm. At 100 ppm inhibitor dosage, the temperature of 60 °C is the most favorable one for SLD and HAD, followed by RT, and then 90 °C. In the case of DLD, temperature increase from 60 °C to 90 °C leads to lower inhibition efficiency. At RT its efficiency reaches a minimum. ACAB demonstrates lower % inhibitory efficiency as the temperature increases at both inhibitor concentrations. For the 250 ppm dosage, SLD and DLD present slightly higher inhibition at 60 °C than at 90 °C, while at RT their efficiency is even lower. Finally, HAD presents slightly higher inhibition at 60 °C than at RT, while at 90 °C a significant drop in efficiency is noted.

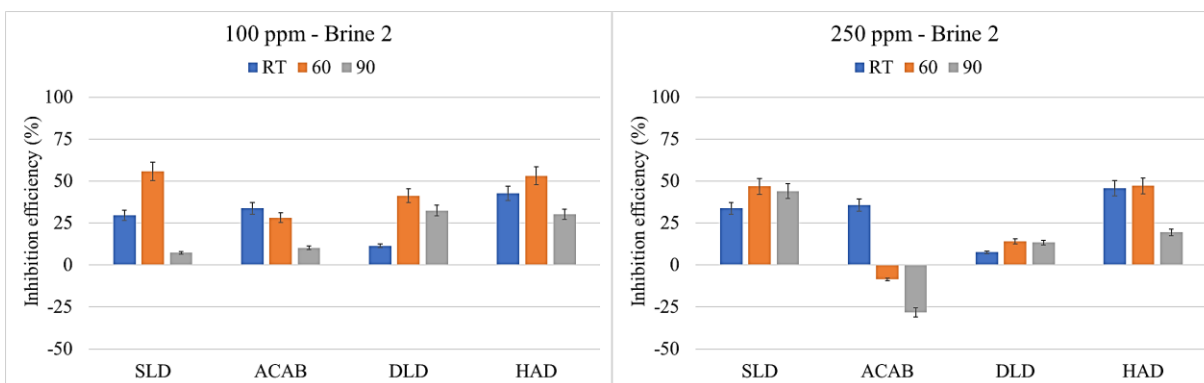


Figure 4.24. The correlation between corrosion rates and temperature for non-phosphonate inhibitors in Brine 2 for concentrations a. 100 ppm (left) and b. 250 ppm (right). Color codes: *blue* RT, *orange* 60 °C and *grey* 90 °C.

Effect of mechanical stirring

Corrosion experiments under stirring were performed at RT in large glass bottles of total experiment volume 1200 mL. In this case, the specimens did not rest at the bottom of the bottle, in order to avoid any contact with the magnetic stirrer. Two different stirring rates were selected (200 rpm and 400 rpm). The same experiments were also performed under the same conditions and with the same experimental set-up under non-stirring conditions. The dosage of each inhibitor was 100 ppm.

Figure 4.25 shows the corrosion rates and the % inhibition of three different inhibitors. It is worth mentioning that increasing the stirring rate results in higher corrosion rates of the control experiments. Overall, it is observed that the three inhibitors tested under these conditions exhibit three different behaviors. For HAD, the highest inhibition is observed at static conditions, followed by the experiments at 400 rpm stirring rate. The lowest inhibition is observed at 200 rpm. In the case of SLD, the best performance is demonstrated in experiments at 200 rpm, followed by that at non-stirring conditions. Finally, the lowest inhibition is observed for the experiments at 400 rpm stirring rate. Regarding ACAB, the best inhibition efficiency is observed at the highest stirring rate. On the contrary, the lowest inhibition efficiency is noted for the experiments performed at 200 rpm.

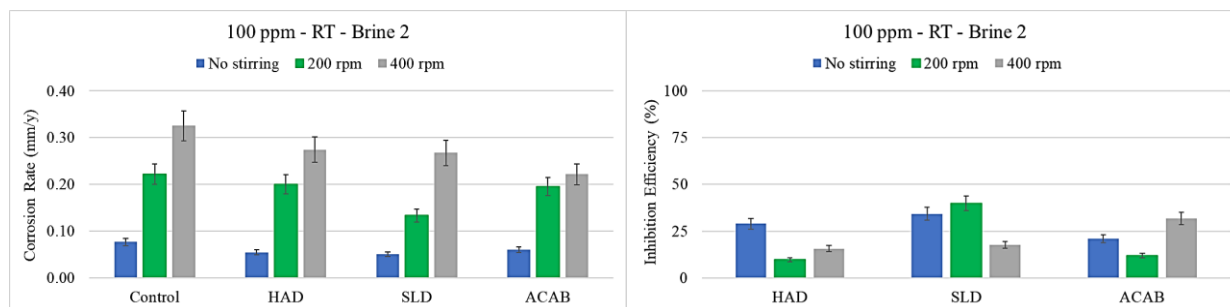


Figure 4.25. The correlation between corrosion rates and stirring rates (left) and % inhibition efficiency and stirring rates (right) for the non-phosphonate inhibitors in Brine 2 at RT. Color codes: *blue* no stirring, *green* 200 rpm and *grey* 400 rpm.

The glass bottles with the carbon steel specimens in the presence of the various non-phosphonate inhibitors at the end of the experimental period are presented in Figure 4.26. Precipitates are visible at the bottom of the containers in the static experiments. In addition, it is observed that in many cases the orange-colored solutions (indicative of high iron levels), do not necessarily mean low performance. For example, SLD exhibits its highest corrosion inhibition at 200 rpm, despite the fact that higher iron concentration is observed in the respective solution than the rest of the experiments in the presence of SLD.

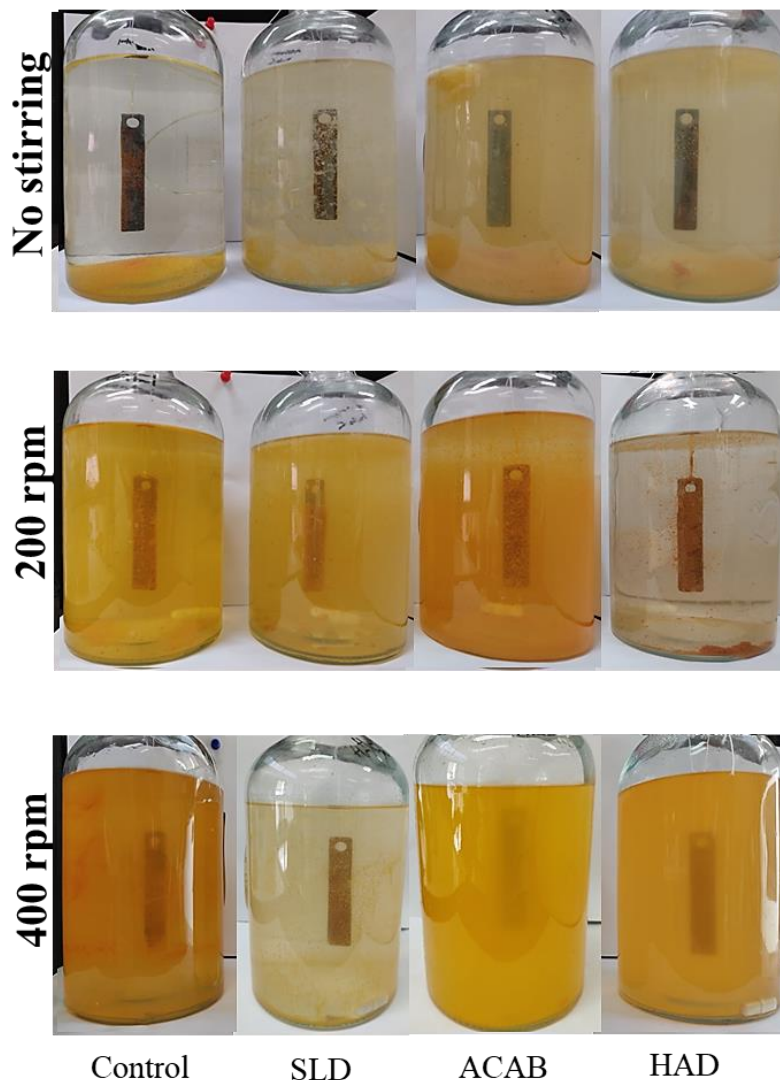


Figure 4.26. Visual representation of the experiments at different stirring rates, as shown.

Effect of sulfides

Corrosion experiments in the presence of sulfides were performed at RT. Two types of experiments were performed, in order to observe corrosion aggressiveness and inhibitor performance, both in the presence and in the absence of dissolved oxygen, along with the presence of sulfides. Thus, in addition to the experiments in glass bottles with caps, experiments were performed under argon atmosphere as well. In order to remove the oxygen from the solution inside the flask, degassing was performed before each experiment for at least 30 minutes, by bubbling

argon. Sulfides were quantified, before and after the experiments, with the methylene blue method (see Chapter 2.3). Figure 4.27 gives the results of corrosion experiments in the presence of 50 ppm sulfides (expressed as 50 ppm S^{2-}), for three different inhibitors at concentrations 100 ppm and 250 ppm.

In the presence of both oxygen and sulfides in the solution, higher corrosion rates are observed compared to those under argon atmosphere. In the presence of oxygen, for 100 ppm inhibitor concentration, HAD appears to be the most effective inhibitor, followed by SLD, while ACAB shows higher corrosion rates than the respective control. For 250 ppm, the same conclusion can be reached, although ACAB shows a similar corrosion rate to that for the control.

Under argon atmosphere, HAD exhibits the best performance for the protection of carbon steel, regardless of its concentration. For the 100 ppm dosage, the second most effective inhibitor is ACAB. For 250 ppm, the second most effective inhibitor is SLD. ACAB presents a higher corrosion rate than the control under these conditions.

The glass bottles with the specimens of the corrosion experiments in the presence of non-phosphonate inhibitors at the end of the experimental period are presented in Figure 4.28. Visual observations agree with the corresponding corrosion rates. In the presence of oxygen HAD produced green colored solutions under argon atmosphere, however the surfaces of the specimens appear to be “clean” from iron deposits. As mentioned in Chapter 3, this color is a strong indication of Fe(II) formation. In the case of ACAB, green solutions in combination with visible precipitates under both atmospheres are noticed. Finally, for the experiments in the presence of SLD, precipitates are observed, especially under argon atmosphere.

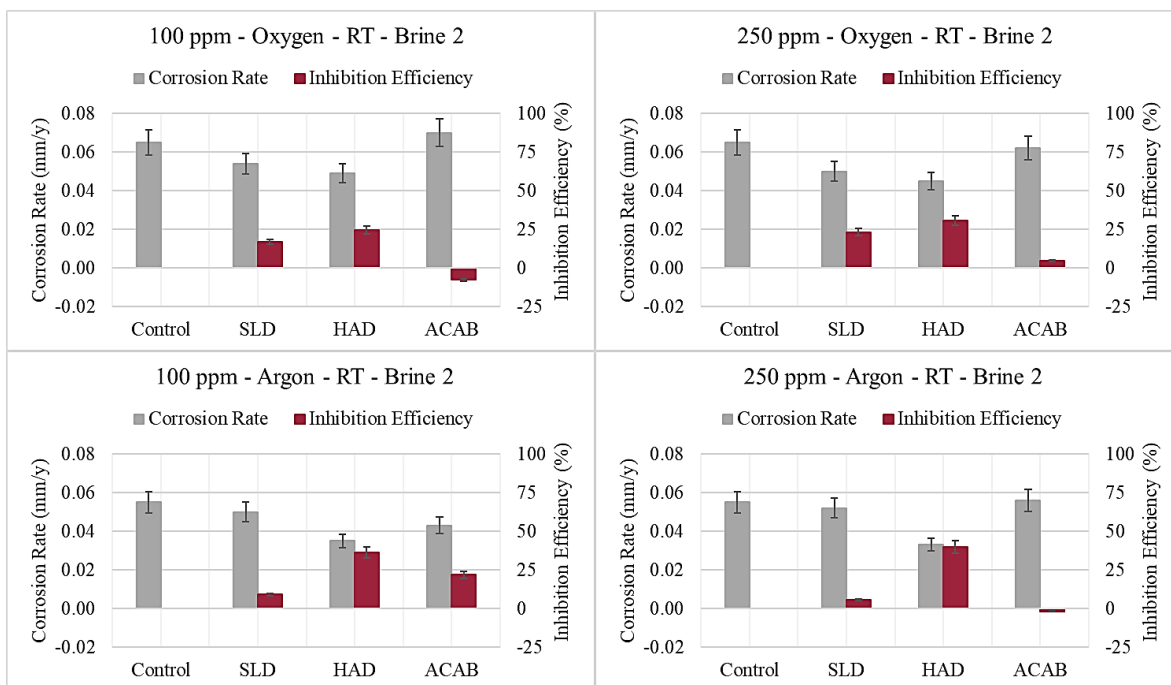


Figure 4.27. Results obtained in the absence (control) and presence of non-phosphonate inhibitors in DI water at RT in the presence of 50 ppm S^{2-} for: a. 100 ppm inhibitor concentration under oxygen (upper left), b. 250 ppm inhibitor concentration under oxygen (upper right), c. 100 ppm inhibitor concentration under argon (bottom left) and d. 100 ppm inhibitor concentration under argon (bottom right). Color codes: Corrosion rates *grey* and % inhibition efficiency *burgundy*.

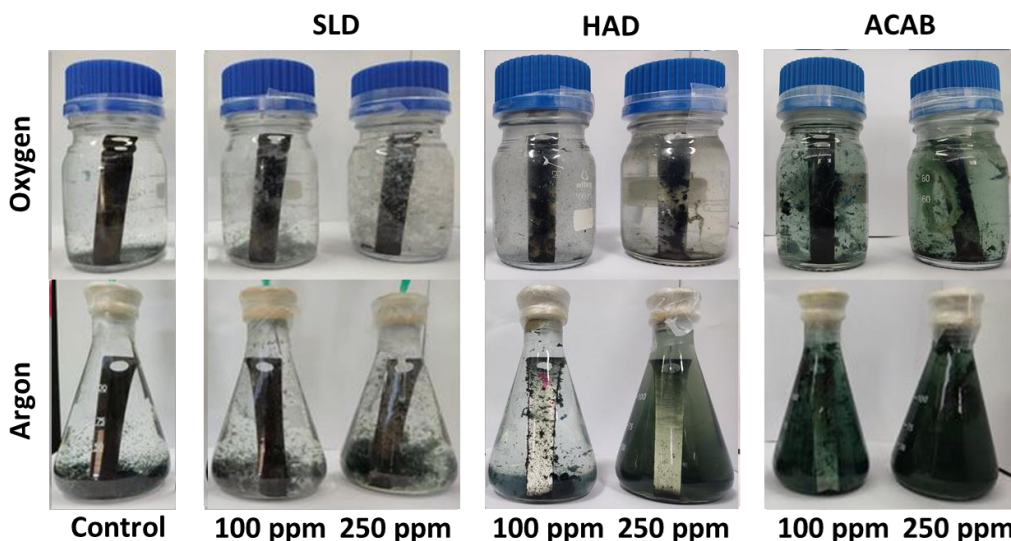


Figure 4.28. Visual representation of the experiments in the presence of sulfides.

4.3 Concluding remarks

4.3.1 Phosphonate inhibitors

In this chapter, corrosion experiments were performed in artificial Brine 2 at pH 7. The anticorrosion efficiency of the inhibitors was examined at different temperatures and at several inhibitor concentrations. Their performance was evaluated by gravimetric measurements, according to the NACE standard method ^[9]. Comparing the % inhibition values between the two methods, the results of the colorimetric method of total iron determination showed a deviation from the results based on mass loss in several cases, however the differences were less significant in this water quality (Brine 2) than in artificial Brine 1 and in DI water.

Overall, phosphonate inhibitors appear to be more efficient anti-corrosion agents under these conditions as their concentrations in solution increase. The corrosion experiments at HP-HT conditions (130 °C) are an exception to the aforementioned conclusion. Specifically, 2 mM of C4, 1 mM and 2 mM of C6, 0.1 mM, 1 mM and 2 mM of C8, and 0.1 mM, 1 mM and 2 mM of C12 are the most beneficial concentrations among the seven different inhibitor dosages tested. In addition, C12 seems to perform optimally at 1 mM concentration at 60 °C and 90 °C, while at RT C12 presents similar % inhibition regardless of its concentration. A universal correlation between inhibitor structure and anti-corrosion efficiency cannot be reliably discerned, although a tendency for better protection against corrosion under these conditions was observed for “smaller” molecules compared to the “large” C12.

In some cases, white precipitates were observed on the metal surfaces. These were isolated and characterized by ATR-IR spectroscopy. The corresponding spectra are shown in Chapter 8.6. The vibrational bands of the phosphonate groups appear to be shifted, compared to those of the respective “free” phosphonate inhibitor. This is an indication of a metal-phosphonate formation. In addition, EDS study (see Chapter 8.6) confirmed the presence of phosphorus in them. An exception is the case of 0.01 mM of C12 at 90 °C in which the bands that appear in the corresponding ATR-IR spectrum are not characteristic for the phosphonates, which is also confirmed by the absence of phosphorus in the respective EDS data.

4.3.2 Non-phosphonate inhibitors

At RT, HAD is the most efficient inhibitor and DLD is the least efficient inhibitor for both dosages tested. At 60 °C, SLD shows the highest inhibition and ACAB the lowest inhibition for both dosages tested. At 90 °C, DLD and HAD present the highest efficiencies for 100 ppm, however when a dosage increase to 250 ppm results in a significantly increased inhibition for SLD.

In addition, experiments in the presence of non-phosphonate inhibitors were performed under stirring conditions. It is worth noting that the corrosion rates measured for the controls under non-stirring conditions increase as the stirring rate increases. The corrosion rates obtained from the experiments in the presence of all the non-phosphonate inhibitors follow the same pattern, however no discernible universal trend was established for the inhibition efficiencies.

Finally, corrosion experiments in the presence of sulfides indicated that when both oxygen and sulfides are present in solution, corrosion rates are higher than those in experiments performed under argon atmosphere. HAD is the most effective inhibitor amongst the non-phosphonate inhibitors tested under these conditions.

4.4 References

10. Cui, H.; Ren, W.; Lin, P.; Liu, Y. Structure Control Synthesis of Iron Oxide Polymorph Nanoparticles through an Epoxide Precipitation Route. *Journal of Experimental Nanoscience* **2012**, *8* (7-8), 869–875.
11. Schwertmann, U.; Cornell, R. M. Iron Oxides in Laboratory. *Soil Science* **1993**, *156* (5), 369.
12. Raman, A.; Kuban, B.; Razvan, A. The Application of Infrared Spectroscopy to the Study of Atmospheric Rust Systems—I. Standard Spectra and Illustrative Applications to Identify Rust Phases in Natural Atmospheric Corrosion Products. *Corrosion Science* **1991**, *32* (12), 1295–1306.
13. Robertson, J.M. Crystal Structures by R.W.G. Wyckoff. *Acta Crystallographica* **1954**, *7* (12), 867–867.
14. Finger, L. W.; King, H. A Revised Method of Operation of the Single-Crystal Diamond Cell and Refinement of the Structure of NaCl at 32 Kbar. *American Mineralogist* **1978**, *63* (3-4), 337–342.
15. Wechsler, B. A.; Lindsley, D. H.; Prewitt, C. T. Crystal Structure and Cation Distribution in Titanomagnetites (Fe₃-XTi_xO₄). *American Mineralogist* **1984**, *69* (7-8), 754–770.
16. Blake, R.; Hessevick, R. E.; Zoltai, T.; Finger, L. Refinement of the Hematite Structure. *American Mineralogist* **1966**.
17. Lavagna, L.; Nisticò, R.; Musso, S.; Pavese, M. Hydrophobic Cellulose Ester as a Sustainable Material for Simple and Efficient Water Purification Processes from Fatty Oils Contamination. *Wood Science and Technology* **2018**, *53* (1), 249–261.
18. NACE Standard TM0169-95 (Item No. 21200), National Association of Corrosion Engineers, Houston TX, U.S.A. (www.nace.org).

Chapter 5: Corrosion experiments under mild “stress”

5.1 Characterization of the corrosion products

In this chapter, the results of the corrosion experiments in DI water (and not in a “stressful” geothermal fluid) are presented, in order to make the necessary comparisons between “low” and “high” stress geothermal conditions. Instrumentation, reagents, stock solution preparation and experimental set up for the corrosion experiments under the different conditions are mentioned in Chapter 2. Three different temperatures were studied, mimicking the different physical conditions (temperature and pressure) of the geothermal systems. In addition, experiments were performed at RT for comparison reasons. Corrosion rates and iron concentrations of the control experiments are presented in Table 5.1 and Figure 5.1.

T (°C)	RT		60		90		130	
	CR (mm/y)	Fe (ppm)	CR (mm/y)	Fe (ppm)	CR (mm/y)	Fe (ppm)	CR (mm/y)	Fe (ppm)
DI water	0.060	91	0.097	148	0.078	119	0.143	433

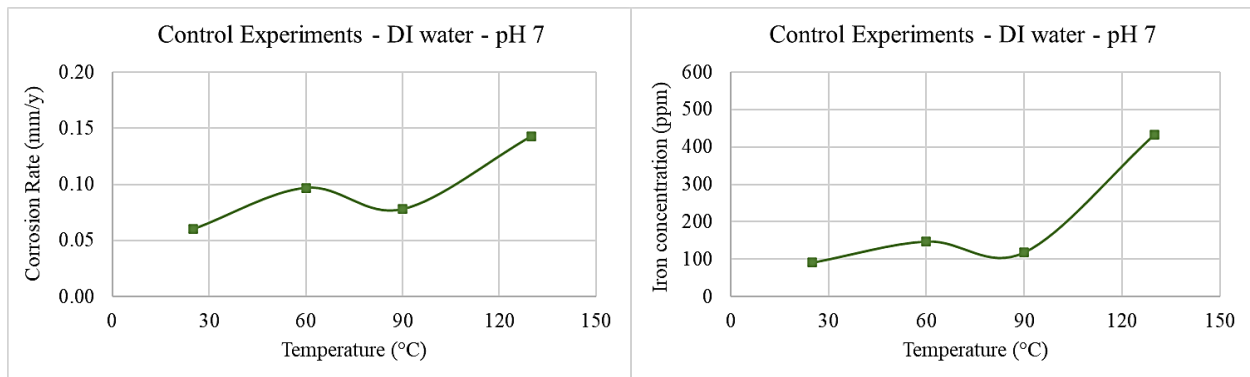


Figure 5.1. Results obtained in the absence of chemical additives in deionized water at pH 7. *left* Corrosion Rates and *right* Iron concentrations.

Comparing the surfaces of the samples exposed to experiments (see Figure 5.2), the color variation between the different corrosion products is, once again, obvious, as for the two artificial

Brines 1 and 2. In the case of 90 °C and 130 °C, the grey-black color is a strong indication of the formation of a magnetite film, which can lead to lower corrosion rates than the formation of lepidocrocite, which appears to dominate in the case of RT and 60 °C, as indicated by the orange-brown color of the corresponding surfaces ^[1,2]. In order to confirm the aforementioned hypothesis, precipitates were selected and then characterized by ATR-IR spectroscopy and powder X-Ray Diffraction, so that the iron oxide products could be identified. Both characterization techniques point to the same conclusion. The amount of the precipitate which was collected from the control experiment at 130 °C was very small and could not be removed from the filter membrane used for the filtration. Thus, samples from the pristine membrane were taken and used as a background for the ATR-IR studies, so the bands associated with its material can be easily identified (see the grey inset at the bottom spectrum). The respective spectrum of the membrane filter is shown in the Annex (Chapter 8).



Figure 5.2. *left* Corroded carbon steel surfaces of the specimens exposed to “control” solutions in deionized water at pH 7.

Figure 5.3 presents the ATR-IR spectra of the control experiments. Examining the ATR-IR spectra of the iron deposits in control experiments at RT and 60 °C, it is observed that they are identical to the respective spectrum of lepidocrocite (available in the literature), showing

characteristic vibrations at 1625 cm^{-1} , 1152 cm^{-1} , 1017 cm^{-1} and 737 cm^{-1} [3]. The characteristic bands of magnetite and hematite appear at low energies, at 570 cm^{-1} and 390 cm^{-1} for magnetite, and 535 cm^{-1} , 464 cm^{-1} and 308 cm^{-1} for hematite [4,5]. Unfortunately, the resolution of the instrument does not allow certain conclusions to be drawn about the iron species at temperatures $90\text{ }^{\circ}\text{C}$ and $130\text{ }^{\circ}\text{C}$.

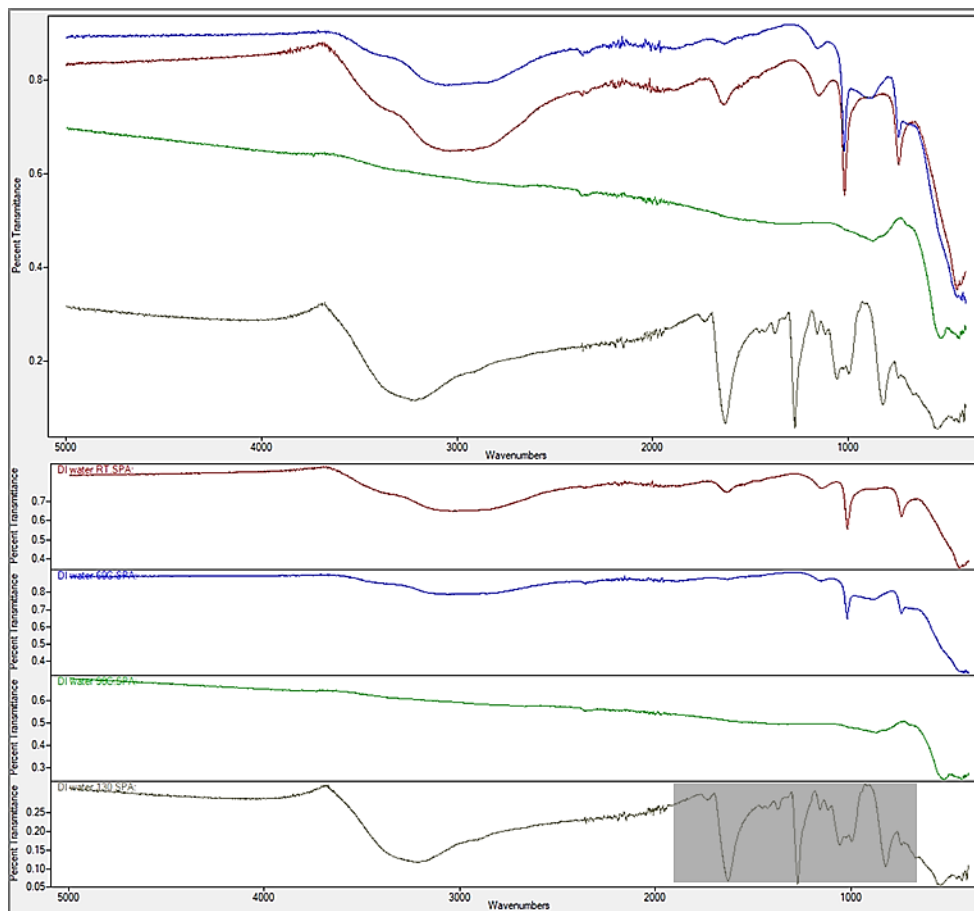


Figure 5.3. ATR-IR spectra of the precipitates collected from control corrosion experiments in DI water. Color codes: *red* RT, *blue* 60°C , *green* 90°C and *grey* 130°C .

Figure 5.4 presents the powder XRD patterns of the control experiments. In the powder XRD patterns of deposits collected from the control experiments at RT and $60\text{ }^{\circ}\text{C}$, the characteristic peaks of lepidocrocite at 2θ values 14.29° , 27.16° and 36.54° are observed [6]. In addition, in the

powder XRD pattern of the experiment at 60 °C, the low intensity peak at 34.46° is characteristic of magnetite, hence this deposit is a mixture of lepidocrocite and magnetite. The powder XRD pattern of the precipitate which was collected from the experiment at 90 °C and at 130 °C, is an indication that the corrosion product formed at both temperatures is magnetite, as its characteristic peaks at 2 θ values 30.11°, 34.46°, 37.09°, 43.10°, 57.00° and 62.59° are observed [7]. The crystal data of the aforementioned structures are shown in the Annex for comparison. Unfortunately, the amount of the precipitate from the control experiment at 130 °C was very small and could not be removed from the filtration membrane used for filtration. Thus, samples from the specific membrane were taken and used as a background, as it is shown in the grey inset. The broad peak at 26° which is observed in the respective XRD pattern of the control experiment at 130 °C is attributed to the filter membrane [8].

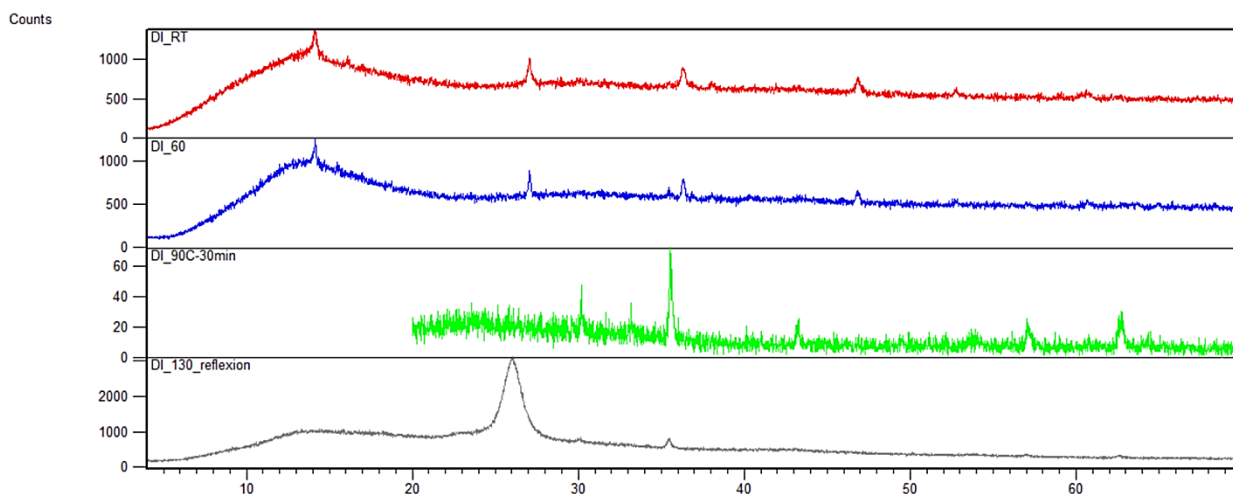


Figure 5.4. XRD spectra of the precipitates collected from control corrosion experiments in DI water. Color codes: *red* RT, *blue* 60 °C, *green* 90 °C and *grey* 130 °C.

Finally, the precipitates were studied by Scanning Electron Microscopy (SEM) in order to examine the morphology, the texture and the size of the particles. Figure 5.5 shows the SEM images. As the temperature increases, the formation of magnetite as the only corrosion product (90 °C) or as a mixture with lepidocrocite (60 °C), appears to change the morphology of the iron precipitates into spherical particles.

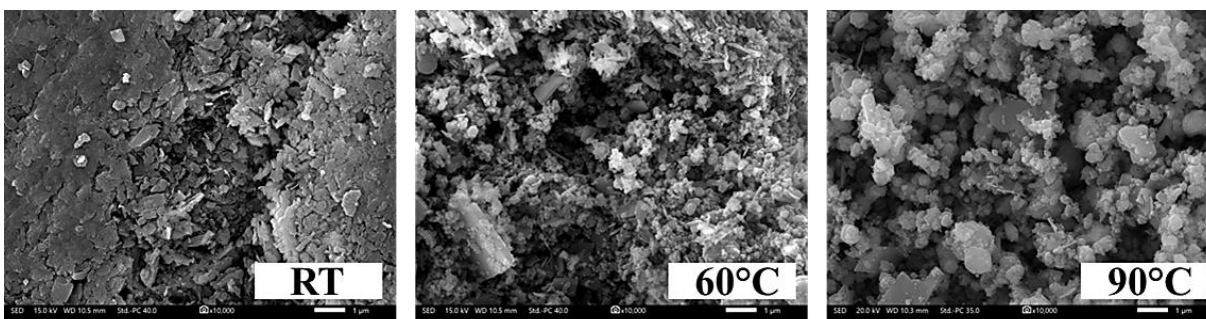


Figure 5.5. SEM images of the precipitates that collected from the experiments at *left* RT, *center* 60 °C and *right* 90 °C.

5.2 Results

5.2.1 Phosphonate inhibitors

This section discusses the results from experiments performed in the presence of phosphonate-based inhibitors in deionized water at four temperatures (RT, 60 °C, 90 °C and 130 °C) for four inhibitor concentrations (0.01 mM, 0.1 mM, 1 mM and 2 mM). In addition, at 130 °C (HP-HT conditions), further experiments were performed in the presence of inhibitors at higher concentrations (3 mM, 4 mM and 5 mM). The different working solutions were prepared by diluting the desired volumes of the corresponding inhibitor stock solutions in Brine 1, followed by the pH adjustment to 7, if needed. The total volume of each working solution was 120 mL for corrosion studies at RT, 60 °C and 90 °C, and 4 mL for 130 °C.

Each specimen was weighed before and after the experiment, after being first dried and then cleaned using abrasive paper. Corrosion rates were calculated according to Equation 1, given in Chapter 2.3 ^[9]. Furthermore, aliquots were taken from the working solution at the end of the experimental period, in order to determine the iron concentration for each corrosion experiment^[10,11]. One of the goals here was to evaluate whether the iron determination method could be used for corrosion evaluation and quantification. Inhibition efficiencies (in %) based on both methods were calculated according to Equation 2 and Equation 3, as given in Chapter 2.3 . The absence of corrosion product on the metal surfaces as the inhibitor concentration increases does not necessarily imply well-protected surfaces. There are cases in which the presence of a

phosphonate additive can lead to deposit dissolution. This means that, although a corrosion product may transiently form, it can undergo dissolution by the phosphonate additive [12, 13].

EDTMP-C2

Corrosion rate and iron concentration values obtained from the experiments performed under these conditions in the presence of C2, as well as the calculated inhibition efficiency (in %), are presented in Table 5.2.

Table 5.2. Corrosion rates, iron concentrations and inhibition efficiency percentages based on both methods in the presence of C2 in DI water.								
T (°C)	RT		60		90		130	
c (mM)	CR (mm/y)	Fe (ppm)	CR (mm/y)	Fe (ppm)	CR (mm/y)	Fe (ppm)	CR (mm/y)	Fe (ppm)
<i>Control</i>	<i>0.060</i>	<i>91</i>	<i>0.097</i>	<i>148</i>	<i>0.078</i>	<i>119</i>	<i>0.143</i>	<i>443</i>
0.01	0.053 12 %	75 18 %	0.066 32 %	83 44 %	0.068 13 %	143 - 20 %	0.099 31 %	358 17 %
0.10	0.030 50 %	69 24 %	0.056 42 %	96 35 %	0.039 50 %	98 18 %	0.105 27 %	317 27 %
1.00	0.033 45 %	79 13 %	0.072 25 %	138 7 %	0.064 17 %	141 - 18 %	0.087 39 %	199 54 %
2.00	0.039 35 %	76 16 %	0.103 - 6 %	165 - 11 %	0.073 6 %	123 - 3 %	0.126 12 %	221 49 %
3.00	-	-	-	-	-	-	0.131 8 %	256 41 %
4.00	-	-	-	-	-	-	0.128 10 %	376 13 %
5.00	-	-	-	-	-	-	0.123 14 %	355 18 %

Figure 5.6 presents results from corrosion experiments in the presence of C2. At RT, the lowest corrosion rate is observed for 0.1 mM inhibitor concentration, therefore in this case C2 presents its optimal inhibition efficiency, 50 %. The highest corrosion rate is obtained in the presence of 0.01 mM of C2, ie. 12 % inhibition. However, a large discrepancy between the two determination methods is observed, as it is noticed that the total iron method shows similar iron concentration values (69-79 ppm) for all of the inhibitor concentrations, ie. 13-24 % inhibition. Regarding the experiments performed at 60 °C, the deviation between the gravimetric and the iron measurements is smaller. Again, 0.1 mM of C2 shows the lowest corrosion rate (42 % inhibition), followed by 0.01 mM (32 % inhibition). Further inhibitor dosage increase results in higher corrosion rates. Iron concentration increases gradually as the inhibitor concentration increases. At 90 °C, once again, it is observed that 0.1 mM of C2 is the most beneficial concentration (50 % inhibition), also confirmed by total iron determination method. Finally, under HP-HT conditions (130 °C) the dosage 1 mM appears to be the most effective, 39 % inhibition, however, further increase does not enhance the anticorrosion efficiency of C2.

Table 5.3 shows visuals of the specimens from the corrosion experiments in the presence of C2 at RT, 60 °C and 90 °C. Despite the fact that C2 performs better as corrosion inhibitor at 0.1 mM concentration, increasing the concentration of C2 causes the surfaces of the coupons to appear less corroded. Therefore, C2 at high concentrations leads to iron oxide deposit dissolution under these conditions.

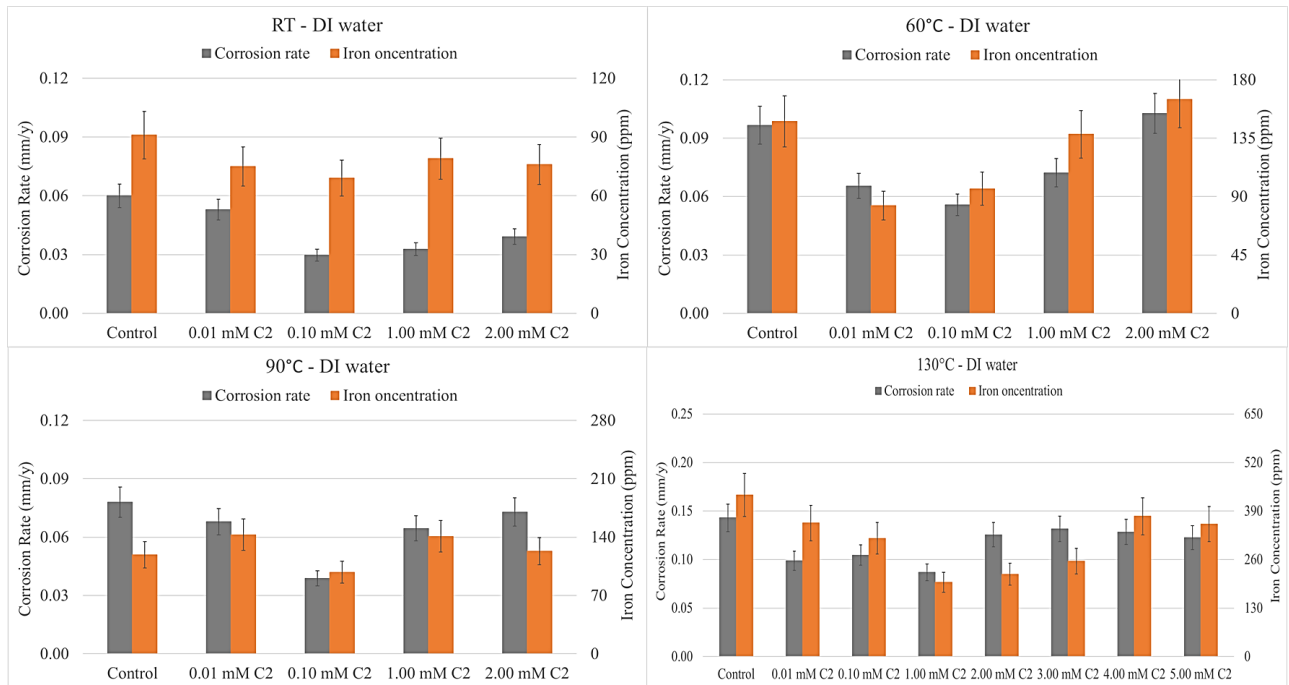


Figure 5.6. Corrosion experiments in the presence of C2 in DI water at: a. RT (upper left), b. 60 °C (upper right), c. 90 °C (bottom left) and d. 130 °C (bottom right). Color codes: *grey* Corrosion rate and *orange* Iron concentration.

Table 5.3. Visual representation of the specimens from the experiments of C2 in DI water.

	RT	60 °C	90 °C
Control			
0.01 mM			
0.10 mM			
1.00 mM			
2.00 mM			

TMTMP-C4

Corrosion rate and iron concentration values obtained from the experiments performed under these conditions in the presence of C4, as well as the calculated inhibition efficiency (in %), are presented in Table 5.4.

Table 5.4. Corrosion rates, iron concentrations and inhibition efficiency percentages based on both methods in the presence of C4 in DI water.								
T (°C)	RT		60		90		130	
c (mM)	CR (mm/y)	Fe (ppm)	CR (mm/y)	Fe (ppm)	CR (mm/y)	Fe (ppm)	CR (mm/y)	Fe (ppm)
<i>Control</i>	<i>0.060</i>	<i>91</i>	<i>0.097</i>	<i>148</i>	<i>0.078</i>	<i>119</i>	<i>0.143</i>	<i>443</i>
0.01	0.051 16 %	70 23 %	0.073 24 %	43 71 %	0.053 32 %	116 3 %	0.051 64 %	97 78 %
0.10	0.033 45 %	85 7 %	0.050 49 %	104 30 %	0.058 26 %	112 6 %	0.093 35 %	268 38 %
1.00	0.035 41 %	100 - 10 %	0.057 41 %	151 - 2 %	0.075 4 %	253 - 113 %	0.181 - 26 %	573 - 32 %
2.00	0.032 47 %	91 0 %	0.052 46 %	121 18 %	0.076 2 %	159 - 34 %	0.137 4 %	318 27 %
3.00	-	-	-	-	-	-	0.193 - 35 %	277 36 %
4.00	-	-	-	-	-	-	0.185 - 30 %	339 22 %
5.00	-	-	-	-	-	-	0.193 - 35 %	498 - 15 %

Figure 5.7 presents results from corrosion experiments in the presence of C4. At room temperature, C4 shows a similarly good performance for 0.1 mM, 1 mM and 2 mM (41-47 % inhibition), while the iron concentrations are higher as inhibitor dosage increases. The same trend in anticorrosion efficiency of C4 is observed at 60 °C. Again, higher iron concentrations are observed at higher inhibitor dosages. At 90 °C, as the concentration of C4 increases, the inhibition

efficiency drops. The greatest inhibition is noted at 0.01 mM, 32 %. The iron determination test showed high iron concentrations for 1 mM and 2 mM of C4. Finally, concerning the experiments at 130 °C, similarly to 90 °C, the most beneficial C4 concentration is 0.01 mM. In fact, under these conditions, C4 exhibits its highest % inhibition so far, 64 %. It is worth noting that inhibitor concentrations higher than 2 mM result in higher corrosion rate values.

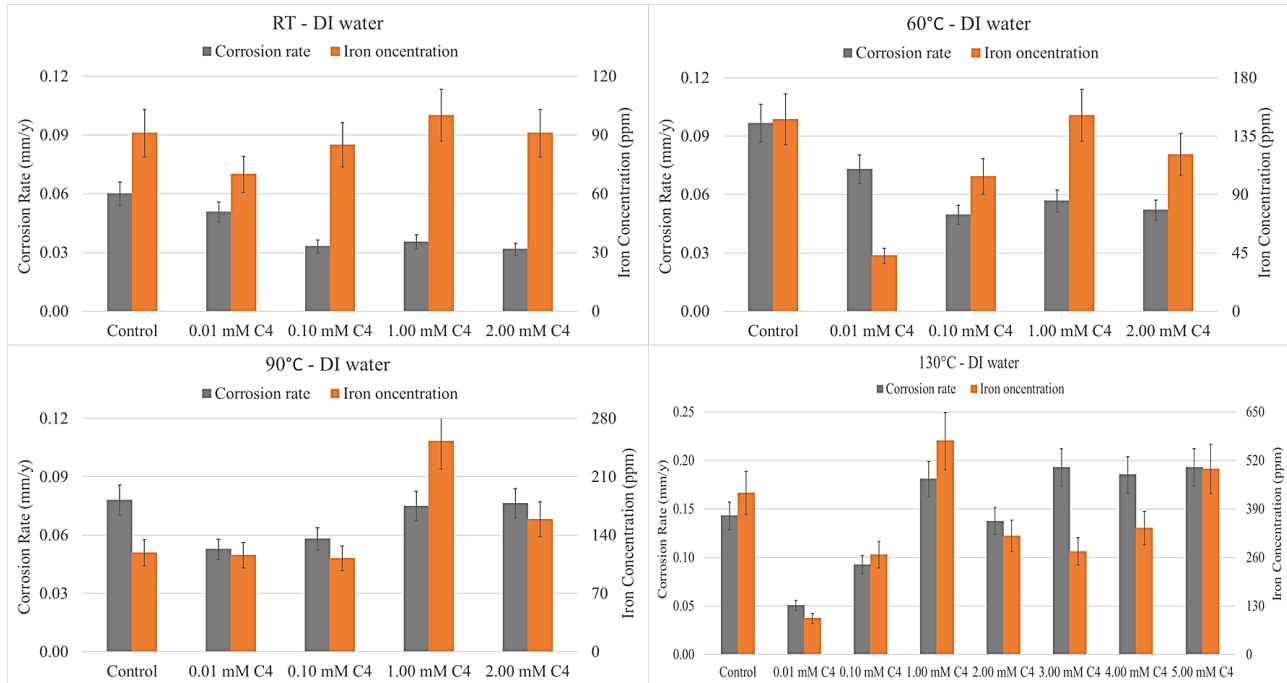

















Figure 5.7. Corrosion experiments in the presence of C4 in DI water at: a. RT (upper left), b. 60 °C (upper right), c. 90 °C (bottom left) and d. 130 °C (bottom right). Color codes: *grey* Corrosion rate and *orange* Iron concentration.

Table 5.5 shows visuals of the specimens from corrosion experiments in the presence of C4, at RT, 60 °C and 90 °C. The appearance of the coupons verifies the phenomenon of iron oxide deposit dissolution in the presence of high inhibitor concentrations.

Table 5.5. Visual representation of the specimens from the experiments of C4 in DI water.

	RT	60 °C	90 °C
Control			
0.01 mM			
0.10 mM			
1.00 mM			
2.00 mM			

HDTMP-C6

Corrosion rate and iron concentration values obtained from the experiments performed under these conditions in the presence of C6, as well as the calculated inhibition efficiency (in %), are presented in Table 5.6.

Table 5.6. Corrosion rates, iron concentrations and inhibition efficiency percentages based on both methods in the presence of C6 in DI water.

T (°C)	RT		60		90		130	
c (mM)	CR (mm/y)	Fe (ppm)	CR (mm/y)	Fe (ppm)	CR (mm/y)	Fe (ppm)	CR (mm/y)	Fe (ppm)
<i>Control</i>	<i>0.060</i>	<i>91</i>	<i>0.097</i>	<i>148</i>	<i>0.078</i>	<i>119</i>	<i>0.143</i>	<i>443</i>
0.01	0.051 15 %	105 - 15 %	0.072 26 %	111 25 %	0.057 27 %	76 36 %	0.091 36 %	279 36 %
0.10	0.033 44 %	81 11 %	0.052 46 %	126 15 %	0.059 24 %	176 - 48 %	0.051 64 %	245 43 %
1.00	0.035 42 %	101 - 11 %	0.096 1 %	192 - 30 %	0.190 - 144 %	384 - 223 %	0.196 - 37 %	573 - 32 %

2.00	0.044 26 %	99 - 9 %	0.110 - 14 %	219 - 48 %	0.266 - 241 %	261 - 119 %	0.160 - 12 %	332 23 %
3.00	-	-	-	-	-	-	0.152 - 7 %	259 40 %
4.00	-	-	-	-	-	-	0.149 - 4 %	326 25 %
5.00	-	-	-	-	-	-	0.170 - 19 %	498 - 15 %

Results from corrosion experiments in the presence of C6 are shown in Figure 5.8. At RT, C6 shows the lowest corrosion rate values for the concentrations 0.1 mM and 1 mM (44 % and 42 %, respectively), while iron concentration values are approximately equal, regardless of the anticorrosion efficiency. In the case of 60 °C, the most efficient concentration of C6 is 0.1 mM (46 % inhibition). Comparing the results from the gravimetric measurements and those from the iron determination, a notable deviation is observed. Despite that, the two methods show the same pattern when comparing the behavior of the different concentrations of C6. In the case of 90 °C, lower corrosion rates are noted at 0.01 mM and 0.1 mM, 27 % and 24 % inhibition, respectively. In addition, the anticorrosion efficiency drops as C6 concentration increases. Similarly to previous results, the iron determination showed rather high iron concentrations for 1 mM and 2 mM of C6. Finally, the lowest corrosion rate is observed for 0.01 mM inhibitor concentration at 130 °C, 64 % inhibition.

Table 5.7 shows visuals of the specimens from the corrosion experiments in the presence of C6 at RT, 60 °C and 90 °C. Iron dissolution in the presence of high inhibitor concentrations is visually observed, a phenomenon also observed for other tetraphosphonate inhibitors.

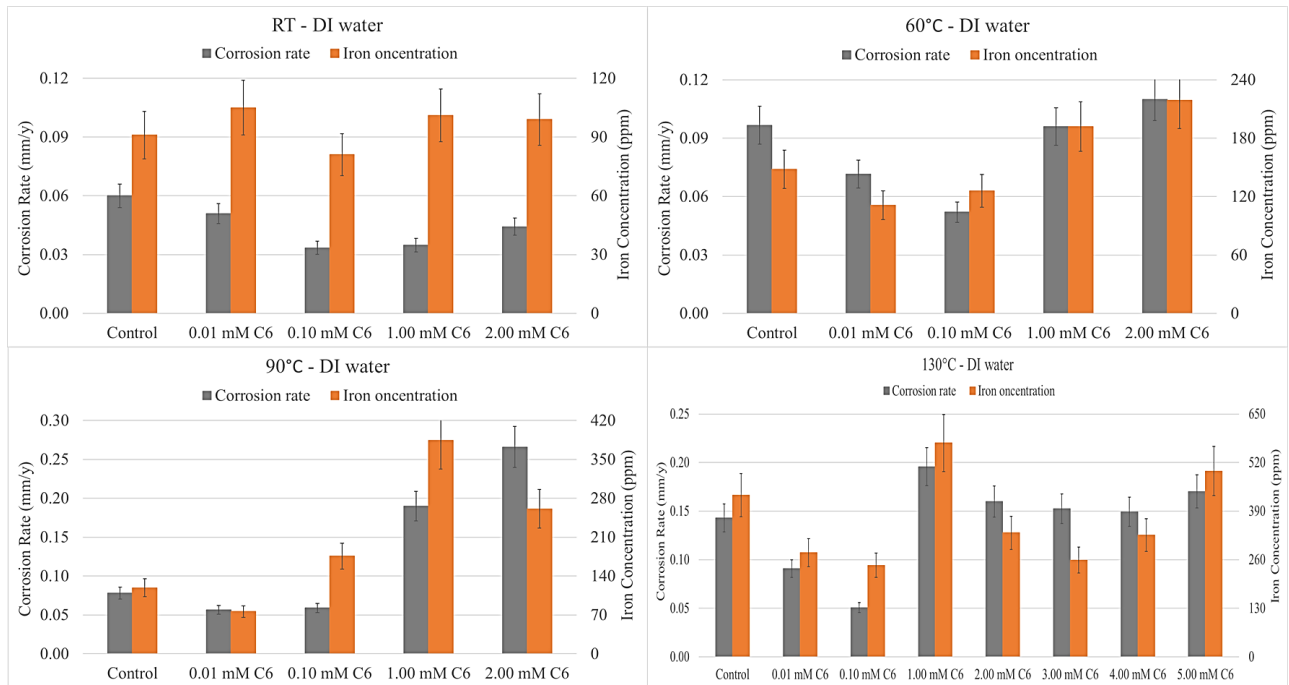


Figure 5.8. Corrosion experiments in the presence of C6 in DI water at: a. RT (upper left), b. 60 °C (upper right), c. 90 °C (bottom left) and d. 130 °C (bottom right). Color codes: *grey* Corrosion rate and *orange* Iron concentration.

Table 5.7. Visual representation of the specimens from the experiments of C6 in DI water.

	RT	60 °C	90 °C
Control			
0.01 mM			
0.10 mM			
1.00 mM			
2.00 mM			

ODTMP-C8

Corrosion rate and iron concentration values obtained from the experiments performed under these conditions in the presence of C8, as well as the calculated inhibition efficiency (in %), are presented in Table 5.8.

Table 5.8. Corrosion rates, iron concentrations and inhibition efficiency percentages based on both methods in the presence of C8 in DI water.

T (°C)	RT		60		90		130	
c (mM)	CR (mm/y)	Fe (ppm)	CR (mm/y)	Fe (ppm)	CR (mm/y)	Fe (ppm)	CR (mm/y)	Fe (ppm)
<i>Control</i>	<i>0.060</i>	<i>91</i>	<i>0.097</i>	<i>148</i>	<i>0.078</i>	<i>119</i>	<i>0.143</i>	<i>443</i>
0.01	0.055 8 %	70 23 %	0.087 10 %	111 25 %	0.048 39 %	63 47 %	0.108 24 %	407 6 %
0.10	0.041 32 %	77 15 %	0.078 20 %	135 9 %	0.075 4 %	149 - 25 %	0.067 53 %	275 36 %
1.00	0.034 43 %	88 3 %	0.084 13 %	172 - 16 %	0.118 - 52 %	248 - 108 %	0.149 - 4 %	404 7 %
2.00	0.042 30 %	94 - 3 %	0.091 6 %	192 - 30 %	0.187 - 139 %	403 - 239 %	0.137 4 %	398 8 %
3.00	-	-	-	-	-	-	0.078 45 %	258 40 %
4.00	-	-	-	-	-	-	0.090 37 %	429 1 %
5.00	-	-	-	-	-	-	0.182 - 27 %	513 - 18 %

Figure 5.9 presents results from corrosion experiments carried out in the presence of C8. At RT, the lowest corrosion rate is observed for 1 mM inhibitor concentration, thus C8 exhibits its highest inhibition efficiency, 43 %. In experiments performed at 60 °C, 0.1 mM C8 shows the lowest corrosion rate (20 % inhibition). At 90 °C, it is observed that 0.01 mM of C8 is the most beneficial concentration (39 % inhibition). Further dosage increase results in a gradual drop in the

anticorrosion efficiency of C8. Comparing the results of the two different quantification methods, the same pattern is observed, although there is a notable deviation in terms of % inhibition efficiencies. Finally, at 130 °C, 0.1 mM C8 appears to be the most effective concentration (53 % inhibition). It is worth noting that increasing the concentration to 3 mM and 4 mM is the first case in which a phosphonate inhibitor presents good inhibition efficiencies (45 % and 37 % inhibition, respectively), under HP-HT conditions.

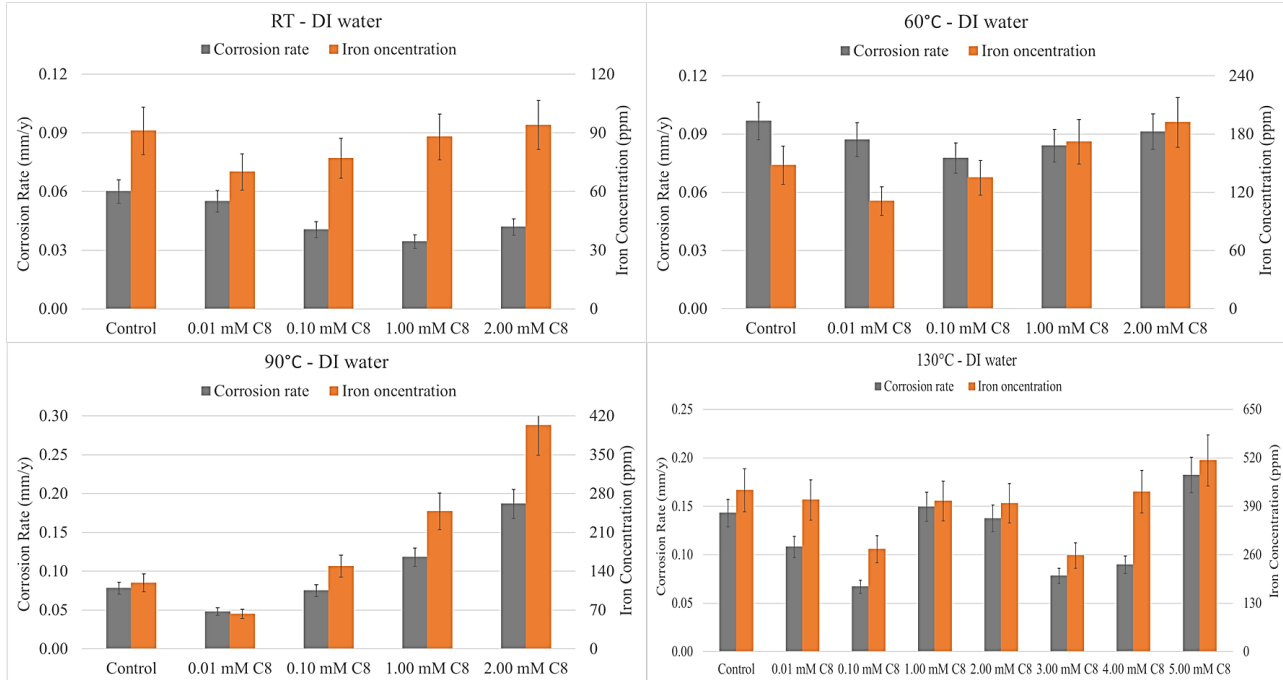










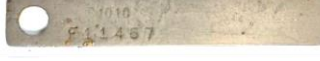






Figure 5.9. Corrosion experiments in the presence of C8 in DI water at: a. RT (upper left), b. 60 °C (upper right), c. 90 °C (bottom left) and d. 130 °C (bottom right). Color codes: *grey* Corrosion rate and *orange* Iron concentration.

Table 5.9 shows visuals of the specimens from the corrosion experiments in the presence of C8 at RT, 60 °C and 90 °C. Regarding the higher inhibitor concentrations at 60 °C and 90 °C, the appearance of the “clean” coupons is impressive, in comparison with the high corrosion rates and iron concentration values.

Table 5.9. Visual representation of the specimens from the experiments of C8 in DI water.

	RT	60 °C	90 °C
Control			
0.01 mM			
0.10 mM			
1.00 mM			
2.00 mM			

DDTMP-C12

Corrosion rate and iron concentration values obtained from the experiments performed under these conditions in the presence of C12, as well as the calculated inhibition efficiency (in %), are presented in Table 5.10.

Table 5.10. Corrosion rates, iron concentrations and inhibition efficiency percentages based on both methods in the presence of C12 in DI water.

T (°C)	RT		60		90		130	
	CR (mm/y)	Fe (ppm)	CR (mm/y)	Fe (ppm)	CR (mm/y)	Fe (ppm)	CR (mm/y)	Fe (ppm)
<i>Control</i>	<i>0.060</i>	<i>91</i>	<i>0.097</i>	<i>148</i>	<i>0.078</i>	<i>119</i>	<i>0.143</i>	<i>443</i>
0.01	0.052 13 %	57 37 %	0.084 13 %	39 74 %	0.047 39 %	89 25 %	0.108 25 %	231 47 %
0.10	0.036 39 %	52 43 %	0.034 65 %	69 53 %	0.045 42 %	132 - 11 %	0.048 67 %	196 55 %
1.00	0.024 60 %	54 41 %	0.038 61 %	29 80 %	0.031 60 %	40 66 %	0.024 83 %	63 85 %

2.00	0.029 52 %	53 42 %	0.047 51 %	73 51 %	0.018 77 %	31 74 %	0.030 79 %	75 83 %
3.00	-	-	-	-	-	-	0.078 46 %	359 17 %
4.00	-	-	-	-	-	-	0.024 83 %	102 76 %
5.00	-	-	-	-	-	-	0.018 87 %	94 78 %

Figure 5.10 shows the results from corrosion experiments in the presence of C12. This is the first case where an increase in inhibitor dosage, in general, causes an enhancement of the anticorrosion efficiency. In addition, the two different methods show close results. At RT, the lowest corrosion rate values are noticed for 1 mM and 2 mM concentration (60 % and 52 % inhibition, respectively). Regarding the experiments performed at 60 °C, 0.1 mM and 1 mM of C12 yield the highest inhibition, 65 % and 61 %, respectively. At 90 °C, corrosion rates decrease as C12 dosage increases, reaching 77 % inhibition for the 2 mM concentration. Impressively, at 130 °C, 5 mM C12 exhibits 87 % inhibition.

Table 5.11 shows visuals of the specimens from corrosion experiments, in the presence of C12 at RT, 60 °C and 90 °C. At the end of the experiments, spotty deposits on the surfaces of the coupons were observed, thus they were collected and characterized by ATR-IR spectroscopy and the corresponding spectra are provided in the Annex.

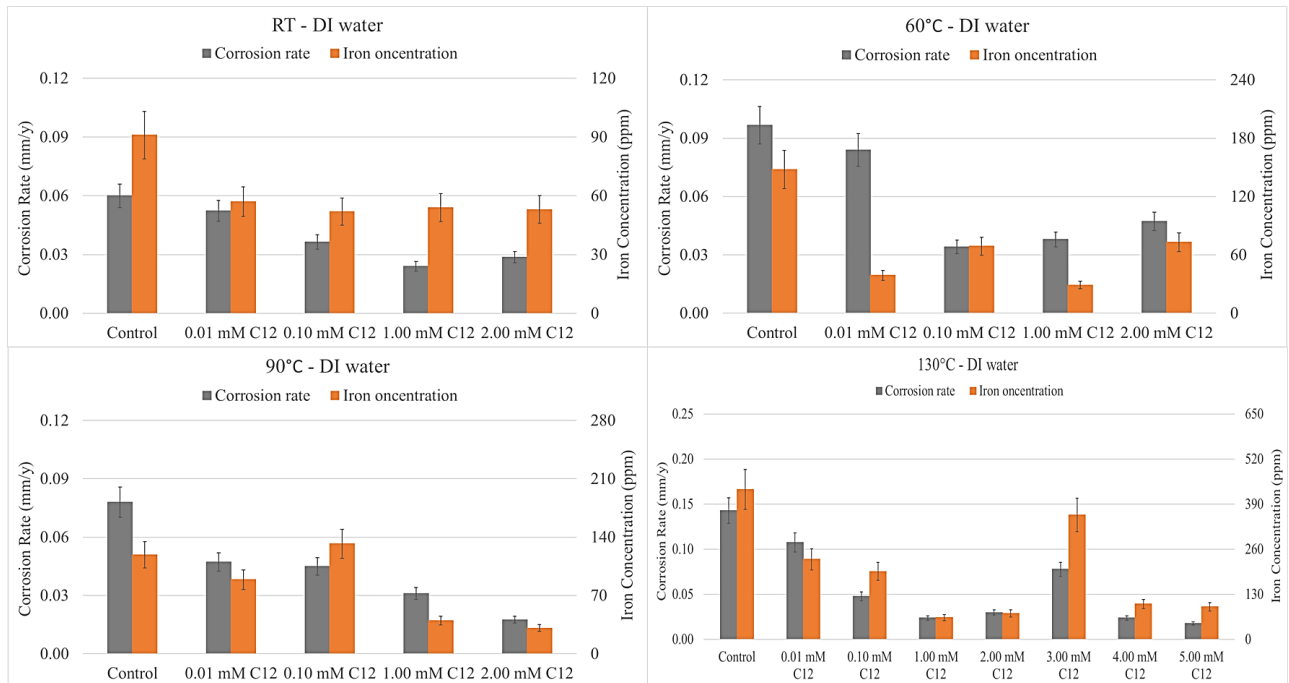


Figure 5.10. Corrosion experiments in the presence of C12 in DI water at: a. RT (upper left), b. 60 °C (upper right), c. 90 °C (bottom left) and d. 130 °C (bottom right). Color codes: grey Corrosion rate and orange Iron concentration.

Table 5.11. Visual representation of the specimens from the experiments of C12 in DI water.

	RT	60 °C	90 °C
Control			
0.01 mM			
0.10 mM			
1.00 mM			
2.00 mM			

Comparing the % inhibition efficiencies at RT from the two methods, the members of the tetraphosphonate family show higher iron concentrations than expected compared to the respective values of corrosion rates. This is observed when the inhibitor concentration is either 1 mM or 2 mM, except the experiments in the presence of C12, where C12 presents higher iron levels for the lowest concentration. The same conclusion is valid for the experiments performed at 60 °C. In most cases, higher iron concentrations are again observed at higher inhibitor dosages, except for cases of C2 and C12. In the case of C2, similar inhibition % efficiencies (within the experimental error) are calculated for both methods, while 0.01 mM of C12 presents lower iron concentration than expected. Regarding the experiments performed at 90 °C, again, higher iron concentrations are observed, when the concentration of the inhibitor is either 1 mM or 2 mM, except the experiments in the presence of C12, where C12 presents higher iron levels for the 0.1 mM concentration. In contrast, in most corrosion experiments performed at 130 °C and at high inhibitor concentrations, a trend of lower iron levels is observed, except for the experiments in the presence of C8 and C12. In these cases, both inhibitors show higher iron levels at high inhibitor concentrations.

Effect of concentration

As mentioned in the Introduction, the anticorrosion action of the inhibitors was studied for four different concentrations for the experiments performed at room temperature, at 60 °C and at 90 °C, and for seven different concentrations for the experiments under HP-HT conditions (130 °C). This section focuses on the effect of inhibitor concentration, step-by-step from lowest to highest.

Figure 5.11 shows the fluctuation in corrosion rate values, as the concentration of each inhibitor systematically increases. At RT, 60 °C and 90 °C, increasing the concentration of C2 from 0.01 mM to 0.1 mM, lowers the corrosion rate values. A further dosage increase results in a gradual increase in corrosion rates. In addition, at RT and at 90 °C, the highest corrosion rates are observed in the case of 0.01 mM. On the contrary, at 60 °C the highest inhibitor concentration shows the highest corrosion rate as well. At 130 °C, the three lower concentrations yield lower corrosion rates, reaching inhibition ranging between 27 % and 39 %, and when the concentration is higher than 1 mM, the efficiency drops to 8-14 %.

Regarding C4 at RT and at 60 °C, increasing the concentration from 0.01 mM to 0.1 mM causes lower corrosion rates and then the values remain almost constant regardless of the C4 concentration. At 90 °C and 130 °C, increasing inhibitor concentration from 0.01 mM to 1 mM results in higher corrosion rates. Upon increasing the concentration to 2 mM, at 90 °C no significant change is observed, in contrast to a lower corrosion rate observed at 130 °C. However, the most beneficial concentration is 0.1 mM.

At RT, C6 presents similar behavior to C4. At 60 °C and increasing the concentration from 0.01 mM to 0.1 mM results in lower corrosion rates. In the case of 1 mM, the corrosion rate is increased and then, at 2 mM, remains almost constant. At 90 °C, corrosion rate values increase as inhibitor concentration increases. Finally, at 130 °C C6 follows an S-shaped trend, as corrosion rate is lower at 0.1 mM than at 0.01 mM, then increases at its highest value for 1 mM C6 concentration and then decreases again. Still, C6 at 0.1 mM concentration shows the best performance against corrosion.

C8 exhibits a similar pattern to C4 and C6 at RT. At 60 °C, the concentration of the inhibitor does not affect its inhibitory activity dramatically. At 90 °C, corrosion rate values increase as inhibitor dosage increases. Finally, at 130 °C C8 shows the same S-shaped trend as C6.

Regarding C12, at RT increasing the concentration from 0.01 mM to 1 mM, causes the corrosion rate values to decrease. Furthermore, in the case of 2 mM, C12 presents a similar corrosion rate to 0.1 mM concentration. At 60 °C, an increase from 0.01 mM to 1 mM results in a significantly lower corrosion rate. Then, for 2 mM of C12, the corrosion rate is slightly higher than that at 1 mM, but lower than that at 0.01 mM. Importantly, in contrast to what has been observed in most cases at 90 °C, corrosion rates values decrease as C12 concentration increases. A similar pattern is observed at 130 °C, with the sole exception of 2 mM at which the corrosion rate is slightly higher than that at 1 mM, but lower than that at 0.1 mM.

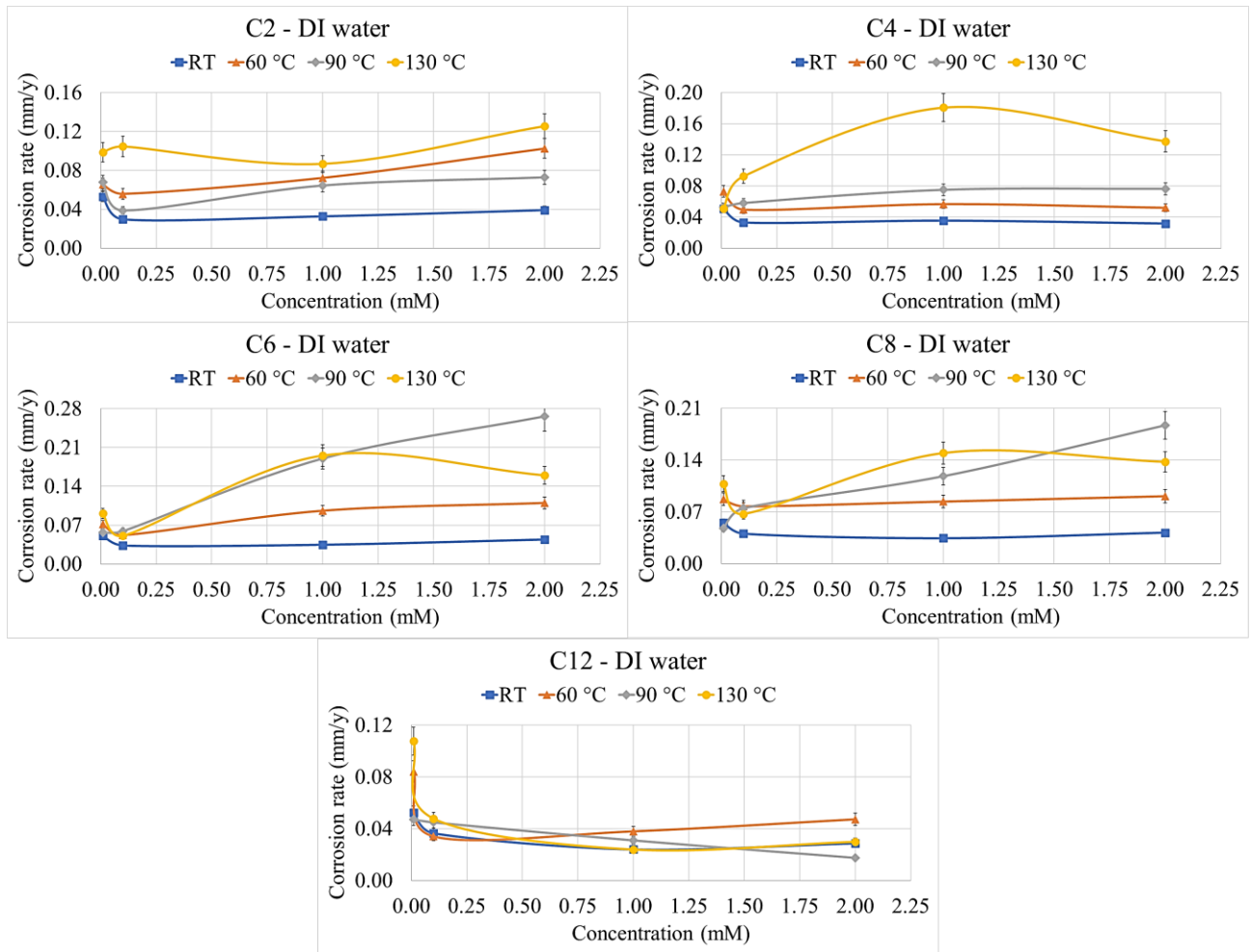


Figure 5.11. The correlation between corrosion rates and tetraphosphonate inhibitor concentration in DI water. Color codes: *blue* RT, *orange* 60 °C, *grey* 90 °C and *yellow* 130 °C.

At 130 °C (HP-HT conditions), further corrosion experiments were performed in the presence of phosphonate inhibitors at higher concentrations (3 mM, 4 mM and 5 mM). Figure 5.12 shows the results of these experiments, including the lower concentrations, for comparison.

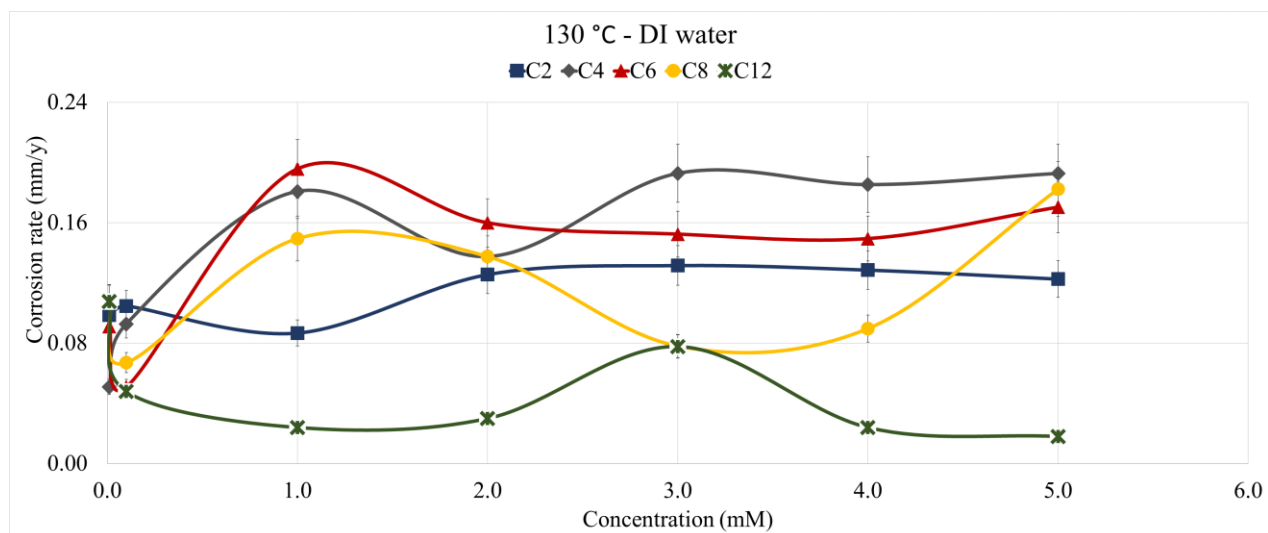


Figure 5.12. The correlation between corrosion rates and inhibitor concentration in DI water at 130 °C. Color codes: *blue* C2, *grey* C4, *red* C6, *yellow* C8 and *green* C12.

The aforementioned results of corrosion experiments for inhibitors were grouped by concentration at each temperature in an attempt to derive a potential pattern in their behavior.

Experiments performed at RT

- Concentration increase from 0.01 mM to 0.1 mM: a significant increase in the efficiency of all corrosion inhibitors is observed, reaching values in the range 32-50 %.
- Concentration increase from 0.1 mM to 1 mM: for C2, C4 and C6 no significant change in efficiency is observed, while C8 and C12 show improved performance.
- Concentration increase from 1 mM to 2 mM: A small drop in efficiency is noted, except for C4 whose efficiency is almost constant.

Experiments performed at 60 °C

- Concentration increase from 0.01 mM to 0.1 mM: increasing the concentration is beneficial for all tetraphosphonates. Importantly, the anti-corrosion performance of C12, reaches 65 % inhibition.

- Concentration increase from 0.1 mM to 1 mM: the efficiency drops from 42 % to 25 % for C2 and from 46 % to 1 % for C6. No significant change in the efficiency is observed for the rest of the inhibitors.
- Concentration increase from 1 mM to 2 mM: A small drop for all the inhibitors occurs, except for C4 whose efficiency is almost constant. In fact, C2 and C6 show corrosive behavior under these conditions.

Experiments performed at 90 °C

- Concentration increase from 0.01 mM to 0.1 mM: for C4, C6 and C12 the corrosion rate values remain almost constant, while in the case of C8 the efficiency drops from 39 % to 4 % inhibition. On the contrary, the inhibitory performance of C2 is enhanced, reaching 50 % inhibition. This is the first time that the increase of inhibitor concentration to 0.1 mM does not enhance anticorrosion efficiency for all tetraphosphonates.
- Concentration increase from 0.1 mM to 1 mM: higher inhibition for C12 (from 42 % to 60 %), but lower inhibition for the rest of the tetraphosphonates is observed. Interestingly, C6 and C8 show corrosive behavior at 1 mM.
- Concentration increase from 1 mM to 2 mM: for C4 and C12 the corrosion rates remain almost unchanged, while in the case of C2, C6 and C8 the efficiency drops. Again, C6 and C8 are corrosive at 2 mM.

Experiments performed at 130 °C

- Concentration increase from 0.01 mM to 0.1 mM: an increase in the anticorrosion performance of the “larger” inhibitors C6, C8 and C12 is observed (reaching 64 %, 53 % and 67 %, respectively), while a decrease from 64 % to 35 % is observed in the case of C4. The performance of C2 is constant.
- Concentration increase from 0.1 mM to 1 mM: higher corrosion rates and enhanced corrosive behavior for C4, C6 and C8 are noted. In contrast, C2 and C12 show higher inhibition, 39 % and 83 %, respectively.

- Concentration increase from 1 mM to 2 mM: The efficiency of C2 drops while those of C8 and C12 are almost constant. C4 and C6 present lower corrosion rates.
- Concentration increase to 3 mM – 4 mM – 5 mM: for C2 and C6 the efficiency is not affected. C8 exhibits enhanced efficiency at the 3 mM and 4 mM dosages compared to that of 2 mM, although they are not the optimal for C8, overall. Importantly, C12 presents the only case in which concentration results in lower corrosion rate values, with the sole exception of 3 mM. The greatest anticorrosion efficiency is shown at 5 mM C12, 87 %.

A very important observation is that inhibitors exhibit lower corrosion rates for 0.1 mM inhibitor concentration in about half the cases. In addition, it is observed that “low” concentrations (0.01 mM and 0.1 mM) are beneficial for the anticorrosion efficiency of C2, C4, C6 and C8 in an almost absolute way (valid 13 out of 16 times). On the contrary, C12 appears to perform better at higher concentrations.

Effect of temperature

In this section, the influence of temperature on the efficiency of each tetraphosphonate is examined in detail. Due to different corrosion rate values of the controls at different temperatures, the comparisons are made based on % inhibition, thus Figure 5.13 presents correlations between % inhibition efficiencies and temperature, at each inhibitor concentration.

Starting with the runs at 0.01 mM inhibitor concentration, for C2 lower inhibition is observed at RT and at 90 °C, but higher inhibition is demonstrated at 60 °C and 130 °C. Concerning C4 and C6, an increase in inhibition efficiency as the temperature rises is observed. In the cases of C8 and C12, the best performance is noted at 90 °C, followed by 130 °C. Both inhibitors show similar inhibitory activity at RT and 60 °C, showing their lowest inhibition.

At 0.1 mM concentration, C2 shows higher inhibition at RT and 90 °C, followed by 60 °C and, finally, by 130 °C. In the case of C4, its highest efficiency at RT and 60 °C is observed. The lowest inhibition is observed for the experiments at 90 °C. The three “larger” size inhibitors, C6, C8 and C12, exhibit their best performance at 130 °C, and their worst performance at 90 °C and RT, in the case of C12. In addition, C6 shows similar inhibition performance at RT and 60 °C, as already

mentioned for C4. Regarding the rest of the experiments of C8, as the temperature increases from RT to 90 °C, the efficiency gradually decreases.

At 1 mM, it is evident that increasing the temperature causes a significant drop in the efficiency of C6 and C8. The same conclusion is valid for the case of C4, when the temperature is increased above 60 °C. On the contrary, C12 appears to perform better upon raising the temperature. C2 presents higher inhibition at RT, followed by 130 °C, then 60 °C and, finally, 90 °C.

At 2 mM, higher efficiencies for C2, C6 and C8 are noted at RT. C2 presents higher inhibition at RT and 60 °C, but when the temperature rises to 90 °C and 130 °C, its inhibition is approximately equal to 0. Finally, an increase in temperature is beneficial for C12, similar to the case of 1 mM of C12.

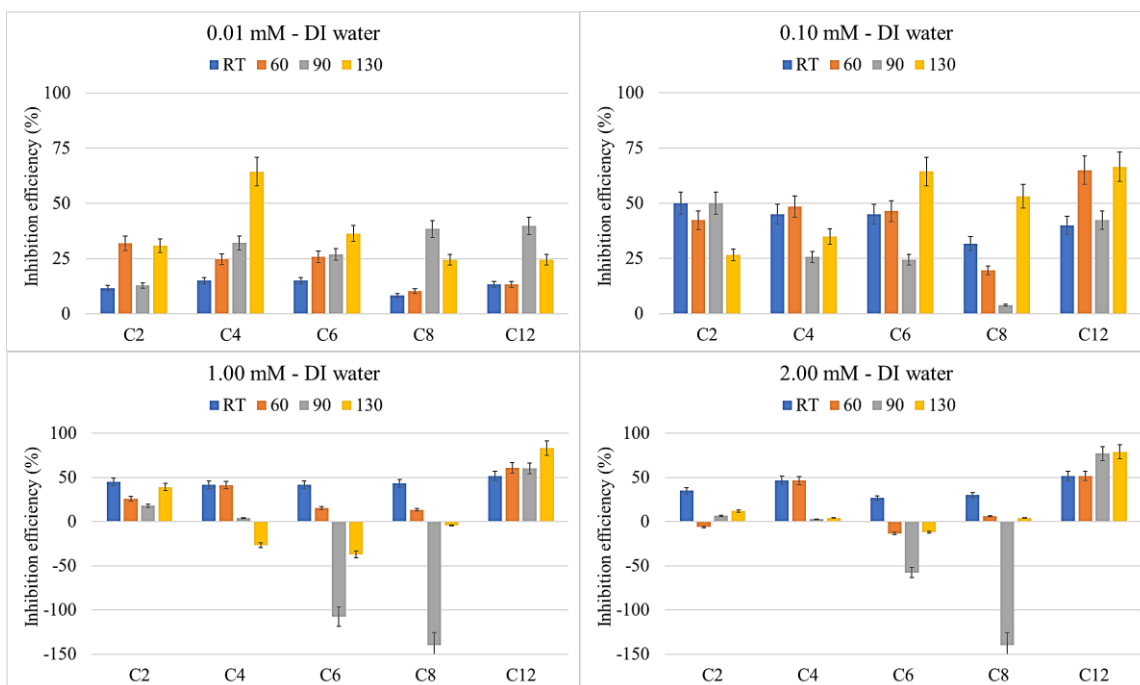


Figure 5.13. Correlation between inhibition efficiency (%) and temperature for tetraphosphonates in DI water for concentrations a. 0.01 mM (upper left), b. 0.10 mM (upper right), c. 1 mM (bottom left) and d. 2 mM (bottom right). Color codes: *blue* RT, *orange* 60 °C, *grey* 90 °C and *yellow* 130 °C.

Overall, no universal correlation between temperature and efficiency was established. However, it is observed that C4, C6 and C8 at higher concentrations, are affected by the increase in temperature, resulting in corrosive behavior for most cases. C12 appears to be the only inhibitor presenting high inhibition at high temperatures and low inhibition at RT. In addition, for 0.01 mM inhibitor concentration, the rest of the phosphonate inhibitors present their lowest inhibition at RT as well, in contrast to high concentrations, in the case of which at RT the greatest inhibition is observed.

Effect of inhibitor molecular size

A structural feature of this family of tetraphosphonate inhibitors is the systematically elongated carbon (polymethylene) chain connecting the two N atoms on each side of the molecule. In other words, as we visualize the structures of these inhibitors, moving from C2 up to C12, the length (or the size) of the molecule increases. In the following section, we attempt to correlate the length of the carbon chain between the amine groups with the efficiency of the corresponding inhibitor. Hence, the values of corrosion rates are presented in comparison with the number of carbon atoms contained in the structure of each phosphonate inhibitor. In addition, iron concentrations of the respective experiments are presented as well. Zero carbon atoms represent the respective control corrosion experiments.

Figure 5.14 focuses on the experiments performed at room temperature. Regarding the lowest concentration of 0.01 mM, it is observed that all tetraphosphonates show a similar low inhibitory activity, with their inhibition in the range 8-15 %. C6 induces higher iron concentration than the rest of the inhibitors, while C12 allows the lowest iron. C2, C6 and C8 show similar iron concentrations. For the 0.1 mM inhibitor dosage, C8 seems to be the least effective inhibitor. In general, the highest corrosion inhibition is noted for the “smaller” molecules, although higher iron concentrations are noticed. Again, C12 presents the lowest amount of iron. Increasing the concentration to 1 mM and then to 2 mM, the “largest” molecule C12 shows the most effective anticorrosion performance, verified by both gravimetric measurements and iron determination. Overall, C12 shows the lowest iron concentrations, followed by C2 in most cases. C4, C6 and C8 present the highest amounts of iron, regardless of their efficiency.

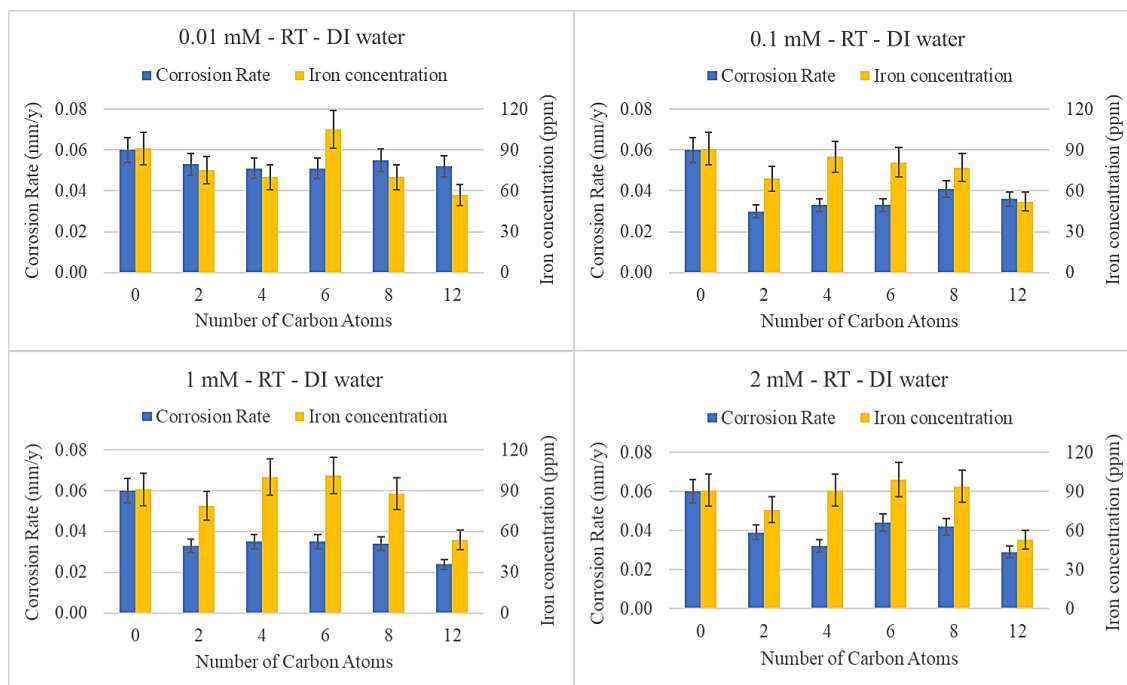


Figure 5.14. Correlation between the number of carbon atoms on the polymethylene linker of each phosphonate inhibitor and the results obtained from the corrosion experiments performed at RT in DI water.

Figure 5.15 focuses on the experiments performed at 90 °C. Regarding the lowest concentration of 0.01 mM, a trend towards to more efficient anticorrosion performance of the “smaller” molecules is observed. However, C4 and C12 present the lowest iron concentrations. For the 0.1 mM inhibitor dosage, C8 seems to be the least effective inhibitor, as observed in the results at the corresponding concentration at RT. Iron concentration increases gradually with inhibitor size, although C12 shows the lowest iron amount again. A further increase in inhibitor concentration to 1 mM and then to 2 mM results in the general observation that the most efficient inhibitor is C12, followed by C4. Interestingly, in the presence of 2 mM C12 high iron concentration is observed for the first time. However, C4 shows low iron concentrations in both cases.

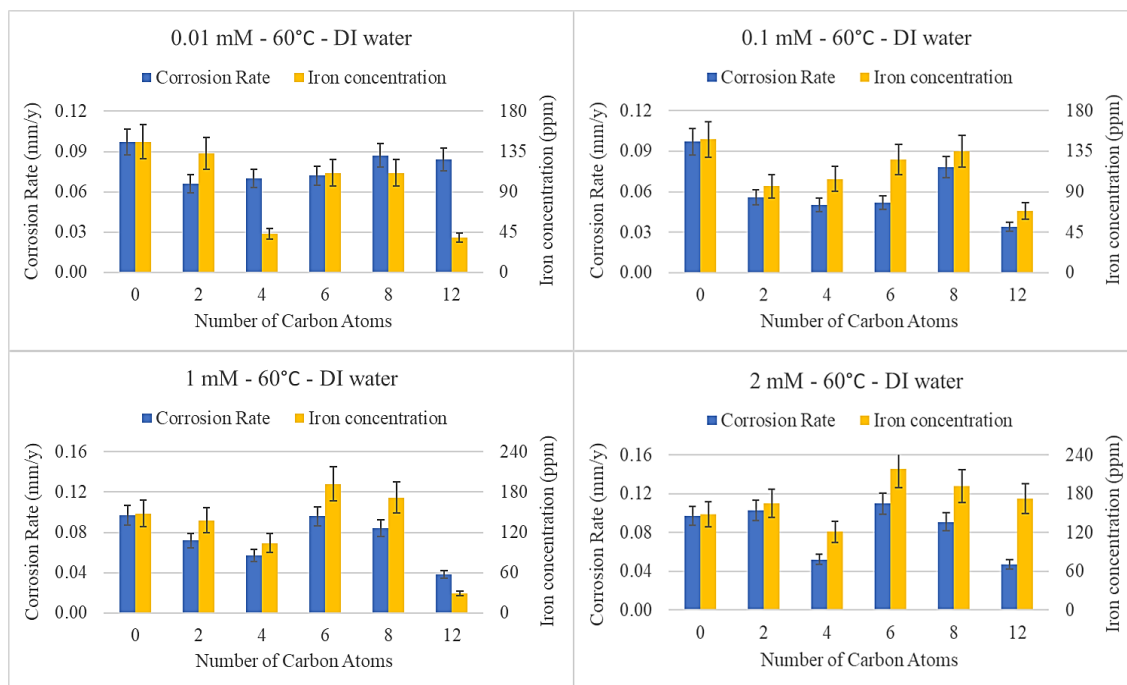


Figure 5.15. Correlation between the number of carbon atoms on the polymethylene linker of each phosphonate inhibitor and the results obtained from the corrosion experiments performed at 60 °C in DI water.

Figure 5.16 focuses on the experiments performed at 90 °C. Regarding the lowest concentration of 0.01 mM, the two “larger” inhibitors, C8 and C12, provide the highest anticorrosion efficiency. Iron concentration decreases as the number of carbon atoms increases from 2 to 8, and then increases again in the presence of C12. For the 0.1 mM inhibitor dosage, C8 is the least effective inhibitor, while C2 is the most effective, followed by C12. Under these conditions, the “larger” size inhibitors present higher iron amounts in their working solutions. At the higher concentrations, C12 shows the highest inhibition, while C6 and C8 present a corrosive action under these conditions, verified also by the corresponding iron concentrations.

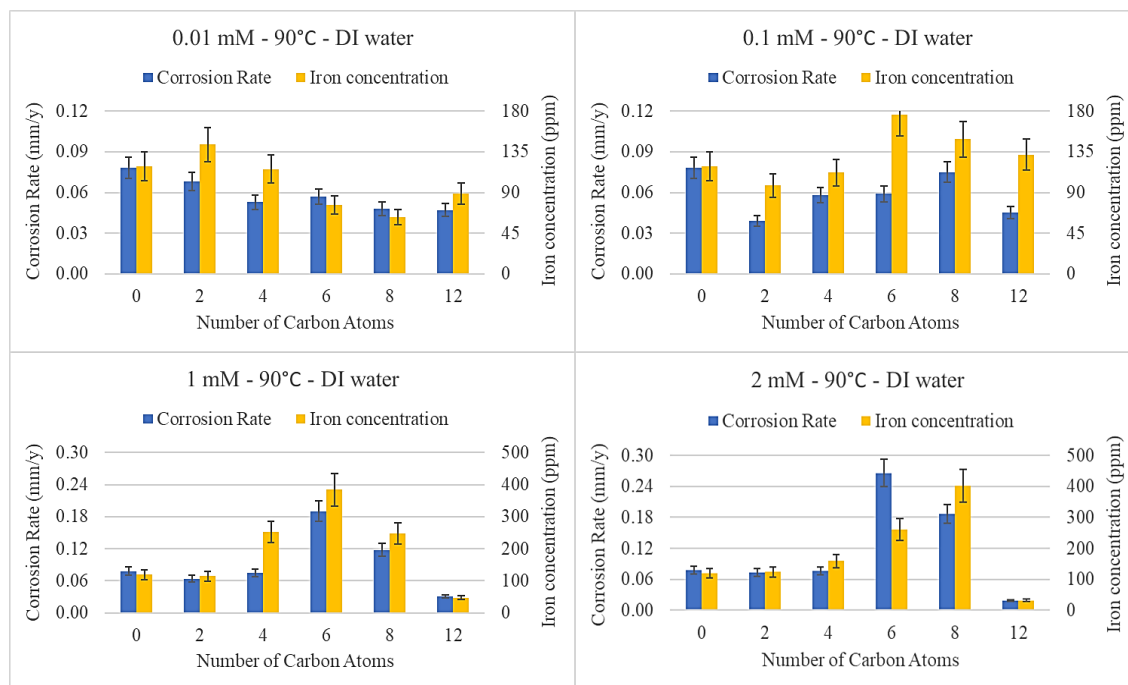


Figure 5.16. Correlation between the number of carbon atoms on the polymethylene linker of each phosphonate inhibitor and the results obtained from the corrosion experiments performed at 90 °C in DI water.

Figure 5.17 refers to the experiments performed under the harshest temperature conditions at 130 °C. In this case, C4 shows an optimal behavior as a corrosion inhibitor for the lowest concentration, followed by C6 and C2, while C8 and C12 are the least effective inhibitors. Iron determination results follow the same pattern as the corrosion rates, with the sole exception of C12 in the presence of which lower iron concentrations than expected are noted, compared to the respective corrosion rate. Increasing inhibitor dosage to 0.1 mM induces a trend towards higher efficiency for the “larger” molecules. C6 and C8 show higher iron amounts than expected. Once again, C12 presents the lowest iron concentration. In the case of 1 mM, C12 shows the highest inhibition, while C4 and C6 present a corrosive character. These results are also confirmed by the high iron results. Finally, in the presence of 2 mM C12 gives the lowest corrosion rate, as well as the lowest iron concentration. Regarding the rest of the inhibitors, a trend is observed that higher corrosion rates and iron concentrations are noted as the number of carbon atoms increase, although C8 presents lower corrosion rate than C6, but higher iron levels. Overall, a universally applicable

correlation between structure (linker length) and anticorrosion efficiency cannot be discerned. However, the best candidate as a corrosion inhibitor under these conditions appears to be the “largest” molecule, C12.

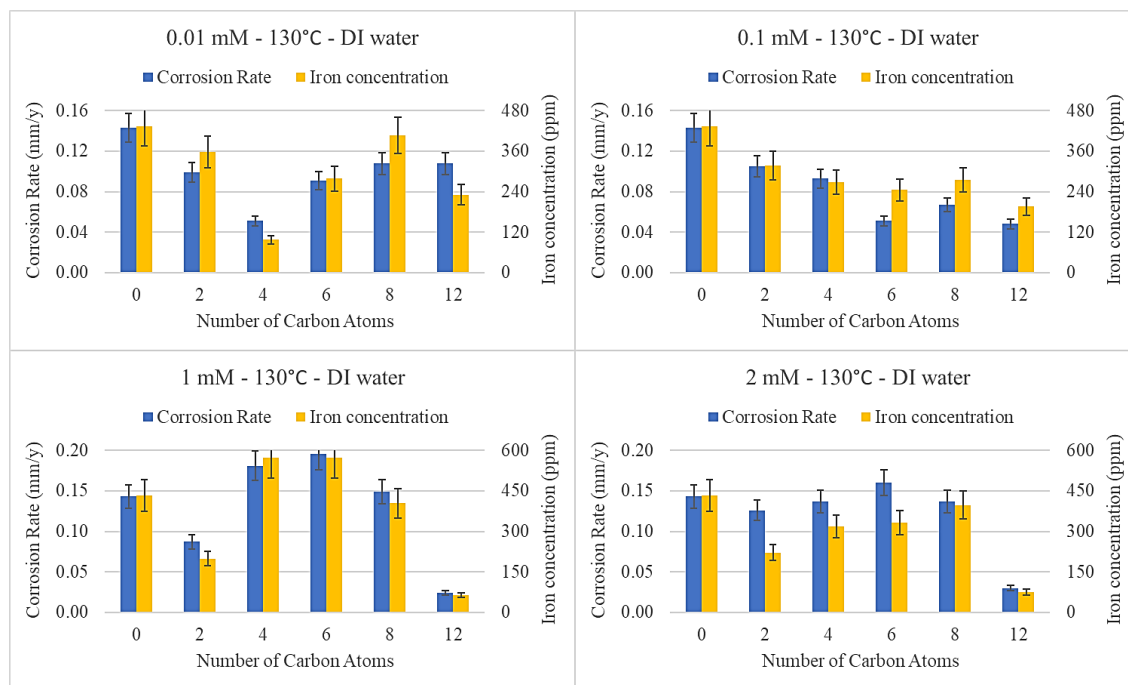


Figure 5.17. Correlation between the number of carbon atoms on the polymethylene linker of each phosphonate inhibitor and the results obtained from the corrosion experiments performed at 130 °C in DI water.

Effect of metal ions (synergy test)

In previous work from our group, it was clearly shown that certain metal ions (eg. alkaline earth metals and zinc) demonstrate synergy with corrosion inhibitors (commonly phosphonates) under certain conditions [13-24]. This synergy is demonstrated as reduced corrosion rates in the presence of both metal ion and corrosion inhibitor, compared to those with only inhibitor present. Such behavior has been assigned to formation of metal phosphonate protective films on the metal surface, which are effective in inhibiting general corrosion. Thus, this concept was investigated in the present work, under “mild” and “harsh” conditions. All experiments were performed at pH 7.

At this pH value the phosphonic groups are most likely doubly deprotonated and can strongly interact with metal ions present in solution, thus functioning synergistically, as mentioned in Chapter 1. Hence, corrosion experiments were performed in DI water at RT, 60 °C, 90 °C and 130 °C, in the presence of purposely added calcium and magnesium ions. In all cases, the molar ratio between phosphonates and metal ions was 1:1.

Regarding C2 (see Figure 5.18) at RT and at 60 °C, in general, the addition of calcium or magnesium ions does not result in altered corrosion rates compared with the “free” inhibitor. Increasing the temperature to 90 °C, an improved inhibitory performance is observed in the presence of magnesium for the two intermediate concentrations. On the contrary, calcium addition causes a drop in the efficiency in the corresponding experiments. In the case of 130 °C, 0.01 mM Mg^{2+} - C2 presents almost 3 times higher corrosion rate value than C2 alone. Increasing the concentrations to 2 mM and 3 mM, causes the corrosion rates to be lower than C2. The presence of calcium ions, at concentrations > 2 mM is beneficial.

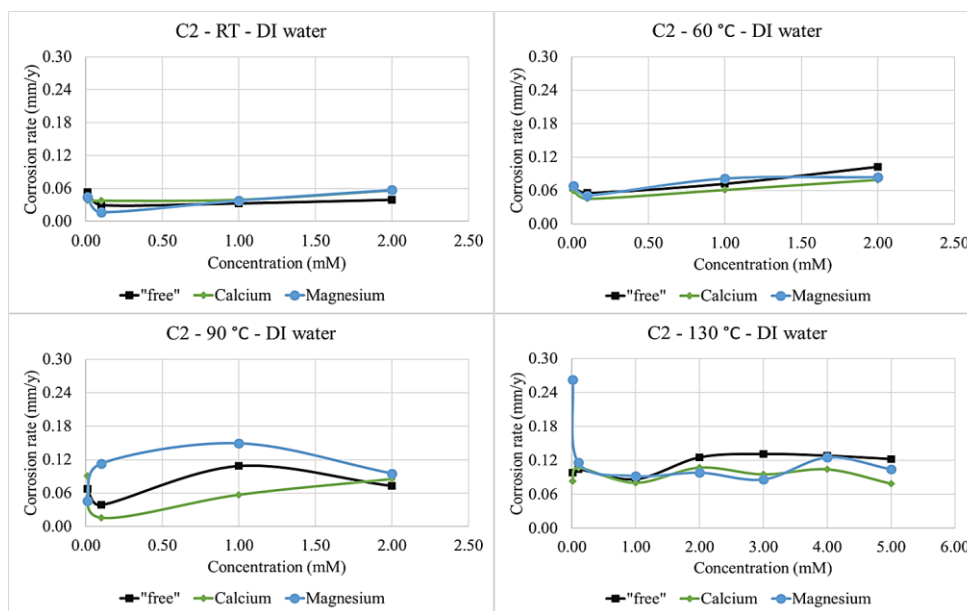


Figure 5.18. Comparison between corrosion rates in the absence and presence of metal ions for C2 in DI water at: a. RT (upper left), b. 60 °C (upper right), c. 90 °C (bottom left) and d. 130 °C (bottom right). Color codes: *black* C2 as “free” inhibitor, *green* Ca^{2+} - C2 and *light blue* Mg^{2+} - C2.

Concerning the experiments for C4 (see Figure 5.19) at RT and 60 °C, no significant differences in the anticorrosion efficiency have been observed, except the lowest concentration of 0.01 mM, in which the addition of both metal ions (separately) results in lower corrosion rates compared to C4 alone. As the temperature rises to 90 °C, Ca²⁺- C4 presents higher corrosion rates for the two lower concentrations. The presence of magnesium favors the inhibitory action of C4 when the concentration is 1 mM. However, for 2 mM Mg²⁺- C4 a much higher corrosion rate than the respective value of “free” C4 is noted. At 130 °C, in general both metal-phosphonate inhibitors show higher inhibition efficiency than C4, with the exceptions of 0.01 mM Ca²⁺- C4, 0.01 mM Mg²⁺- C4 and 0.1 mM Mg²⁺- C4.

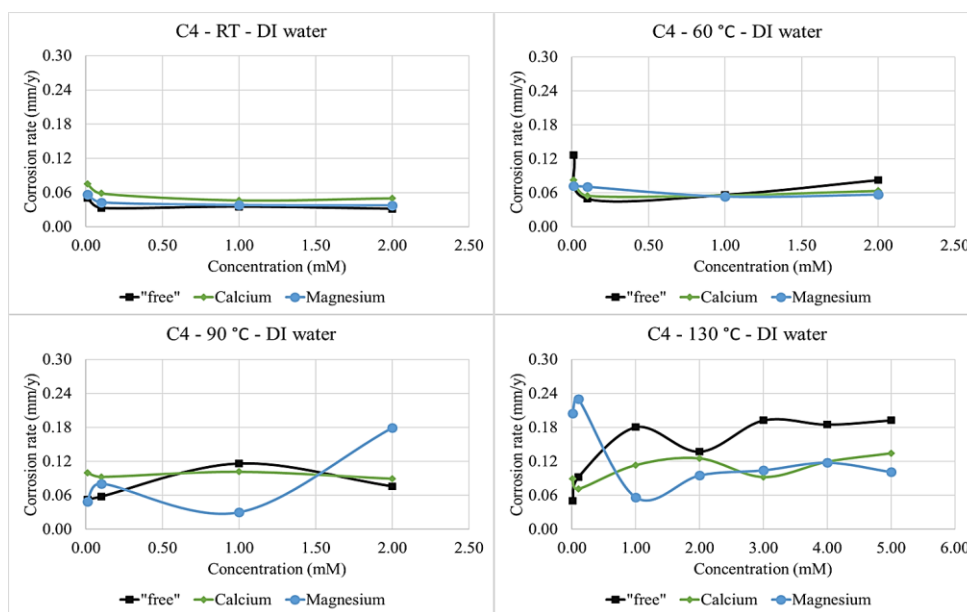


Figure 5.19. Comparison between corrosion rates in the absence and presence of metal ions for C4 in DI water at: a. RT (upper left), b. 60 °C (upper right), c. 90 °C (bottom left) and d. 130 °C (bottom right). Color codes: *black* C4 as “free” inhibitor, *green* Ca²⁺- C4 and *light blue* Mg²⁺- C4.

In the case of C6 (see Figure 5.20) at RT and 60 °C, the addition of Ca²⁺ and Mg²⁺ does not affect the performance of C6, with the sole exception of 2 mM inhibitor concentration in which both metal ions present lower corrosion rates comparing to the “free” phosphonate. In the case of 90 °C, even for the low 0.1 mM inhibitor concentration, Ca²⁺- C6 presents the highest corrosion

rate, but increasing the concentration results in higher inhibitory activity of C6 in the presence of calcium compared to Mg^{2+} -C6 and C6 alone. At 130 °C, the addition of metal ions enhances the performance of C6, when the concentration is > 1 mM.

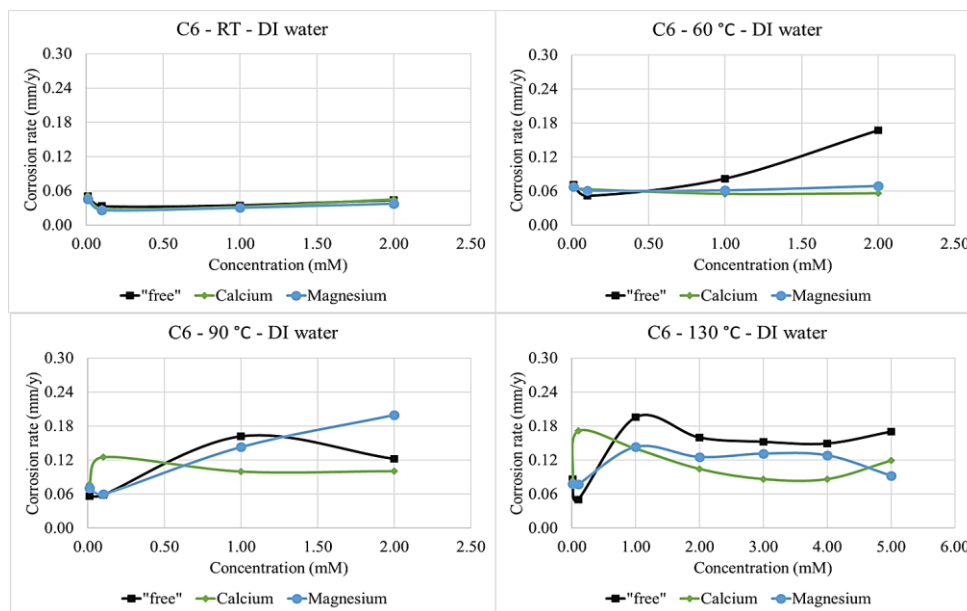


Figure 5.20. Comparison between corrosion rates in the absence and presence of metal ions for C6 in DI water at: a. RT (upper left), b. 60 °C (upper right), c. 90 °C (bottom left) and d. 130 °C (bottom right). Color codes: *black* C6 as “free” inhibitor, *green* Ca²⁺-C6 and *light blue* Mg²⁺-C6.

In the case of C8 (see Figure 5.21) at RT and 60 °C, no substantial differences were observed between the anticorrosion efficiency of the phosphonate and of the metal phosphonate blend. At 90 °C and 130 °C, Ca²⁺-C8 and Mg²⁺-C8 show lower corrosion rates than C8 alone when the concentration is 1 mM and 2 mM. In addition, the presence of calcium and magnesium is beneficial in the case of 5 mM at 130 °C. Overall, results at the two higher temperatures for the two lower concentrations show that the addition of magnesium causes higher corrosion rate values.

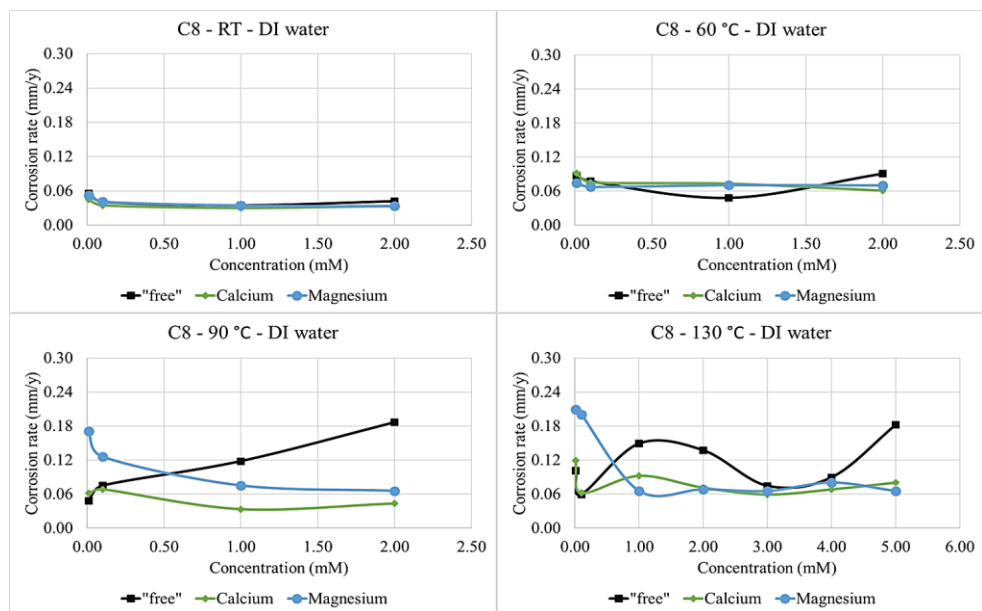


Figure 5.21. Comparison between corrosion rates in the absence and presence of metal ions for C8 in DI water at: a. RT (upper left), b. 60 °C (upper right), c. 90 °C (bottom left) and d. 130 °C (bottom right). Color codes: *black* C8 as “free” inhibitor, *green* Ca²⁺- C8 and *light blue* Mg²⁺- C8.

Finally, for C12 (see Figure 5.22), an overall similar inhibitory activity between the phosphonate as “free” inhibitor and the metal C12 blend with calcium or with magnesium is observed, under the conditions tested. There are some notable exceptions, for example, in the case of 1 mM C12 at 60 °C and at 130 °C the presence of metal ions is beneficial for the protection of carbon steel and in the case of 2 mM C12 at 90 °C, the inhibitor shows the lowest corrosion rate value.

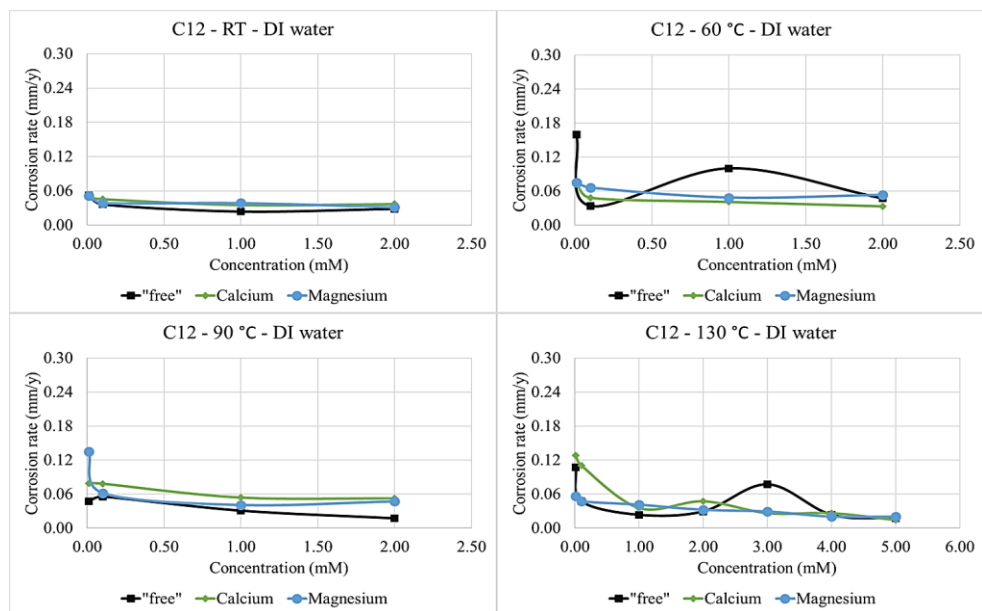


Figure 5.22. Comparison between corrosion rates in the absence and presence of metal ions for C12 in DI water at: a. RT (upper left), b. 60 °C (upper right), c. 90 °C (bottom left) and d. 130 °C (bottom right). Color codes: *black* C12 as “free” inhibitor, *green* Ca²⁺- C12 and *light blue* Mg²⁺-C12.

5.2.2 Non-phosphonate inhibitors

This section presents the results of the experiments performed in the presence of non-phosphonate in DI water at three temperatures (RT, 60 °C and 90 °C) for two inhibitor concentrations (100 ppm and 250 ppm). The inhibitor solutions were prepared by appropriate dilutions of the corresponding stock solutions in DI water, followed by pH adjustment to 7, if needed. The total volume of each experiment was 120 mL. Corrosion rate values obtained from the experiments under these conditions as well as the calculated % inhibition efficiency, categorized by inhibitor concentration, are presented in Table 5.12 and Table 5.13.

Table 5.12. Corrosion rates, iron concentrations and inhibition efficiency percentages based on both methods for 100 ppm of non-phosphonate inhibitors in DI water.						
T (°C)	RT		60		90	
	CR (mm/y)	Fe (ppm)	CR (mm/y)	Fe (ppm)	CR (mm/y)	Fe (ppm)
<i>Control</i>	<i>0.060</i>	<i>91</i>	<i>0.097</i>	<i>148</i>	<i>0.078</i>	<i>119</i>
SLD	0.028 54 %	23 75 %	0.028 71 %	33 78 %	0.029 62 %	36 70 %
ACAB	0.058 4 %	62 32 %	0.101 - 4 %	133 10 %	0.097 - 24 %	135 - 13 %
DLD	0.069 - 15 %	120 - 32 %	0.115 - 19 %	198 - 34 %	0.077 2 %	123 - 3 %
HAD	0.019 69 %	27 70 %	0.056 42 %	105 29 %	0.104 - 33 %	100 16 %

Table 5.13. Corrosion rates, iron concentrations and inhibition efficiency percentages based on both methods for 250 ppm of non-phosphonate inhibitors in DI water.						
T (°C)	RT		60		90	
	CR (mm/y)	Fe (ppm)	CR (mm/y)	Fe (ppm)	CR (mm/y)	Fe (ppm)
<i>Control</i>	<i>0.060</i>	<i>91</i>	<i>0.097</i>	<i>148</i>	<i>0.078</i>	<i>119</i>
SLD	0.022 63 %	22 76 %	0.031 68 %	14 91 %	0.021 73 %	26 78 %
ACAB	0.037 38 %	41 55 %	0.151 - 56 %	205 - 39 %	0.127 - 63 %	183 - 54 %
DLD	0.052 13 %	110 - 21 %	0.101 - 4 %	143 3 %	0.091 - 16 %	170 - 43 %
HAD	0.020 66 %	51 44 %	0.041 58 %	101 32 %	0.038 51 %	30 75 %

Figure 5.23 presents the results of corrosion experiments in the presence of non-phosphonate inhibitors at RT. HAD exhibits the lowest corrosion rates at both concentrations, 69 % inhibition for 100 ppm, and 66 % inhibition for 250 ppm, followed by SLD with 54 % and 63 % inhibition, respectively. ACAB at 100 ppm shows corrosion rate values no different than the control, although increasing its concentration, results in a lower corrosion rate, reaching 38 % inhibition. It appears that DLD is the least effective inhibitor under these conditions. Based on the results from the iron determination method, HAD gives higher iron concentrations, compared to the corresponding corrosion rates. For example, in the case of 100 ppm, HAD and SLD show similar iron concentration values, even though SLD shows higher corrosion rates. In addition, HAD at 250 ppm gives higher iron levels than SLD and ACAB, while it presents the lowest corrosion rate.

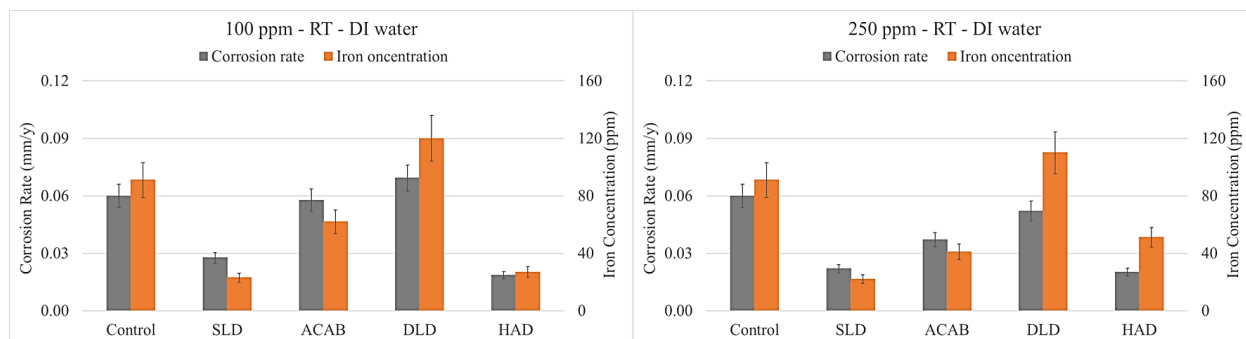


Figure 5.23. Corrosion experiments in the presence of non-phosphonate inhibitors in DI water at RT. (left) 100 ppm and (right) 250 ppm. Color codes: *grey* Corrosion rate and *orange* Iron concentration.

Figure 5.24 shows the results of the corrosion experiments in the presence of non-phosphonate inhibitors at 60 °C. Temperature increase favors the anticorrosion efficiency of SLD for both dosages, with approximately 70 % inhibition. HAD is the second best with 29 % and 58 % inhibition, at 100 ppm and 250 ppm, respectively. An important observation is that the gravimetric measurements and the iron determination data are consistently in agreement and give reliable conclusions regarding the anticorrosion efficiency of the inhibitors.

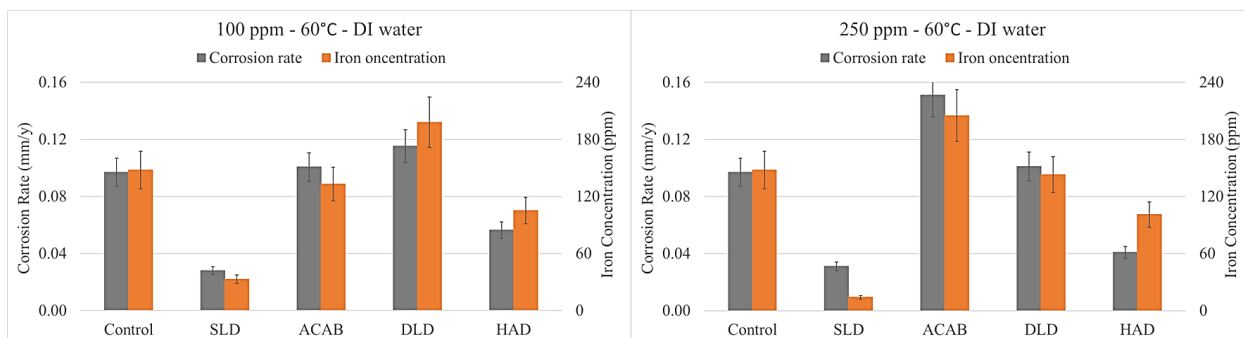


Figure 5.24. Corrosion experiments in the presence of non-phosphonate inhibitors in DI water at 60 °C. (left) 100 ppm and (right) 250 ppm. Color codes: *grey* Corrosion rate and *orange* Iron concentration.

Figure 5.25 presents the results of the corrosion experiments in the presence of non-phosphonate inhibitors at 90 °C. Similar observations are valid under these conditions as before, as SLD presents the lowest corrosion rates (with 62 % and 73 % inhibition), while in the case of 250 ppm HAD is again the second best inhibitor with 51 % inhibition. Finally, HAD presents higher iron levels, compared to the corresponding corrosion rate values, although the two methods result in similar conclusions in terms of inhibition efficiencies.

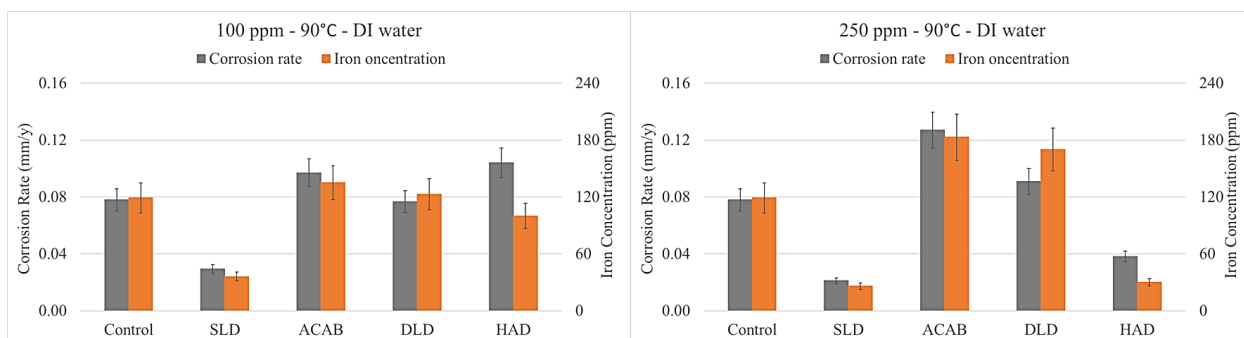


Figure 5.25. Corrosion experiments in the presence of non-phosphonate inhibitors in DI water at 90 °C. (left) 100 ppm and (right) 250 ppm. Color codes: *grey* Corrosion rate and *orange* Iron concentration.

SLD shows slightly lower iron concentrations than expected compared to the corresponding corrosion rate values when the experiments were performed at RT and 60 °C, while at 90 °C similar inhibition efficiency percentages are observed at both inhibitor dosages. Importantly, ACAB shows lower iron levels in all cases. For DLD, higher iron concentrations are observed at RT, for its lowest concentration at 60 °C and its highest one at 90°C. DLD at 250 ppm at 60 °C and 100 ppm at 90 °C shows similar % efficiency. Finally, for HAD 250 ppm, higher iron levels are observed at 60 °C and at RT, while at 90°C, lower iron concentrations are noted. Inhibition results (%) are approximately equal in the case of 100 ppm of HAD at RT.

The glass containers with the carbon steel specimens in the presence of non-phosphonate inhibitors at the end of the experimental period are presented in Figure 5.26. Overall, visual observations are in agreement with the corresponding results of the gravimetric measurement and of the iron determination test, with the sole exception of the experiments in the presence of 250 ppm inhibitor dosage at RT. In this case, the solution of SLD appears to be “cleaner” than the solution of HAD, despite the fact that HAD presents the greatest inhibition under these conditions. It is worth noting that the experiment in the presence of 250 ppm of ACAB at 90 °C is the only one with a black colored solution, which is a strong indication of magnetite formation, as previously mentioned in introduction.

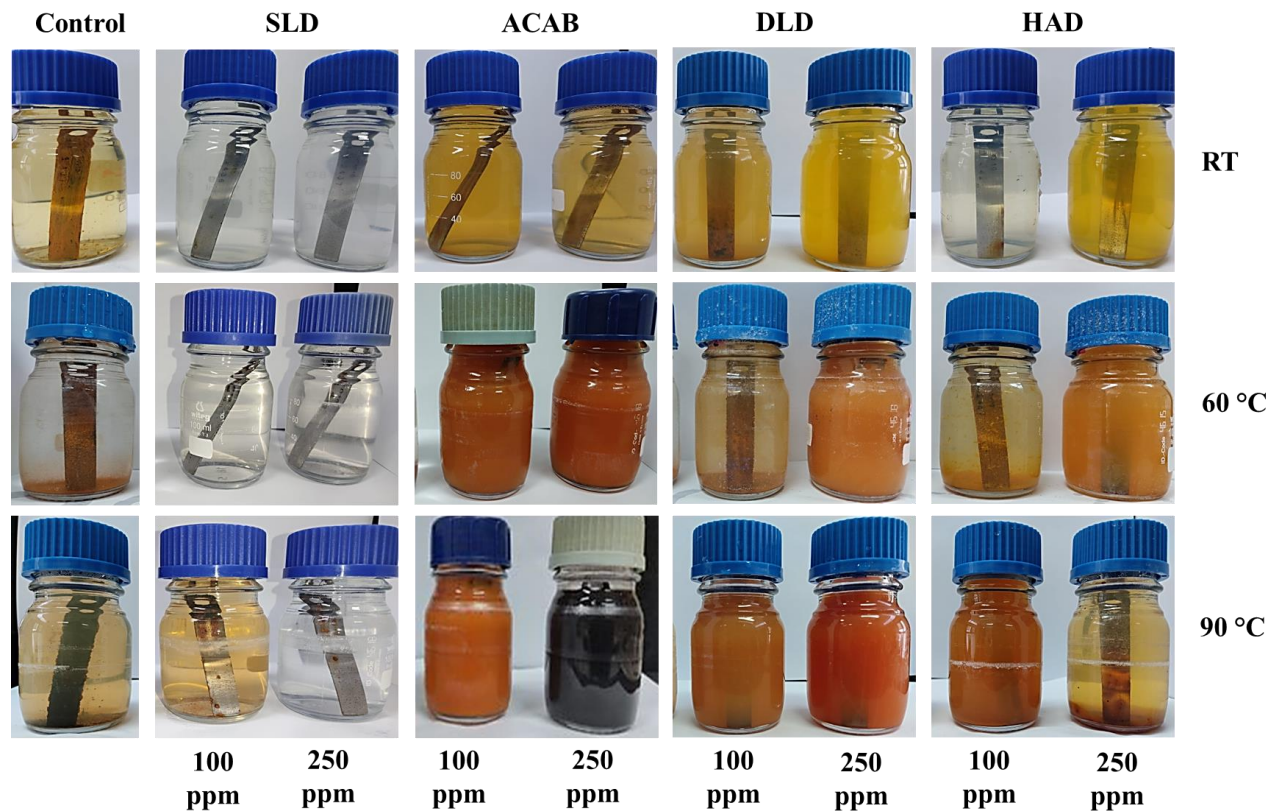


Figure 5.26. Visual representation of the experiments in the presence of non-phosphonate inhibitors in DI water at RT, 60 °C and 90 °C.

Effect of concentration

Figure 5.27 presents correlations between concentration and corrosion rate values in the presence of each inhibitor at RT, 60 °C and 90 °C. SLD shows lower corrosion rates as concentration increases, at all temperatures. At RT, ACAB shows the same trend, however when the temperature is raised to 60 °C and 90 °C, increased concentration results in higher corrosion rates. In the case of DLD, at RT and 60 °C, corrosion rate decreases as the concentration increases, but at 90 °C slightly higher corrosion rates are observed. For the experiments in the presence of HAD at RT, the increase in concentration appears to have no effect on the corrosion rate. On the contrary, raising the temperature to 60 °C slightly lowers the corrosion rate at higher inhibitor concentration. At 90 °C, the same trend is evident, but this time the decrease is more significant.

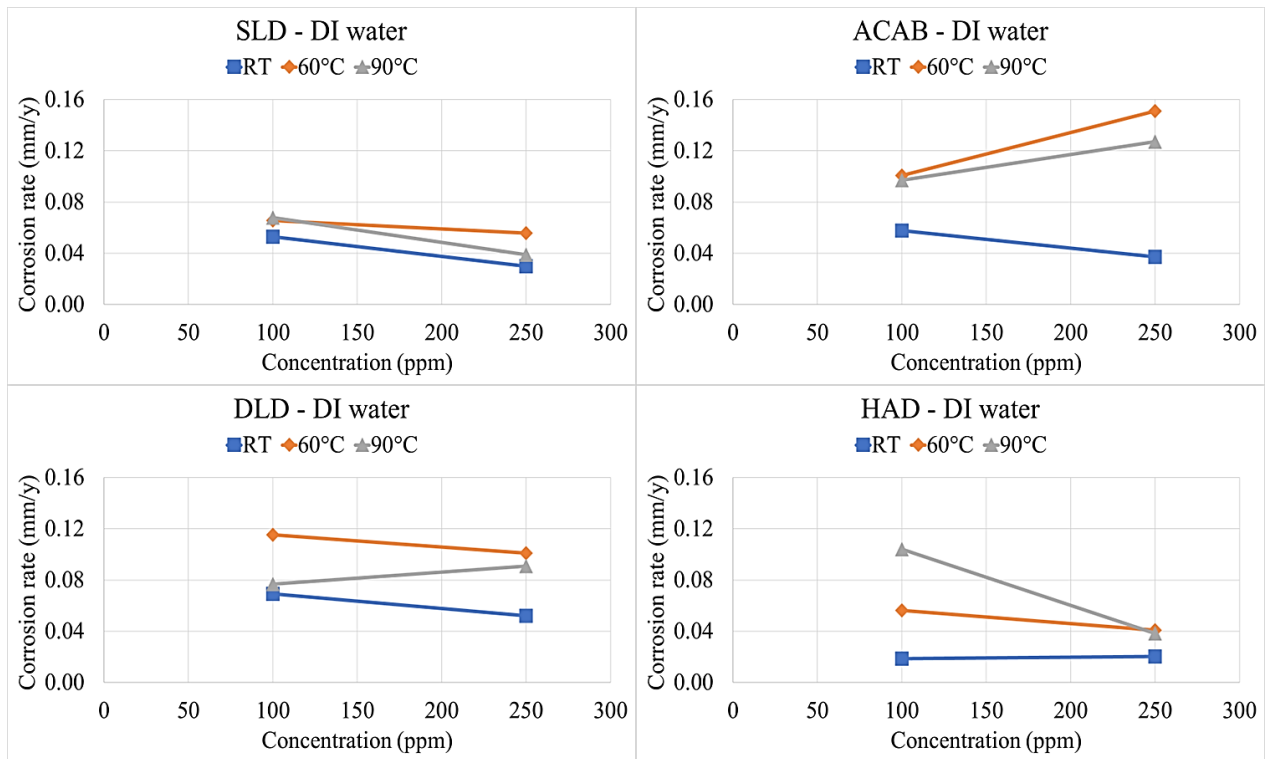


Figure 5.27. The correlation between corrosion rates and inhibitor concentration for non-phosphonates in DI water. Color codes: *blue* RT, *orange* 60 °C and *grey* 60 °C.

Additional corrosion experiments at RT were performed with several non-phosphonate inhibitors at concentrations < 100 ppm and > 250 ppm. Figure 5.28 shows the correlation between corrosion rates and inhibitor concentration under these conditions. It should be noted that, in some cases, corrosion rates of different inhibitors are exactly the same or very close and they are not clearly visible in the graph. Therefore, Table 5.14 shows the numerical values of the corrosion rates to aid the reader.

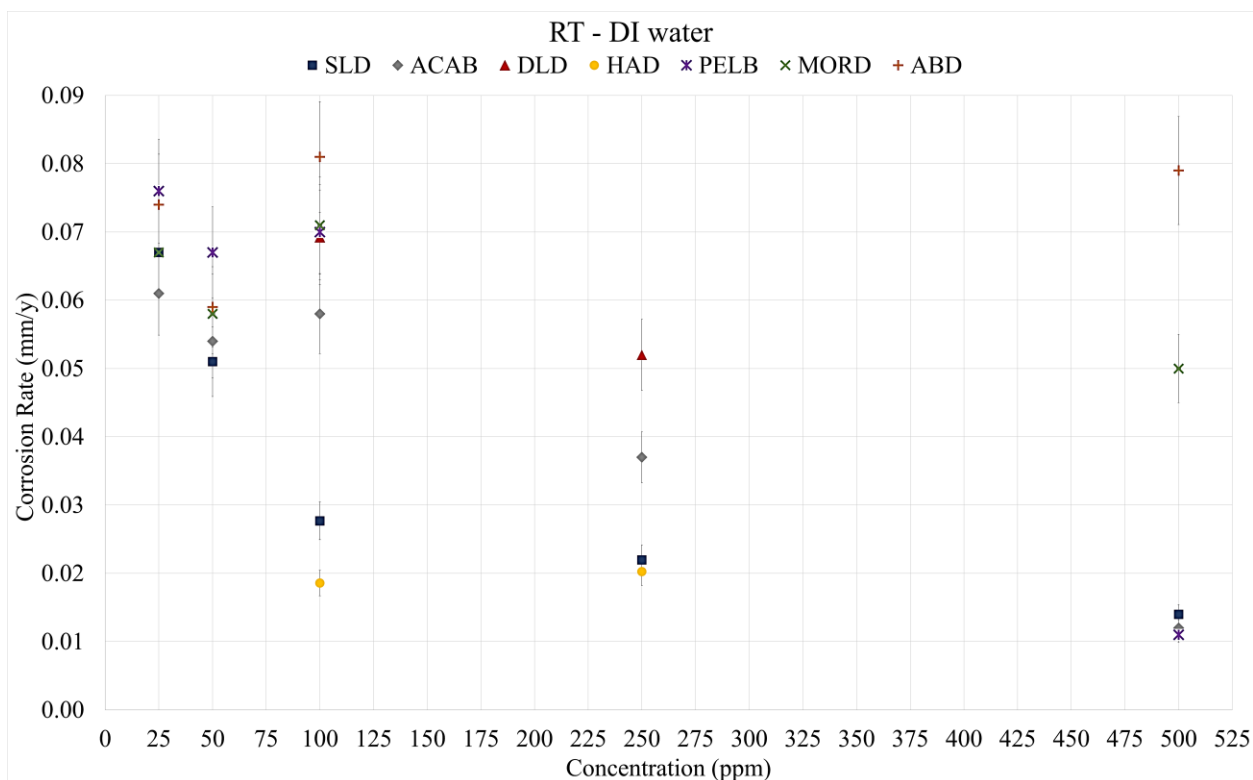


Figure 5.28. Correlation between corrosion rates and inhibitor concentration for non-phosphonates in DI water at RT. Color codes: *blue* SLD, *grey* ACAB, *red* DLD, *yellow* HAD, *purple* PELB, *green* MORD and *brown* ABD.

Table 5.14. Corrosion rates obtained in the presence of non-phosphonates at several dosages.

Inhibitor	Concentration (ppm)				
	25	50	100	250	500
	Corrosion Rates (mm/y)				
SLD	0.067	0.051	0.028	0.022	0.014
ACAB	0.061	0.054	0.058	0.037	0.012
DLD	-	-	0.069	0.052	-
HAD	-	-	0.019	0.020	-
PELB	0.076	0.067	0.070	-	0.011
MORD	0.067	0.058	0.071	-	0.050
ABD	0.074	0.059	0.081	-	0.079

Increasing SLD concentration causes a gradual decrease in corrosion rate values. Inhibition efficiency, starting from -12 % at the lowest concentration, reaches 77 % at the highest concentration. In the case of ACAB, the same general pattern is observed. Specifically, inhibition from -2 % at 25 ppm inhibitor concentration reaches 80 % at 500 ppm, although the corrosion rate at 100 ppm dosage is slightly higher than the corrosion rate of 50 ppm. The same conclusion is valid for PELB, with % inhibition values being equal to -27 % at 25 ppm and 82 % at 500 ppm. The increase in concentration does not significantly affect the performance of ABD, as it presents similarly high corrosion rates in most cases, except in the case of 50 ppm, in which it shows 2 % inhibition. MORD shows the lowest corrosion rate value, therefore its highest inhibition efficiency (17 %), for the highest concentration, followed by the dosage of 50 ppm. As already mentioned, DLD presents its lowest corrosion rate at its highest concentration (13 %), while HAD presents similar behavior at both concentrations, approximately 70 %. Overall, 500 ppm inhibitor concentration is beneficial for the non-phosphonate inhibitors tested, with the sole exception of ABD. The highest inhibition efficiency percentages are observed in the presence of SLD, ACAB and PELB equal to 77 %, 80 % and 82 % respectively.

At 130 °C (HP-HT conditions), corrosion experiments at 250 ppm and 500 ppm inhibitor concentration were performed. Figure 5.29 shows the results from these experiments. Overall, non-phosphonate inhibitors show reduced anti-corrosion performance in such conditions. Almost every case, non-phosphonates show corrosive behavior, giving higher corrosion rates than the control. The only exception is the case of 250 ppm MORD, showing 12 % inhibition. Increase in SLD and PELB concentration is beneficial, resulting in lower corrosion rates than those at the lower dosages, although still higher than the corresponding control. For the rest of the inhibitors tested under these conditions, increased concentration results in even higher corrosion rates.

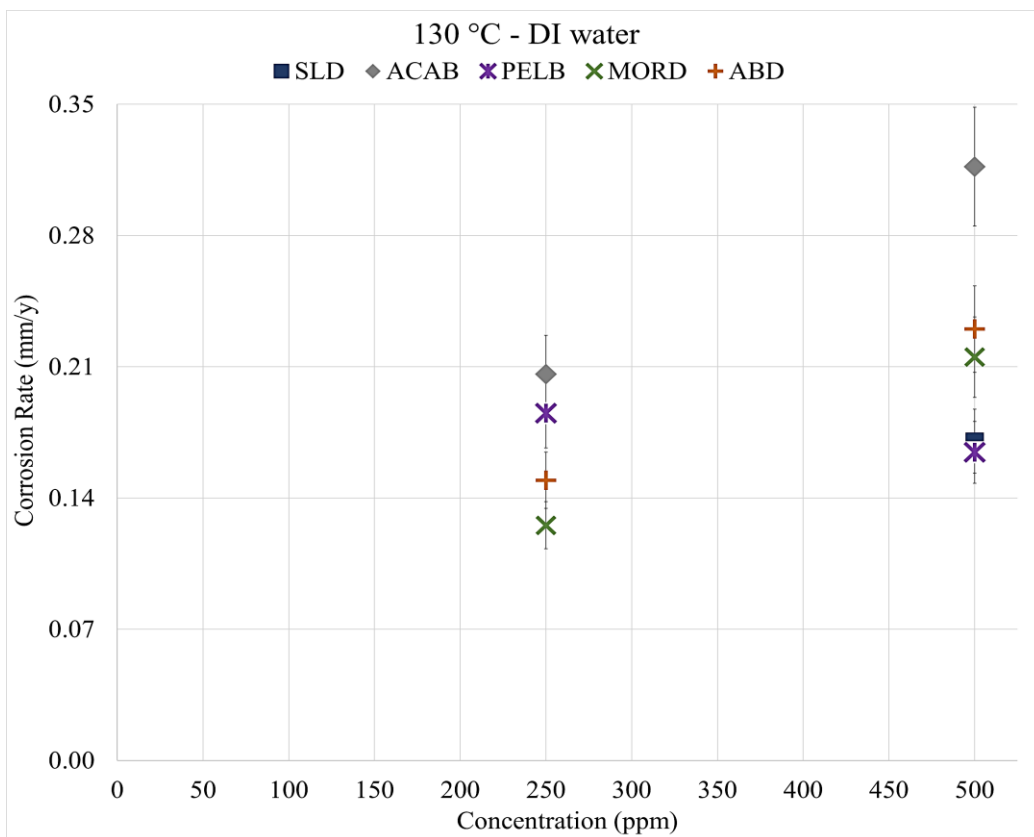


Figure 5.29. Correlation between corrosion rates and inhibitor concentration for non-phosphonates in DI water at 130 °C. Color codes: *blue* SLD, *grey* ACAB, *purple* PELB, *green* MORD and *brown* ABD.

Effect of temperature

Figure 5.30 presents the correlation between temperature and corrosion rate values obtained in the presence of each inhibitor at 100 ppm and 250 ppm concentrations. Regarding the 100 ppm dosage, 60 °C is the most favorable temperature for SLD, followed by 90 °C and then RT. ACAB and HAD present lower inhibition efficiencies, as the temperature increases. In the case of DLD, experiments performed at 90 °C present the highest % inhibition, albeit close to zero. At 250 ppm inhibitor concentration, ACAB, DLD and HAD show lower performance as the temperature decreases. On the contrary, SLD exhibits better behavior as the temperature is raised from RT to 90 °C.

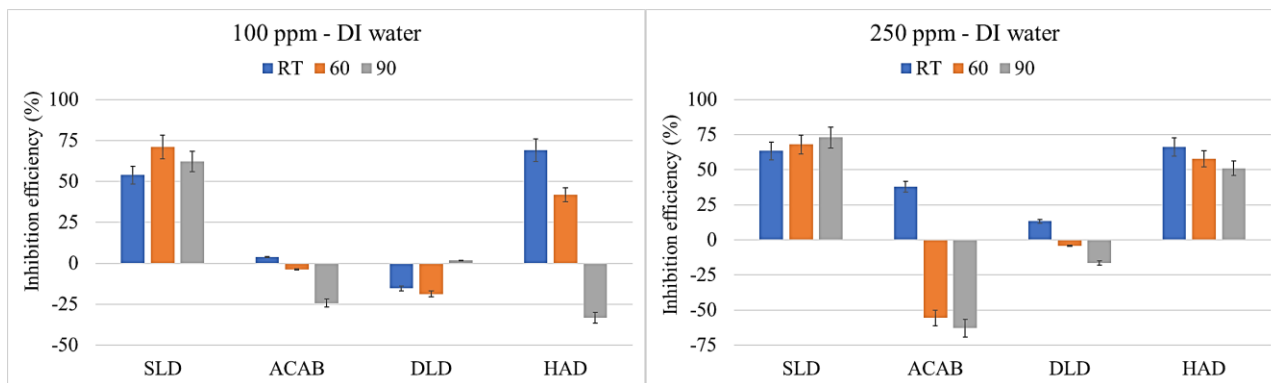


Figure 5.30. Correlation between corrosion rates and temperature for non-phosphonates in DI water for inhibitor concentrations: a. 100 ppm (left) and b. 250 ppm (right). Color codes: *blue* RT, *orange* 60 °C and *grey* 90 °C.

Effect of mechanical stirring

Corrosion experiments under stirring conditions were performed at RT in large glass bottles of total volume of the working solution 1200 mL. In this case, specimens did not rest at the bottom of the bottle to avoid any contact with the magnetic stirrer. Two different stirring rates were selected (200 rpm and 400 rpm) and the experiments were also repeated under non-stirring conditions for comparison. The dosage of each inhibitor was 100 ppm.

Figure 5.31 presents the corrosion rates and the inhibition efficiencies of three representative inhibitors. It is worth noting that the corrosion rate for the control under non stirring conditions is 4-5 times lower than that under stirring. Also, the control at 200 rpm shows a higher corrosion rate than that at 400 rpm. Comparing the results between “no stirring” and the two different stirring rates, a trend of enhanced anticorrosion efficiencies is observed as the stirring rate increases in the case of HAD and SLD. In the case of ACAB, similar behavior is noted regardless of the stirring conditions. However, ACAB appears to perform better when the experiment is static, followed by the experiments at the 400 rpm stirring rate. Finally, ACAB at 200 rpm shows the highest corrosion rate and the lowest inhibition efficiency. Overall, no universal trend was established regarding the relationship of anti-corrosion efficiency with stirring conditions. We conclude that the results are inhibitor specific.

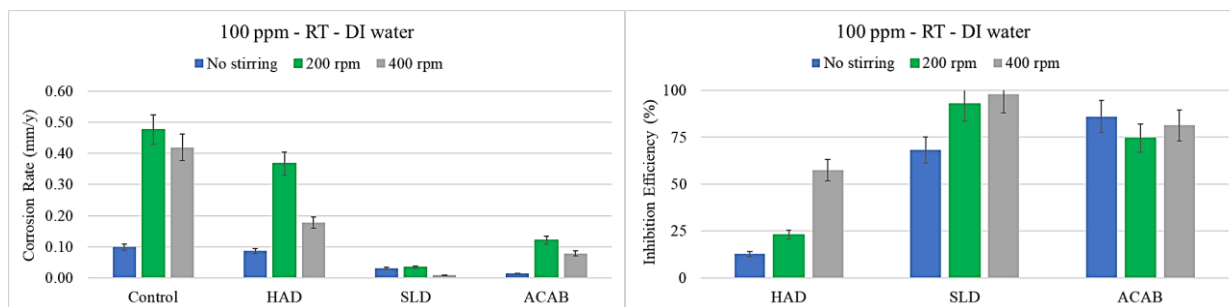


Figure 5.31. Correlation between corrosion rates and stirring rates (left) and inhibition efficiency and stirring rates (right) for non-phosphonates in DI water at RT. Color codes: *blue* no stirring, *green* 200 rpm and *grey* 400 rpm.

The glass containers with the specimens in the presence of non-phosphonate inhibitors at the end of the experimental period are presented in Figure 5.32. Visual observations are in full agreement with the observed corrosion rates.

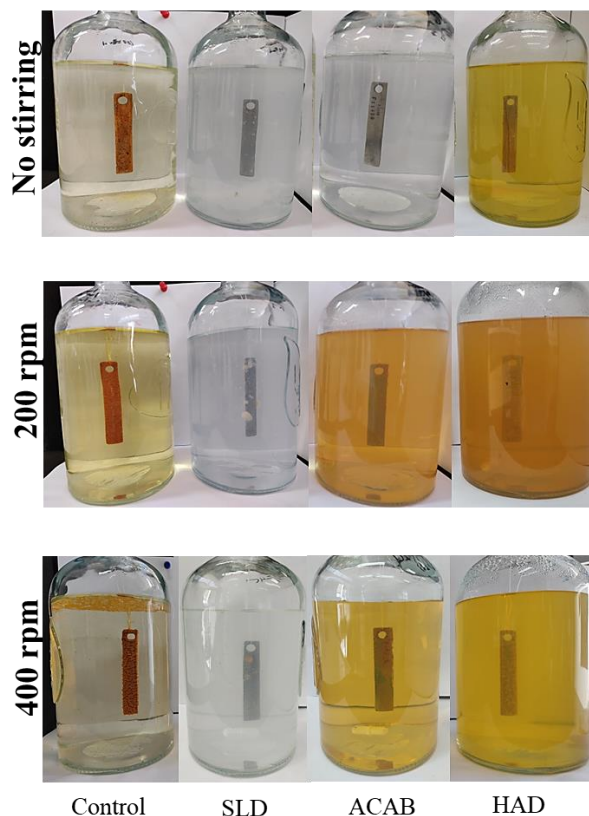


Figure 5.32. Visual representation of the experiments at different stirring rates.

Effect of sulfides

Corrosion experiments in the presence of sulfides were also performed at RT. Two types of experiments were performed in order to evaluate corrosion aggressiveness and inhibitor performance, both in the presence and in the absence of dissolved oxygen in solution, but with the presence of sulfides. Thus, in addition to the experiments in glass bottles with caps, experiments were performed under argon atmosphere as well. In order to remove the oxygen from the working solution, before each experiment degassing was performed for at least 30 minutes by bubbling argon.

Sulfide concentrations, before and after the experiments, were measured with the methylene blue method (see Chapter 2.3). Figure 5.33 gives the results from corrosion experiments in the presence of 50 ppm sulfides (expressed as “ppm S”), for three different inhibitors at 100 ppm and 250 ppm dosages.

In the presence of both oxygen and sulfides in solution, higher corrosion rates are observed than in the case pure argon atmosphere. ACAB appears to be the most effective inhibitor in the presence of oxygen, followed by HAD, for both concentrations, however, their efficiency is enhanced at higher dosages. SLD shows the highest corrosion rates, presenting even higher values upon dosage increase, therefore it is the worst candidate as corrosion inhibitor under these conditions.

Under argon atmosphere, HAD exhibits the best anti-corrosion performance, regardless of its concentration. For 100 ppm dosage of each inhibitor, SLD and ACAB show similar behavior. On the contrary, increasing inhibitor concentration causes a drop in SLD efficiency, reaching essentially zero inhibition. Finally, ACAB presents slightly higher anticorrosion efficiency at the higher dosage.

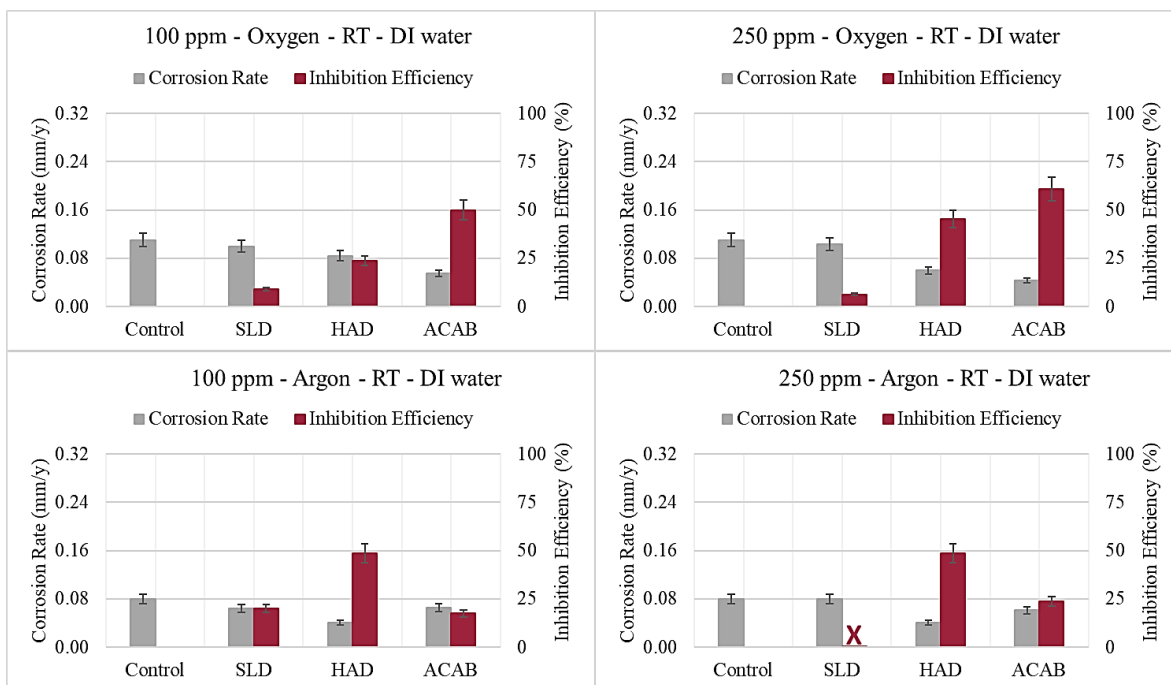


Figure 5.33. Results obtained in the absence (control) and presence of non-phosphonates in DI water at RT in the presence of 50 ppm S^{2-} for: a. 100 ppm inhibitor concentration under oxygen (upper left), b. 250 ppm inhibitor concentration under oxygen (upper right), c. 100 ppm inhibitor concentration under argon (bottom left) and d. 100 ppm inhibitor concentration under argon (bottom right). Color codes: *grey* Corrosion rates and *burgundy* Inhibition efficiency percentages.

The glass containers with the specimens in the presence of non-phosphonate inhibitors at the end of the experimental period are presented in Figure 5.34. Visual observations are in agreement with the corresponding trends in corrosion rates. The sole exception comes from the experiments in the presence of 100 ppm inhibitor under argon atmosphere. In the case of ACAB, a visible black precipitate is observed, most of which can be seen at the bottom of the flask. Note that the green color in the working solutions is a strong indication of the presence of Fe(II), while black precipitates are consistent with the presence of Iron(II) sulfide(s).

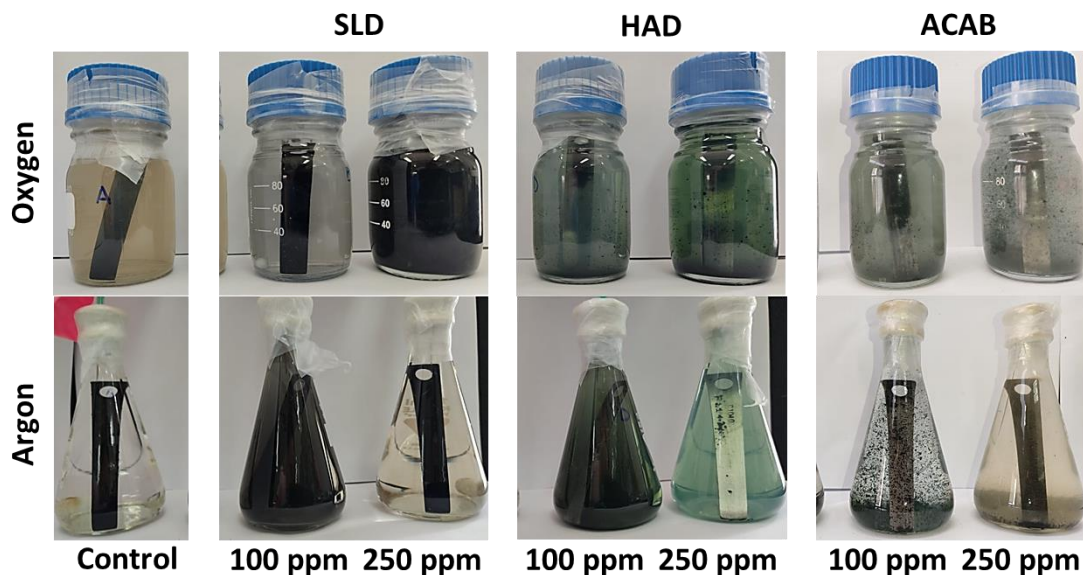


Figure 5.34. Visual representation of the corrosion experiments in the presence of sulfides.

5.3 Concluding remarks

5.3.1 Phosphonate inhibitors

In this chapter, corrosion experiments were performed in DI water at pH 7. The anti-corrosion efficiency of the inhibitors was evaluated at different temperatures and several concentrations. In addition, corrosion experiments in the presence of non-phosphonate inhibitors were performed under stirring conditions and in the presence of sulfides. Their performance was evaluated by the gravimetric methodology, according to the NACE standard method ^[9]. The results of the colorimetric method of total iron determination point to deviations from the results based on mass loss, thus this method needs further optimization as a corrosion quantification method.

Regarding the concentration of the phosphonate inhibitors, 0.01 mM and 0.1 mM are beneficial for the anti-corrosion efficiency of C2, C4, C6 and C8 in most cases, while C12 appears to perform better at higher concentrations. Furthermore, no universal trend between temperature and inhibition efficiency was established. However, it is observed that the performance of C4, C6 and C8 at higher concentrations is affected by the increase in temperature, resulting in corrosive behavior in most cases. Visual observations are consistent with the fact that increasing

tetraphosphonate dosage results in gradually “cleaner” surfaces. The metal specimens from the experiments at high inhibitor concentrations, give either low iron levels or are rust-free. Comparing these specimens with the respective corrosion rates, it is concluded that tetraphosphonates act as *surface cleaners* at higher dosages. C12 appears to be the only inhibitor giving high inhibition at high temperatures and low inhibition at RT. Finally, a universal correlation between structure and anticorrosion efficiency cannot be reliably discerned. However, the best candidate as a corrosion inhibitor under these conditions appears to be the “largest” molecule, C12.

Experiments were also performed in the presence of two different metal ions. Calcium and magnesium were added to the working solutions (in 1:1 molar ratio to each inhibitor). It was found that the synergy between metal ions and phosphonates was beneficial under several conditions. Overall, the presence of these metal ions enhanced the inhibitory activity of the tetraphosphonates at 130 °C and high inhibitor concentrations. In addition, C6 and C12 exhibit higher anticorrosion efficiency at 60 °C, again at higher dosages. Specifically, the addition of calcium ions resulted in higher inhibition for C2 and C6 at 90 °C. In the presence of both C12 and calcium, formation of precipitates was observed. They were isolated and characterized by ATR-IR spectroscopy. The corresponding spectra are provided in Chapter 8.6. The vibrational bands of the phosphonate groups appear to be shifted, compared to the respective spectrum of pristine C12. This is an indication of a Ca-C12 precipitate formation. In addition, EDS results (see Chapter 8.6) confirmed the presence of phosphorus in the chemical composition.

5.3.2 Non-phosphonate inhibitors

At RT, HAD exhibited the lowest corrosion rates at both concentrations, followed by SLD, while DLD is the least effective inhibitor under these conditions. Increase in temperature to 60 °C enhanced the anticorrosion efficiency of SLD for both dosages and HAD was again the second best inhibitor. The gravimetric measurements and the iron determination data are in agreement regarding the anticorrosion efficiency of the inhibitors. The same conclusion is valid at 90 °C. Regarding 100 ppm inhibitor concentration, SLD appears to be more effective at higher temperatures than at RT. ACAB and HAD present lower inhibition efficiency as the temperature increases. At 250 ppm inhibitor concentration, ACAB, DLD and HAD showed lower performance

as the temperature decreases. On the contrary, SLD exhibits better behavior as the temperature is raised from RT to 90 °C. Overall, visual observations are in agreement with the corresponding results of the gravimetric measurements and of the iron determination test data.

In addition, experiments in the presence of non-phosphonate inhibitors were performed under stirring conditions. It is worth noting that corrosion rate of the control under non-stirring conditions is 4-5 times lower than that under stirring, while control experiment performed at 200 rpm shows higher corrosion rate than the control at 400 rpm. Overall, no global trend was established regarding the anti-corrosion efficiency. Each inhibitor exhibits different behavior. For example, a trend of enhanced anticorrosion efficiencies as the stirring rate increasing is observed in the case of HAD and SLD. On the contrary, ACAB appears to perform better when the experiment is static. Visual observations are in full agreement with the corresponding corrosion rates.

Finally, results from corrosion experiments in the presence of sulfides point to the conclusion that when both oxygen and sulfides are present in solution, corrosion rates are higher than those under argon. ACAB appears to be the most effective inhibitor in the presence of oxygen, while SLD is the least effective. Under argon, HAD exhibits the highest inhibition efficiency. Overall, visual observations are in agreement with the corresponding corrosion rates.

5.4 References

1. Faria, D.; Antunes, R. Characterization of Corrosion Products Formed on Steels in the First Months of Atmospheric Exposure. *Materials Research* **2003**, 403-408.
2. Bowles, J.F.W. *Oxides* in *Encyclopedia of Geology*. Elias, S.A.; Alderton, D.H.M.; Academic Press: London; San Diego, Ca, United States, **2021**.
3. Cui, H.; Ren, W.; Lin, P.; Liu, Y. Structure Control Synthesis of Iron Oxide Polymorph Nanoparticles through an Epoxide Precipitation Route. *Journal of Experimental Nanoscience* **2012**, 8 (7-8), 869–875.
4. Schwertmann, U.; Cornell, R. M. Iron Oxides in Laboratory. *Soil Science* **1993**, 156 (5), 369.
5. Raman, A.; Kuban, B.; Razvan, A. The Application of Infrared Spectroscopy to the Study of Atmospheric Rust Systems—I. Standard Spectra and Illustrative Applications to Identify Rust Phases in Natural Atmospheric Corrosion Products. *Corrosion Science* **1991**, 32 (12), 1295–1306.
6. Robertson, J.M. Crystal Structures by R.W.G. Wyckoff. *Acta Crystallographica* **1954**, 7 (12), 867–867.
7. Wechsler, B.A.; Lindsley, D.H.; Prewitt, C. T. Crystal Structure and Cation Distribution in Titanomagnetites (Fe₃-XTi_xO₄). *American Mineralogist* **1984**, 69 (7-8), 754–770.
8. Lavagna, L.; Nisticò, R.; Musso, S.; Pavese, M. Hydrophobic Cellulose Ester as a Sustainable Material for Simple and Efficient Water Purification Processes from Fatty Oils Contamination. *Wood Science and Technology* **2018**, 53 (1), 249–261.
9. NACE Standard TM0169-95 (Item No. 21200), National Association of Corrosion Engineers, Houston TX, U.S.A. (www.nace.org).
10. Gendel, Y.; Lahav, O. Accurate Determination of Fe(II) Concentrations in the Presence of a Very High Soluble Fe(III) Background. *Applied Geochemistry* **2008**, 23 (8), 2123–2129.
11. Elmagirbi, A.; Sulistyarti, H.; Atikah, A. Study of Ascorbic Acid as Iron(III) Reducing Agent for Spectrophotometric Iron Speciation. *The Journal of Pure and Applied Chemistry Research* **2012**, 1 (1), 11–17.
12. Veres, A.; Reinhard, G.; Kalman, E. Chemical passivation of ferrous materials in presence of salts of phosphonic acids, *Brit. Corros. J.* **1992**, 27, 147–150.

13. Demadis, K.D.; Lykoudis, P.; Raptis, R.G.; Mezei, G. Phosphonopolycarboxylates as Chemical Additives for Calcite Scale Dissolution and Metallic Corrosion Inhibition Based on a Calcium–Phosphonotricarboxylate Organic–Inorganic Hybrid. *Cryst. Growth Des.* **2006**, *6*, 1064–1067.
14. Demadis, K.D.; Katarachia, S.D.; Koutmos, M. Crystal Growth and Characterization of Zinc–(Amino-Tris-(Methylenephosphonate)) Organic–Inorganic Hybrid Networks and Their Inhibiting Effect on Metallic Corrosion. *Inorganic Chemistry Communications* **2005**, *8* (3), 254–258.
15. Demadis, K.D.; Mantzaridis, C.; Raptis, R.G.; Mezei, G. Metal–Organotetraphosphonate Inorganic–Organic Hybrids: Crystal Structure and Anticorrosion Effects of Zinc Hexamethylenediaminetetrakis(Methylenephosphonate) on Carbon Steels. *Inorganic Chemistry* **2005**, *44* (13), 4469–4471.
16. Demadis, K.D.; Mantzaridis, C.; Lykoudis, P. Effects of Structural Differences on Metallic Corrosion Inhibition by Metal–Polyphosphonate Thin Films. *Industrial & Engineering Chemistry Research* **2006**, *45* (23), 7795–7800.
17. Demadis, K.D.; Papadaki, M.; Raptis, R.G.; Zhao, H. 2D and 3D Alkaline Earth Metal Carboxyphosphonate Hybrids: Anti-Corrosion Coatings for Metal Surfaces. *Journal of Solid State Chemistry* **2008**, *181* (3), 679–683.
18. Demadis, K.D.; Papadaki, M.; Raptis, R.G.; Zhao, H. Corrugated, Sheet-like Architectures in Layered Alkaline-Earth Metal *R,S*-Hydroxyphosphonoacetate Frameworks: Applications for Anticorrosion Protection of Metal Surfaces. *Chemistry of Materials* **2008**, *20* (15), 4835–4846.
19. Demadis, K.D.; Barouda, E.; Raptis, R.G.; Zhao, H. Metal Tetraphosphonate “Wires” and Their Corrosion Inhibiting Passive Films. *Inorganic Chemistry* **2008**, *48* (3), 819–821.
20. Papadaki, M.; Demadis, K.D. Structural Mapping of Hybrid Metal Phosphonate Corrosion Inhibiting Thin Films. *Comments on Inorganic Chemistry* **2009**, *30* (3-4), 89–118.
21. Demadis, K.D.; Papadaki, M. Single-Crystalline Thin Films by a Rare Molecular Calcium Carboxyphosphonate Trimer Offer Prophylaxis from Metallic Corrosion. *ACS Applied Materials & Interfaces* **2010**, *2* (7), 1814–1816.
22. Colodrero, R.M.P.; Angeli, G.K.; Bazaga-Garcia, M.; Olivera-Pastor, P.; Villemin, D.; Losilla, E.R.; Martos, E.Q.; Hix, G.B.; Aranda, M.A.G.; Demadis, K.D.; Cabeza, A.

Structural Variability in Multifunctional Metal Xylenediaminetetraphosphonate Hybrids. *Inorganic Chemistry* **2013**, 52 (15), 8770–8783.

23. Demadis, K.D.; Papadaki, M.; Varouchas, D. Metal Phosphonate Anti-Corrosion Coatings. in *Green Corrosion Chemistry and Engineering: Opportunities and Challenges*, Sharma, S.K. Editor, Wiley-VCH Verlag GmbH & Co., Germany **2012**, Chapter 9, pp. 243-296.
24. Demadis, K.D.; Angeli, G. “Good Scale”–“Bad Scale”. How Metal–Phosphonate Materials Contribute to Corrosion Inhibition in *Mineral Scales in Biological and Industrial Systems*, Taylor and Francis, New York: **2013**, Chapter 19, pp. 353-370.

Chapter 6: A combined corrosion and scale inhibition study

6.1 Introduction

In addition to the corrosion problems, it is well known that industrial systems can suffer from scale deposition. The dissolved species in an aqueous solution, due to a change in the conditions, such as pH, temperature or supersaturation, can precipitate as solids resulting in their deposition and scale formation on the surfaces of the equipment ^[1]. Like the formation of the different types of corrosion products, the diverse geothermal conditions affect the type of scale deposits ^[2]. Amongst the different scale mitigation strategies ^[3,4,5], the use of scale inhibitors is one of the most advantageous. Phosphonate-based additives are the most effective scale inhibitors ^[6,7].

The prevention of scale formation is beyond the main scope of this research, however the identification of the presence of calcite in the XRD patterns of the control corrosion experiments in artificial Brine 1 (see Chapter 3), created the concept of a set of combined experiments in order to achieve a possible simultaneous corrosion and scale inhibition under these conditions. Phosphonate-based inhibitors are reported to play a significant role in the prevention of CaCO₃ formation ^[8]. It is important to note that, in the corrosion experiments so far, the addition of the inhibitors took place after the preparation of the artificial brine with the selected water chemistry. However, in order to study the efficiency of phosphonates against CaCO₃ formation, the phosphonate inhibitors were added in a solution containing only the scaling cations. By following this procedure, the calcium ions become unavailable to the scale anions, due to the chelating ability of the phosphonates ^[9,10].

6.2 Calcium tolerance

In the presence of a phosphonate inhibitor in a cation-rich solution, the risk of the precipitation of a “metal-phosphonate” complex is high, particularly when calcium exists at high concentrations. If that happens, the “active” inhibitor concentration will be decreased. Hence, calcium compatibility of a certain inhibitor is typically the main issue ^[8,11-15]. Therefore, calcium tolerance was studied for the members of the tetraphosphonate family under the same conditions as the corrosion inhibition studies. Two phosphonate concentrations were tested in 120 mL of deionized

water. Next, 260 ppm of Ca^{2+} were added to the aqueous inhibitor solutions. The pH of each solution was adjusted to 7. The mixtures were shaken well and then left undisturbed at RT for 7 days. The appearance of the solution was detected and reported at $t = 1$ h and at the end of 1 week. In addition to the visual observations, the turbidity of the mixtures was measured as well, by the Formazin method (expressed in FAU units) using a HACH DR/890 spectrophotometer. The experimental error is ± 1 %. Deionized water is expected to have 0 FAU and is used as a blank solution for zeroing. For the calcium compatibility test procedure, each working solution was slowly transferred to a 25 mL, 1 cm path length glass sample cell and left undisturbed for 30 minutes before the measurement. Table 6.1 shows the results of the tolerance study. At $t = 1$ h, all experiments produced clear solutions with no turbidity, except in the case of 1 mM of C12 which showed a hazy solution and 30 FAU turbidity. At $t = 168$ h, a hazy solution was observed for 1 mM of C2 with 35 FAU turbidity. In addition, in the presence of 1 mM of C12, the formation of a precipitate was observed, although the corresponding solution showed 30 FAU turbidity.

Table 6.1. Calcium tolerance study for phosphonates. Calcium concentration is 260 ppm.

		C2		C4		C6		C8		C12	
c (mM)	time (hours)	Visual	Turbidity (FAU)	Visual	Turbidity (FAU)	Visual	Turbidity (FAU)	Visual	Turbidity (FAU)	Visual	Turbidity (FAU)
0.10	1	Clear	0	Clear	0	Clear	0	Clear	0	Clear	0
	168	Clear	0	Clear	0	Clear	0	Clear	0	Clear	0
1.00	1	Clear	0	Clear	0	Clear	0	Clear	0	Hazy	30
	168	Hazy	35	Clear	5	Clear	1	Clear	2	Precipit	13

6.3 Results and Discussion

This section discusses the results from experiments performed in the presence of phosphonate-based inhibitors in Brine 1 at RT for two inhibitor concentrations (0.1 mM and 1 mM). Table 6.2 contains the chemical composition of the artificial Brine 1. The different aqueous inhibitor solutions were prepared by diluting the calculated volumes of the corresponding inhibitor stock

solutions in an aqueous solution which contained only the desired volume of the calcium stock solution A (see Chapter 2.4 for the preparation of stock), followed by the pH adjustment at 7, if needed. Then, the slow addition of the desired volumes of the stock solutions of the anions (stock solution B, C and D in Chapter 2.4) was followed carefully so that the pH values did not exceed 7, because calcium carbonate formation is enhanced at pH above 7. The total volume of each experiment was 120 mL. These specific conditions were selected in order to study the dual inhibition in a representative geothermal fluid. Hence, calcium is in excess compared to both inhibitor dosages.

Table 6.2. Chemical composition of Brine 1.

Ca ²⁺	Cl ⁻	SO ₄ ²⁻	HCO ₃ ⁻
260 ppm	1000 ppm	200 ppm	1200 ppm

For the corrosion inhibition, the NACE standard procedure was followed, as before. Each specimen was weighed before and after the experiment, after being first dried and cleaned using abrasive paper ^[16]. Corrosion rates were calculated according to CR formula (see Equation 1 in Chapter 2.3). Corrosion rate values obtained from the experiments performed under these conditions are presented in Table 6.3 and Figure 6.1. Inhibition efficiencies (in %) were calculated according to Equation 2, as given in Chapter 2.3.

Table 6.3. Corrosion rates and inhibition efficiency percentages for the experiments in Brine 1.

Inhibitor c (mM)	C2		C4		C6		C8		C12	
	CR (mm/y)	IE (%)	CR (mm/y)	IE (%)	CR (mm/y)	IE (%)	CR (mm/y)	IE (%)	CR (mm/y)	IE (%)
<i>Control</i>	0.078	0	0.078	0	0.078	0	0.078	0	0.078	0
0.1	0.064	19	0.073	7	0.043	45	0.060	23	0.035	55
1	0.017	78	0.003	96	0.001	99	0.012	85	0.012	85

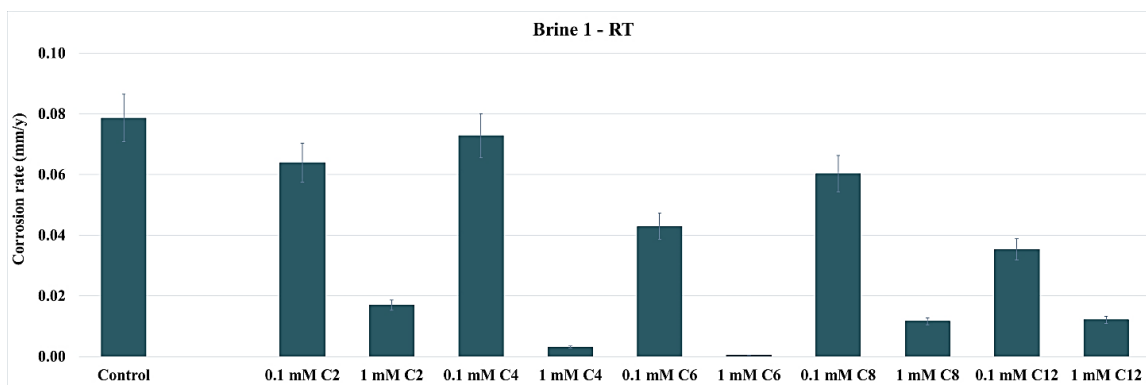


Figure 6.1. Corrosion rates obtained from the experiments in Brine 1 at RT.

Regarding scale inhibition, the well-established EDTA titration method for the quantification of calcium was followed [17,18]. Table 6.4 and Figure 6.2 show the calcium concentrations as determined by the calcium titration method, at the end of 1 week. Inhibition efficiencies (in %) were calculated according to Equation 4, as given in Chapter 2.3.

Inhibitor	C2		C4		C6		C8		C12	
	Ca ²⁺ (ppm)	IE (%)	Ca ²⁺ (ppm)	IE (%)	Ca ²⁺ (ppm)	IE (%)	Ca ²⁺ (ppm)	IE (%)	Ca ²⁺ (ppm)	IE (%)
<i>Control</i>	136	0	136	0	136	0	136	0	136	0
0.1	260	91	220	62	236	74	224	65	208	53
1	252	85	260	91	224	65	244	79	248	82

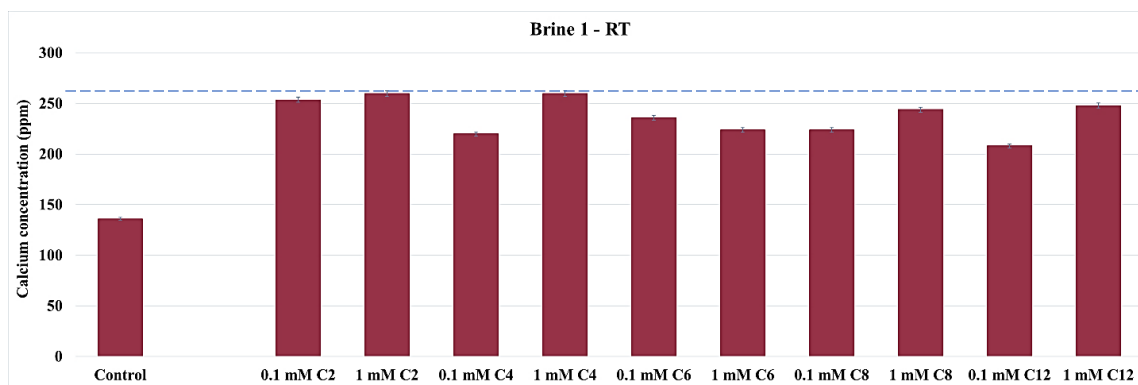


Figure 6.2. Calcium concentrations as determined for the experiments in Brine 1 at RT at the end of 1 week. The dashed line represents the initial calcium concentration.

Even though this strategy could affect the anti-corrosion efficiency of the inhibitors due to possible Ca^{2+} -phosphonate precipitation, the results of the dual inhibition study showed that most of the members of the tetraphosphonate family successfully protected the metal surfaces against corrosion. Regarding corrosion, the higher inhibitor concentration enhanced the anti-corrosion efficiency of all of the inhibitors, leading to high performance for the protection of carbon steel under these conditions. Importantly, the inhibitory activity of C4 and of C6 is outstanding, reaching 96 % and 99 % inhibition, respectively.

As stated above, the initial calcium concentration in the brine was 260 ppm. After 7 days, the calcium concentration of the control experiment was 136 ppm, which means that, even under “low stress” conditions (pH = 7, RT), 48 % of the calcium ions reacted with the bicarbonate ions resulting in the formation of calcium carbonate. Regarding the experiments in the presence of the phosphonates, the increase in concentration appears to be beneficial for C4, C8 and C12, while C2 is the best scale inhibitor under these conditions. The inhibition performance (%) data against both corrosion and CaCO_3 inhibition are shown in Figure 6.3. Collectively, the % anti-corrosion and anti-scaling efficiencies are at their highest values in the case of 1 mM of C4, reaching 96 % and 91 % inhibition, respectively, followed by 1 mM of C2, reaching 78 % and 85 % inhibition, respectively. Visual observations verify the corrosion inhibition studies (see Table 6.5), as the specimens of the experiments in the presence of the inhibitors at the higher dosages showed more protected surfaces.

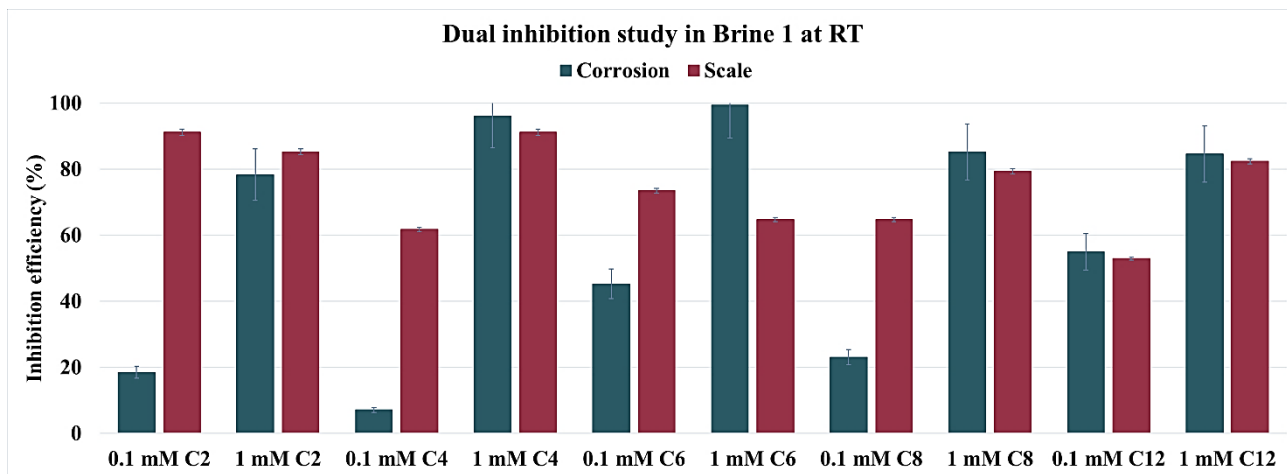


Figure 6.3. Inhibition efficiency (%) for the experiments in Brine 1 at RT. Color code: *blue* Corrosion inhibition and *purple* Scale inhibition.

Table 6.5. Visual representation of the specimens from the experiments Brine 1.

	0.1 mM	1 mM
Control		
C2		
C4		
C6		
C8		
C12		

6.4 Concluding remarks

In this chapter, the results of the combined corrosion and scale inhibition study at RT are reported. Two inhibitor concentrations were selected (0.1 mM and 1 mM). The members of the tetraphosphonate family appear to be effective dual corrosion and CaCO_3 inhibitors under these conditions. Corrosion inhibition was determined according to the NACE standard procedure, while regarding scale inhibition, the EDTA titration method for calcium quantification was followed. Even though 1 mM of C6 exhibit outstanding anti-corrosion performance, reaching 99 % inhibition, concerning the prevention of CaCO_3 formation, C6 for 1 mM concentration showed lower efficiency, presenting 65 % CaCO_3 inhibition, while C2 is the best scale inhibitor under these conditions. In terms of combined corrosion and CaCO_3 inhibition, C4 is the most efficient inhibitor for 1 mM concentration, presenting 96 % and 91 % inhibition, respectively. Overall, the increase in concentration appears to be beneficial for C4, C8 and C12 regarding their performance as dual inhibitors.

6.5 References

1. Amjad, Z.; Demadis, K. D. *Water-Formed Deposits: Fundamentals and Mitigation Strategies*; Elsevier, **2022**.
2. Gallup, D. Geochemistry of Geothermal Fluids and Well Scales, and Potential for Mineral Recovery. *Ore Geology Reviews* **1998**.
3. Henley, R.W. pH and Silica Scaling Control in Geothermal Field Development. *Geothermics* **1983**, *12* (4), 307–321.
4. Rothbaum, H. P.; Anderton, B. H.; Harrison, R. F., Rohde, A. G., Slatter, A. Effect of silica polymerization and pH on geothermal scaling. *Geothermics* **1979**, *8* (1).
5. Gallup, D.L. Brine pH modification scale control technology. *Geotherm. Resour. Counc. Trans.* **1996**, *20*, 749–755.
6. Sangwal, K. Additives and crystallization processes: From fundamentals to applications. John Wiley & Sons, Ltd: Chichester, UK, **2007**.
7. Sevrain, C.M.; Berchel, M.; Couthon, H.; Jaffrs, P.A. Phosphonic acid: Preparation and applications. *Beilstein J. Org. Chem.* **2017**, *13*, 2186–2213
8. Amjad, Z.; Zuhl, R.W. Influence of Cationic polymers on the Performance of anionic polymers as precipitation inhibitors for calcium phosphonates. *Phosphorus Research Bulletin* **2002**, *13*, 59-65.
9. Raistrick, B. The influence of foreign ions on crystal growth from solution. 1. The stabilization of the supersaturation of calcium carbonate solutions by anions possessing O-P-O-P-O chains. *Discuss. Faraday Soc.* **1949**, *5*, 234-237.
10. Putnis, A.; Junta-Rosso, J.L.; Hochella, M.F. Dissolution of barite by a chelating ligand: An atomic force microscopy study. *Geochimica et Cosmochimica Acta* **1995**, *59*, 4623-4632.
11. Amjad, Z.; Zuhl, R.W.; Zibrida, J.F. Factors Influencing the Precipitation of Calcium-Inhibitor Salts in Industrial Water Systems. In Association of Water Technologies, Inc: Annual Convention, Phoenix, AZ, USA, **2003**.
12. Tantayakom, V.; Fogler, H.S.; Charoensirithavorn, P.; Chavadej, S. Kinetic Study of Scale Inhibitor Precipitation in Squeeze Treatment. *Cryst. Growth Des.* **2005**, *5*, 329-335.

13. Kan, A.T.; Oddo, J.E.; Tomson, M.B. Formation of Two Calcium Diethylenetriaminepentakis(methylenephosphonic acid) Precipitates and Their Physical Chemical Properties. *Langmuir* **1994**, 10, 1450-1455.
14. Pairat, R.; Sumeath, C.; Browning, F.H.; Fogler, H.S. Precipitation and Dissolution of Calcium-ATMP Precipitates for the Inhibition of Scale Formation in Porous Media. *Langmuir* **1997**, 13, 1791-1798.
15. Wiencek, K. M.; Chapman, J.S. Water Treatment Biocides: How Do They Work and Why Should You Care? National Association of Corrosion Engineers Annual Conference, **1999**, Corrosion 99, San Antonio, Texas, 308.
16. NACE Standard TM0169-95 (Item No. 21200), National Association of Corrosion Engineers, Houston TX, U.S.A. (www.nace.org)
17. Patton, J.; Reeder, W. New Indicator for Titration of Calcium with (Ethylenedinitrilo) Tetraacetate. *Analytical Chemistry* **1956**, 28(6), 1026-1028.
18. Eaton, A.D.; Clesceri, L.S.; Rice, E.W.; Greenberg, A.E.; Franson, M.H. Standard Methods for Examination of Water & Wastewater, American Public Health Association, Washington DC, **2005**.

Chapter 7: Concluding remarks and perspectives

7.1 Corrosion products

The exploitation of geothermal energy presents several important challenges. Apart from the engineering logistics several problems arise due to the variation in chemical and physical parameters of the geothermal fluids, which may differ dramatically among geothermal waters around the globe. One challenge is corrosion, whose mitigation starts with the identification of the identity of corrosion products formed during a corrosive event but needs to be implemented by mitigation strategies (including corrosion inhibitors). Accordingly, great interest is placed on the type of corrosion products and how the corrosion rate is affected by the quality of the films that will form on the metal surface ^[1]. On the other hand, identification (and prediction) and mitigation of scale deposits that form is another challenge. This also requires proper mitigation approaches, among which, scale inhibitors.

As mentioned in the Introduction, the chemical composition of geothermal fluids depends on the location of the geothermal reservoir. In the present research, two representative geothermal fluids were selected (Brine 1 and Brine 2) for the corrosion experiments. In addition, further experiments were performed in deionized (DI) water, for comparison reasons. Corrosion rates and iron concentrations of the controls are shown in Table 7.1 and Figure 7.1. It is noticed that the corrosion rates do not increase linearly as the temperature increases. Corrosion products can form films on the metal surface, affecting the corrosion aggressiveness, and thus corrosion rates. The same phenomenon was observed for all water qualities, as the results showed an S-shaped trend. The corrosion rates reach their lowest values at RT and at their highest values at 130 °C. It is important to underline the corrosion rate values for the two “intermediate” temperatures. These are lower at 90 °C than at 60 °C. The identification of the corrosion products that formed under the selected experimental conditions was achieved by the characterization of the iron deposits collected from the control experiments. The color of the corrosion products on the metal surfaces was the first indication of the formation lepidocrocite and magnetite films, as it is demonstrated by the orange and black color of the films on the specimens, respectively (Figure 7.2).

T (°C)	RT		60		90		130	
	CR (mm/y)	Fe (ppm)	CR (mm/y)	Fe (ppm)	CR (mm/y)	Fe (ppm)	CR (mm/y)	Fe (ppm)
DI water	0.060	91	0.097	148	0.078	119	0.143	433
Brine 1	0.062	95	0.110	168	0.087	133	0.148	448
Brine 2	0.053	80	0.103	157	0.094	143	0.177	536

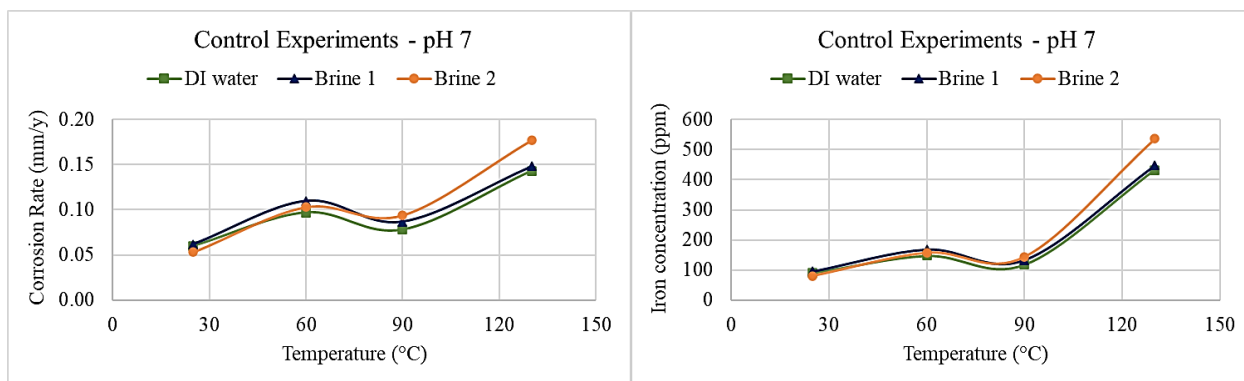


Figure 7.1. Results obtained for the controls (absence of chemical additives) at pH 7. *Left* Corrosion Rates and *right* Iron concentrations. Color codes: *green* Deionized water, *blue* Brine 1 and *orange* Brine 2.

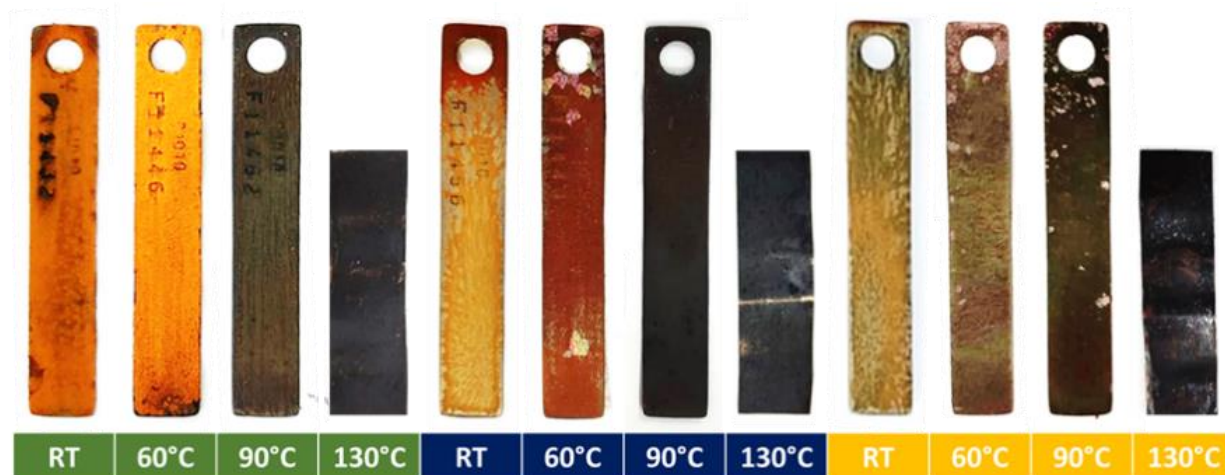


Figure 7.2. Corroded carbon steel surfaces of the specimens exposed to “control” solutions at pH 7. Color codes: *green* Deionized water, *blue* Brine 1 and *orange* Brine 2.

The identities of the corrosion products are shown in Table 7.2. In several cases, a mixture of different iron oxides and/or hydroxides is observed. In addition, the formation of calcite and halite was observed for corrosion experiments in the artificial Brines 1 and 2, respectively. In general, it is expected that the presence of a magnetite film on the metal surface can slow down the corrosion process.

Table 7.2. Corrosion products.				
T (°C)	RT	60	90	130
DI water	Lepidocrocite	Lepidocrocite + Magnetite	Magnetite	Magnetite
Brine 1	Chukanovite	Chukanovite	Chukanovite+ Magnetite	Magnetite
Brine 2	Lepidocrocite	Lepidocrocite	Lepidocrocite + Magnetite	Magnetite + Hematite

7.2 Corrosion inhibition studies

The protection of carbon steel from corrosion was studied in the presence of phosphonate and non-phosphonate inhibitors. The anticorrosion efficiency of the inhibitors was examined by changing several experimental parameters, eg. in different brines, and at several temperatures and concentrations. In addition to these conditions, corrosion experiments in the presence of non-phosphonate inhibitors were also performed under stirring conditions and in the presence of sulfides. Their performance was evaluated based on data from gravimetric measurements, according to the NACE standard method ^[2]. The results of the colorimetric method for total iron determination revealed deviations between the two quantification methods. Thus, this method needs further optimization as an anti-corrosion performance quantification method.

Phosphonate inhibitors

Regarding the corrosion experiments in the presence of phosphonate inhibitors, it is apparent that the increase in inhibitor dosage does not necessarily enhance the anti-corrosion performance. The corresponding results showed that the optimum concentration depends on several conditions,

such as the temperature and the water quality. In addition, it is concluded that phosphonates at high dosages act as rust cleaners. Visual observations verified that increasing the dosage of the tetraphosphonates results in gradually cleaner surfaces. Similar observations have been reported in the literature, for example, for HEDP^[3] and PBTC^[4].

Furthermore, the presence of metal ions in the solution enhances the anticorrosion efficiency of the phosphonate, thus acting synergistically due to the formation of a metal phosphonate “complex” protective film on the metal surface. However, this behavior is variable and depends on several factors, such as the nature of the phosphonate and the metal ion, solution pH, metal:phosphonate molar ratio, etc.^[5]. In the present work, calcium and magnesium ions were used as representative ions in solution, but the molar ratio between the ions and the phosphonates depends on the water quality and the inhibitor dosage. For example, corrosion experiments were performed in DI water in the presence of calcium or magnesium and the molar ratio was selected to be 1:1 to each inhibitor dosage. However, the concentrations of the metal ions in the two artificial brines are based on the corresponding chemical compositions of the representative geothermal fluids. The highest inhibitor concentration was 2 mM for the experiments at RT, 60 °C and 90 °C, and 5 mM for the experiments at 130 °C, hence the ions are in excess when the experiments were performed in Brine 1 and in Brine 2.

In general, C2 seems to perform better at 0.1 mM dosage in DI water, while under HP-HT conditions 1 mM is a beneficial concentration as well. It appears that the presence of calcium and magnesium in the solution does not offer any significant advantage at RT and at 60 °C, while at 90 °C the addition of calcium enhance the performance of C2. On the contrary, in the presence of magnesium, higher corrosion rates are observed. At 130 °C, the synergy between the metal ions and C2 results in higher inhibition for many inhibitor dosages. In Brine 1, once again, 0.1 mM is the optimum concentration at RT. A trend of higher inhibition as the dosage increases is observed at 60 °C. Regarding the experiments at 90 °C, 0.01 mM and 1 mM of C2 present the greatest inhibition, while at 130 °C the optimum dosage is 1 mM. In Brine 2, overall, inhibition efficiency increases as the inhibitor dosage increases as well.

Regarding C4 and the corrosion experiments in DI water at RT and at 60 °C, enhanced inhibition is observed for higher inhibitor concentrations. In contrast, higher inhibition is observed for lower inhibitor concentrations for the experiments at 90 °C and at 130 °C. The presence of

calcium and magnesium in the solution does not significantly affect the performance of C4 at RT and at 60 °C. In the case of 90 °C, 1 mM of a Ca²⁺-C4 blend stands out, while concerning the experiments at 130 °C, higher efficiencies are observed for 1 mM inhibitor concentration and higher. In Brine 1, the optimum concentration is 0.1 mM for the experiments at RT, 60 °C and 130 °C, while in the case of 90 °C the most efficient concentration is 0.01 mM of C4. In Brine 2, overall, inhibition efficiency increases as the inhibitor dosage increases as well.

Overall, the optimum concentration for C6 in DI water is 0.1 mM. Once again, the presence of calcium and magnesium in the solution does not affect the behavior of C6 at RT, while at 60 °C it is observed better performance in the case of 2 mM inhibitor dosage. Magnesium appears to enhance the efficiency of C6 at 90 °C, while the synergy with both metal ions is beneficial for C6 at 130 °C for concentrations > 1 mM. Regarding Brine 1, C6 appears to perform better at high dosages at RT. The most beneficial concentration is 1 mM in the case of 60 °C, while 0.01 mM and 1 mM of C6 present the highest inhibition at 90 °C. At 130 °C, greater inhibition is observed for lower inhibitor dosages. In Brine 2, inhibition efficiency increases as the inhibitor dosage increases as well in most cases, except the HP-HT conditions under which the best performance is observed for the concentrations 1 mM and 2 mM.

For C8 in DI water, the most beneficial dosage is 1 mM at RT, while 0.1 mM of C8 present the greatest efficiency at 60 °C and 130 °C. In the case of 90 °C, the optimum dosage is 0.01 mM. It appears that the presence of calcium and magnesium in the solution does not offer any significant advantage at RT and at 60 °C, while at 90 °C and at 130 °C the presence of these metal ions enhances the performance of C8 at higher inhibitor concentrations. For Brine 1 at RT, the two most beneficial dosages are 0.1 mM and 1 mM. At 60 °C, 1 mM of C8 gives the highest inhibition, while at 90 °C the inhibition increases as the inhibitor concentration increases as well. Concerning the experiments at 130 °C, the optimum dosage is 0.01 mM. In Brine 2, the increase in inhibitor concentration enhances the performance of C8 at RT and at 60 °C. The optimum dosage for the experiments at 90 °C is 0.1 mM. Regarding the experiments at 130 °C, higher efficiencies are observed for the lower dosages.

For DI water in the presence of C12, overall, the increase in inhibitor dosage is beneficial. Regarding the possible synergy between C12 and the metal ions, no change is observed in the presence of these ions at RT. At 60 °C, better performance is observed 0.01 mM and 1 mM of C12

with the addition of both calcium and magnesium, while at 90 °C slightly higher inhibition is observed in the case of “free” C12. At 130 °C, in general, no significant change is observed. In Brine 1, C12 seems to perform better overall as the concentration increases. In Brine 2, at RT the performance of C12 seems to be insensitive to concentration increase. The most beneficial dosage for C12 is 1 mM for the experiments at 60 °C and 90 °C, while at 130 °C 0.01 mM C12, 1 mM C12, 2 mM C12 and 4 mM C12 exhibit the lowest corrosion rates.

Overall, phosphonates appear to be more efficient as corrosion inhibitors in Brine 2 compared to Brine 1 and DI water. A direct correlation between structure and anti-corrosion efficiency cannot be discerned based on available data. Furthermore, no general trend between temperature and inhibition efficiency has been established. In the past, our group studied the performance of tetraphosphonate corrosion inhibitors in acidic conditions and reported that C6 exhibits the best protection against corrosion. Once again, no correlation between structure and anti-corrosion efficiency was observed. Interestingly, the XPS study showed that the tetraphosphonates become significantly deprotonated upon interaction with the carbon steel surface ^[6].

Non-phosphonate inhibitors

As mentioned in Chapter 2, due to confidentiality reasons, the identities of the non-phosphonate inhibitors cannot be disclosed. Nevertheless, information regarding the active species of each inhibitor are available. Corrosion experiments focused on four non-phosphonate inhibitors. Specifically, SLD contains an amino acid derivative, ACAB contains a blend of amines, DLD contains fatty amine derivatives and HAD contains imidazole derivatives. Hence, based on the available information about their structures, it is apparent that these inhibitors can protect the metal against corrosion, by forming films on the surface. In general, film forming agents such as imidazolines, amides, amidoamines and amines are considered efficient corrosion inhibitors. Their anti-corrosion performance as well as the factors that affect it have been reported ^[7-15]. It is important to have knowledge on the active species of an inhibitor. This allows us to correlate structure with function. The limited available information on the non-phosphonate inhibitors does not allow direct comparisons with data published in the literature on inhibitors with “similar”

structure, since several chemical groups on the inhibitor structure may influence the efficiency of the corrosion inhibitor.

In Brine 1, ACAB presents the highest inhibition for 100 ppm dosage and DLD for 250 ppm dosage, both at RT. At 60 °C, DLD is the best inhibitor for 100 ppm, however when the dosage is increased up to 250 ppm, this results in a significantly increased inhibition for SLD, thus becoming the most effective inhibitor under these conditions. Increase in temperature to 90 °C favors the anticorrosion efficiency of DLD for both dosages (100 and 250 ppm).

In addition, experiments in the presence of non-phosphonate inhibitors were performed under “turbulent” conditions (mechanical stirring). In this case, the corrosion rate of the control experiment under non stirring conditions is 4-5 times lower than the respective values of the experiments under stirring. Overall, no general trend was established regarding the anti-corrosion efficiency. Each inhibitor exhibits different behavior. Specifically, a trend of enhanced anticorrosion efficiencies as the stirring rate increases is observed in the case of HAD and ACAB. On the contrary, SLD appears to perform better as the stirring rate decreases.

Finally, data from corrosion experiments in the presence of sulfides revealed some important facts. When both oxygen and sulfides are present in solution, the corrosion rates are higher than those under argon atmosphere. HAD appears to be the most effective inhibitor in the presence of oxygen at 100 ppm dosage, while ACAB is the best at 250 ppm. Under argon atmosphere, HAD exhibits the highest inhibition efficiency at 100 ppm. In the case of 250 ppm inhibitor concentration, none of the non-phosphonate inhibitors present acceptable inhibitory activity.

Regarding the experiments in Brine 2, HAD is the most efficient at RT. At 60 °C, SLD presents the highest corrosion inhibition for both inhibitor dosages. At 90 °C, DLD and HAD present the highest efficiency for 100 ppm, however when the dosage is increased up to 250 ppm, results in a significantly increased inhibition for SLD.

For the corrosion experiments under stirring, it is important to note that corrosion rates for the control under non stirring conditions increase as the stirring rate increases. The corrosion rates obtained from the experiments in the presence of all inhibitors follow the same pattern, however no specific trend was established for the inhibition efficiencies. Specifically, HAD and ACAB showed their best performance at 200 rpm, while SLD at 400 rpm.

Furthermore, the results from corrosion experiments in the presence of sulfides pointed to the fact that when both oxygen and sulfides are present in solution, the corrosion rate is higher than those under the argon atmosphere. HAD is the most effective inhibitor amongst the inhibitors tested under these conditions.

In DI water at RT, HAD exhibits the lowest corrosion rates at both concentrations. The increase in temperature at 60 °C favors the anticorrosion efficiency of SLD for both inhibitor dosages and HAD is the second best inhibitor. The gravimetric and the iron determination measurements are in agreement, giving similar anti-corrosion efficiencies for the inhibitors. The same conclusion is valid at 90 °C. Overall, visual observations are in agreement with the corresponding results of the gravimetric measurement and of the iron determination test.

Regarding the experiments under stirring, once again, no trend was established regarding the anti-corrosion efficiency. Each inhibitor exhibits different behavior. For example, a trend of enhanced anticorrosion efficiencies as the stirring rate increasing is observed in the case of HAD and SLD. On the contrary, ACAB appears to perform best when the experiment is static.

Finally, corrosion experiments in the presence of sulfides concluded that when both oxygen and sulfides are present in the solution, corrosion rate is higher than the experiments performed under argon atmosphere. ACAB appears to be the most effective inhibitor in the presence of oxygen, while under argon atmosphere, HAD exhibits the greatest inhibition efficiency.

7.3 Perspectives

As can be expected, choosing the most efficient corrosion inhibitor is a decision for which a multitude of factors and variables must be considered. In this work, corrosion inhibition experiments were performed by varying several parameters. Appropriately, to say the least, this study established the importance of knowing the targeted conditions in order to select the proper corrosion inhibitor at its optimum dosage.

The operation of geothermal systems includes complex operational parameters, like temperature and pressure changes, even within the same system, as well as the intricacies of

corrosion itself. Hence, it would be interesting to study the performance of the inhibitors as the temperature and the pressure conditions will change successively in one system.

The formation of different corrosion products can affect the corrosion aggressiveness and induce different types of corrosion (uniform, pitting, etc). Erosion is a type of corrosion which is commonly observed in the pipelines of the geothermal systems. Even though this research reported results under stirring conditions, the concept of studying the anti-corrosion efficiency of the inhibitors in a system in which the fluid could flow through tubes (turbulent conditions) will be closer to a more realistic scenario. In addition, the variety of the geothermal fluids, in terms of chemical composition and physical characteristics, constitutes a guide of conditions to which the experimental conditions in the laboratory must be adapted.

This research focused on carbon steel, a very common metallurgy in geothermal systems, however other materials, such as stainless steel or nickel alloys are selected for specific parts of equipment. As mentioned in Introduction, these materials could also be subject to corrosion processes depending on the conditions, resulting in more aggressive forms of corrosion, such as pitting and SCC. Thus, it is very important to evaluate the anti-corrosion efficiency of the inhibitors studied on carbon steel surfaces, but on several other metallurgies.

Finally, cost is an important and realistic factor in industry, where the application of a chemical additive (either as a scale or corrosion inhibitor) is implemented on a large scale. Hence, discovering effective inhibitors that can be effective at low dosages is always a subject of intense research. In addition, great interest arises in the use of inhibitors which can perform efficiently *both* as corrosion and scale inhibitors. Further studies can focus on finding the optimum inhibitor concentrations for combined (corrosion and scale) inhibition.

7.4 References

1. Ohtsuka, T. Characterization of Corrosion Products on Steel Surfaces; Waseda, Y., Suzuki, S., Eds.; Springer Berlin Heidelberg, **2006**; Chapter 2, pp 19-32.
2. NACE Standard TM0169-95 (Item No. 21200), National Association of Corrosion Engineers, Houston TX, U.S.A. (www.nace.org)
3. Veres, A.; Reinhard, G.; Kálmán, E. Chemical Passivation of Ferrous Materials in Presence of Salts of Phosphonic Acids. *British Corrosion Journal* **1992**, 27 (2), 147–150.
4. Demadis, K.; Lykoudis, P.; Raptis, R.; Mezei, G. Phosphonopolycarboxylates as Chemical Additives for Calcite Scale Dissolution and Metallic Corrosion Inhibition Based on a Calcium-Phosphonotricarboxylate Organic-Inorganic Hybrid. *Crystal Growth & Design* **2006**, 6, 1064-1067.
5. M. Papadaki, K.D. Demadis, Structural mapping of hybrid metal phosphonate corrosion inhibiting thin film, *Comment Inorg. Chem.* **2009**, 30, 89–118.
6. A. Moschona, N. Plesu, G. Mezei, A.G. Thomas, K.D. Demadis, Corrosion protection of carbon steel by tetraphosphonates of systematically different molecular size, *Corrosion Science*, **2018**.
7. T. Schott, F. Liautaud, *Mater. Corros.* **2022**, 73:1916–1942.
8. Mundhenk, N.; Huttenloch, P.; Kohl, T.; Steger, H.; Zorn, R. Metal Corrosion in Geothermal Brine Environments of the Upper Rhine Graben – Laboratory and On-Site Studies. *Geothermics* **2013**, 46, 14–21.
9. Aslam, J.; Aslam, R.; Aslam, A. *Chapter18 - Amino acids and their derivatives as corrosion inhibitor*, Editor(s): L. Guo, C. Verma, D. Zhang, Eco-Friendly Corrosion Inhibitors, *Elsevier* **2022**, 311-330.
10. Cui, H.; Ren, W.; Lin, P.; Liu, Y. Structure Control Synthesis of Iron Oxide Polymorph Nanoparticles through an Epoxide Precipitation Route. *Journal of Experimental Nanoscience* **2012**, 8 (7-8), 869–875.
11. Rao, B.; Venkateswara Rao, M.; Rao, S.; Sreedhar, B. “N,N-Bis(Phosphonomethyl) Glycine, Zn 2+ and Tartrate” -A New Ternary Inhibitor Formulation for Corrosion Control of Carbon Steel. *International Journal of Materials and Chemistry* **2013** (2), 17–27.
12. Lahhit, N.; Bouyanzer, A.; Desjobert, J-M.; Hammouti, B.; Salghi, R.; Costa, J.; Jama, C.; Bentiss, F.; Majidi, L. Fennel (Foeniculum Vulgare) Essential Oil as Green Corrosion

- Inhibitor of Carbon Steel in Hydrochloric Acid Solution. *Portugaliae Electrochimica Acta* **2011**, 29 (2), 127–138.
13. Chen, H. J.; Jepson, W. P.; Hong, T. High Temperature Corrosion Inhibition Performance of Imidazoline and Amide, Nace corrosion, **2000**.
 14. Rivera-Grau, L. M.; Casales, M.; Regla, I.; Ortega-Toledo, D.; Cuervo, D.; Asencio, J.; Rodriguez, J. G. G.; Martine-Gomez, L. Corrosion Inhibition by a Coconut Oil Modified Imidazoline for Carbon Steel under the Combined Effect of CO₂ and H₂S. *International Journal of Electrochemical Science* **2012**.
 15. Kaesche, H.; Hackerman, N. Corrosion Inhibition by Organic Amines. *Journal of The Electrochemical Society* **1958**, 105 (4), 191.

Chapter 8: Annex

8.1 Abbreviations

NMR: Nuclear Magnetic Resonance Spectroscopy

ATR-IR: Attenuated Total Reflectance Infrared Spectroscopy

P-XRD: Powder X-Ray Diffraction

SEM: Scanning Electron Microscopy

EDS: Electron Dispersive Spectrometry

FAU: Formazin Attenuation Units

EDTMP-C2: ethylenediamine-*tetrakis*(methylenephosphonic acid

TMTMP-C4: tetramethylenediamine-*tetrakis*(methylenephosphonic acid

HDTMP-C6: hexamethylenediamine-*tetrakis*(methylenephosphonic acid

ODTMP-C8: octamethylenediamine-*tetrakis*(methylenephosphonic acid

DDTMP-C12: dodecamethylenediamine-*tetrakis*(methylenephosphonic acid

SLD: Amino acid derivative

ACAB: Blend of organic amines

DLD: Fatty amine derivative

HAD: Imidazole derivative

PELB: Phosphate ester blend

MORD: Fatty amine derivative

ADB: Amine derivatives blend

8.2 Characterization of tetraphosphonates

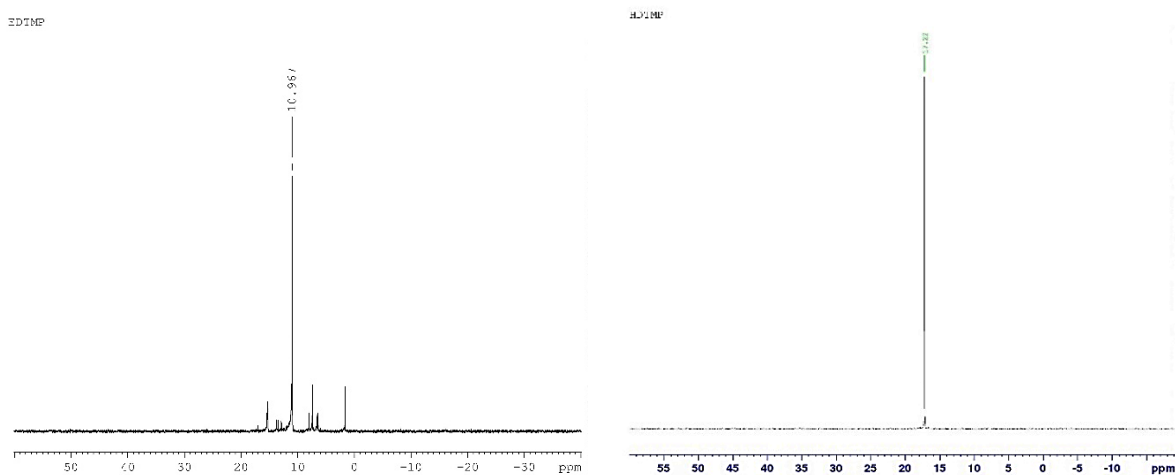


Figure 8.1. ^{31}P NMR for the commercially available products EDTMP Dequest 2046 and HDTMP Dequest 2054.

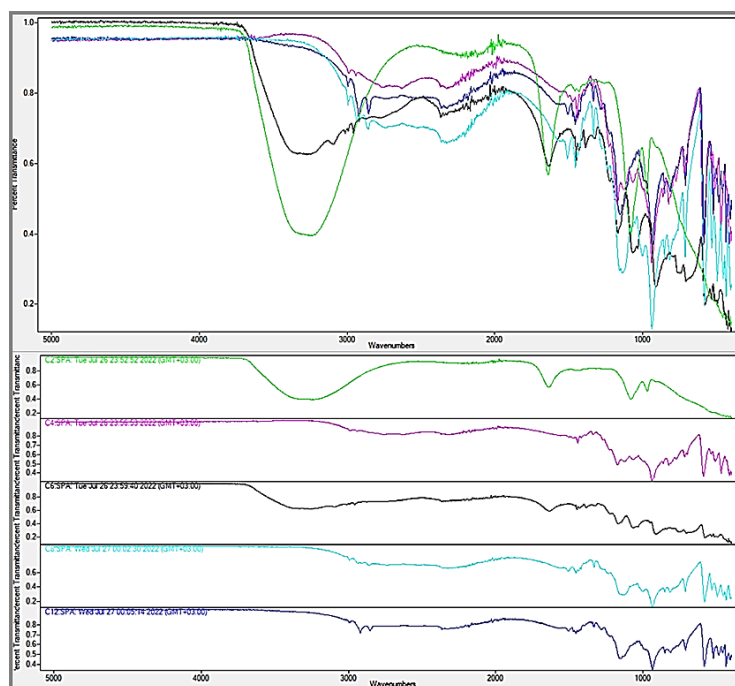


Figure 8.2. ATR-IR spectra for (from top to bottom) C2, C4, C6, C8 and C12.

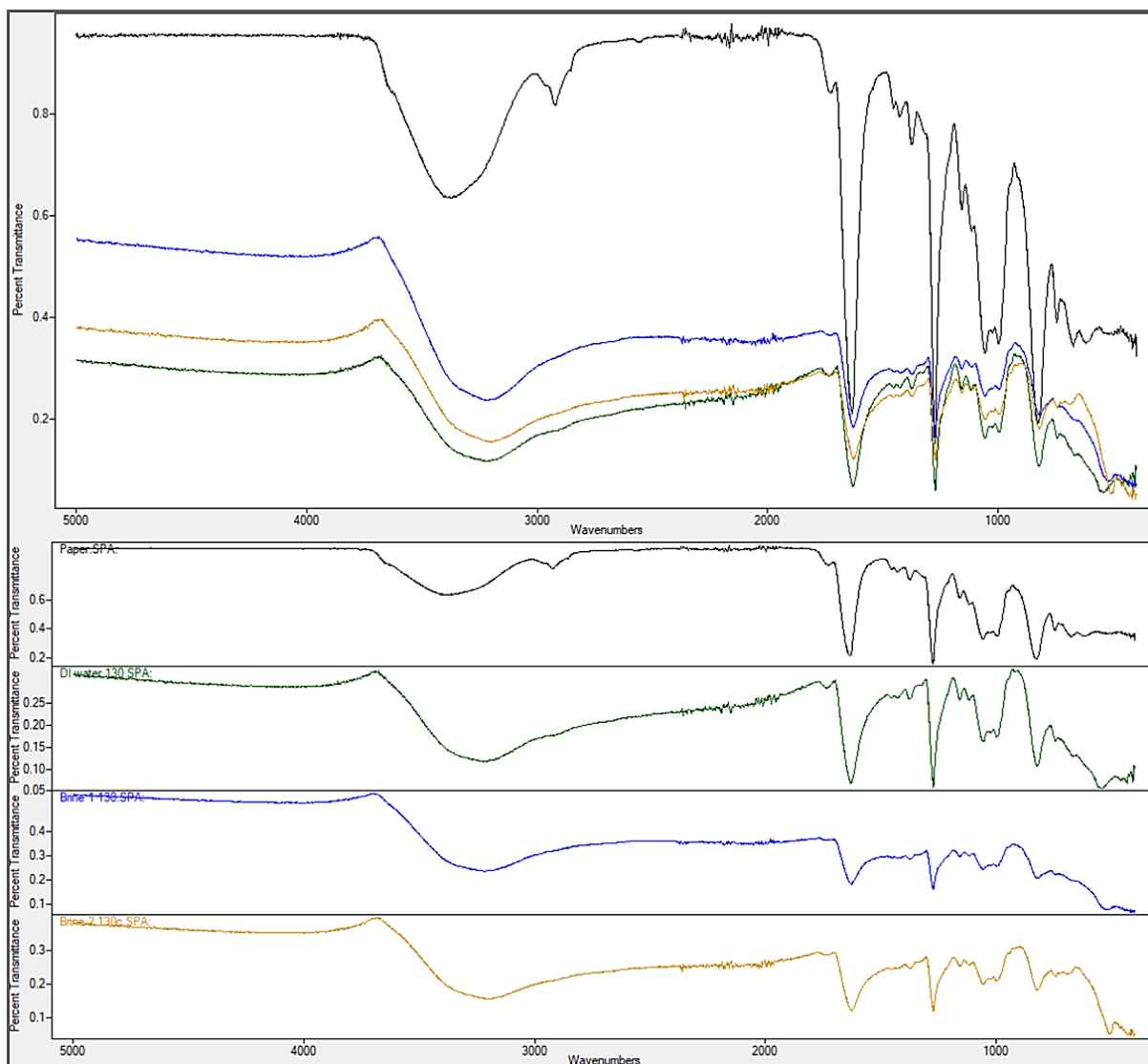


Figure 8.3. ATR-IR spectra of the precipitates collected from control corrosion experiments at 130°C on the filter membrane. Color codes: *black* filter membrane, *green* DI water, *blue* Brine 1 and *brown* Brine 2.

8.3 Calcium tolerance test

Table 8.1. Calcium tolerance study for the phosphonates. Calcium concentration is 260 ppm.




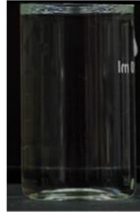


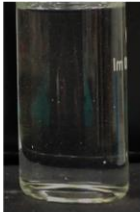



	C2	C4	C6	C8	C12
0.10 mM					
1.00 mM					

Table 8.2. Calcium tolerance study for phosphonates. Calcium concentration is 260 ppm.

		C2		C4		C6		C8		C12	
C (mM)	time (hours)	Visual	Turbidity (FAU)	Visual	Turbidity (FAU)	Visual	Turbidity (FAU)	Visual	Turbidity (FAU)	Visual	Turbidity (FAU)
0.10	1	Clear	0	Clear	0	Clear	0	Clear	0	Clear	0
	168	Clear	0	Clear	0	Clear	0	Clear	0	Clear	0
1.00	1	Clear	0	Clear	0	Clear	0	Clear	0	Hazy	30
	168	Hazy	35	Clear	5	Clear	1	Clear	2	Precipit	13

8.4 Crystal data for the minerals from American Mineralogist Crystal Structure Database.

2-THETA	INTENSITY	D-SPACING	H K L	Multiplicity
14.29	100.00	6.2000	2 0 0	2
27.16	64.11	3.2829	2 1 0	4
28.80	1.02	3.1000	4 0 0	2
30.08	3.94	2.9709	1 0 1	4
36.54	52.08	2.4594	3 0 1	4
37.16	7.76	2.4195	4 1 0	4
38.19	16.34	2.3566	1 1 1	8
43.60	3.22	2.0757	3 1 1	8
43.80	4.24	2.0667	6 0 0	2
46.96	18.35	1.9350	0 2 0	2
47.17	22.54	1.9267	5 0 1	4
49.34	6.51	1.8471	2 2 0	4
53.10	16.55	1.7248	5 1 1	8
56.78	1.37	1.6214	1 2 1	8
59.65	4.81	1.5500	8 0 0	2
60.51	7.06	1.5300	0 0 2	2
60.92	17.75	1.5207	3 2 1	8
62.53	2.76	1.4854	2 0 2	4
64.79	1.46	1.4389	8 1 0	4
65.49	9.84	1.4253	7 1 1	8
66.16	2.27	1.4125	6 2 0	4
67.55	6.56	1.3868	2 1 2	8
68.76	10.66	1.3653	5 2 1	8
73.19	2.36	1.2931	4 1 2	8
75.24	2.22	1.2630	2 3 0	4
77.65	1.34	1.2297	6 0 2	4
79.18	3.32	1.2097	8 2 0	4
79.93	4.89	1.2002	0 2 2	4
81.31	1.76	1.1833	1 3 1	8
81.51	3.94	1.1809	10 1 0	4
81.73	2.11	1.1783	2 2 2	8

Figure 8.4. Crystal data for Lepidocrocite.

2-THETA	INTENSITY	D-SPACING	H K L	Multiplicity
18.30	7.93	4.8473	1 1 1	8
30.11	28.10	2.9684	2 2 0	12
35.46	100.00	2.5314	3 1 1	24
37.09	8.27	2.4237	2 2 2	8
43.10	20.13	2.0989	4 0 0	6
53.47	9.59	1.7138	4 2 2	24
57.00	24.94	1.6158	5 1 1	24
57.00	6.40	1.6158	3 3 3	8
62.59	41.80	1.4842	4 4 0	12
71.00	3.54	1.3275	6 2 0	24
74.04	8.82	1.2803	5 3 3	24
75.05	3.94	1.2657	6 2 2	24
79.01	2.64	1.2118	4 4 4	8
86.81	3.92	1.1219	6 4 2	48
89.71	8.92	1.0930	7 3 1	48
89.71	5.54	1.0930	5 5 3	24

Figure 8.5. Crystal data for Magnetite.

2-THETA	INTENSITY	D-SPACING	H K L	Multiplicity
24.15	28.73	3.6855	0 1 2	6
33.15	100.00	2.7028	1 0 4	6
35.64	73.67	2.5190	1 1 0	6
39.25	2.05	2.2953	0 0 6	2
40.86	17.99	2.2084	1 1 3	12
43.52	1.94	2.0797	2 0 2	6
49.46	37.43	1.8428	0 2 4	6
54.05	45.13	1.6966	1 1 6	12
57.46	2.34	1.6037	1 2 2	12
57.56	8.52	1.6014	0 1 8	6
62.44	30.65	1.4873	2 1 4	12
64.02	29.47	1.4543	3 0 0	6
69.56	3.04	1.3514	2 0 8	6
71.89	10.86	1.3133	1 0 10	6
72.24	1.73	1.3078	1 1 9	12
75.48	6.96	1.2595	2 2 0	6
77.74	1.26	1.2285	0 3 6	6
77.74	1.26	1.2285	3 0 6	6
80.61	1.58	1.1918	3 1 2	12
80.69	4.23	1.1909	1 2 8	12
82.90	5.63	1.1646	0 2 10	6
84.95	8.65	1.1416	1 3 4	12
88.56	7.94	1.1042	2 2 6	12

Figure 8.6. Crystal data for Hematite.

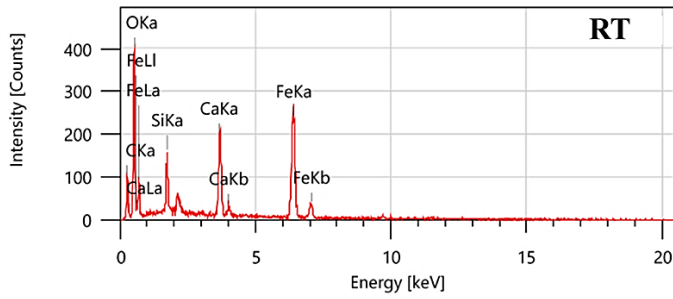
2-THETA	INTENSITY	D-SPACING	H K L	Multiplicity
28.35	8.45	3.1485	1 1 1	8
32.85	100.00	2.7266	2 0 0	6
47.14	59.35	1.9280	2 2 0	12
55.92	1.96	1.6442	3 1 1	24
58.64	17.40	1.5742	2 2 2	8
68.87	7.00	1.3633	4 0 0	6
78.43	17.31	1.2194	4 2 0	24
87.67	12.02	1.1132	4 2 2	24

Figure 8.7. Crystal data for Halite.

2-THETA	INTENSITY	D-SPACING	H K L	Multiplicity
23.07	8.10	3.8550	0 1 2	6
29.42	100.00	3.0357	1 0 4	6
31.46	2.43	2.8436	0 0 6	2
36.00	13.71	2.4950	1 1 0	6
39.44	20.16	2.2848	1 1 3	12
43.19	14.26	2.0946	2 0 2	6
47.15	6.16	1.9275	0 2 4	6
47.54	19.67	1.9125	0 1 8	6
48.54	20.02	1.8754	1 1 6	12
56.61	3.73	1.6259	2 1 1	12
57.44	9.18	1.6042	1 2 2	12
60.72	5.28	1.5253	2 1 4	12
61.05	2.41	1.5179	2 0 8	6
61.43	3.18	1.5094	1 1 9	12
63.10	2.29	1.4733	1 2 5	12
64.71	6.84	1.4405	3 0 0	6
65.67	3.91	1.4218	0 0 12	2
69.24	1.51	1.3569	2 1 7	12
70.30	2.13	1.3390	0 2 10	6
72.95	2.69	1.2967	1 2 8	12
77.23	1.93	1.2353	1 1 12	12
81.60	2.24	1.1799	2 1 10	12
83.84	1.57	1.1539	1 3 4	12

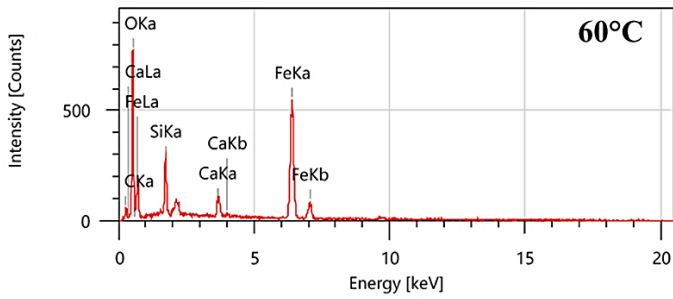
Figure 8.8. Crystal data for Calcite.

8.5 EDS analysis



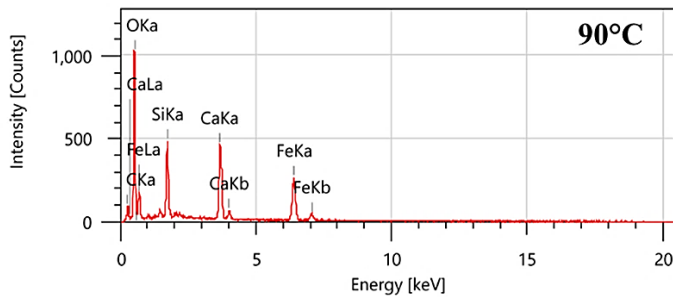
Display name	Standard data	Quantification method	Result Type
Spc_003	Standardless	ZAF	Metal

Element	Line	Mass%	Atom%
C	K	16.53±0.61	28.64±1.05
O	K	40.69±1.28	52.95±1.67
Si	K	3.44±0.23	2.55±0.17
Ca	K	8.13±0.36	4.22±0.19
Fe	K	31.21±1.05	11.63±0.39
Total		100.00	100.00
Spc_003			Fitting ratio 0.0742



Display name	Standard data	Quantification method	Result Type
Spc_004	Standardless	ZAF	Metal

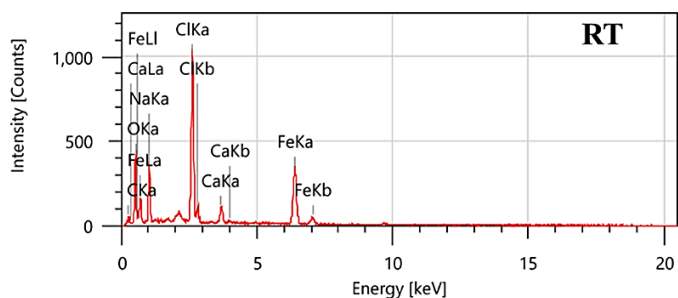
Element	Line	Mass%	Atom%
C	K	6.52±0.36	13.32±0.73
O	K	39.11±0.86	60.01±1.33
Si	K	5.32±0.25	4.65±0.22
Ca	K	2.71±0.18	1.66±0.11
Fe	K	46.35±1.08	20.37±0.47
Total		100.00	100.00
Spc_004			Fitting ratio 0.0452



Display name	Standard data	Quantification method	Result Type
Spc_001	Standardless	ZAF	Metal

Element	Line	Mass%	Atom%
C	K	8.27±0.33	13.53±0.55
O	K	57.62±1.10	70.75±1.36
Si	K	6.45±0.23	4.51±0.16
Ca	K	10.70±0.31	5.25±0.15
Fe	K	16.96±0.59	5.97±0.21
Total		100.00	100.00
Spc_001			Fitting ratio 0.0405

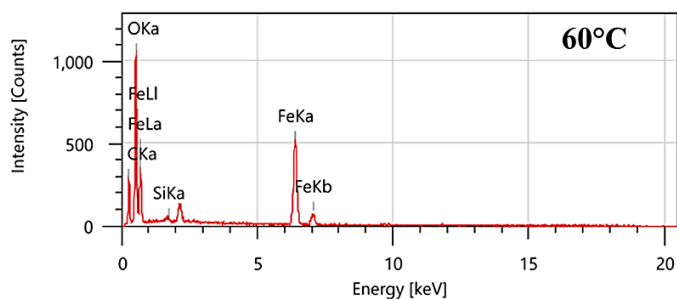
Figure 8.9. EDS data of the precipitates that collected from the experiments in Brine 1 at (top) RT, (center) 60°C and (bottom) 90°C.



Display name	Standard data	Quantification method	Result Type
Spc_002	Standardless	ZAF	Metal

Element	Line	Mass%	Atom%
C	K	11.34±0.68	21.77±1.30
O	K	29.38±0.91	42.34±1.31
Na	K	10.82±0.44	10.85±0.44
Cl	K	19.30±0.38	12.55±0.25
Ca	K	2.75±0.18	1.58±0.10
Fe	K	26.39±0.78	10.90±0.32
Total		100.00	100.00

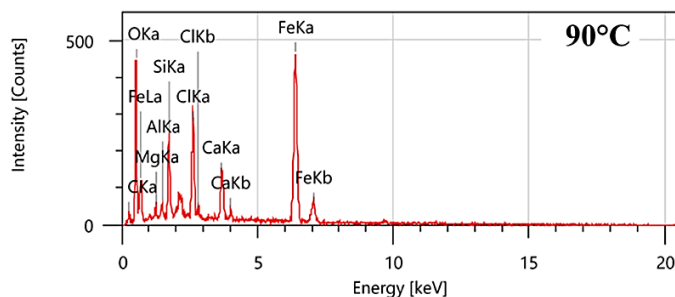
Spc_002 Fitting ratio 0.0428



Display name	Standard data	Quantification method	Result Type
Spc_003	Standardless	ZAF	Metal

Element	Line	Mass%	Atom%
C	K	21.31±0.47	34.18±0.75
O	K	44.94±0.86	54.12±1.04
Si	K	0.15±0.05	0.10±0.04
Fe	K	33.60±0.79	11.59±0.27
Total		100.00	100.00

Spc_003 Fitting ratio 0.0525

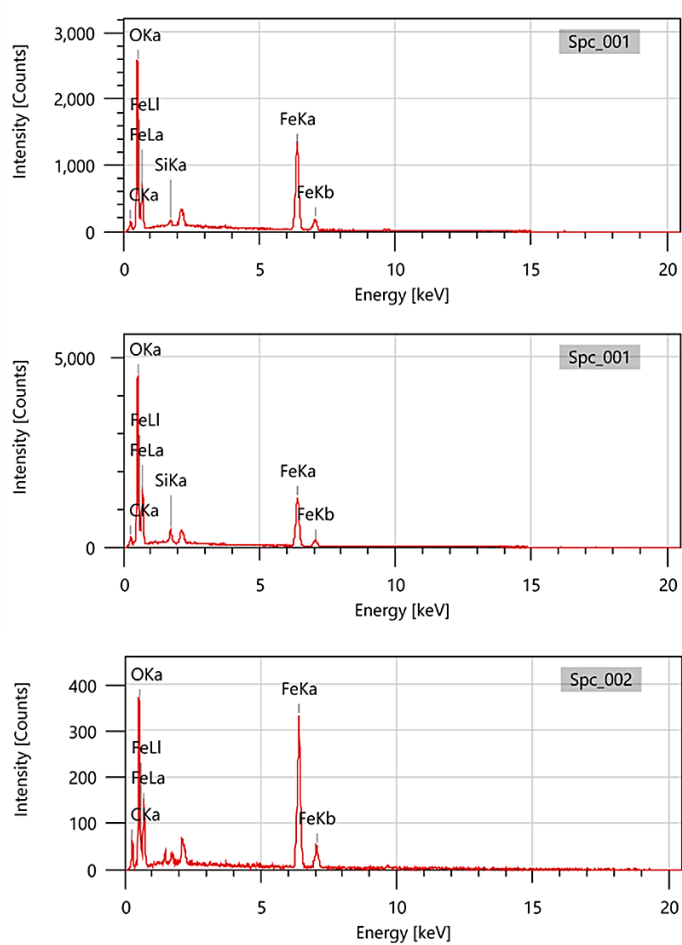


Display name	Standard data	Quantification method	Result Type
Spc_005	Standardless	ZAF	Metal

Element	Line	Mass%	Atom%
C	K	6.45±0.45	13.86±0.97
O	K	32.11±0.93	51.83±1.51
Mg	K	1.07±0.14	1.14±0.15
Al	K	0.92±0.13	0.89±0.12
Si	K	4.81±0.25	4.42±0.23
Cl	K	6.62±0.26	4.82±0.19
Ca	K	4.62±0.25	2.98±0.16
Fe	K	43.40±1.10	20.07±0.51
Total		100.00	100.00

Spc_005 Fitting ratio 0.0511

Figure 8.10. EDS data of the precipitates that collected from the experiments in Brine 2 at (top) RT, (center) 60°C and (bottom) 90°C.



Display name	Standard data	Quantification method	Result Type
Spc_001	Standardless	ZAF	Metal

Element	Line	Mass%	Atom%
C	K	3.51±0.11	9.16±0.30
O	K	26.16±0.32	51.18±0.63
Si	K	0.46±0.06	0.51±0.06
Fe	K	69.87±1.04	39.16±0.58
Total		100.00	100.00
Spc_001			Fitting ratio 0.0298

Display name	Standard data	Quantification method	Result Type
Spc_001	Standardless	ZAF	Metal

Element	Line	Mass%	Atom%
C	K	4.99±0.12	10.86±0.26
O	K	37.57±0.35	61.38±0.57
Si	K	1.90±0.08	1.76±0.08
Fe	K	55.54±0.84	25.99±0.39
Total		100.00	100.00
Spc_001			Fitting ratio 0.0334

Display name	Standard data	Quantification method	Result Type
Spc_002	Standardless	ZAF	Metal

Element	Line	Mass%	Atom%
C	K	13.00±0.64	25.50±1.25
O	K	35.99±1.15	52.99±1.69
Fe	K	51.00±1.57	21.51±0.66
Total		100.00	100.00
Spc_002			Fitting ratio 0.0935

Figure 8.11. EDS data of the precipitates that collected from the experiments in DI water at (top) RT, (center) 60°C and (bottom) 90°C.

8.6 Corrosion experiments data tables

Table 8.3. Corrosion rates and inhibition efficiency percentages for 0.01 mM of phosphonates in the presence of Ca²⁺ in DI water.

	RT		60 °C		90 °C		130 °C	
	CR (mm/y)	IE %	CR (mm/y)	IE %	CR (mm/y)	IE %	CR (mm/y)	IE %
Control	0.060	-	0.097	-	0.078	-	0.143	-
Ca ²⁺ - C2	0.038	37	0.060	38	0.091	-17	0.084	41
Ca ²⁺ - C4	0.076	-27	0.083	14	0.100	-28	0.090	37
Ca ²⁺ - C6	0.051	15	0.066	32	0.077	1	0.084	41
Ca ²⁺ - C8	0.045	25	0.092	5	0.062	21	0.120	16
Ca ²⁺ - C12	0.049	18	0.076	22	0.079	-1	0.128	10

Table 8.4. Corrosion rates and inhibition efficiency percentages for 0.1 mM of phosphonates in the presence of Ca²⁺ in DI water.

	RT		60 °C		90 °C		130 °C	
	CR (mm/y)	IE %	CR (mm/y)	IE %	CR (mm/y)	IE %	CR (mm/y)	IE %
Control	0.060	-	0.097	-	0.078	-	0.143	-
Ca ²⁺ - C2	0.038	37	0.046	53	0.016	79	0.108	24
Ca ²⁺ - C4	0.059	2	0.055	43	0.093	-19	0.072	50
Ca ²⁺ - C6	0.029	52	0.063	35	0.126	-62	0.172	-20
Ca ²⁺ - C8	0.035	42	0.076	22	0.069	12	0.063	56
Ca ²⁺ - C12	0.046	23	0.049	49	0.078	0	0.111	22

Table 8.5. Corrosion rates and inhibition efficiency percentages for 1 mM of phosphonates in the presence of Ca²⁺ in DI water.

	RT		60 °C		90 °C		130 °C	
	CR (mm/y)	IE %	CR (mm/y)	IE %	CR (mm/y)	IE %	CR (mm/y)	IE %
Control	0.060	-	0.097	-	0.078	-	0.143	-
Ca ²⁺ - C2	0.040	33	0.061	37	0.057	27	0.081	43
Ca ²⁺ - C4	0.047	22	0.056	42	0.102	-31	0.114	20
Ca ²⁺ - C6	0.032	47	0.055	43	0.100	-28	0.140	2
Ca ²⁺ - C8	0.030	50	0.073	25	0.033	58	0.093	35
Ca ²⁺ - C12	0.035	42	0.041	58	0.054	31	0.036	75

Table 8.6. Corrosion rates and inhibition efficiency percentages for 2 mM of phosphonates in the presence of Ca²⁺ in DI water.

	RT		60 °C		90 °C		130 °C	
	CR (mm/y)	IE %	CR (mm/y)	IE %	CR (mm/y)	IE %	CR (mm/y)	IE %
Control	0.060	-	0.097	-	0.078	-	0.143	-
Ca ²⁺ - C2	0.056	7	0.080	18	0.085	-9	0.108	24
Ca ²⁺ - C4	0.050	17	0.064	34	0.089	-14	0.126	12
Ca ²⁺ - C6	0.045	25	0.056	42	0.101	-29	0.105	27
Ca ²⁺ - C8	0.034	43	0.061	37	0.044	44	0.072	50
Ca ²⁺ - C12	0.037	38	0.033	66	0.053	32	0.048	66

Table 8.7. Corrosion rates and inhibition efficiency percentages for 0.01 mM of phosphonates in the presence of Mg²⁺ in DI water.

	RT		60 °C		90 °C		130 °C	
	CR (mm/y)	IE %	CR (mm/y)	IE %	CR (mm/y)	IE %	CR (mm/y)	IE %
Control	0.060	-	0.097	-	0.078	-	0.143	-
Mg ²⁺ -C2	0.045	25	0.069	29	0.046	41	0.263	-84
Mg ²⁺ -C4	0.057	5	0.072	26	0.049	37	0.205	-43
Mg ²⁺ -C6	0.046	23	0.068	30	0.071	9	0.079	45
Mg ²⁺ -C8	0.052	13	0.075	23	0.171	-119	0.209	-46
Mg ²⁺ -C12	0.052	13	0.075	23	0.135	-73	0.057	60

Table 8.8. Corrosion rates and inhibition efficiency percentages for 0.1 mM of phosphonates in the presence of Mg²⁺ in DI water.

	RT		60 °C		90 °C		130 °C	
	CR (mm/y)	IE %	CR (mm/y)	IE %	CR (mm/y)	IE %	CR (mm/y)	IE %
Control	0.060	-	0.097	-	0.078	-	0.143	-
Mg ²⁺ -C2	0.017	72	0.051	47	0.113	-45	0.117	18
Mg ²⁺ -C4	0.043	28	0.071	27	0.081	-4	0.230	-61
Mg ²⁺ -C6	0.027	55	0.061	37	0.060	23	0.078	45
Mg ²⁺ -C8	0.041	32	0.068	30	0.126	-62	0.200	-40
Mg ²⁺ -C12	0.039	35	0.066	32	0.062	21	0.048	66

Table 8.9. Corrosion rates and inhibition efficiency percentages for 1 mM of phosphonates in the presence of Mg²⁺ in DI water.

	RT		60 °C		90 °C		130 °C	
	CR (mm/y)	IE %	CR (mm/y)	IE %	CR (mm/y)	IE %	CR (mm/y)	IE %
Control	0.060	-	0.097	-	0.078	-	0.143	-
Mg ²⁺ -C2	0.038	37	0.082	15	0.149	-91	0.093	35
Mg ²⁺ -C4	0.038	37	0.054	44	0.030	62	0.057	60
Mg ²⁺ -C6	0.031	48	0.061	37	0.143	-83	0.143	0
Mg ²⁺ -C8	0.034	43	0.071	27	0.075	4	0.066	54
Mg ²⁺ -C12	0.039	35	0.049	49	0.041	47	0.042	71

Table 8.10. Corrosion rates and inhibition efficiency percentages for 2 mM of phosphonates in the presence of Mg²⁺ in DI water.

	RT		60 °C		90 °C		130 °C	
	CR (mm/y)	IE %	CR (mm/y)	IE %	CR (mm/y)	IE %	CR (mm/y)	IE %
Control	0.060	-	0.097	-	0.078	-	0.143	-
Mg ²⁺ -C2	0.057	5	0.084	13	0.095	-22	0.099	3
Mg ²⁺ -C4	0.037	38	0.057	41	0.179	-129	0.096	-27
Mg ²⁺ -C6	0.038	37	0.070	28	0.200	-156	0.126	30
Mg ²⁺ -C8	0.033	45	0.070	28	0.066	15	0.069	67
Mg ²⁺ -C12	0.032	47	0.053	45	0.047	40	0.033	53

Table 8.11. Corrosion rates and inhibition efficiency percentages for experiments at high concentrations for phosphonates in DI water.

	3 mM		4 mM		5 mM	
	CR (mm/y)	IE %	CR (mm/y)	IE %	CR (mm/y)	IE %
Control	0.143	-	0.143	-	0.143	-
C2	0.131	8	0.128	10	0.123	14
Ca ²⁺ - C2	0.096	33	0.105	27	0.079	45
Mg ²⁺ - C2	0.087	39	0.126	12	0.105	27
C4	0.193	-35	0.185	-29	0.193	-35
Ca ²⁺ - C4	0.093	35	0.120	16	0.134	6
Mg ²⁺ - C4	0.105	27	0.118	17	0.102	29
C6	0.152	-6	0.149	-4	0.170	-19
Ca ²⁺ - C6	0.087	39	0.087	39	0.120	16
Ca ²⁺ - C6	0.131	8	0.128	10	0.093	35
C8	0.075	48	0.090	37	0.182	-27
Ca ²⁺ - C8	0.060	58	0.069	52	0.081	43
Mg ²⁺ - C8	0.066	54	0.081	43	0.066	54
C12	0.078	45	0.024	83	0.018	87
Ca ²⁺ - C12	0.027	81	0.027	81	0.015	90
Mg ²⁺ - C12	0.030	79	0.021	85	0.021	85

8.7 Specimens from the corrosion experiments under HP-HT conditions

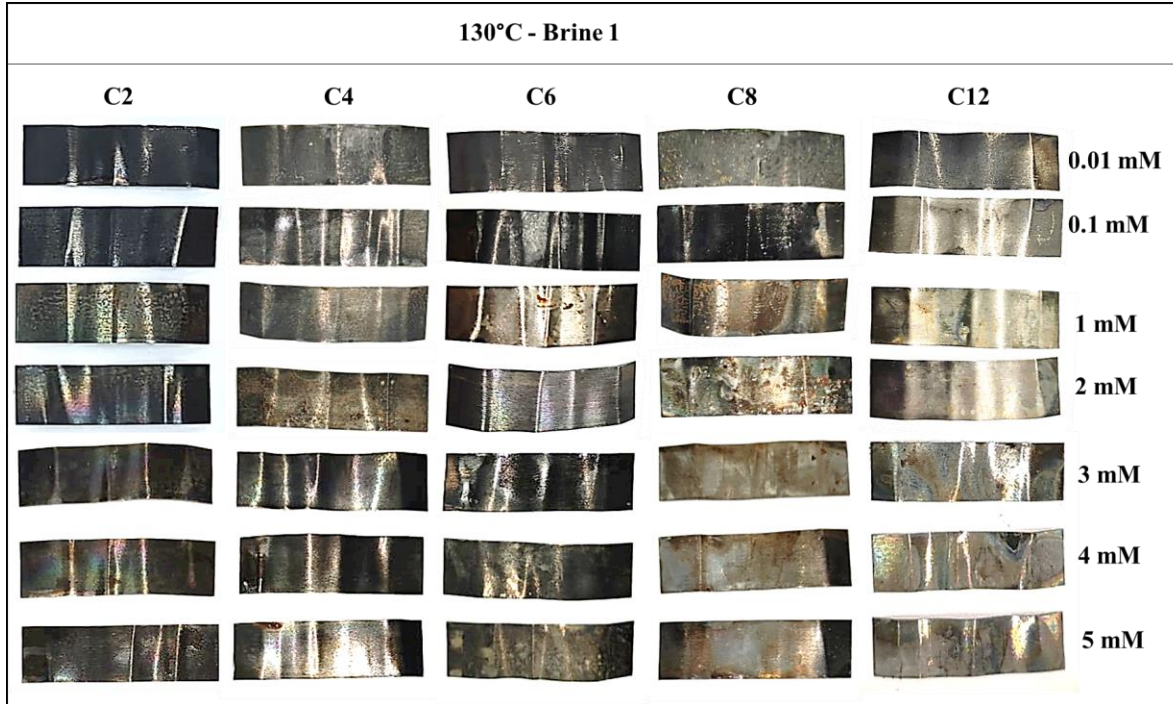


Figure 8.12. The specimens from the corrosion experiments at 130 °C in Brine 1.

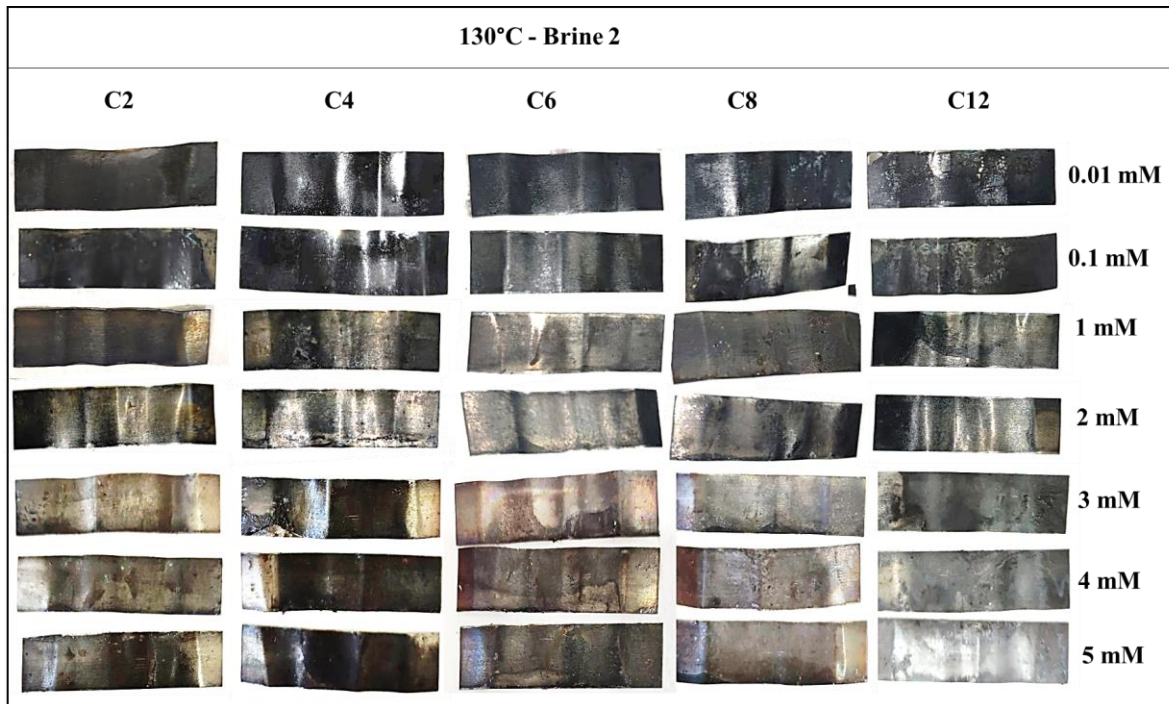


Figure 8.13. The specimens from the corrosion experiments at 130 °C in Brine 2.

8.8 Characterization of the precipitates collected from the corrosion experiments

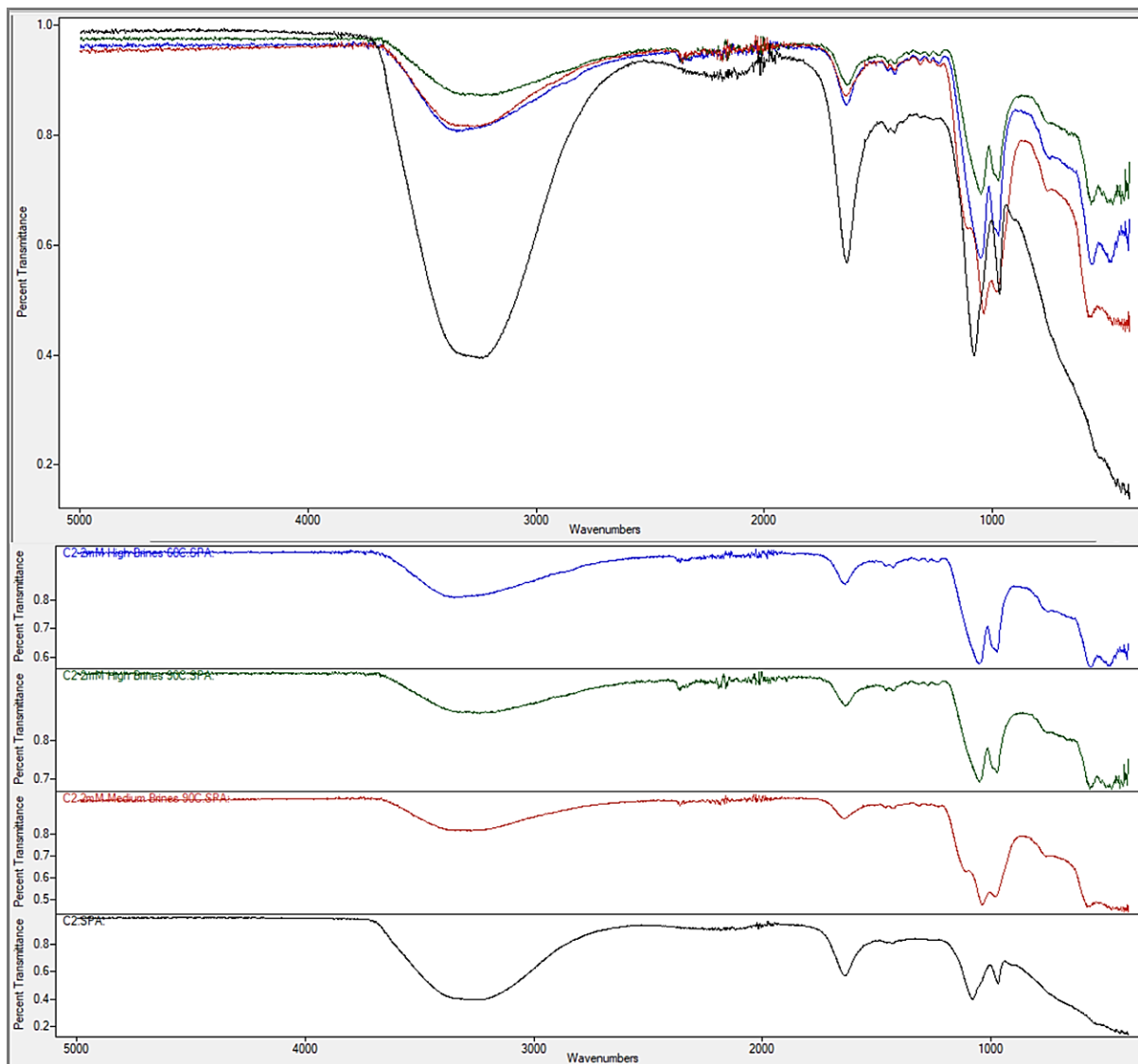


Figure 8.14. ATR-IR spectra of the precipitates collected from corrosion experiments in the presence of C2. Color codes: *black* “free” C2, *red* 2 mM C2 in Brine 1 at 90°C, *green* 2 mM C2 in Brine 2 at 90°C and *blue* 2 mM C2 in Brine 2 at 60°C.

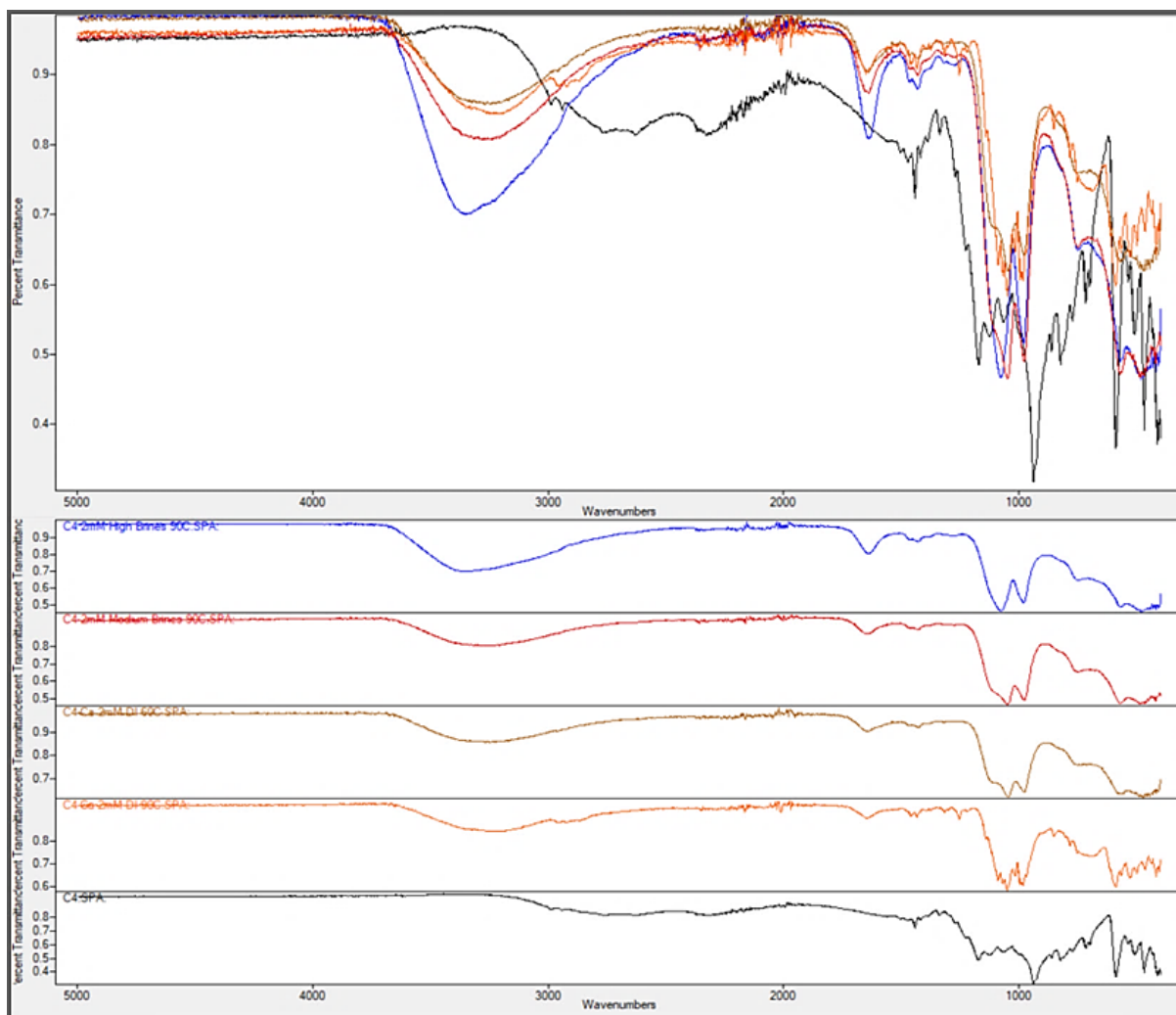


Figure 8.15. ATR-IR spectra of the precipitates collected from corrosion experiments in the presence of C4. Color codes: *black* “free” C4, *orange* 2 mM Ca²⁺-C4 in DI water at 90°C, *brown* 2 mM Ca²⁺-C4 in DI water at 60°C, *red* 2 mM C4 in Brine 1 at 90°C and *blue* 2 mM C4 in Brine 2 at 90°C,

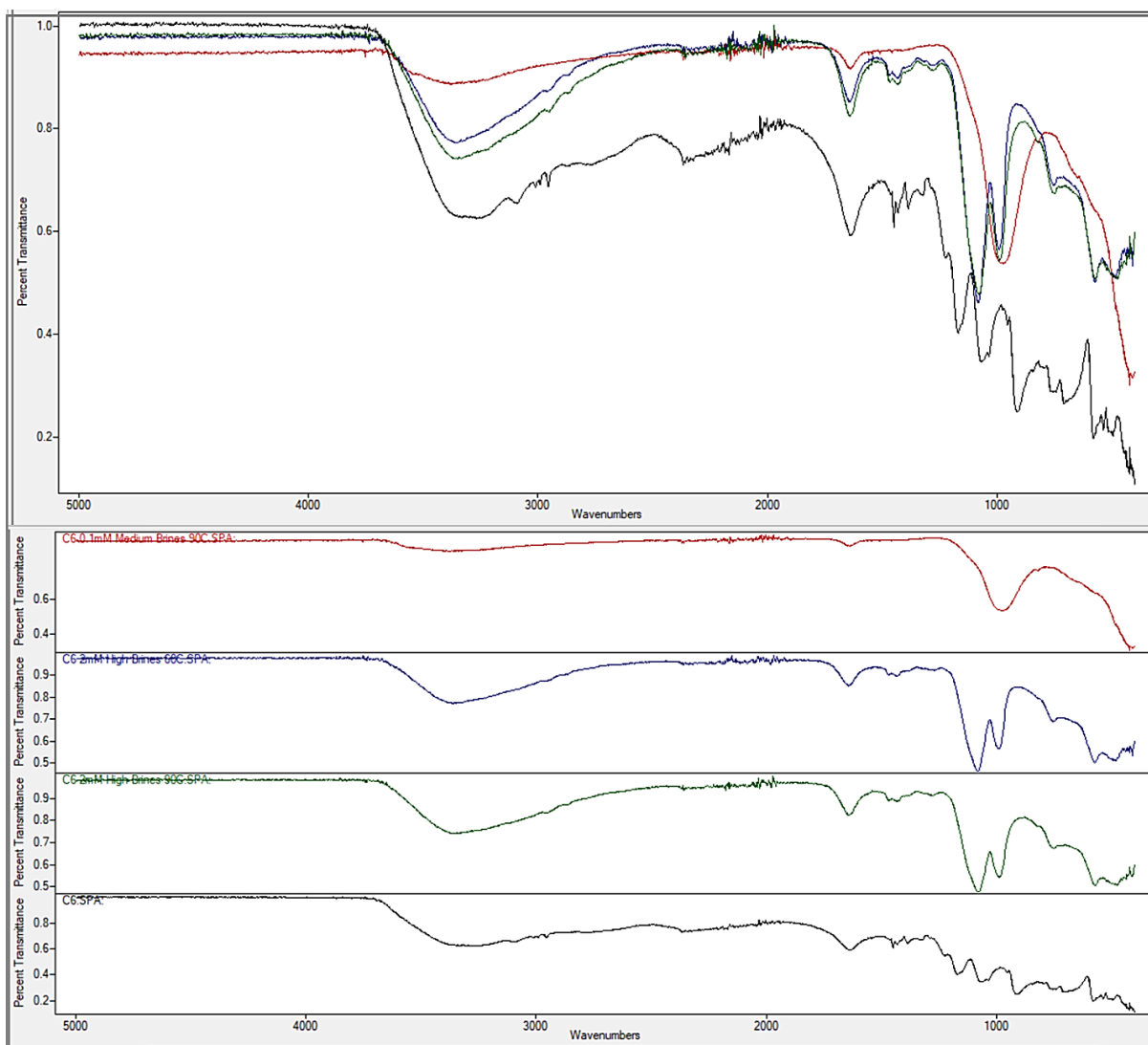


Figure 8.16. ATR-IR spectra of the precipitates collected from corrosion experiments in the presence of C6. Color codes: *black* “free” C6, *green* 2 mM C6 in Brine 2 at 90°C, *blue* 2 mM C6 in Brine 2 at 60°C and *red* 0.1 mM C6 in Brine 1 at 90°C.

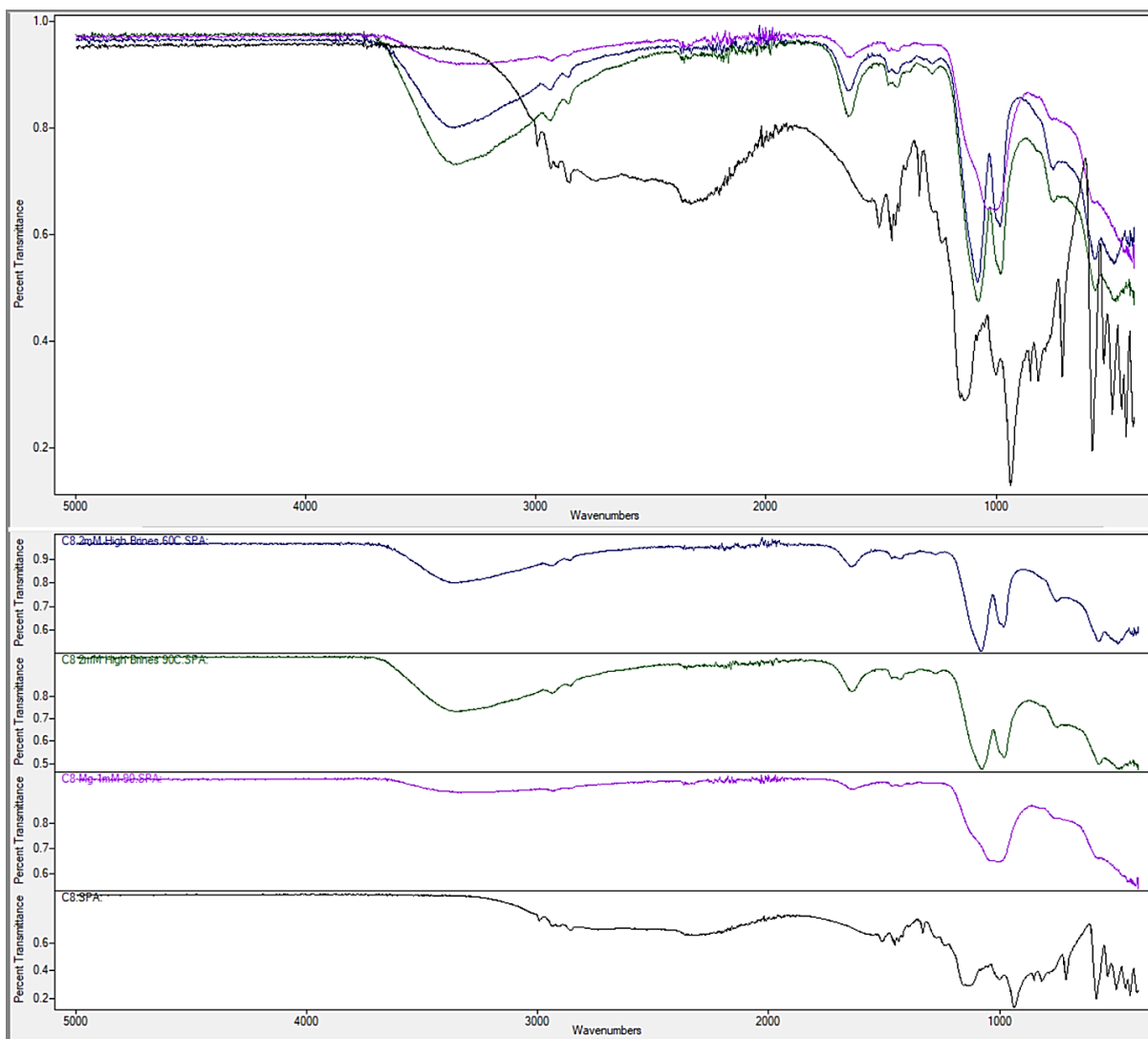


Figure 8.17. ATR-IR spectra of the precipitates collected from corrosion experiments in the presence of C8. Color codes: *black* “free” C8, *purple* 1 mM Mg²⁺-C8 in DI water at 90°C, *green* 2 mM C8 in Brine 2 at 90°C and *blue* 2 mM C8 in Brine 2 at 60°C.

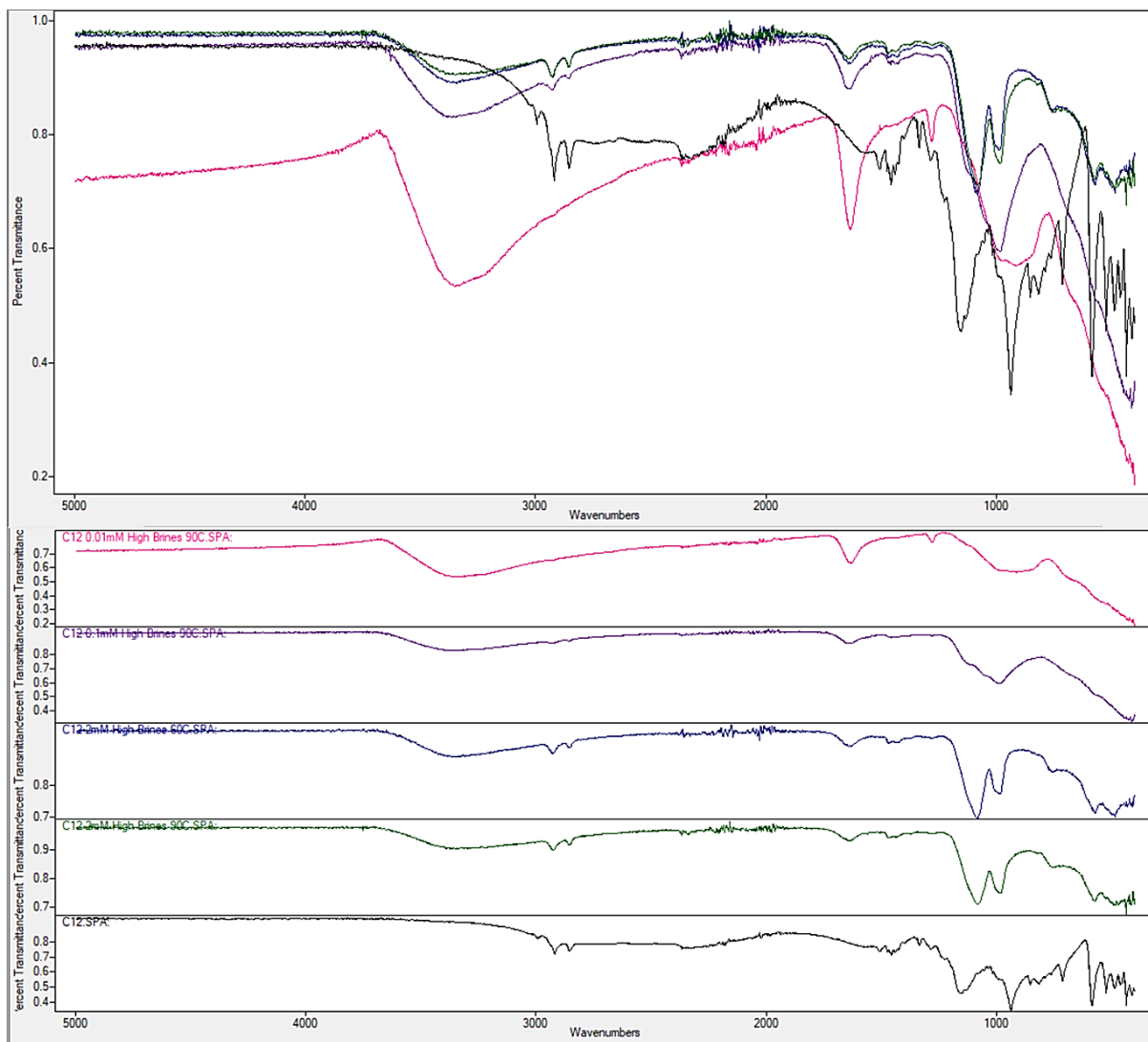


Figure 8.18. ATR-IR spectra of the precipitates collected from corrosion experiments in the presence of C12. Color codes: *black* “free” C12, *green* 2 mM C12 in Brine 2 at 90°C, *blue* 2 mM C12 in Brine 2 at 60°C, *purple* 0.1 mM C12 in Brine 2 at 90°C and *pink* 0.01 mM C12 in Brine 2 at 90°C.

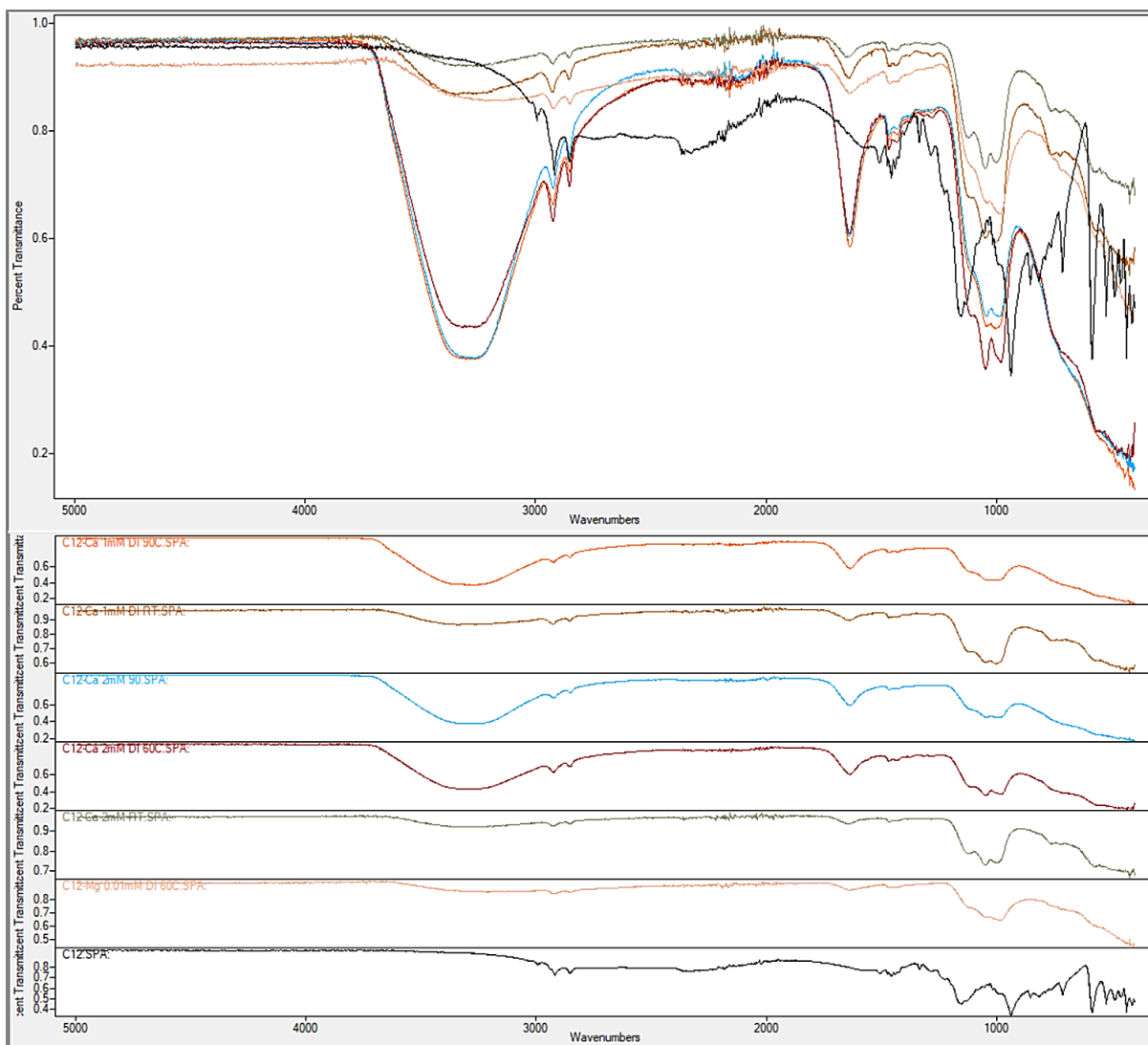


Figure 8.19. ATR-IR spectra of the precipitates collected from corrosion experiments in the presence of C12. Color codes: *black* “free” C12, *pink* 0.01 mM Mg²⁺-C12 in DI water at 60°C, *grey* 2 mM Ca²⁺-C12 in DI water at RT, *red* 2 mM Ca²⁺-C12 in DI water at 60°C, *light blue* 2 mM Ca²⁺-C12 in DI water at 90°C, *brown* 1 mM Ca²⁺-C12 in DI water at RT and *orange* 1 mM Ca²⁺-C12 in DI water at 90°C.

8.9 SEM/EDS study of the precipitates collected from the corrosion experiments

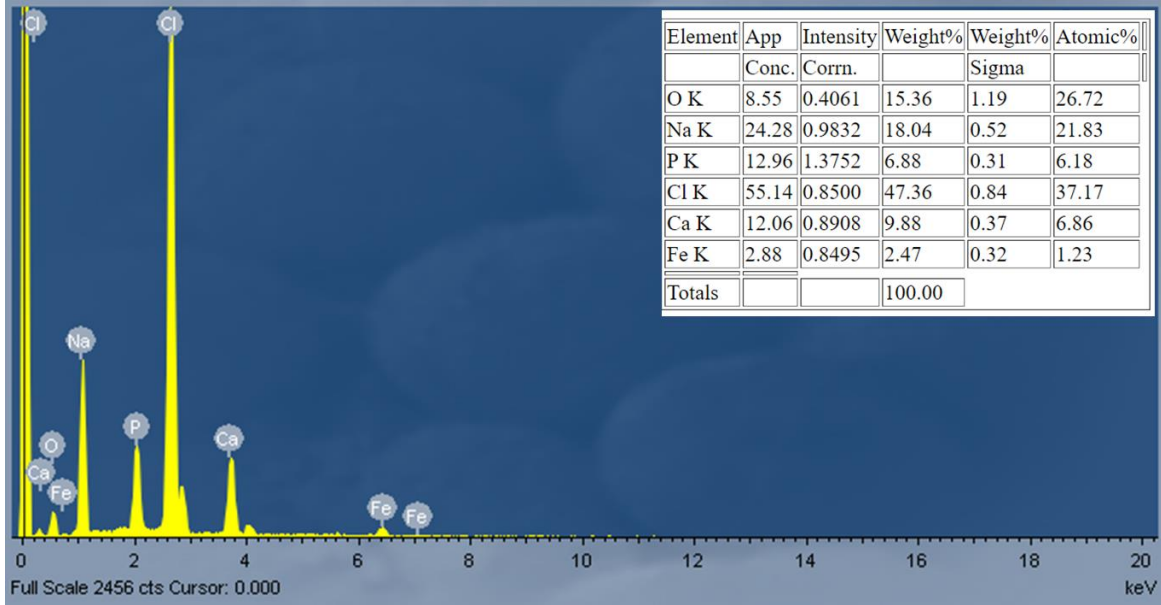


Figure 8.20. EDS data of the precipitate which collected from the corrosion experiment in the presence of 2 mM of C2 in Brine 2 at 90°C.

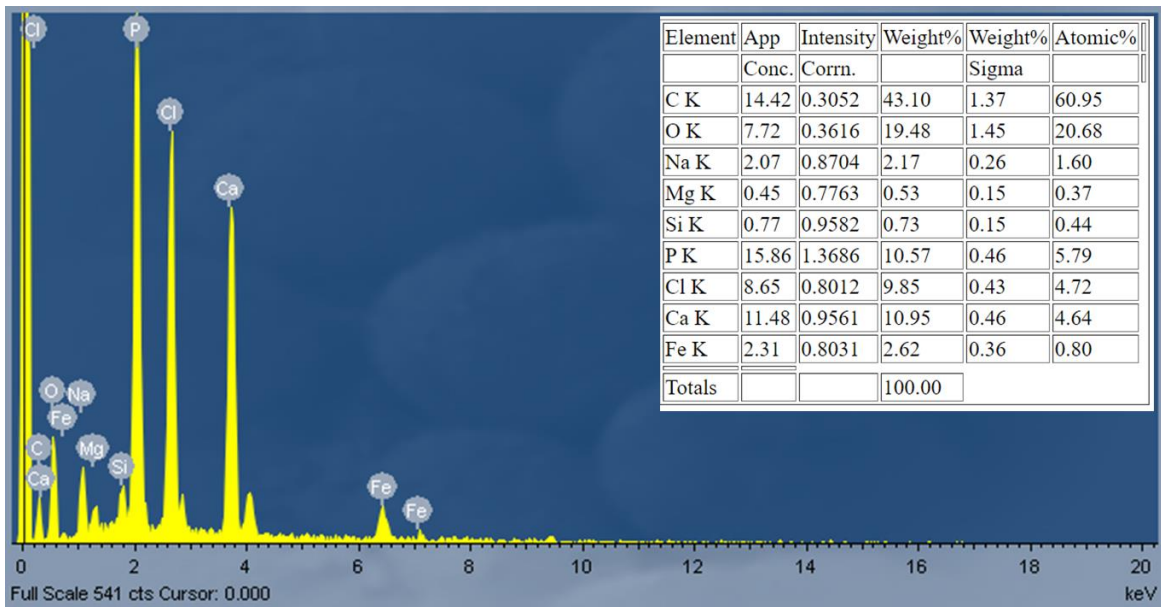


Figure 8.21. EDS data of the precipitate which collected from the corrosion experiment in the presence of 2 mM of C4 in Brine 2 at 90°C.

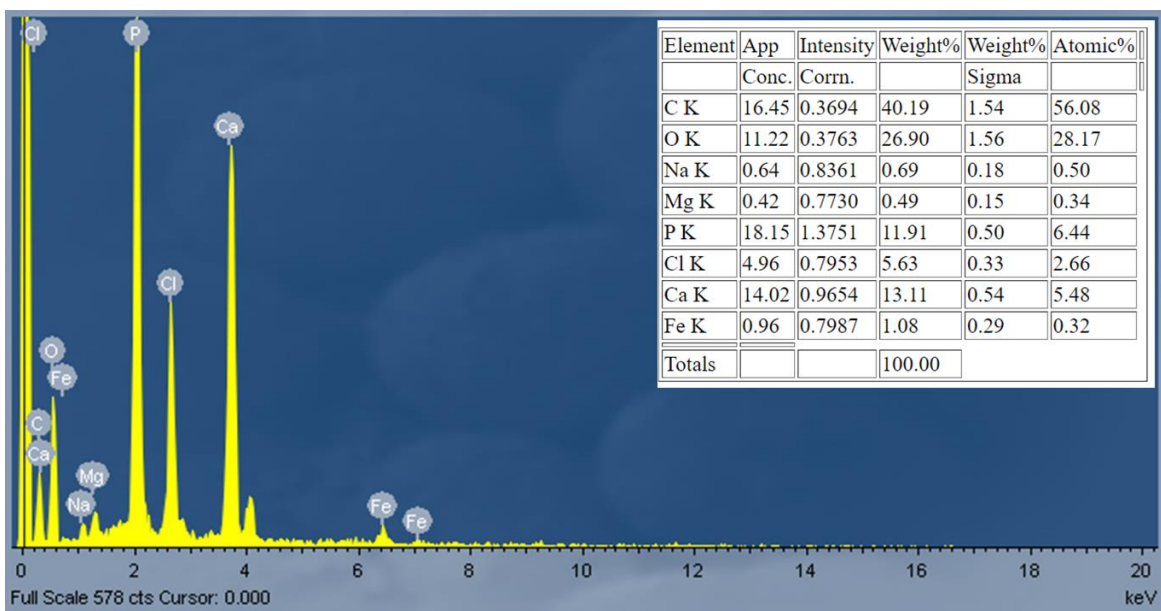


Figure 8.22. EDS data of the precipitate which collected from the corrosion experiment in the presence of 2 mM of C6 in Brine 2 at 90°C.

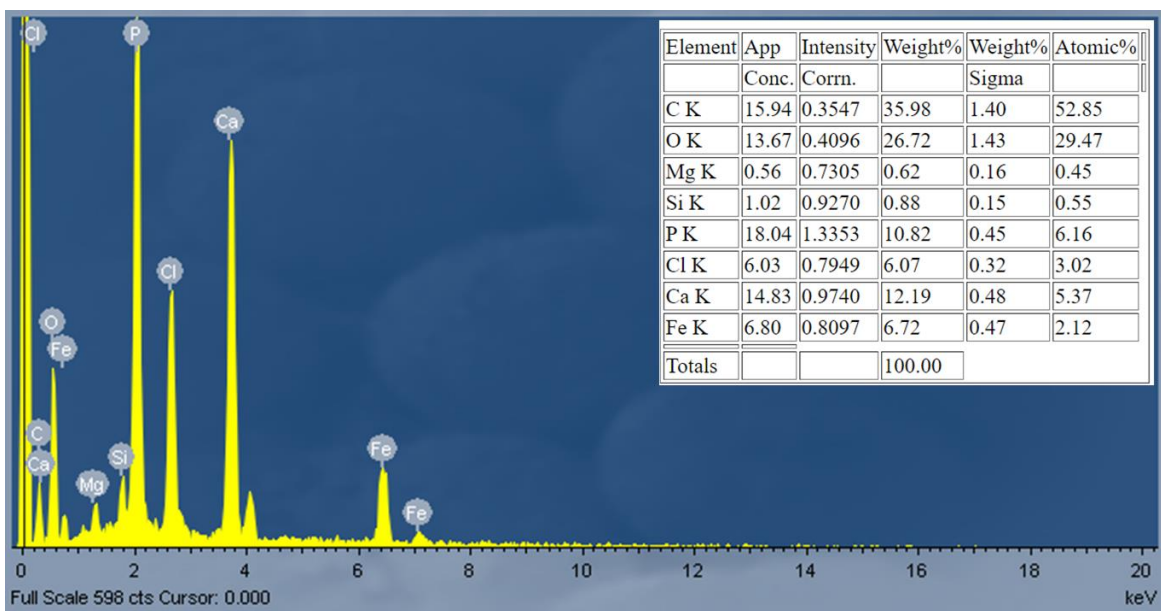


Figure 8.23. EDS data of the precipitate which collected from the corrosion experiment in the presence of 2 mM of C8 in Brine 2 at 90°C.

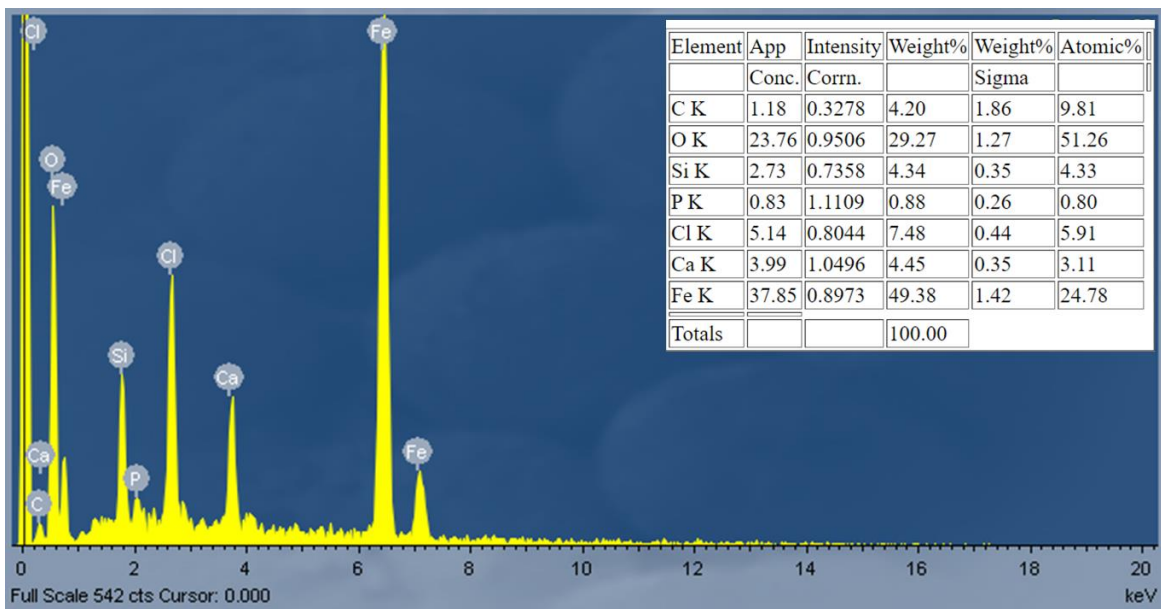


Figure 8.24. EDS data of the precipitate which collected from the corrosion experiment in the presence of 0.01 mM of C12 in Brine 2 at 90°C.

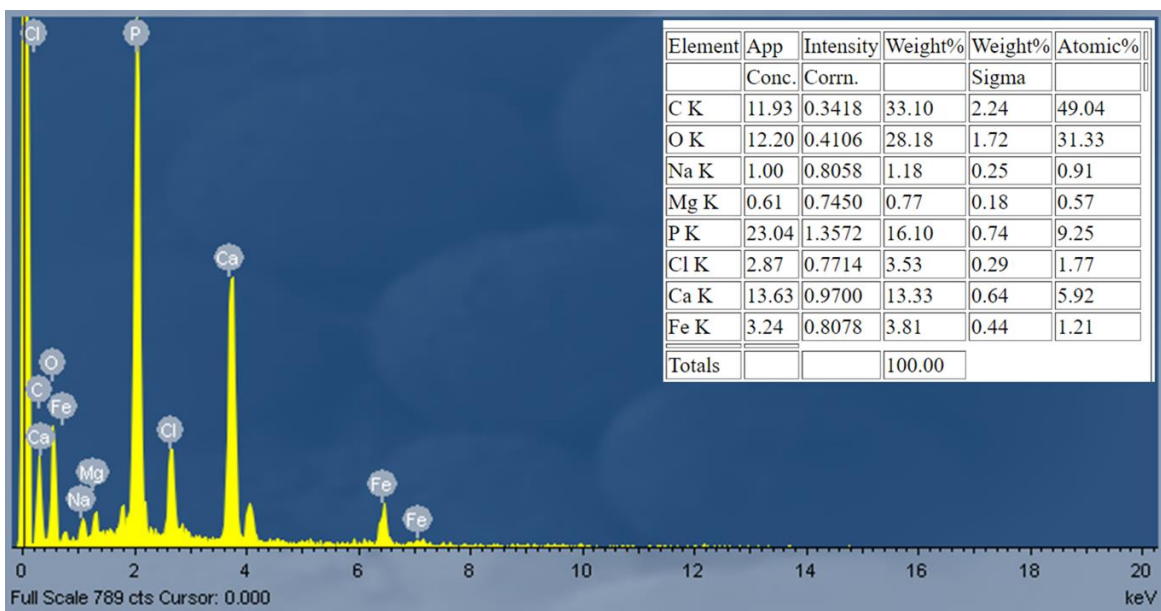


Figure 8.25. EDS data of the precipitate which collected from the corrosion experiment in the presence of 2 mM of C12 in Brine 2 at 90°C.

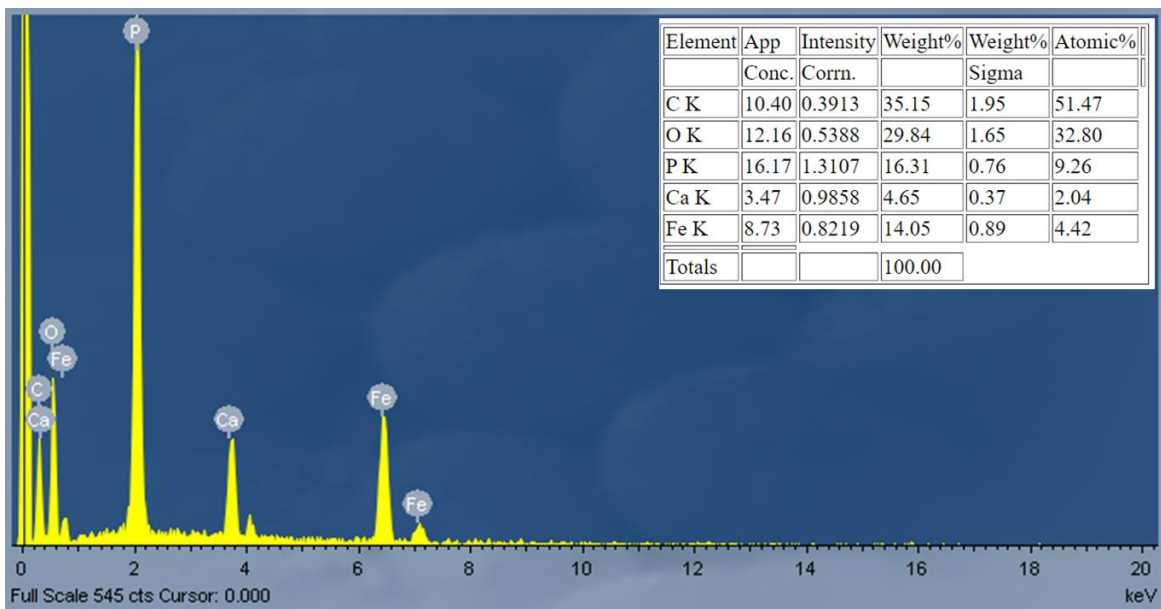


Figure 8.26. EDS data of the precipitate which collected from the corrosion experiment in the presence of 1 mM of Ca^{2+} -C12 (1:1 molar ratio) in DI water at RT.

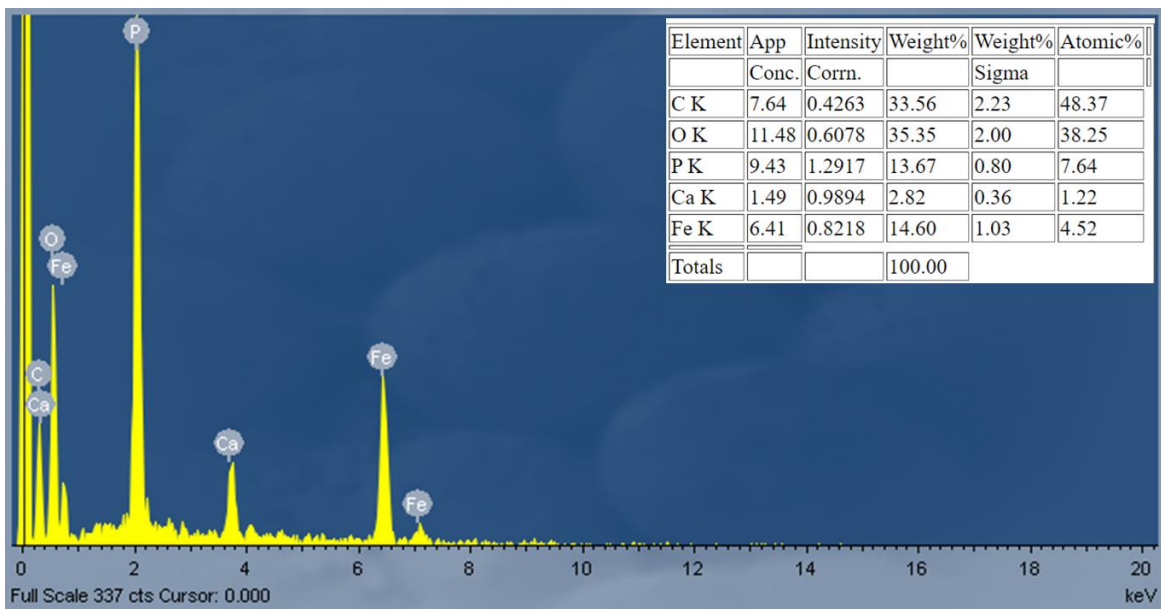


Figure 8.27. EDS data of the precipitate which collected from the corrosion experiment in the presence of 2 mM of Ca^{2+} -C12 (1:1 molar ratio) in DI water at 60°C.

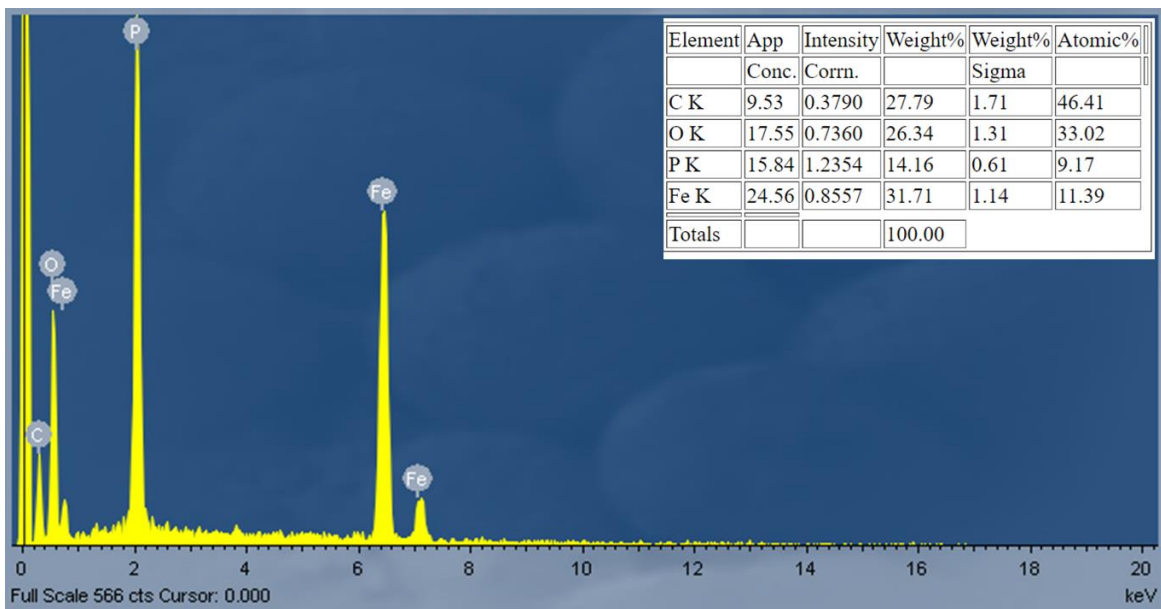


Figure 8.28. EDS data of the precipitate which collected from the corrosion experiment in the presence of 0.01 mM of Mg^{2+} -C12 (1:1 molar ratio) in DI water at 60°C.

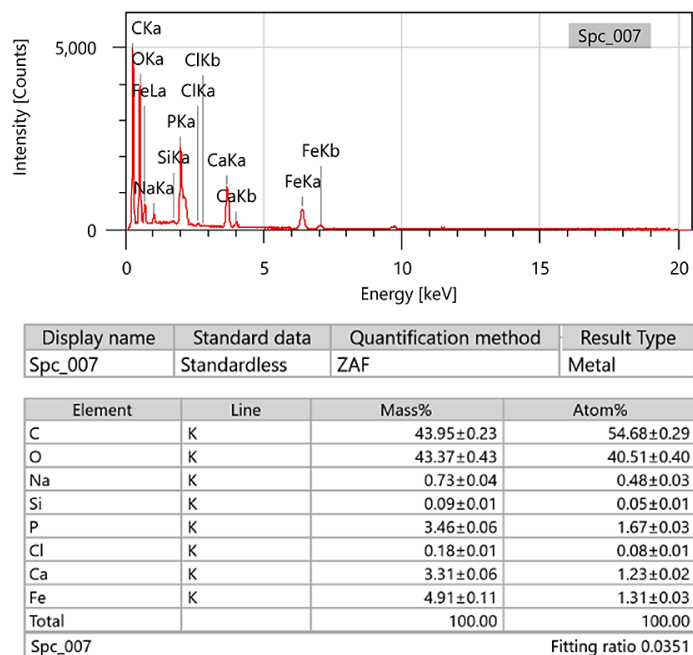


Figure 8.29. EDS data of the precipitate which collected from the corrosion experiment in the presence of 1 mM of C2 in Brine 1 at RT.

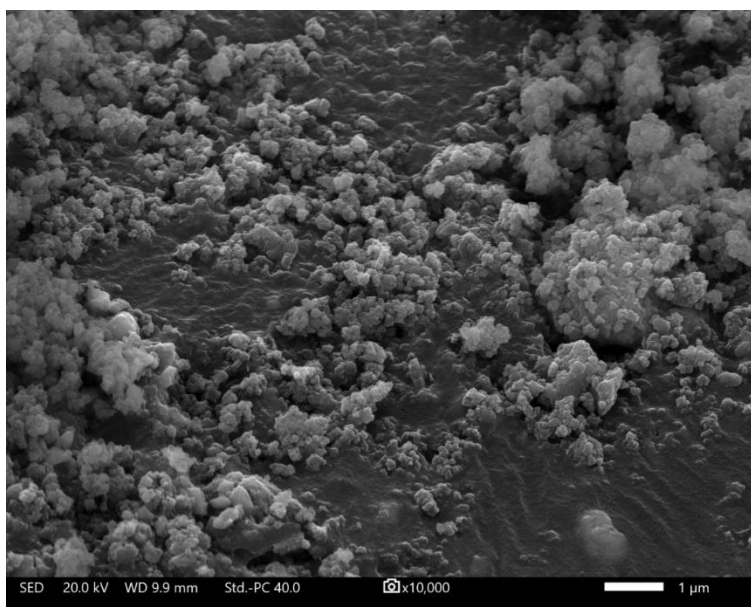


Figure 8.30. SEM image of the precipitate which collected from the corrosion experiment in the presence of 1 mM of C2 in Brine 1 at RT.

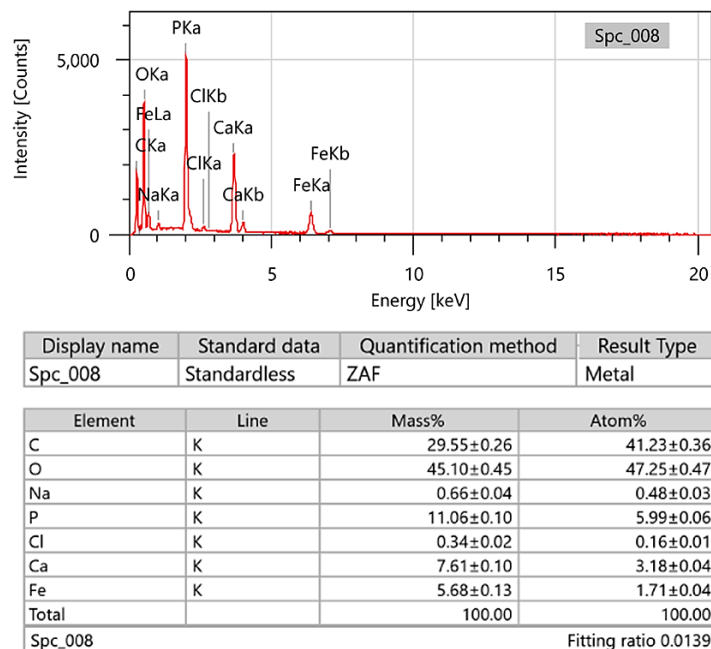


Figure 8.31. EDS data of the precipitate which collected from the corrosion experiment in the presence of 1 mM of C4 in Brine 1 at RT.

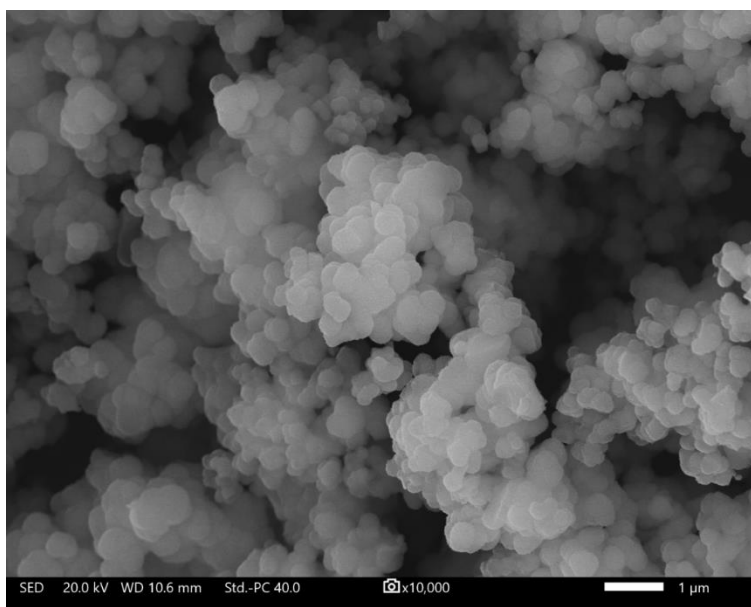


Figure 8.32. SEM image of the precipitate which collected from the corrosion experiment in the presence of 1 mM of C4 in Brine 1 at RT.

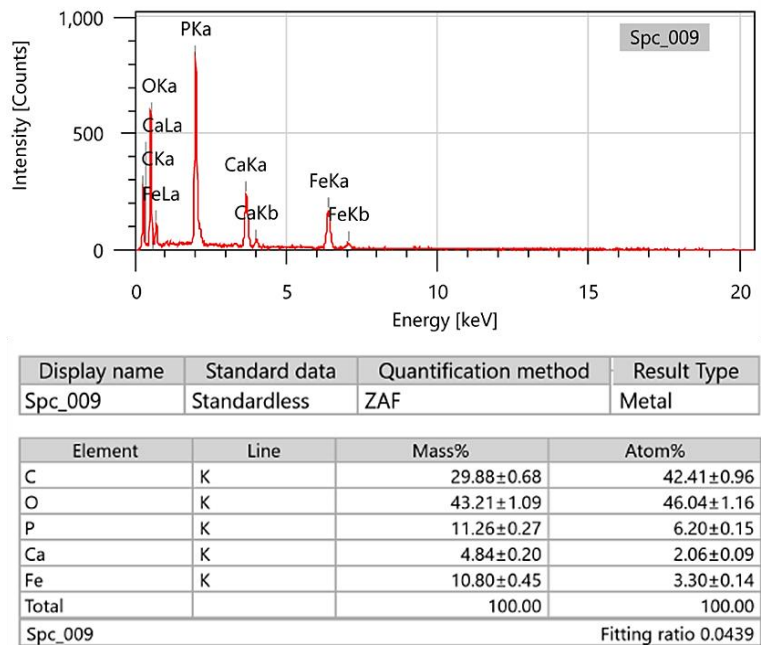


Figure 8.33. EDS data of the precipitate which collected from the corrosion experiment in the presence of 1 mM of C6 in Brine 1 at RT.

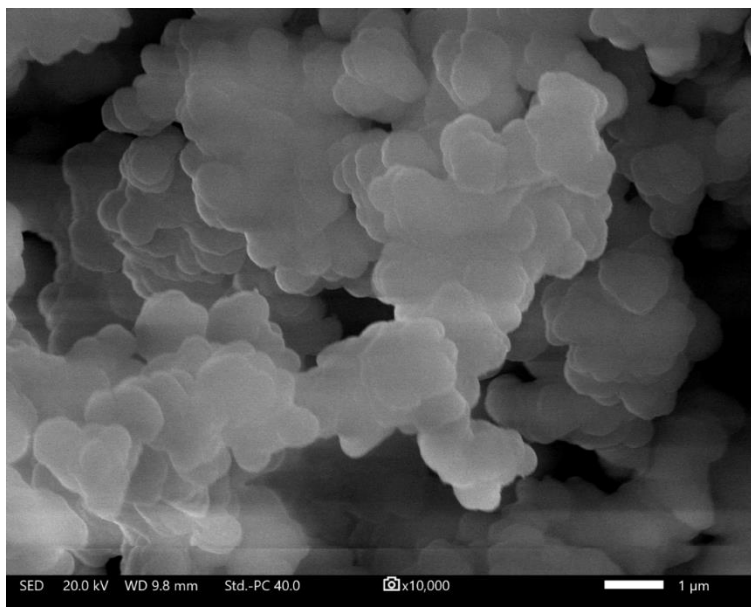


Figure 8.34. SEM image of the precipitate which collected from the corrosion experiment in the presence of 1 mM of C6 in Brine 1 at RT.

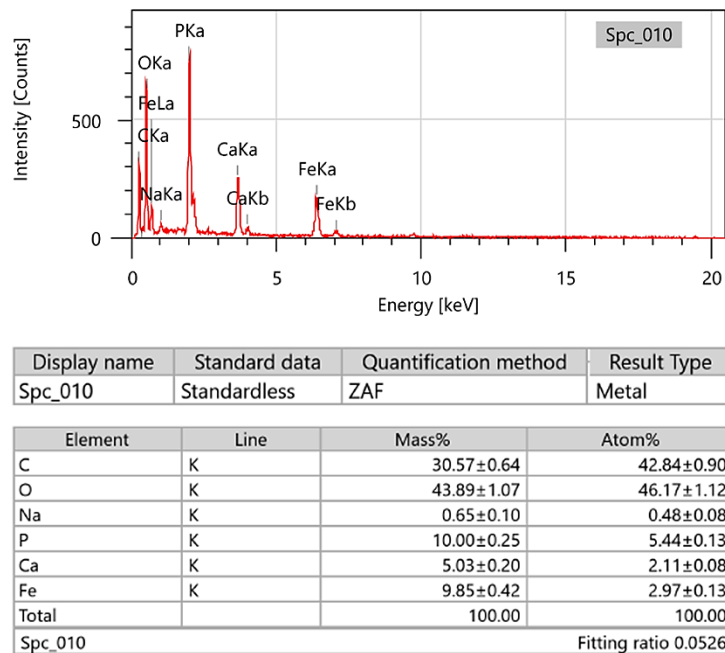


Figure 8.35. EDS data of the precipitate which collected from the corrosion experiment in the presence of 1 mM of C8 in Brine 1 at RT.

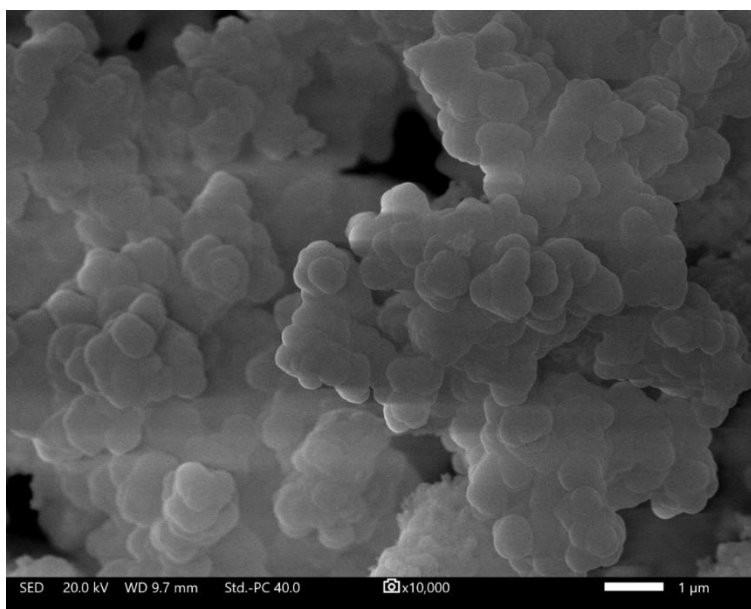


Figure 8.36. SEM image of the precipitate which collected from the corrosion experiment in the presence of 1 mM of C8 in Brine 1 at RT.

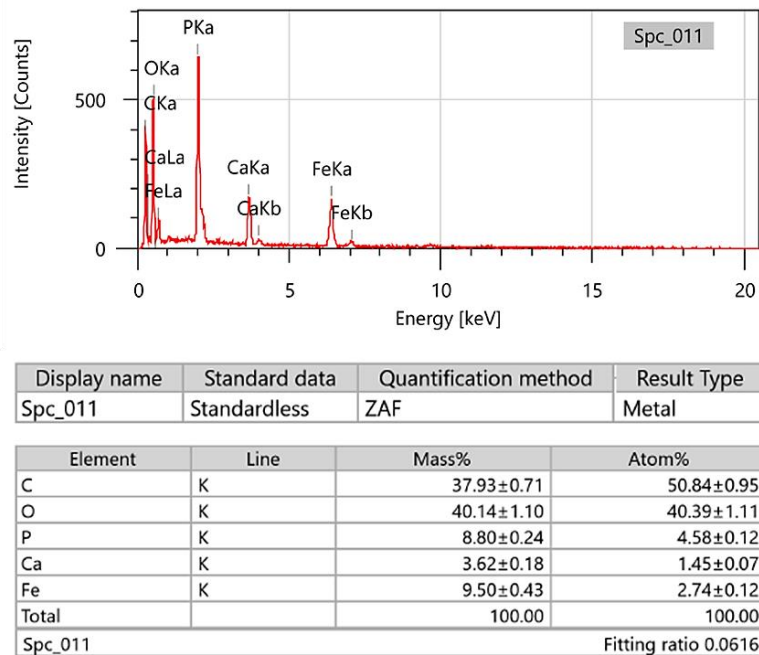


Figure 8.37. EDS data of the precipitate which collected from the corrosion experiment in the presence of 1 mM of C12 in Brine 1 at RT.

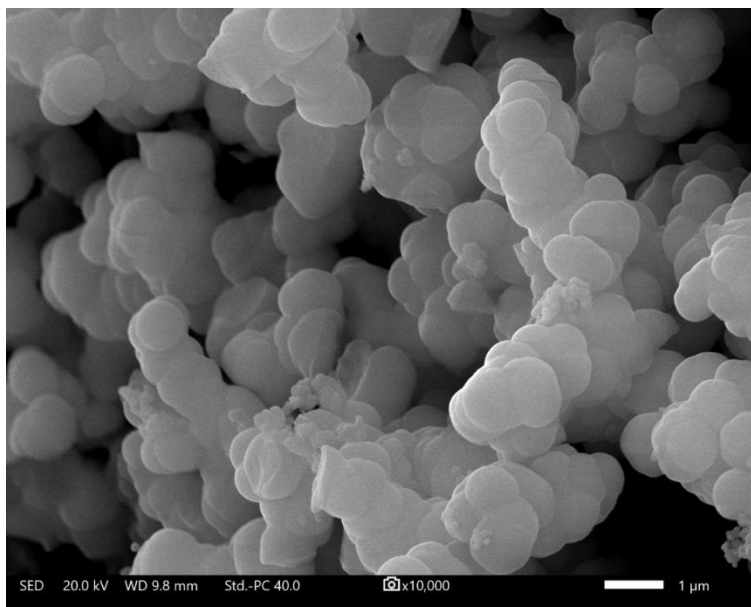


Figure 8.38. SEM image of the precipitate which collected from the corrosion experiment in the presence of 1 mM of C12 in Brine 1 at RT.